

Mechanistic Understanding of Colloidal III-V Semiconductor Quantum Dots formation

A Thesis Submitted

To

Sikkim University



In Partial Fulfilment of the Requirement for the
Degree of Doctor of Philosophy

By

Siddhant Basel

Department of Chemistry
School of Physical sciences

May 2023

Dedicated to my parents...

Sunil Basel and Usha Basel

6 माइल, सामदुर, तादोंग -737102
गंगटोक, सिक्किम, भारत
फोन-03592-251212, 251415, 251656
टेलीफैक्स -251067
वेबसाइट - www.cus.ac.in



6th Mile, Samdur, Tadong -737102
Gangtok, Sikkim, India
Ph. 03592-251212, 251415, 251656
Telefax: 251067
Website: www.cus.ac.in

सिक्किम विश्वविद्यालय SIKKIM UNIVERSITY

(भारत के संसद के अधिनियम द्वारा वर्ष 2007 में स्थापित और नैक (एनएएसी) द्वारा वर्ष 2015 में प्रत्यायित केंद्रीय विश्वविद्यालय)
(A central university established by an Act of Parliament of India in 2007 and accredited by NAAC in 2015)

DECLARATION

The Ph.D. Thesis entitled "*Mechanistic Understanding of Colloidal III-V Semiconductor Quantum Dots formation*" has been solely prepared by me under the supervision of Dr. Sudarsan Tamang, Assistant Professor, Department of Chemistry, Sikkim University. No part of this work has been submitted previously for fulfilment of any other degree, diploma, associate or fellowship

Siddhant Basel

Siddhant Basel

Roll no: 16PDCH03

Reg no: 16/PhD./CMS/03

Department of Chemistry,
School of Physical Sciences,
Sikkim University.

Place: Sikkim University, Gangtok
Date: 26th April 2023

We recommend that this thesis be placed before examiners for evaluation

Dr. Sudarsan Tamang
Supervisor
(Dr. Sudarsan Tamang)
26/4/23

Prof. Sanjay Dahal
27/4/23
Head of the Department
(Prof. Sanjay Dahal)

6 माइल, सामदुर, तादोंग -737102
गंगटोक, सिक्किम, भारत
फोन-03592-251212, 251415, 251656
टेलीफैक्स -251067
वेबसाइट - www.cus.ac.in



6th Mile, Samdur, Tadong -737102
Gangtok, Sikkim, India
Ph. 03592-251212, 251415, 251656
Telefax: 251067
Website: www.cus.ac.in

सिक्किम विश्वविद्यालय SIKKIM UNIVERSITY

(भारत के संसद के अधिनियम द्वारा वर्ष 2007 में स्थापित और नैक (एनएएसी) द्वारा वर्ष 2015 में प्रत्यायित केंद्रीय विश्वविद्यालय)
(A central university established by an Act of Parliament of India in 2007 and accredited by NAAC in 2015)

CERTIFICATE

This is to certify that the thesis entitled "*Mechanistic Understanding of Colloidal III-V Semiconductor Quantum Dots formation*" submitted to **Sikkim University** for the award of **Doctor of Philosophy, Ph.D. in Chemistry** is a result of *bonafide* research work carried out by **Mr. Siddhant Basel** under my supervision in the **Department of Chemistry, Sikkim University**. No part of this dissertation has not been previously submitted for any degree, diploma, associateship, or fellowship.

26/4/23
Dr. Sudarsan Tamang

Assistant Professor,
Department of Chemistry,
School of Physical Sciences
Sikkim University
Sikkim, India - 737102

Place: Sikkim University, Gangtok
Date: 26th April, 2023

6 माइल, सामदुर, तादोंग -737102
गंगटोक, सिक्किम, भारत
फोन-03592-251212, 251415, 251656
टेलीफैक्स -251067
वेबसाइट - www.cus.ac.in



6th Mile, Samdur, Tadong -737102
Gangtok, Sikkim, India
Ph. 03592-251212, 251415, 251656
Telefax: 251067
Website: www.cus.ac.in

सिक्किम विश्वविद्यालय SIKKIM UNIVERSITY

(भारत के संसद के अधिनियम द्वारा वर्ष 2007 में स्थापित और नैक (एनएएसी) द्वारा वर्ष 2015 में प्रत्यायित केंद्रीय विश्वविद्यालय)
(A central university established by an Act of Parliament of India in 2007 and accredited by NAAC in 2015)

Date: 26th April 2023

PLAGIARISM CHECK REPORT

This is to certify that plagiarism check has been carried out for the following Ph.D. Thesis with the help of **URKUND Software** and the result is 1%, which is within the permissible limit (below 10% tolerance rate) as per the norms of Sikkim University.

“Mechanistic Understanding of Colloidal III-V Semiconductor Quantum Dots formation”

Submitted by, **Siddhant Basel** under the supervision of **Dr. Sudarsan Tamang, Assistant Professor, Department of Chemistry, School of Physical Sciences, Sikkim University, Gangtok.**

Siddhant Basel

(Siddhant Basel)

Signature of Research Scholar

Sudarsan Tamang 26/4/23

(Dr. Sudarsan Tamang)

Signature of Supervisor

[Signature]

Vetted by Librarian

केंद्रीय पुस्तकालय Central Library
सिक्किम विश्वविद्यालय
Sikkim University

Acknowledgement

Completing a Ph.D. is a challenging and rewarding journey that requires the support and encouragement of many individuals and institutions. Expressing gratitude towards the individuals who have played a part in shaping the experience, facilitating the completion of the work, and providing ongoing assistance serves as a testament to the significance of acknowledging and thanking those who have contributed to a successful Ph.D. journey.

I would like to express my sincere gratitude to **Dr. Sudarsan Tamang** for his exceptional guidance, mentorship, and support throughout my Ph.D. journey. His enthusiasm for science, keen understanding of the research, and adept management of the team, even in adverse circumstances, are admirable. Throughout my Ph.D., his meticulous and organized approach has been invaluable, and I have learned so much from his guidance. I am grateful for the opportunity to work in his functional material team, where I have never stopped learning and growing. I am forever indebted to him for his leadership qualities, composed nature, and profound knowledge of nano chemistry.

I thank **Dr. Anand Pariyar** for his invaluable suggestions and guidance. He has been an exceptional mentor to me, providing clear explanations for anything I did not comprehend, without making me feel inadequate. I am extremely appreciative of the smooth administrative assistance and research amenities provided to me by **Sikkim University**. I extend my heartfelt gratitude to **Prof. Sanjay Dahal**, the Head of the Department of Chemistry, Sikkim University, for his unceasing guidance. I owe a great debt to all the other faculty members of the Department of Chemistry, namely **Dr. Biswajit Gopal Roy, Dr. Somendra Nath Chakraborty, and Dr. Akhilesh**

Kumar Gupta, for their valuable comments, suggestions, and remarks. **Mr. Binod Chettri**, the Laboratory Assistant in the Department of Chemistry at Sikkim University, deserves appreciation for his considerate behaviour, prompt action, and cooperation towards fulfilling the official procedures.

I would like to express my profound gratitude towards **Dr. Sajan Pradhan** for his open-mindedness, valuable suggestions, and unwavering support throughout my academic journey. Additionally, I extend my heartfelt thanks to **Dr. Graeme Stasuik**, Associate Professor at Kings College, United Kingdom for sharing his expertise and guidance that has helped me become a capable researcher. I am also grateful to his team members, **Mitchell, Michelle**, and **Tom**, who have imparted their knowledge and taught me various research techniques.

I express my sincere gratitude to the **Department of Science and Technology**, Ministry of Science and Technology, Government of India, for awarding me the esteemed National Fellowship under DST INSPIRE program [**IF160689** (2017-2022)].

Undoubtedly, I am immensely grateful for the unwavering support and encouragement I have received from my colleagues, seniors, and juniors during my time at Sikkim University. I extend my sincerest thanks to **Debesh Sharma, Sagarmani Rasaily, Surakcha Thapa, Bikram Gurung, Karan Chhetri, Shivanand Chettri, Deshaj Bhujel, Sailendra Pradhan, Subas Chandra Mohanta, Dr. Samuzal Bhuyan, Susanta Mandal, Karishma Bhardwaj** and **Nobina Regmi** from the Department of Chemistry at Sikkim University, who have been a constant source of inspiration and support for me. Their guidance and assistance have truly been invaluable to me, and I will always cherish their contributions. Additionally, I am deeply grateful to **Dr. Ranjan Kaushal Tirwa** and **Dr. Sayak Das** from the

Department of Microbiology, Sikkim University, and **Dr. Prajwal Chettri** from the Department of Physics, Sikkim University, for their continuous encouragement and support. I could not have asked for a better environment to work in, and I am extremely fortunate to have made lifelong friends and learned valuable lessons in research aptitude from my like-minded colleagues across various departments during my time here.

I express my sincere gratitude to all the **teachers** of my alma mater (**Mount View school, Saint Robert's H.S. School, and Saint Joseph's College, Darjeeling**) whom have played a significant role in shaping my academic journey. Without the guidance and knowledge imparted by my teachers, I would not have been able to develop the skills and abilities necessary to complete this thesis.

I am deeply grateful for the untiring support and love of my family throughout my academic journey. I would like to express my deepest appreciation to my dear parents, **Shri. Sunil Basel** and **Smt. Usha Basel**, and my dear brother, **Dr. Sayel Basel**, for their constant encouragement and sacrifices. Without their guidance and emotional support, I would not have been able to made such accomplishments. Their presence in my life means everything to me and I cannot thank them enough for always being there for me.

I would like to extend my deepest gratitude to my dear wife, **Anuja Dutraj** for her love and support during the toughest times. Her constant presence has been my anchor, and without her, the path would have been incredibly challenging. Finally, I thank her for more things than space allows, but mostly for her love and support.

Siddhant Basel
Sikkim University
Date: 26th April 2023

Abstract

Colloidal semiconductor nanocrystals are versatile materials for applications in electronic devices and biological imaging. Among these nanocrystals, III-V semiconductor nanocrystals are a unique type of semiconductor material that is relatively non-toxic and possess excellent properties such as size-dependent electrical and optical, direct band gap, high Bohr's exciton radii and high carrier charge mobility. However, their colloidal synthesis is rather difficult compared to other types of semiconductors such as II-IV and IV-VI due to their covalent nature. Previous mechanistic studies of III-V semiconductor nanocrystals have extensively investigated the role of group V precursor, but have overlooked the influence of the group III precursor on the size and size distribution of III-V nanocrystals. Also, the existing vacuum method for preparing metal salts of fatty acids for colloidal III-V quantum dot synthesis is not well-defined in terms of product purity and composition. The central focus of this thesis is to conduct a comprehensive investigation into the formation of III-V colloidal quantum dots which involves (a) the rational design of precursors, (b) an analysis of the impact of group III precursor reactivity on the size and size distribution of the nanocrystals, as well as (c) an examination of the intermediate clusters.

We successfully developed a facile one-step method to synthesize highly pure group III precursor from the reaction of fatty acids and metal salts in the presence of 1,8-diazabicyclo[5.4.0]undec-7-ene as a base catalyst. The method is general and highly scalable. We prepared a variety of group III precursors with different reactivity and polarity such as alpha halide substituted indium tri-myristates, partially substituted indium myristates (containing less than three myristic acid groups per metal ion) and

9, 10-dihydroxy substituted indium stearate. Compared to the reaction of tris(trimethylsilyl)phosphine with indium myristate prepared *in situ* using the vacuum method, pure indium myristate precursor prepared using 1,8-diazabicyclo[5.4.0]undec-7-ene as the catalyst, formed larger and slightly more uniformly sized nanocrystals. The alpha halide substituted indium myristates, partially substituted indium myristates (containing less than three myristic acid groups) and 9, 10-dihydroxy indium stearate produced highly polydisperse nanocrystals. Indium precursors containing longer chain carboxylates (e.g., indium stearates) formed thermally less stable magic-sized clusters and subsequently led to a decrease in the size distribution of the nanocrystals. Interestingly, primary amines destabilized magic-sized clusters. This explains why quantum dots are, in general, formed at lower temperatures when the primary amine is present. The magic-sized clusters were isolated and used as monomer sources for the growth of InAs and InP nanocrystals. While the size-focussing growth phenomenon was observed in the case of InAs nanocrystals, in the case of InP nanocrystals, no such effect was observed indicating strong surface effects in the latter case.

Table of Content

<i>Contents</i>	<i>Page No.</i>
Abstract	<i>ix</i>
List of Figures	<i>xvi</i>
List of Tables	<i>xxv</i>
List of Schemes	<i>xxvi</i>
List of Abbreviations, Symbols and Acronyms	<i>xxvii</i>
Chapter I: General Introduction.	1-37
1.1. Background.	2-3
1.2. Quantum dots.	4-16
1.2.1. Definition and Overview.	4-5
1.2.2. Quantum Confinement Effect.	6-8
1.2.3. Synthesis.	8-10
1.2.3.1. Hot Injection Method.	9-10
1.2.4. Mechanistic Studies.	10-16
1.2.4.1. Nucleation.	10-12
1.2.4.2. Growth.	12-16
1.2.4.2.1. Diffusion-controlled growth.	13-14
1.2.4.2.2. Reaction/ Surface controlled growth.	14-14
1.2.4.2.3. Gibbs Thomson effect.	14-16
1.3. Magic-Sized Clusters (MSCs).	16-18
1.4. III-V semiconductor NCs.	18-20

1.5. Research outline.	20-20
1.6. References.	21-37
Chapter II: Preparation of precursor of CQDs synthesis.	38-87
2.1. Introduction.	39-43
2.1.1. Saponification method.	40-40
2.1.2. Double decomposition or precipitation method.	40-41
2.1.3. Fusion method.	41-41
2.1.4. Direct reaction of fatty acid with metal.	42-42
2.1.5. Vacuum method.	42-43
2.2. Determination of purity of MFAs prepared by vacuum method.	43-44
2.3. Preparation of MFAs from combined saponification and double decomposition methods.	45-49
2.4. DBU-catalysed synthesis of MFAs.	49-59
2.4.1. Optimization studies.	51-53
2.4.2. Substrate scope.	53-57
2.4.3. Mechanism.	58-58
2.4.4. Multi-gram scale synthesis.	59-59
2.5. Preparation of group V precursors.	60-62
2.5.1. Tris(trimethylsilyl) group V.	60-61
2.5.2. Tris(dialkylamino) group V.	61-62
2.6. Conclusion.	62-62
2.7. Experimental section.	62-75
2.7.1. General method.	62-64
2.7.2. Preparation of indium stearate by vacuum method.	64-64

2.7.3. Preparation of MFAs from combined saponification and double decomposition methods.	64-67
2.7.4. Preparation of MFA salts by DBU method.	67-74
2.7.5. Preparation of group V precursors.	74-75
2.8. References.	76-87
Chapter III: Role of metal precursors on size and size distribution.	88-124
3.1. Introduction.	89-94
3.2. Rationally resigned indium carboxylates for the study.	94-95
3.3. Optimization of reaction temperature of InP NCs synthesis.	95-96
3.4. Effect of indium precursor.	96-107
3.4.1. Effect of free acid on InP QDs synthesis and growth.	99-101
3.4.2. Partially-substituted indium precursor.	101-102
3.4.3. Increasing the reactivity of indium precursors.	103-107
3.5. Conclusion.	107-108
3.6. Experimental section.	108-113
3.6.1. General information.	108-109
3.6.2. Preparation of InP QDs.	109-113
3.6.3. <i>In situ</i> ¹ H NMR studies.	113-113
3.6.4. DFT calculations.	113-113
3.7. References.	114-124
Chapter IV: Effect of intermediate clusters on size.	125-162
4.1. Introduction.	126-127
4.2. Preparation and isolation of intermediate clusters.	127-130
4.3. MSCs as a single source of InP QDs synthesis.	130-137

4.3.1. In-My1, In-My2 and In-My3 precursors.	133-135
4.3.2. Mechanism of conversion of MSCs to QDs.	135-137
4.4. MSCs and QDs from pure In(My) ₃ .	137-138
4.5. Effect of carbon chain length on MSCs and QDs.	138-140
4.6. Effect of additives on MSCs and QDs synthesis.	140-143
4.6.1. Effect of primary amine.	141-141
4.6.2. Effect of phosphines.	141-143
4.7. Size-focusing growth of InP and InAs QDs.	143-146
4.8. Conclusion.	146-147
4.9. Experimental section.	147-152
4.9.1. General information.	147-148
4.9.2. Preparation of InP MSCs.	148-151
4.9.3. Preparation of InP QDs from MSCs.	152-152
4.9.4. Size-focusing growth of InP and InAs QDs.	152-152
4.10. References.	152-162
Chapter V: Synthesis of diverse CQDs using MFA as precursors.	163-177
5.1. Introduction.	164-164
5.2. Preparation of different colloidal NCs from as-synthesized MFAs.	164-168
5.3. Conclusion.	168-168
5.4. Experimental section.	169-173
5.4.1. General information.	169-169
5.4.2. Preparation of colloidal NCs.	169-173
5.5. References.	173-177
<i>Annexure A: Instrumentation and additional information.</i>	178-269

<i>Annexure A1: Instrumentation techniques.</i>	178-210
<i>Annexure A2: Additional information for Chapter II.</i>	211-248
<i>Annexure A3: Additional information for Chapter III.</i>	249-263
<i>Annexure A4: Additional information for Chapter IV.</i>	264-269
<i>Annexure B: List of publications, patents, conferences and seminars.</i>	270-287

List of Figures

Entry	Legend	Page No.
Figure 1.1.	A brief timeline of the evolution of colloidal quantum dots research. The figure represents the seminal work and applications of quantum dots in various fields <i>viz.</i> , LEDs, biological applications, lasers, magic-sized clusters, solar cells, image sensors, display and perovskite.	3
Figure 1.2.	(a) Archetypal structural representation of semiconductor quantum dot. (b) A 5 nm PbS quantum dot stabilized by oleic acid and hydroxyl ions obtained through computational studies.	4
Figure 1.3.	Energy state in molecules, QDs and bulk semiconductors showing a discrete energy state in QDs compared to bulk semiconductors owing to its unique size-dependent properties.	6
Figure 1.4.	A representation of the hot injection method.	10
Figure 1.5.	The plot depicting the relationship between particle radius and crystallization-free energy.	11
Figure 1.6.	Growth of NCs occurs through (a) diffusion and (b) surface reaction.	12
Figure 1.7.	Characteristic absorption spectra of families of CdS MSCs showing a sharp peak at 311 and 322 nm. Reprinted (adapted) with permission from ref 94. Copyright 2018 Springer Nature.	17
Figure 1.8.	Size-dependent absorption spectra of InAs NCs. Reprinted (adapted) with permission from ref. 133. Copyright 2016 American Chemical Society.	20

Figure 2.1.	Characterization of indium stearate prepared through vacuum method. (a) Scheme for preparation of indium stearate through vacuum method. (b) TGA analysis depicts the loss of ~8% consistent with one acetate group. (c) PXRD of the residual mass obtained from TGA (red) compared with the standard In ₂ O ₃ (black, JCPDS card no.: 01-088-2160) (d) FTIR shows the impurity peak at 1726 cm ⁻¹ .	44
Figure 2.2.	(a) FTIR to myristic acid (grey), and indium myristate (red) shows the major carbonyl shift of myristic acid with the addition of respective metals. (b) TGA of indium myristate depicting an initial loss of ~72% consistent with two myristate groups (75%) and a final loss of ~6% consistent with one chloride group (6%). (c) ESIMS of as-synthesized indium myristate shows the molecular ion peak at 622 which accounts for In(OCOC ₁₃ H ₂₇) ₂ Cl + H ₂ O (M + H ₂ O).	46
Figure 2.3.	(a) Comparative FTIR spectrum of myristic acid (grey), and indium myristate (red) showing the significant shift in carbonyl peak (1710 cm ⁻¹) of myristic acid confirming the addition of metal. (b) TGA thermogram of as-synthesized indium myristate with total loss of ~85% consistent with three myristate groups.	48
Figure 2.4.	Characterization of as-synthesized indium stearate (2.4.2a). (a) FTIR of stearic acid (grey) and indium stearate (red) showing some signature stretching and bending peaks. (b) TGA thermogram of indium stearate with the loss of 85% weight consistent with three stearates. (c) ¹ H NMR in presence of internal standard 1,3,5-trimethoxybenzene (1 mmol) suggesting the presence of three stearates (1 mmol).	51

Figure 2.5.	(a) A plausible mechanism for the formation of MFAs in presence of DBU as a catalyst. The substrate and intermediates are colours in grey, red, blue and green for co-relating them with their corresponding FTIR. (b) FTIR of stearic acid (grey) with signature carbonyl stretching frequency at 1712 cm^{-1} , pristine DBU (red) with signature $\text{C}=\text{N}$ stretching at 1608 cm^{-1} , intermediate A (blue) formed after deprotonation of stearic acid by DBU and intermediate B (green) formed at the end of the reaction.	58
Figure 2.6.	(a) Scheme for preparing zinc stearate from zinc chloride and stearic acid in presence of DBU catalyst. (b) A comparative FTIR of as-prepared zinc stearate (red) and stearic acid (grey) showing a shift in the carbonyl peak of acid from 1712 cm^{-1} to 1537 cm^{-1} . (c) A visual description of as-prepared zinc stearate and ₹5 coin (Diameter: 23 mm) for relative assimilation.	59
Figure 2.7.	Characterization of PTMS with NMR in presence of CDCl_3 as solvent. (a) ^1H NMR peak with a signature methyl chemical shift at 0.27 and 0.28 ppm. The peaks at 3.37 and 3.52 ppm are a peak for the 1,2-DME present as an impurity. Inset: expansion of ^1H NMR between 0.31 to 0.24 ppm showing a distinct doublet of methyl hydrogen from PTMS. (b) ^{13}C {H} NMR of PTMS with methyl carbon chemical shift at 4.16 and 4.05 ppm. The two peaks at 59.2 and 71.97 ppm are for $-\text{CH}_3$ and $-\text{CH}_2$ respectively of 1,2-DME.	61
Figure 3.1.	Schematic representation of the formation of QDs.	90
Figure 3.2.	Overview of previous work and the studies carried out in this chapter.	94

Figure 3.3.	(a) Scheme for preparation of InP QDs using the typical hot injection method. (b). UV-Visible spectra of InP QDs taken at the end of growth time (3600 s) at two different injection temperatures. (c) Tabular description of λ_{\max} (indicative of size) and HWHM (indicative of size distribution) observed from UV-Visible spectra of InP QDs at 250 °C and 270 °C injection temperature.	96
Figure 3.4.	(a) Scheme for preparation of InP QDs from pure indium myristate (complex 3.2) (b) Temporal evolution of InP QDs formation monitored using UV-Visible spectroscopy. (Inset: Image of a colloidal dispersion of InP QDs in hexane under normal light). (c) TEM micrograph of the InP QDs (Inset: size distribution graph).	97
Figure 3.5.	Data extracted from the UV-Visible spectra of InP QDs growth using complex 3.1 and 3.2 . (a) LEET vs. growth time; (b) FWHM at different times; (c) Evolution of absorbance at 310 nm (A_{310}); (d) Representative absorption spectra (measured with 45 min aliquots).	99
Figure 3.6.	Data extracted from the UV-Visible absorption spectra of InP QDs growth under various concentrations of free ligand (a) Reaction scheme (b) LEET vs. reaction time; (c) FWHM of absorption peak against reaction time; (d) Representative absorption traces for 45 min aliquots of experiment 1, 2 and 3.	101
Figure 3.7.	(a) Scheme for preparation of InP QDs from acid substituted InCl_3 . (b) Temporal evolution of absorption spectra with (b) complex 3.3 and (c) complex 3.4 and (d) complex 3.4 + 1.0 myristic acid.	102

Figure 3.8.	Data extracted from the UV-Visible spectra of InP QDs growth using complex 3.2 and 3.5 . (a) Reaction scheme for the preparation of InP QDs from complex 3.5 . (b) Energy of LEET vs. reaction time; (c) FWHM of the absorption peak vs. reaction time; (d) Representative absorption spectra for two complexes (45 min aliquots); (f) TEM image of InP QDs prepared from complex 3.5 . Inset: Size distribution obtained from TEM data.	105
Figure 3.9.	<i>In situ</i> ¹ H NMR studies of the reaction of indium precursor with PTMS. (a) <i>In situ</i> ¹ H NMR for InP NCs synthesis from complex 3.2 . The peaks are for PTMS before injection and 5 min after injection. (b) <i>In situ</i> ¹ H NMR for InP NCs synthesis from complex 3.5 . The peaks are for PTMS before injection and 5 min after injection. (c) concentration (C) profiles of TMS-MA protons determined at 5 min time intervals from the integration of spectra represented in figures 3.9a and b.	106
Figure 3.10.	(a) The structural difference between complex 3.6 and complex 3.7 . (b) Comparative absorption spectra of complex 3.6 and complex 3.7 . A distinct absorption peak is observed for complex 3.7 at 550 nm which is absent in complex 3.6 .	107
Figure 4.1.	Graphical representation of (a) classical and (b) non-classical nucleation models.	126
Figure 4.2.	(a) Preparation of MSCs of InP. The picture in the scheme is the colloidal dispersion of MSCs in hexane. (b) Temporal evolution of MSCs of InP studied through UV-Visible absorption spectroscopy by collecting aliquots at respective time intervals. (c) A graphical representation of the evolution of HWHM	129

	with growth time.	
Figure 4.3.	(a) The absorption spectrum of 386-InP MSCs2. (b) Absorption spectrum of 386-InP MSCs3. (c) FTIR spectra of 386-InP MSCs indicating the symmetric and asymmetric stretching of carbonyl bonds of indium bound myristate groups. (d) PXRD of as-synthesized MSCs (red) compared with standard zinc blende structure of bulk InP (PDF number: 96-101-0147, black).	130
Figure 4.4.	(a) Scheme for the synthesis of InP QDs from 386-InP MSCs. The picture in the scheme is a colloidal dispersion of QDs in hexane. (b). The UV-Visible absorption spectrum of QD2. (c) The UV-Visible absorption spectrum QD3. (d) A comparative representation of the absorption spectrum of QD2 and QD3. (e) PXRD of as-synthesized QD2 (blue) and QD3 (red) compared with standard zinc blende structure of bulk InP (PDF number: 96-101-0147, black) (f) TEM image QD2 indicating a size of $\sim 3.92 \pm 0.91$ nm (Inset: size distribution graph). (g) TEM image QD3 indicates a size of $\sim 4.7 \pm 0.47$ nm (Inset: size distribution graph).	132
Figure 4.5.	(a) FTIR spectra of indium precursors In-My1 (black), In-My2 (blue) and In-My3 (red). (b) TGA thermogram of In-My1 precursor depicting the weight loss of $\sim 7\%$ at temperature 130-200 °C for one acetate group. (c) TGA thermogram of In-My2 precursor depicting the weight loss of $\sim 1.5\%$ at temperature 85-130 °C and $\sim 78\%$ at a temperature range of 180- 510 °C. (d) TGA thermogram of In-My3 precursor showing a weight loss of $\sim 78\%$ at a temperature range of 180- 510 °C.	134

Figure 4.6.	(a) DSC plot of indium precursors In-My2 (blue) and In-My3 (red). Inset: melting point analysis where T_i is the initial temperature and T_f is the final temperature. (b) PXRD of undissolved part of In-My2 (blue) indexed with a standard file of indium hydroxide (PDF no.: 96-901-2825, black).	135
Figure 4.7.	(a) Temporal evolution of conversion of 386-InP MSCs to InP QDs. The absorption maxima of MSCs decrease concurrently with the increase in absorption peak of QDs whilst no other peaks are detected. (b) A graphical representation of change in absorbance at 386 nm (blue) and 620 nm (red) subtracting the underlying baseline. The black dotted line indicates the range of zero values for respective absorbances.	137
Figure 4.8.	(a) The UV-Visible absorption spectrum of QDs prepared from pure indium myristate complex at an injection temperature of 170 °C. Inset: The reaction mixture at the end of growth time (30 min). (b) TEM image of as-synthesized InP QDs with a diameter of $\sim 2.8 \pm 0.44$ nm (Inset: size distribution graph).	138
Figure 4.9.	(a) A comparable representation of the absorption spectrum of InP MSCs prepared by using different capping ligands. (b) The UV-Visible absorption spectra of InP QDs prepared from InP MSCs capped with fatty acid ligands of different chain lengths.	139
Figure 4.10.	A study of thermal stability (a) 386-InP MSCs (C_{14}). (b) 386-InP MSCs (C_{18}) was obtained by tuning the chain length of capping ligands through absorption spectroscopy by collected aliquots at different temperature intervals.	140

Figure 4.11.	The UV-Visible absorption spectrum of MSCs prepared in presence of oleylamine as additives with no distinct excitonic peak.	141
Figure 4.12.	(a) The UV-Visible absorption spectrum of clusters prepared in presence of TOP as additive. (Inset: colloidal dispersion of cluster in hexane prepared in presence of TOP additive). (b) Comparative analysis of FTIR spectra of precursor used for preparing InP MSCs in absence of TOP (red) and in presence of TOP (blue).	142
Figure 4.13.	Temporal evolution of first excitonic peak of InP QDs prepared from an as-synthesized cluster. (Inset: colloidal dispersion of QDs in hexane-prepared from former clusters).	143
Figure 4.14.	Absorption spectra of the evolution of size distribution in InAs QDs prepared by a continuous supply of InAs nanoclusters externally.	144
Figure 4.15.	TEM image of InAs QDs (a) before cluster injection and (b) after cluster injection.	145
Figure 4.16.	Absorption spectra of the evolution of size distribution in InP QDs prepared by a continuous supply of 386-InP MSCs externally.	145
Figure 4.17.	TEM image of InP QDs (a) before cluster injection and (b) after cluster injection.	146
Figure 5.1.	Optical studies of visible emitting colloidal NCs. (a) Absorption (blue) and emission spectrum (red) of CsPbBr ₃ perovskite NCs (excited at 400 nm). Inset: Photograph of a colloidal dispersion of CsPbBr ₃ NCs in hexane under a UV lamp. (b) Absorption (blue) and emission spectrum (red) of CdSe NCs (excited at 480	166

	nm). Inset: Photograph of a colloidal dispersion of CdSe NCs in hexane under a UV lamp. (c) Absorption (blue) and emission (red) of InP NCs (excited at 500 nm). Inset: Photograph of a colloidal dispersion of InP NCs in hexane under a UV lamp.	
Figure 5.2.	Optical studies of NIR emitting and CuFeS ₂ NCs. (a) Absorption spectrum of PbS NCs (excited at 950 nm). Inset: Photograph of a colloidal dispersion of PbS NCs in hexane. (b) Absorption (blue) and emission spectrum (red) Ag ₂ S NCs (excited at 800 nm). Inset: Photograph of a colloidal dispersion of Ag ₂ S NCs in hexane, and (c) surface plasmon resonance band (black) of CuFeS ₂ of NCs. Inset: Photograph of a colloidal dispersion of CuFeS ₂ NCs in hexane.	166
Figure 5.3.	Powder X-ray diffraction studies of (a) CsPbBr ₃ NCs (red) indexed with standard PDF 00-054-0752 (black). (b) CdSe NCs (red) indexed with standard PDF 65-2891(black). (c) InP NCs (red and blue) indexed with standard PDF 96-101-0147 (black). (d) PbS NCs (red) indexed with standard PDF 05-0592 (black). (e) Ag ₂ S NCs (red) indexed with standard PDF 00-014-0072 (black) and (f) CuFeS ₂ NCs (red) indexed with standard PDF 00-037-0471 (black).	167
Figure 5.4.	Photoluminescence excitation (PLE, blue line) spectrum of CsPbBr ₃ NCs in hexane, λ_{ex} = 497 nm (emission wavelength 515 nm). The corresponding photoluminescence (PL, red line) emission spectrum exhibits emission maximum (λ_{em}) at 515 nm (excitation: 400 nm).	168

List of Tables

Entry	Table description	Page No.
Table 1.1.	Some parameters of selected semiconductors.	5
Table 2.1.	Indium carboxylates prepared from the combination of saponification and double decomposition method.	48
Table 2.2.	Optimization studies for novel one-pot synthesis of indium stearate.	52
Table 2.3.	Synthesis of metal carboxylates from fatty acid and metal salt.	54
Table 3.1.	Study of effect of free acid on InP QDs synthesis and growth.	100
Table 3.2.	Summary of DFT studies.	103
Table 5.1.	Details of the MFAs used for the synthesis of various NCs.	165

List of Schemes

Entry	Scheme description	Page No.
Scheme 1.1.	Preparation of InP using Well's dehalosilylation method.	19
Scheme 2.1.	Preparation of alkali metal carboxylates through saponification reaction.	40
Scheme 2.2.	Preparation of metal stearate through double decomposition method.	41
Scheme 2.3.	Formation of metal stearate by fusion method.	41
Scheme 2.4.	Preparation of indium stearate by direct reaction of indium metal with stearic acid.	42
Scheme 2.5.	Formation of indium stearate from a vacuum method.	42
Scheme 2.6.	Preparation of indium salt of fatty acid by the combination of saponification of double decomposition method.	45
Scheme 2.7.	Preparation of indium myristate from potassium myristate.	47
Scheme 2.8.	Preparation of indium stearate from indium chloride and stearic acid in presence of DABCO.	49
Scheme 2.9.	Preparation of tris(trimethylsilyl)phosphine.	60
Scheme 2.10.	Preparation of tris(diethylamino)phosphine.	62
Scheme 3.1.	Preparation of InP QDs from complex 3.6 .	106

List of Abbreviations, Symbols and Acronyms

• QD	Quantum Dot	• MSC	Magic-Sized Cluster
• QDs	Quantum Dots	• MSCs	Magic-Sized Clusters
• NC	Nanocrystal	• LARP	Ligand-assisted Reprecipitation
• NCs	Nanocrystals	• MBE	Molecular Beam Epitaxy
• 0D	Zero Dimension	• APA	Active Processing Additives
• 1D	One Dimension	• HOMO	Highest Occupied Molecular Orbital
• 2D	Two Dimension	• LUMO	Lowest Unoccupied Molecular Orbital
• 1-ODE	1-octadecene	• CQDs	Colloidal Quantum Dots
• V.s	Volt second	• MFAs	Metal Salt of fatty acids
• Ω m	Ohm meter	• TGA	Thermogravimetric Analysis
• nm	Nanometer	• PXRD	Powder X-ray Diffraction
• Å	Angstrom	• DABCO	1,4-diazabicyclo[2.2.2]octane
• π	Phi	• DBU	1,8-diazabicyclo[5.4.0]undec-7-ene
• h	Hour	• DBN	1,5-diazabicyclo[4.3.0]non-5-ene
• s	Second	• PTMS	tris(trimethylsilyl)phosphine
• min	Minutes	• 1,2- DME	1,2-dimethoxy ethane
• cm	Centimeter	• λ_{\max}	Lamda maximum
• mm	Millimeter	• TOPO	Trioctylphosphineoxide
• V	Volt	• TOP	Trioctylphosphine
• mL	Milliliter	• 3D	Three Dimension
• μ L	Microliter	• FTIR	Fourier Transform Infrared
• g	Grams	• NMR	Nuclear Magnetic Resonance
• mg	Milligram	• ATR	Attenuated Total Reflectance
• μ g	microgram	• ESI	Electronspray Ionization
• mmol	Millimoles	• HWHM	Half-Width at Half Maximum
• kV	Kilovolt	• FWHM	Full Width at Half Maximum
• mA	Milliampere	• TEM	Transmission Electron Microscope

• i.e.	That is	• DSC	Differential Scanning Calorimetry
• viz.	Namely	• UV-VIS-NIR	Ultraviolet Visible Near Infrared
• ₹	Rupees	• PLE	Photoluminescence excitation
• UV	Ultraviolet	• m/z	Mass to charge ratio
• NIR	Near Infrared	• LC	Liquid Chromatography
• TOF	Time of flight	• PDF	Powder Diffraction File
• EI	Electron Impact	• EDX	Energy- Dispersive X-ray
• RF	Radio Frequency	• FID	Free Induction Decay
• JCPDS	Joint Committee on Powder Diffraction Standards		
• HRMS	High Resolution Mass Spectroscopy		
• ESIMS	Electrospray Ionization Mass Spectroscopy		
• MALDI	Matrix-Assisted Laser Desorption/ Ionization		
• HPLC	High- Performance Liquid Chromatography		
• ICDD	International Centre for Diffraction Data		
• LEET	Lowest Energy Electronic Transition		
• COSY	Correlation Spectroscopy		
• HMQC	Heteronuclear Multiple Quantum Coherence		
• NOESY	Nuclear Overhauser Effect Spectroscopy		

Chapter I

General Introduction

1.1. Background.

The term “semiconducting” was first introduced by Alessandro Volta in 1782.¹ Typically, any material having an electrical resistivity between 10^{-6} and $10^2 \Omega \text{ m}$ is considered semiconducting. In other terms, semiconductors are materials with energy band gap between those of insulators and conductors (i.e., 0-4 eV).¹⁻³ In terms of composition and function, semiconductors can be classified as:

- (i). Elemental semiconductor. Examples: Silicon, Germanium etc.
- (ii). Binary compounds. Examples: Indium Phosphide (InP), Lead sulphide (PbS) etc.
- (iii). Oxides. Examples: Cupric oxide (CuO), Cuprous oxide (Cu₂O) etc.
- (iv). Layered. Examples: Lead iodide (PbI₂), Molybdenum sulphide (MoS₂) etc.
- (v). Organic. Examples: Polyacetylene, Polydiacetylene etc.
- (vi). Magnetic. Examples: Europium sulphide (EuS), Cd_{1-x}Mn_xTe etc.⁴

Michael Faraday's publication on the electrical conductivity of silver sulphide in 1833 marks the beginning of the research on semiconductors. He observed that a decrease in the electrical resistance in silver sulphide is directly proportional to the decrease in temperature.^{1,2,5} Throughout the next century semiconductor research saw steady development. However, the development of band theory in the late 1920s and early 1930s along with the revolutionary discovery of transistors in 1947 by John Bardeen, Walter Brattain and William Shockley opened a new vista for semiconductor research.⁵ As the 1970s approached the molecular beam epitaxy (MBE) technique developed which allowed the atom-by-atom deposition of semiconductors. This technical advancement introduced the first 2D quantum well followed by 1D quantum rods and 0D quantum dots.⁵ The term “quantum dots” was reported in 1988 which was InAs on

GaAs substrate utilizing the MBE technique.⁶ Although it was proposed back in the 1960s that the properties of semiconductors can be quantum-engineered for the specific application it was not until 1981 that Alexei Ekimov published an article showing the size-dependent properties of CuCl in a glass matrix.⁷ Similar results were demonstrated by Louis Brus but in colloidal CdS, which is considered to be a low-cost quantum-engineering process.^{8,9} It wasn't until 1993 that Bawendi and co-workers reported the first monodispersed II-VI semiconductor quantum dots¹⁰ which laid the foundations of all the colloidal semiconductor research of the last three decades.^{11–15}

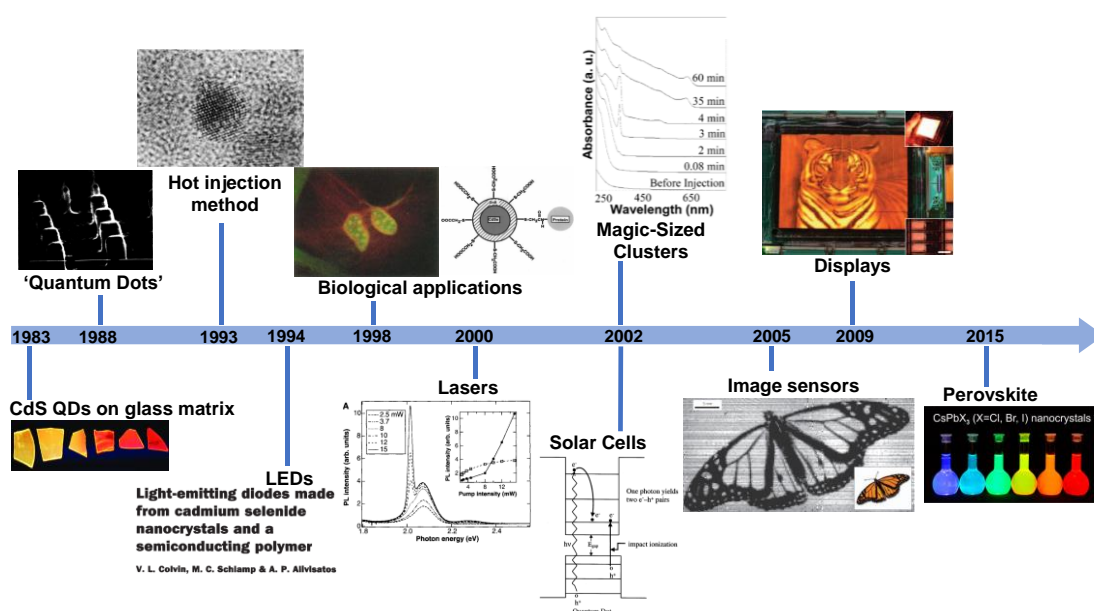


Figure 1.1. A brief timeline of the evolution of colloidal quantum dots research. The figure represents the seminal work and applications of quantum dots in various fields *viz.*, LEDs¹⁶, biological applications^{17,18}, lasers¹⁹, magic-sized clusters²⁰, solar cells²¹, image sensors²², display²³ and perovskite.²⁴

1.2. Quantum dots.

1.2.1. Definition and Overview.

Quantum dots (QDs) or also known as semiconductor nanocrystals (NCs) are nanometre-sized particles that exhibit size-dependent optical and electrical properties (figure 1.2). The NCs exhibit properties that are distinct from that of the bulk solids or molecules due to the effect known as the quantum confinement effect.^{25–27} Due to their unique size-dependent properties the QDs are employed in a wide range of applications such as photovoltaics²⁸, optoelectronics²⁹, biological imaging³⁰ and photocatalysis.³¹

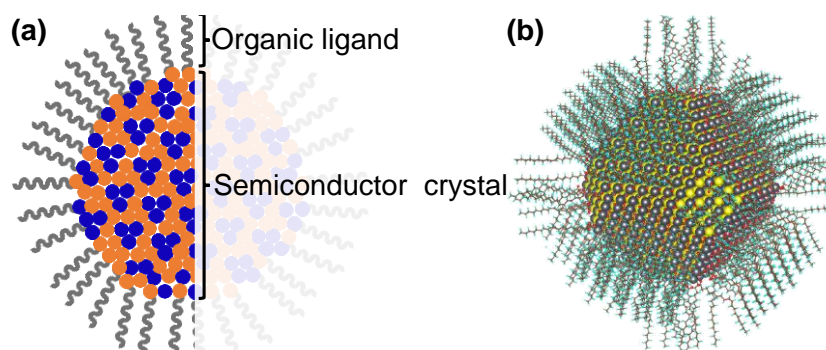


Figure 1.2. (a) Archetypal structural representation of semiconductor quantum dot. (b) A 5 nm PbS quantum dot stabilized by oleic acid and hydroxyl ions obtained through computational studies.³²

The most commonly synthesized QDs are II-VI (binary semiconductor formed from group II B and VI A of the periodic table. Examples: CdS, ZnSe etc)^{33,34}, III-V (binary semiconductor formed from group III A and V A of the periodic table. Example: InP, GaAs etc)^{35,36} and IV-VI (binary semiconductor formed from group IV A and VI A of periodic table. Example: PbS, PbSe etc)^{37,38} Table 1.1. details the characteristics and properties of some II-VI, III-V and IV-VI semiconductors.

Table 1.1. Some parameters of selected semiconductors.^{11,39}

Family	Material	Fractional ionic character	E_g at 300 K (eV)	Crystal structure	Lattice parameter (Å)
II-VI	ZnS	0.62	3.54	Zinc blende	5.41
	ZnSe	0.62	2.69	Zinc blende	5.668
	ZnTe	0.61	2.26	Zinc blende	6.104
	CdS	0.69	2.49	Wurtzite	4.136/6.714
	CdSe	0.70	1.74	Wurtzite	4.3/7.01
	CdTe	0.72	1.43	Zinc blende	6.482
III-V	InN	0.58	0.8	Wurtzite	3.545/5.703
	InP	0.42	1.35	Zinc blende	5.869
	InAs	0.36	0.35	Zinc blende	6.058
	InSb	0.32	0.23	Zinc blende	6.479
	GaN	0.50	3.44	Wurtzite	3.188/5.185
	GaP	0.33	2.27	Zinc blende	5.45
IV-VI	GaAs	0.31	1.42	Zinc blende	5.653
	GaSb	0.26	0.72	Zinc blende	6.096
	PbS	0.77	0.41	Rock salt	2.936
	PbSe	0.72	0.28	Rock salt	6.117
	PbTe	0.63	0.31	Rock salt	6.462

1.2.2. Quantum Confinement Effect.

The bulk semiconductor is characterised by its composition-dependent band gap as shown in figure 1.3. It is the minimum amount of energy needed to elevate an electron from the valence energy band's ground state to the unoccupied conduction band^{25,26}

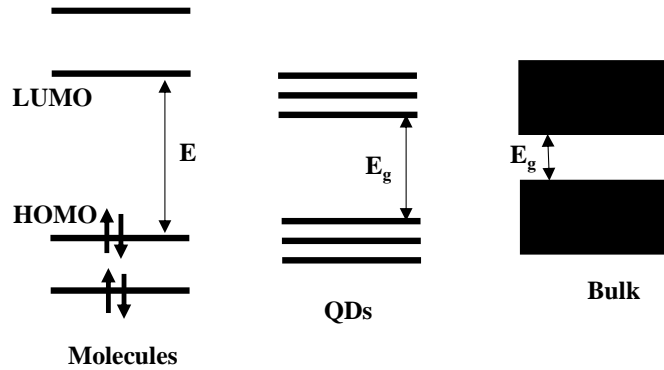


Figure 1.3.: Energy state in molecules, QDs and bulk semiconductors showing a discrete energy state in QDs compared to bulk semiconductors owing to its unique size-dependent properties.

When an electron in a semiconductor is excited from the valence band to the conduction band, a positive valency is formed in the valence band which is referred to as a hole. The electron-hole pair is called an exciton and the radius within which they are bound together is known as Bohr exciton radius⁴⁰ which is expressed as follows:

$$r_B = \frac{4\pi\epsilon\epsilon_0\hbar^2}{\mu q^2} \quad (1.1)$$

here, $\mu = \frac{1}{\left(\frac{1}{m_e} + \frac{1}{m_h}\right)}$

ϵ_0 = Absolute permittivity of the vacuum, ϵ = permittivity of dielectric constant of semiconductor, $\hbar = \frac{h}{2\pi}$, h = Planck's constant, μ = reduced mass, q = charge of an electron, m_e = mass of an electron and m_h = mass of a hole.

For instance, the exciton Bohr radius of CdSe,⁴¹ InP^{13,42} and PbS⁴³ are ~5.4 nm, ~11 nm and ~18 nm respectively.

Quantum confinement is a physical phenomenon where the spatial confinement of particles such as electrons, holes or excitons in a semiconductor leads to the quantization of energy levels meaning it can only have certain discrete energy levels (figure 1.1). The size of the confinement regime (Bohr radius) determines the size of quantized energy levels and therefore has a significant influence on the electronic, optical and transport properties of these materials.^{40,44-48} When the dimensions of a quantum dot (QD) become smaller than the Bohr radius of the semiconductor material, the electron and hole wave functions are confined in three dimensions.⁴⁹ The resulting quantized energy levels are similar to the energy levels in an atom, which can be described by the particle-in-a-box model.⁵⁰⁻⁵² The energy gap between the levels in a QD can be expressed as an increase in the band gap of parent bulk material by the confinement energy (E_c) and decrease in the interaction between holes and electron caused by coulombic force given as⁵³,

$$E_g = E_g^{bulk} + E_c - E_{eh} \quad (1.2)$$

where E_g is the band gap energy of NCs, E_g^{bulk} is the bulk band gap energy of semiconducting material, E_{eh} is the coulombic interaction between holes and electrons. E_c and E_{eh} can be expressed as follows,

$$E_c = \frac{\hbar^2 \pi^2}{2\mu r^2} \quad (1.3)$$

$$E_{eh} = \frac{1.786q^2}{\epsilon r} \quad (1.4)$$

where r is the radius of a nanocrystal (NC). From equations 1.3 and 1.4, equation 1.2 can be expressed as,

$$E_g = E_g^{bulk} + \frac{\hbar^2 \pi^2}{2\mu r^2} - \frac{1.786q^2}{\epsilon r} \quad (1.5)$$

The size dependence of the band gap energy can be seen in equation 1.5, as r decreases significantly below r_B , the band gap energy becomes larger resulting in strong confinement of NCs. However, as r decreases slightly below r_B , resulting in a weaker confinement regime with relatively smaller band gap energy.⁵⁴ Furthermore, from equations 1.1 and 1.5 we can obtain a relation between Bohr exciton radius and band gap energy of NCs in terms of its radius as,

$$E_g = E_g^{bulk} + \frac{2.6}{\epsilon r} \left(2.74 \frac{r_B}{r} - 1 \right) \quad (1.6)$$

In equation 1.6 E_g and E_g^{bulk} are quantified in eV, whereas r_B and r is measured in nm. It is apparent that semiconductor NCs possess a range of energy gaps that can span from near-infrared to ultraviolet. As a result, it is crucial to understand the relationship between the band gap and particle size for specific applications.^{26,55,56}

1.2.3. Synthesis.

Since the inception of NCs, there has been a surge in the production of colloidal quantum dots (CQDs), with varying sizes and narrow size distribution (monodispersed).^{16,20,57} Improved optical and electrical transport properties can be demonstrated by NCs with monodisperse size distributions, and they can be more effectively arranged into 2D or 3D solid films.^{11,58} Therefore, monodispersity is a critical factor for both fundamental research into the optoelectronic characteristics of

nanostructures and practical applications.⁵⁹⁻⁶¹ In this context, several synthetic approaches are employed to produce NCs which include but are not limited to (i). Hot-injection method⁶²⁻⁶⁵, (ii). Heating up method⁶⁶⁻⁶⁹, (iii). Laser illumination method⁷⁰, (iv). Ligand-assisted reprecipitation (LARP) method⁷¹ (v) ultrasonic method⁷² and (vi) microwave-assisted method.⁷³ However, the desired outcome of all the synthetic approaches is to prepare NCs with narrow size distribution, high stability, high quantum yield, a wide range of optical properties and control over the surface.^{58,74} Among various methods, the hot-injection method stands out as the most feasible approach to prepare colloidal NCs with specified characteristics. Therefore, it is widely applied for preparing high-quality NCs in colloidal form.⁷⁴

1.2.3.1. Hot Injection Method.

The pioneering work of Bawendi and co-workers for preparing high-quality monodispersed II-VI NCs (CdS, CdSe and CdTe) using the hot-injection method are well acclaimed.¹⁰ The classical nucleation and growth model of Lamer and Dinegar predicts the formation of monodisperse NCs occurs through temporal separation of nucleation and growth stage.⁷⁵ In the hot-injection method the phenomenon of separated nucleation and growth is achieved by rapid injection of the first precursor (at a lower temperature) into a solution of the second precursor in coordinating solvents at a very high temperature (figure 1.4). As a result, a simultaneous formation of a large number of small nuclei is triggered. The formation of nuclei is immediately quenched due to decrease in two factors *viz.*, temperature (as one of the precursors is at a lower temperature) and supersaturation (as precursor molecules get consumed). The formed nuclei will then undergo growth resulting in monodisperse NCs.^{27,58,63,74}

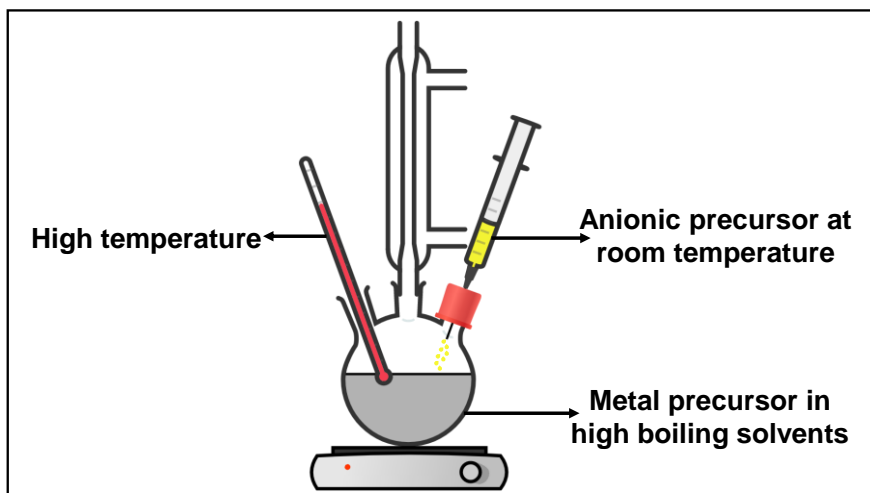


Figure 1.4. A representation of the hot injection method.

1.2.4. Mechanistic Studies.

1.2.4.1. Nucleation.

Nucleation is the process by which new phase(s) form from a parent phase by the formation of small clusters or nuclei. This process is important in many areas, such as crystal growth, phase transitions, and precipitation. The kinetics of nucleation can be described using the classical nucleation theory (CNT), which assumes that the nucleation process occurs in two steps: (1) the formation of a critical nucleus and (2) the growth of the nucleus into a stable phase.^{58,76–78}

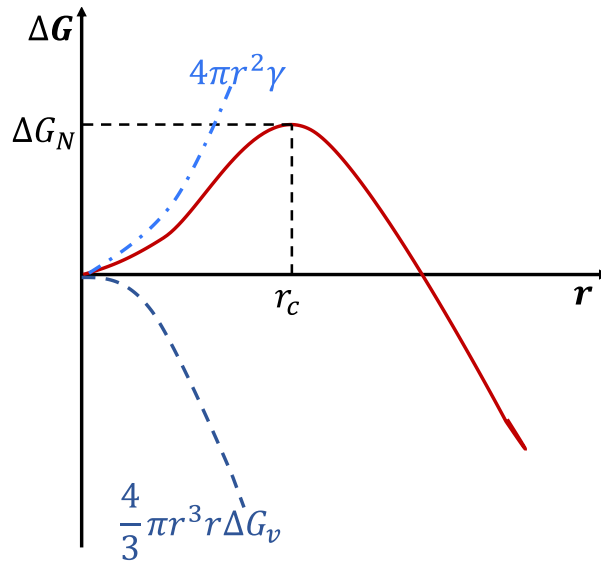


Figure 1.5. The plot depicting the relationship between particle radius and crystallization-free energy.

The formation of a critical nucleus can be described by the thermodynamic concept of free energy.^{79,80} The free energy change (ΔG) associated with the formation of a nucleus of radius r can be expressed as:

$$\Delta G = \frac{4}{3}\pi r^3 \Delta G_V + 4\pi r^2 \gamma \quad (1.7)$$

where ΔG_V is the change in free energy associated with the formation of a unit volume of the new phase, and γ is the interfacial energy between the new phase and the parent phase. The first term on the right-hand side of the equation represents the free energy gained by the formation of the nucleus, while the second term represents the free energy cost associated with the formation of the nucleus interface.^{66,74}

The rate of nucleation, or the number of nuclei formed per unit volume and time, can be expressed as:

$$\frac{dN}{dt} = A e^{\frac{-\Delta G_N}{k_B T}} \quad (1.8)$$

where A denotes the pre-exponential factor, ΔG_N is the activation-free energy, k_B is the Boltzmann constant, and T is the temperature. The activation free energy is the minimum free energy barrier that a nucleus must overcome to reach a critical size, and it is given by:

$$\Delta G_N = \frac{16}{3} \pi \left(\frac{\gamma^3}{\Delta G_V^2} \right) \quad (1.9)$$

The above equations represent the basic principles of classical nucleation theory, which provide a theoretical framework for describing the kinetics of nucleation. However, it is important to note that the assumptions underlying CNT may not always be valid, and other factors, such as impurities, defects, and non-equilibrium effects, may significantly affect the nucleation process in practice.⁷⁹

1.2.4.2. Growth.

The growth of small nuclei formed during nucleation occurs through diffusion and surface reaction.^{58,76,81} The diffusion of monomers occurs initially from the bulk solution to the surface (figure 1.6a) which is followed by surface reaction (figure 1.6b).

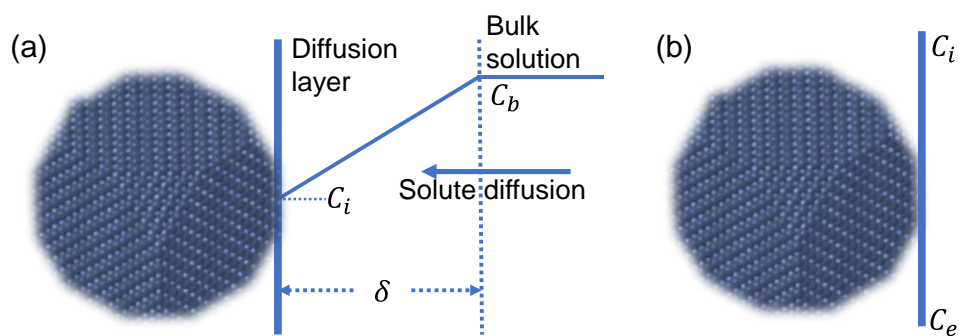


Figure 1.6. Growth of NCs occurs through (a) diffusion and (b) surface reaction.

The first process is governed by diffusion and according to Fick's first law of diffusion the total flux, J for any distance x within the diffusion layer is given as,

$$J = 4\pi x^2 D \frac{dC}{dx} \quad (1.10)$$

where D is the diffusion coefficient and C is the concentration of monomers.

At the surface of a QD, the concentration is C_i (interface concentration) while $x = r$, where r corresponds to particle size. Similarly at a point, far from the surface near the diffusion layer concentration will be equivalent to the bulk concentration C_b while $x = r + \delta$ (where δ thickness of diffusion layer). Integrating the above equation with these parameters gives the flux due to diffusion as,

$$J = \frac{4\pi D r (r + \delta)}{\delta} (C_b - C_i) \quad (1.11)$$

Similarly, the following process (surface reaction) after diffusion will be given as

$$J = 4\pi r^2 k (C_i - C_e) \quad (1.12)$$

where, C_e corresponds to the solubility of particles and k is a first-order reaction rate constant. From the above two equations it follows that,

$$\frac{C_i - C_e}{C_b - C_i} = \frac{D}{kr} \left(1 + \frac{r}{\delta}\right) \quad (1.13)$$

1.4.2.1. Diffusion-controlled growth.

In a diffusion-controlled growth mechanism the value $\frac{D}{kr} \ll 1$ which will deduce equation 1.13 as $C_e = C_i$, and from the relation of growth rate with respect to flux ($J = \frac{4\pi r^2}{V_m} \frac{dr}{dt}$), the rate of diffusion-controlled growth is given as,

$$\frac{dr}{dt} = DV_m \left(\frac{1}{r} + \frac{1}{\delta}\right) (C_b - C_e) \quad (1.14)$$

where V_m is molar volume.

Under constant $(C_b - C_e)$ the above relation shows that the rate of diffusion-controlled growth varies inversely with size meaning the faster the rate smaller the particle size, the slower the rate larger the size which will lead to smaller-sized particles finally catching up with larger particles resulting in monodispersity.

1.4.2.2. Reaction/ Surface controlled.

In a diffusion-controlled growth mechanism the value $\frac{D}{kr} \gg 1$ which will deduce equation 1.13 as $C_i = C_b$, the rate of reaction-controlled growth will be,

$$\frac{dr}{dt} = kV_m(C_b - C_e) \quad (1.15)$$

The expression indicates the growth rate to be size-independent which leads to uneven growth and ultimately attaining polydispersity.

1.4.2.3. Gibbs Thomson effect.

The rate of diffusion-controlled growth depends inversely on its size when C_b and C_e terms from equation 1.14 are independent of size. Therefore, in diffusion-controlled growth, small particles grow faster than larger ones. However, according to Gibbs Thomson effect, smaller particle inclines towards dissolution rather than grow into larger particles due to their relative thermodynamic stability. Furthermore, the concentration terms are reliant on particle size as given by Gibbs Thomson equation,

$$C_e = C_\infty e^{\left(\frac{2\sigma V_m}{rRT}\right)} \quad (1.16)$$

where σ = specific surface energy and C_∞ = solubility of bulk solid.

For NCs, $\frac{2\sigma V_m}{rRT} \ll 1$, then the expression of c_e and c_b will respectively be written as,

$$C_e \cong C_\infty + \left(1 + \frac{2\sigma V_m}{rRT}\right) \quad (1.17)$$

And

$$C_b \cong C_\infty + \left(1 + \frac{2\sigma V_m}{r^*RT}\right) \quad (1.18)$$

where, r_c = equilibrium particle radius with the bulk solution.

Therefore, with proper consideration of Gibbs Thomson effect in a diffusion-controlled growth rate with infinite diffusion layer, equation 1.14 will be transformed and may be written as,

$$\frac{dr}{dt} = \frac{K_D}{r} \left(\frac{1}{r^*} - \frac{1}{r}\right) \quad (1.19)$$

where, $K_D = \frac{2\sigma V_m^2 c_\infty}{RT}$

For a given value of r^* the rate at which the standard deviation change, which is indicative of the change of size distribution, is given as

$$\frac{d(\Delta r)}{dt} = \frac{K_D \Delta r}{\bar{r}^2} \left(\frac{2}{\bar{r}} - \frac{1}{r^*}\right) \quad (1.20)$$

where \bar{r} = average particle radius.

The conditions of narrow size distribution thus follow that rate of change of standard deviation should be zero or less than zero that is, $\frac{d(\Delta r)}{dt} \leq 0$. Under these conditions the ratio $\frac{\bar{r}}{r^*} \geq 2$. In order to maintain the ratio above two, the average particle radius in the reaction system must always be higher than the equilibrium particle size which is possible by maintaining higher supersaturation through increased monomer concentrations.^{82,83} Accordingly, the condition of increased monomer concentration is achieved by supplying supplementary monomers through the growth stage. Peng *et al.*

validated this theory by secondary injection which resulted in size focusing or narrow size distribution for InAs and CdSe QDs.^{83,84}

On other hand, the rate of reaction-controlled growth under Gibbs Thomson effect is given as,

$$\frac{dr}{dt} = K_R \left(\frac{1}{r^*} - \frac{1}{r} \right) \quad (1.21)$$

where, $K_R = \frac{2\sigma kV_m^2 C_\infty}{RT}$

The rate of change in the standard deviation of the size distribution for reaction-controlled growth is expressed as,

$$\frac{d(\Delta r)}{dt} = \frac{K_R \Delta r}{\bar{r}^2} \quad (1.22)$$

Since, $\frac{d(\Delta r)}{dt}$ is independent of r^* , the growth occurs irrespective of monomer concentration change and change in size distribution becomes unavoidable.^{81,82}

1.3. Magic-Sized Clusters (MSCs).

The field of NCs has witnessed the emergence of a new phenomenon known as the formation of MSCs in recent years.⁸⁵⁻⁸⁸ These intermediate clusters exhibit relatively high thermodynamic stability with persistent characteristic sharp absorption features.⁸⁹⁻

⁹¹ In fact, the naming convention for these clusters is based on the λ_{\max} at which they absorb. For example, CdSe MSCs absorbing at 350 are designated as 350-CdSe MSCs or CdSe_(350 nm).⁸⁷ MSCs have a metastable nature, which gives them an advantage over other small species, making them appealing for both gaining an important understanding of the dynamics of nanocrystal formation and controlling reactions.^{92,93}

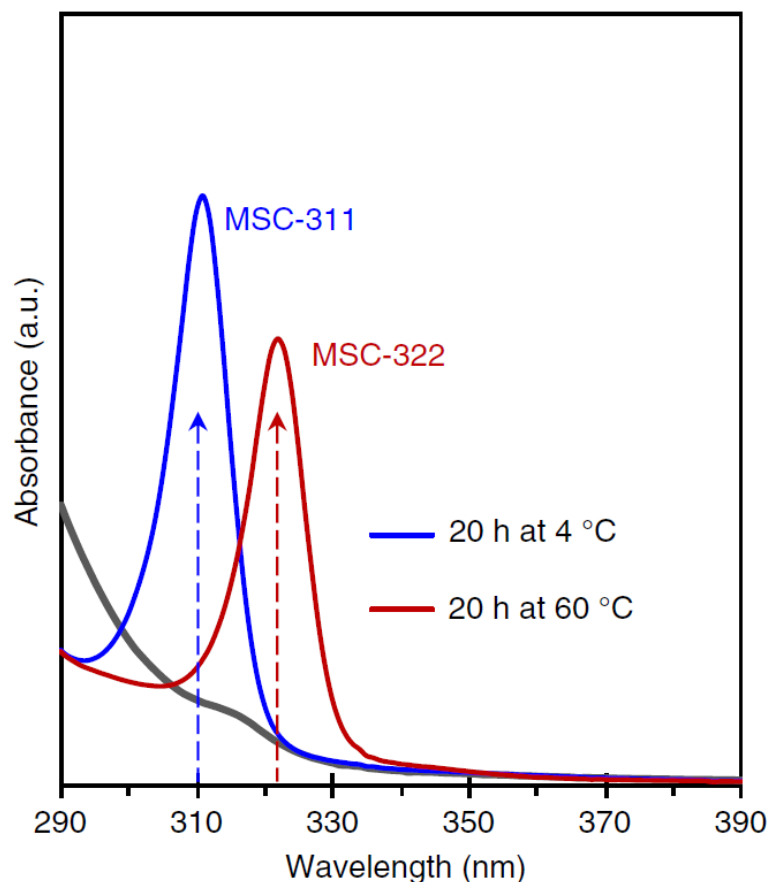


Figure 1.7. Characteristic absorption spectra of families of CdS MSCs showing a sharp peak at 311 and 322 nm.⁹⁴ Reprinted (adapted) with permission from ref 94. Copyright 2018 Springer Nature.

According to Kim *et al.*⁸⁸, there are three ways in which MSCs can be synthesized,

- (i) interruption method, where a cold reagent is injected right after hot injection, which intrudes the growth of large QDs to obtain MSCs.^{95,96}
- (ii) size-focusing method, where the growth of large QDs at high temperature is halted by quenching the reaction, and the resulting large QDs are then subjected to isothermal annealing to decrease their size, which enables the growth of MSCs.^{97,98}
- (iii) low-temperature method, where injection temperature is lowered to enable the formation of thermodynamically stable MSCs.^{99,100}

Over the years, there are various reports of II-VI (CdS)¹⁰¹, III-V (InP)¹⁰² and IV-VI (PbSe)¹⁰³ MSCs which were generally identified by their characteristics narrow absorption features. However, Owen *et al.* determined the exact composition of 380-CdSe and 408-CdSe MSCs as $\text{Cd}_{56}\text{Se}_{35}(\text{O}_2\text{CAr})_{42}(\text{H}_2\text{NR})_{42}$ and $\text{Cd}_{84}\text{Se}_{56}(\text{O}_2\text{CAr})_{56}(\text{H}_2\text{NR})_{56}$ through single crystal analysis.¹⁰⁴ Similarly, Cossairt *et al.* determined the composition of the most widely synthesized III-V MSCs *viz.*, 386-InP MSCs as $\text{In}_{37}\text{P}_{20}(\text{OCOCH}_2\text{Ph})_{51}$.¹⁰⁵

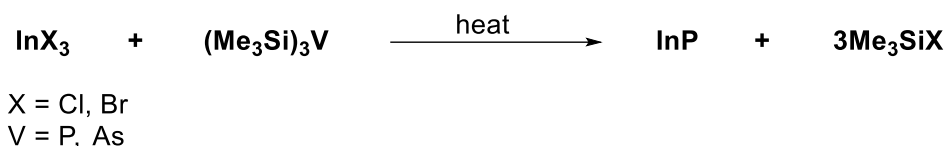
The significance of MSCs lies not only in the identification of novel species but also in their recognized role as precursors in the formation of NCs. Despite significant research efforts in recent years, there is still a lack of consensus among scientists regarding the precise composition, structure, and formation mechanism of MSCs and their functions in the formation of larger NCs. Some studies have suggested that MSCs serve as intermediates in the formation of regular NCs^{20,87,106–109}

1.4. III-V semiconductor NCs.

Semiconductor NCs that contain heavy metals such as Pb and Cd, which belong to the II-VI and IV-V groups, are highly toxic, whereas those belonging to the III-V group are relatively non-toxic and have high electron mobility. For instance, InSb has an electron mobility of $78000 \text{ cm}^2/\text{V.s}$, which is significantly higher than that of silicon ($1400 \text{ cm}^2/\text{V.s}$).^{36,110–112} As a result, III-V semiconductors are used extensively in optoelectronics. The bulk band gap value of InP is 1.35 eV, and InP QDs can cover a wide range of spectral regions, from UV-Visible to near-infrared (figure 1.8)¹¹³, making them highly useful for applications such as light-emitting diodes (LEDs) and biological imaging.^{114–116} Despite having such a wide range of applications its use has been limited mainly due to the challenges involved in its synthesis.^{117–119} Majority of the current

synthetic approach of III-V NCs is based on Well's dehalosilylation method (scheme 1.1)^{120,121}

Scheme 1.1. Preparation of InP using Well's dehalosilylation method.



Nozik *et al.* first adapted Well's dehalosilylation method for the preparation of colloidal InP NCs in coordinating trioctylphosphineoxide (TOPO) and trioctylphosphine (TOP) solvent at elevated temperature (270 °C).¹²² Conversely, Peng *et al.* have shown that using a non-coordinating solvent like 1-octadecene results in smaller reaction times and better size distribution (~4.7%) of III-V NCs.⁸⁴ Even though the synthetic approach has shown significant success in synthesizing III-V NCs, their covalent nature (fractional ionic character, table 1.1) makes them difficult to prepare due to the requirement of very reactive precursors, high reaction temperature, and extensive reaction time compared to II-VI and IV-VI counterparts.^{11,119} Moreover, the low electron affinity of group V makes it even harder to form a precursor with a -3 oxidation state. Consequently, group V precursors are highly reactive compounds with electropositive elements like hydrogen, silicon, sodium etc. (discussed in detail in chapter III).¹²³⁻¹³¹ Thus, controlling the size and size distribution is a major challenge in the synthesis of III-V semiconductor NCs.^{11,13} Another difficulty is the surface oxidation of these materials, as III-V semiconductor nanocrystals such as InP are highly air-sensitive.^{11,132} Furthermore, the exact role of intermediate MSCs in the size evolution of colloidal III-V semiconductor NCs is not yet comprehensively understood.¹³

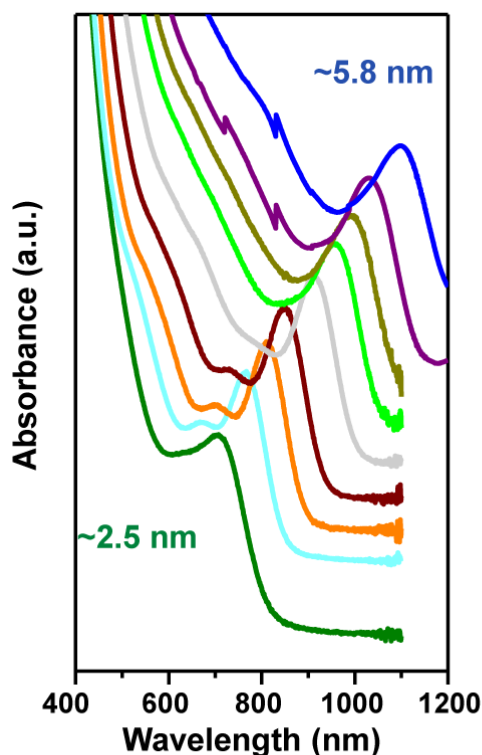


Figure 1.8. Size-dependent absorption spectra of InAs NCs.¹³³ Reprinted (adapted) with permission from ref. 133. Copyright 2016 American Chemical Society.

1.5. Research outline.

Against this background, this thesis aims to investigate the mechanism of the formation of III-V semiconductor NCs, especially InP. In the introduction chapter, we presented a comprehensive overview of CQDs, their properties, synthetic methodologies, mechanistic understanding, and a general idea of intermediate clusters. In chapter 2, we will discuss the preparation of precursors of various CQDs. The third chapter investigates the role of group III precursors in the size and size distribution of colloidal III-V (InP) NCs. Finally, in chapter four, we will study the intermediate MSCs and understand their exact role in the evolution of size and size distribution of colloidal III-V NCs. Additionally, chapter V demonstrates the applicability of metal precursors prepared using the novel method discussed in chapter I in CQDs synthesis in general.

1.6. References.

- (1) Łukasiak, L.; Jakubowski, A. History of Semiconductors. *J Telecommun Inf Technol* **2010**, *1*.
- (2) Jenkins, T. A Brief History of ... Semiconductors. *Phys. Educ.* **2005**, *40*, 430–439.
- (3) Lesnyak, V.; Yarema, M.; Miao, S. Editorial “Colloidal Semiconductor Nanocrystals: Synthesis, Properties, and Applications.” *Front. Chem.* **2019**, *7*, 2–5.
- (4) Yu, P. Y.; Cardona, M. *Fundamentals of Semiconductor Physics and Material Properties*; 2010.
- (5) Qu, J. *Colloidal Semiconductor Nanocrystals for Optoelectronic Applications: Photodetectors and Light Emitting Diodes*, 2021.
- (6) Reed, M. A.; Randall, J. N.; Aggarwal, R. J.; Matyi, R. J.; Moore, T. M.; Wetsel, A. E. Observation of Discrete Electronic States in a Zero-Dimensional Semiconductor Nanostructure. *Phys. Rev. Lett.* **1988**, *60*, 535–539.
- (7) Ekimov, A. I.; Onushchenko, A. A. Quantum Size Effect in Three-Dimensional Microscopic Semiconductor Crystals. *JETP Lett.* **1981**, *34*, 363–366.
- (8) Brus, L. E. Electron-Electron and Electronhole Interactions in Small Semiconductor Crystallites: The Size Dependence of the Lowest Excited Electronic State. *J. Chem. Phys.* **1984**, *80*, 4403–4409.
- (9) Rossetti, R.; Nakahara, S.; Brus, L. E. Quantum Size Effects in the Redox Potentials, Resonance Raman Spectra, and Electronic Spectra of CdS Crystallites in Aqueous Solution. *J. Chem. Phys.* **1983**, *79*, 1086–1088.

-
- (10) Murray, C. B.; Norris, D. J.; Bawendi, M. G. Synthesis and Characterization of Nearly Monodisperse CdE (E = S, Se, Te) Semiconductor Nanocrystallites. *J. Am. Chem. Soc.* **1993**, *115*, 8706–8715.
- (11) Reiss, P.; Carrière, M.; Lincheneau, C.; Vaure, L.; Tamang, S. Synthesis of Semiconductor Nanocrystals, Focusing on Nontoxic and Earth-Abundant Materials. *Chem. Rev.* **2016**, *116*, 10731–10819.
- (12) Tang, R.; Xue, J.; Xu, B.; Shen, D.; Sudlow, G. P.; Achilefu, S. Tunable Ultrasmall Visible-to-Extended near-Infrared Emitting Silver Sulfide Quantum Dots for Integrin-Targeted Cancer Imaging. *ACS Nano* **2015**, *9*, 220–230.
- (13) Tamang, S.; Lincheneau, C.; Hermans, Y.; Jeong, S.; Reiss, P. Chemistry of InP Nanocrystal Syntheses. *Chem. Mater.* **2016**, *28*, 2491–2506.
- (14) Thanh, N. T. K.; Maclean, N.; Mahiddine, S. Mechanisms of Nucleation and Growth of Nanoparticles in Solution. *Chem. Rev.* **2014**, *114*, 7610–7630.
- (15) Reiss, P.; Protière, M.; Li, L. Core/Shell Semiconductor Nanocrystals. *Small* **2009**, *5*, 154–168.
- (16) Colvin, V. L.; Schlamp, M. C.; Alivisatos, A. P. Light-Emitting Diodes Made from Cadmium Selenide Nanocrystals and a Semiconducting Polymer. *Nature* **1994**, *370*, 354–357.
- (17) Bruchez Jr, M.; Maronne, M.; Gin, P.; Weiss, S.; Alivisatos, A. P. Semiconductor Nanocrystals as Fluorescent Biological Labels. *Science* (80-.). **1998**, *281*, 2013–2015.
- (18) Chan, W. C. W.; Nie, S. Quantum Dot Bioconjugates for Ultrasensitive
-

- Nonisotopic Detection. *Science*. **1998**, *281*, 2016–2018.
- (19) Klimov, V. I.; Mikhailovsky, A. A.; Xu, S.; Malko, A.; Hollingsworth, J. A.; Leatherdale, C. A.; Eisler, H.-J.; Bawendi, M. G. Optical Gain and Stimulated Emission in Nanocrystal Quantum Dots. *Science*. **2000**, *290*, 314–317.
- (20) Peng, Z. A.; Peng, X. Nearly Monodisperse and Shape-Controlled CdSe Nanocrystals via Alternative Routes: Nucleation and Growth. *J. Am. Chem. Soc.* **2002**, *124*, 3343–3353.
- (21) Nozik, A. J. Quantum Dot Solar Cells. *Phys. E* **2002**, *12*, 115–120.
- (22) Rauch, T.; Böberl, M.; Tedde, S. F.; Fürst, J.; Kovalenko, M. V.; Hesser, G.; Lemmer, U.; Heiss, W.; Hayden, O. Near-Infrared Imaging with Quantum-Dot-Sensitized Organic Photodiodes. *Nat. Photonics* **2009**, *3*, 332–336.
- (23) Cho, K. S.; Lee, E. K.; Joo, W. J.; Jang, E.; Kim, T. H.; Lee, S. J.; Kwon, S. J.; Han, J. Y.; Kim, B. K.; Choi, B. L.; Kim, J. M. High-Performance Crosslinked Colloidal Quantum-Dot Light-Emitting Diodes. *Nat. Photonics* **2009**, *3*, 341–345.
- (24) Protesescu, L.; Yakunin, S.; Bodnarchuk, M. I.; Krieg, F.; Caputo, R.; Hendon, C. H.; Yang, R. X.; Walsh, A.; Kovalenko, M. V. Nanocrystals of Cesium Lead Halide Perovskites (CsPbX₃, X = Cl, Br, and I): Novel Optoelectronic Materials Showing Bright Emission with Wide Color Gamut. *Nano Lett.* **2015**, *15*, 3692–3696.
- (25) Frecker, T.; Bailey, D.; Arzeta-Ferrer, X.; McBride, J.; Rosenthal, S. J. Quantum Dots and Their Application in Lighting, Displays, and Biology. *J. Solid State*

- Sci. Technol.* **2015**, *5*, R3019--R3031.
- (26) Smith, A. M.; Nie, S. Semiconductor Nanocrystals: Structure, Properties and Band Gap Engineering. *Acc. Chem. Res.* **2010**, *43*, 190–200.
- (27) Chang, J.; Waclawik, E. R. Colloidal Semiconductor Nanocrystals: Controlled Synthesis and Surface Chemistry in Organic Media. *RSC Adv.* **2014**, *4*, 23505–23527.
- (28) Dayal, S.; Kopidakis, N.; Olson, D. C.; Ginley, D. S.; Rumbles, G. Photovoltaic Devices with a Low Band Gap Polymer and CdSe Nanostructures Exceeding 3% Efficiency. *Nano Lett.* **2010**, *10*, 239–242.
- (29) Talapin, D. V.; Lee, J. S.; Kovalenko, M. V.; Shevchenko, E. V. Prospects of Colloidal Nanocrystals for Electronic and Optoelectronic Applications. *Chem. Rev.* **2010**, *110*, 389–458.
- (30) Michalet, X.; Pinaud, F. F.; Bentolila, L. A.; Tsay, J. M.; Doose, S.; Li, J. .; Sundaresan, G.; Wu, A. M.; Gambhir, S. S.; Weiss, S. Quantum Dots for Live Cells, in Vivo Imaging, and Diagnostics. *Science.* **2005**, *307*, 538–545.
- (31) Li, X. B.; Tung, C. H.; Wu, L. Z. Semiconducting Quantum Dots for Artificial Photosynthesis. *Nat. Rev. Chem.* **2018**, *2*, 160–173.
- (32) Zhrebetsky, D.; Scheele, M.; Zhang, Y.; Bronstein, N.; Thompson, C.; Britt, D.; Salmeron, M.; Alivisatos, P.; Wang, L. W. Hydroxylation of the Surface of PbS Nanocrystals Passivated with Oleic Acid. *Science.* **2014**, *344*, 1380–1384.
- (33) Abe, S.; Čapek, R. K.; De Geyter, B.; Hens, Z. Tuning the Postfocused Size of Colloidal Nanocrystals by the Reaction Rate: From Theory to Application. *ACS*

Nano **2012**, 6, 42–53.

- (34) Xie, L.; Zhao, Q.; Jensen, K. F.; Kulik, H. J. Direct Observation of Early-Stage Quantum Dot Growth Mechanisms with High-Temperature Ab Initio Molecular Dynamics. *J. Phys. Chem. C* **2016**, 120, 2472–2483.
- (35) Gary, D. C.; Cossairt, B. M. Role of Acid in Precursor Conversion During InP Quantum Dot Synthesis. *Chem. Mater.* **2013**, 25, 2463–2469.
- (36) Liu, W.; Chang, A. Y.; Schaller, R. D.; Talapin, D. V. Colloidal InSb Nanocrystals. *J. Am. Chem. Soc.* **2012**, 134, 20258–20261.
- (37) Basel, S.; Bhardwaj, K.; Pradhan, S.; Pariyar, A.; Tamang, S. DBU-Catalyzed One-Pot Synthesis of Nearly Any Metal Salt of Fatty Acid (M-FA): A Library of Metal Precursors to Semiconductor Nanocrystal Synthesis. *ACS Omega* **2020**, 5, 6666–6675.
- (38) Schliehe, C.; Juarez, B. H.; Pelletier, M.; Jander, S.; Greshnykh, D.; Nagel, M.; Meyer, A.; Foerster, S.; Kornowski, A.; Klinke, C.; Weller, H. Ultrathin PbS Sheets by Two-Dimensional Oriented Attachment. *Science*. **2010**, 329, 550–553.
- (39) Philips, J. C. *Bonds and Bands in Semiconductors*; 1973.
- (40) Yoffe, A. D. Low-Dimensional Systems: Quantum Size Effects and Electronic Properties of Semiconductor Microcrystallites (Zero-Dimensional Systems) and Some Quasi-Two-Dimensional Systems. *Adv. Phys.* **2002**, 51, 799–890.
- (41) Babentsov, V.; Sizov, F. Defects in Quantum Dots of IIB-VI Semiconductors. *Opto-Electronics Rev.* **2008**, 16, 208–225.

- (42) Clarke, M. T.; Viscomi, F. N.; Chamberlain, T. W.; Hondow, N.; Adawi, A. M.; Sturge, J.; Erwin, S. C.; Bouillard, J. S. G.; Tamang, S.; Stasiuk, G. J. Synthesis of Super Bright Indium Phosphide Colloidal Quantum Dots through Thermal Diffusion. *Commun. Chem.* **2019**, *2*, 1–7.
- (43) Pan, Y.; Li, Y. R.; Zhao, Y.; Akins, D. L. Synthesis and Characterization of Quantum Dots: A Case Study Using PbS. *J. Chem. Educ.* **2015**, *92*, 1860–1865.
- (44) Hong, X.; Ishihara, T.; Nurmikko, A. V. Dielectric Confinement Effect on Excitons in PbI₄-Based Layered Semiconductors. *Phys. Rev. B* **1992**, *45*, 6961–6964.
- (45) Kilina, S. V.; Kilin, D. S.; Prezhdo, O. V. Breaking the Phonon Bottleneck in PbSe and CdSe Quantum Dots: Time-Domain Density Functional Theory of Charge Carrier Relaxation. *ACS Nano* **2009**, *3*, 93–99.
- (46) Takagahara, T.; Takeda, K. Theory of the Quantum Confinement Effect on Excitons in Quantum Dots of Indirect-Gap Materials. *Phys. Rev. B* **1992**, *46*, 15578–15581.
- (47) Fu, H.; Zunger, A. InP Quantum Dots: Electronic Structure, Surface Effects, and the Redshifted Emission. *Phys. Rev. B* **1997**, *56*, 1496–1508.
- (48) Yanhong, L.; Dejun, W.; Qidong, Z.; Min, Y.; Qinglin, Z. A Study of Quantum Confinement Properties of Photogenerated Charges in ZnO Nanoparticles by Surface Photovoltage Spectroscopy. *J. Phys. Chem. B* **2004**, *108*, 3202–3206.
- (49) Pietryga, J. M.; Park, Y. S.; Lim, J.; Fidler, A. F.; Bae, W. K.; Brovelli, S.; Klimov, V. I. Spectroscopic and Device Aspects of Nanocrystal Quantum Dots. *Chem. Rev.* **2016**, *116*, 10513–10622.

- (50) Pradeep, T. *Nano: The Essentials. Understanding Nanoscience and Nanotechnology*; Tata McGraw-Hill Publishing Company Limited, 2007.
- (51) Murphy, C. J. Peer Reviewed: Optical Sensing with Quantum Dots. *Anal. Chem.* **2002**, *74*, 520A-526A.
- (52) Alivisatos, A. P. Nanocrystals: Building Blocks for Modern Materials Design. *Endeavour* **1997**, *21*, 56–60.
- (53) Brus, L. Electronic Wave Functions in Semiconductor Clusters: Experiment and Theory. *J. Phys. Chem.* **1986**, *90*, 2555–2560.
- (54) Einevoll, G. T. Confinement of Excitons in Quantum Dots. *Phys. Rev. B* **1992**, *45* (7), 3410–3417.
- (55) Sathe, K. P.; Garud, N. S.; Bangar, V. B.; Gadakh, N. R. A Review on Quantum Dots (Qds). *J. Adv. Sci. Res.* **2022**, *13*, 23–27.
- (56) Lei, D.; Shen, Y. T.; Feng, Y. Y.; Feng, W. Recent Progress in the Fields of Tuning the Band Gap of Quantum Dots. *Sci. China Technol. Sci.* **2012**, *55*, 903–912.
- (57) Yu, W. W.; Wang, Y. A.; Peng, X. Formation and Stability of Size-, Shape-, and Structure-Controlled CdTe Nanocrystals: Ligand Effects on Monomers and Nanocrystals. *Chem. Mater.* **2003**, *15*, 4300–4308.
- (58) Kwon, S. G.; Hyeon, T. Formation Mechanisms of Uniform Nanocrystals via Hot-Injection and Heat-Up Methods. *Small* **2011**, *7*, 2685–2702.
- (59) Peng, X.; Manna, L.; Yang, W.; Wickham, J.; Scher, E.; Kadavanich, A.; Alivisatos, A. P. Shape Control of CdSe Nanocrystals. *Nature* **2000**, *404*, 59–61.

- (60) Tessier, M. D.; Dupont, D.; De Nolf, K.; De Roo, J.; Hens, Z. Economic and Size-Tunable Synthesis of InP/ZnE (E = S, Se) Colloidal Quantum Dots. *Chem. Mater.* **2015**, *27*, 4893–4898.
- (61) Hendricks, M. P.; Campos, M. P.; Cleveland, G. T.; Plante, I. J. La; Owen, J. S. A Tunable Library of Substituted Thiourea Precursors to Metal Sulfide Nanocrystals. *Science*. **2015**, *348*, 1226–1230.
- (62) Williams, J. V.; Kotov, N. A.; Savage, P. E. A Rapid Hot-Injection Method for the Improved Hydrothermal Synthesis of CdSe Nanoparticles. *Ind. Eng. Chem. Res.* **2009**, *48*, 4316–4321.
- (63) Yarema, M.; Yarema, O.; Lin, W. M. M.; Volk, S.; Yazdani, N.; Bozyigit, D.; Wood, V. Upscaling Colloidal Nanocrystal Hot-Injection Syntheses via Reactor Underpressure. *Chem. Mater.* **2017**, *29*, 796–803.
- (64) Thapa, S.; Bhardwaj, K.; Basel, S.; Pradhan, S.; Eling, C. J.; Adawi, A. M.; Bouillard, J. S. G.; Stasiuk, G. J.; Reiss, P.; Pariyar, A.; Tamang, S. Long-Term Ambient Air-Stable Cubic CsPbBr₃ Perovskite Quantum Dots Using Molecular Bromine. *Nanoscale Adv.* **2019**, *1*, 3388–3391.
- (65) Pradhan, S.; Bhujel, D.; Gurung, B.; Sharma, D.; Basel, S.; Rasaily, S.; Thapa, S.; Borthakur, S.; Ling, W. L.; Saikia, L.; Reiss, P.; Pariyar, A.; Tamang, S. Stable Lead-Halide Perovskite Quantum Dots as Efficient Visible Light Photocatalysts for Organic Transformations. *Nanoscale Adv.* **2021**, *3*, 1464–1472.
- (66) Van Embden, J.; Chesman, A. S. R.; Jasieniak, J. J. The Heat-Up Synthesis of Colloidal Nanocrystals. *Chem. Mater.* **2015**, *27*, 2246–2285.

- (67) Cui, J.; Wang, L.; Yu, X. A Simple and Generalized Heat-up Method for the Synthesis of Metal Sulfide Nanocrystals. *New J. Chem.* **2019**, *43*, 16007–16011.
- (68) Lee, D.; Kim, M. H.; Woo, H. Y.; Chae, J.; Lee, D.; Jeon, S.; Oh, S. J.; Paik, T. Heating-up Synthesis of Cesium Bismuth Bromide Perovskite Nanocrystals with Tailored Composition, Morphology, and Optical Properties. *RSC Adv.* **2020**, *10*, 7126–7133.
- (69) Li, L.; Reiss, P. One-Pot Synthesis of Highly Luminescent InP / ZnS Nanocrystals without Precursor Injection. *J. Am. Chem. Soc.* **2008**, *130*, 11588–11589.
- (70) Lin, Y. W.; Hsieh, M. M.; Liu, C. P.; Chang, H. T. Photoassisted Synthesis of CdSe and Core-Shell CdSe/CdS Quantum Dots. *Langmuir* **2005**, *21*, 728–734.
- (71) Han, D.; Imran, M.; Zhang, M.; Chang, S.; Wu, X. G.; Zhang, X.; Tang, J.; Wang, M.; Ali, S.; Li, X.; Yu, G.; Han, J.; Wang, L.; Zou, B.; Zhong, H. Efficient Light-Emitting Diodes Based on in Situ Fabricated FAPbBr₃ Nanocrystals: The Enhancing Role of the Ligand-Assisted Reprecipitation Process. *ACS Nano* **2018**, *12*, 8808–8816.
- (72) Suslick, K. S.; Fang, M.; Hyeon, T. Sonochemical Synthesis of Iron Colloids. *J. Am. Chem. Soc.* **1996**, *118*, 11960–11961.
- (73) Gerbec, J. A.; Magana, D.; Washington, A.; Strouse, G. F. Microwave-Enhanced Reaction Rates for Nanoparticle Synthesis. *J. Am. Chem. Soc.* **2005**, *127*, 15791–15800.
- (74) De Mello Donegá, C.; Liljeroth, P.; Vanmaekelbergh, D. Physicochemical Evaluation of the Hot-Injection Method, a Synthesis Route for Monodisperse

- Nanocrystals. *Small* **2005**, *1*, 1152–1162.
- (75) LaMer, V. K.; Dinegar, R. H. Theory, Production and Mechanism of Formation of Monodispersed Hydrosols. *J. Am. Chem. Soc.* **1950**, *72*, 4847–4854.
- (76) Thanh, N. T. K.; Maclean, N.; Mahiddine, S. Mechanisms of Nucleation and Growth of Nanoparticles in Solution. *Chem. Rev.* **2014**, *114*, 7610–7630.
- (77) Puntès, V. F.; Zanchet, D.; Erdonmez, C. K.; Alivisatos, A. P. Synthesis of Hcp-Co Nanodisks. *J. Am. Chem. Soc.* **2002**, *124*, 12874–12880.
- (78) Robinson, I.; Zacchini, S.; Tung, L. D.; Maenosono, S.; Thanh, N. T. K. Synthesis and Characterization of Magnetic Nanoalloys from Bimetallic Carbonyl Clusters. *Chem. Mater.* **2009**, *21*, 3021–3026.
- (79) Strey, R.; Wagner, P. E.; Viisanen, Y. The Problem of Measuring Homogeneous Nucleation Rates and the Molecular Contents of Nuclei: Progress in the Form of Nucleation Pulse Measurements. *J. Phys. Chem.* **1994**, *98*, 7748–7758.
- (80) Cölfen, H. Nonclassical Nucleation and Crystallization. *Crystals* **2020**, *10*, 61–63.
- (81) Sugimoto, T. Preparation of Monodispersed Colloidal Particles. *Adv. Colloid Interface Sci.* **1987**, *28*, 65–108.
- (82) Talapin, D. V.; Rogach, A. L.; Shevchenko, E. V.; Kornowski, A.; Haase, M.; Weller, H. Dynamic Distribution of Growth Rates within the Ensembles of Colloidal II-VI and III-V Semiconductor Nanocrystals as a Factor Governing Their Photoluminescence Efficiency. *J. Am. Chem. Soc.* **2002**, *124*, 5782–5790.
- (83) Peng, X.; Wickham, J.; Alivisatos, A. P. Kinetics of II-VI and III-V Colloidal Semiconductor Nanocrystal Growth: “Focusing” of Size Distributions. *J. Am. Ph.D.*

- Chem. Soc.* **1998**, *120*, 5343–5344.
- (84) Battaglia, D.; Peng, X. Formation of High Quality InP and InAs Nanocrystals in Noncoordinating Solvent. *Nano Lett.* **2002**, *2*, 1027–1030.
- (85) Alivisatos, A. P. Semiconductor Clusters, Nanocrystals, and Quantum Dots. *Science.* **1996**, *271*, 933–937.
- (86) Gary, D. C.; Terban, M. W.; Billinge, S. J. L.; Cossairt, B. M. Two-Step Nucleation and Growth of InP Quantum Dots via Magic-Sized Cluster Intermediates. *Chem. Mater.* **2015**, *27*, 1432–1441.
- (87) Palencia, C.; Yu, K.; Boldt, K. The Future of Colloidal Semiconductor Magic-Size Clusters. *ACS Nano* **2020**, *14*, 1227–1235.
- (88) Kwon, Y.; Kim, S. Indium Phosphide Magic-Sized Clusters: Chemistry and Applications. *NPG Asia Mater.* **2021**, *13*, 1–16.
- (89) Harrell, S. M.; McBride, J. R.; Rosenthal, S. J. Synthesis of Ultrasmall and Magic-Sized CdSe Nanocrystals. *Chem. Mater.* **2013**, *25*, 1199–1210.
- (90) Kim, B. H.; Hackett, M. J.; Park, J.; Hyeon, T. Synthesis, Characterization, and Application of Ultrasmall Nanoparticles. *Chem. Mater.* **2014**, *26*, 59–71.
- (91) Cossairt, B. M.; Owen, J. S. CdSe Clusters: At the Interface of Small Molecules and Quantum Dots. *Chem. Mater.* **2011**, *23*, 3114–3119.
- (92) Liu, M.; Wang, K.; Wang, L.; Han, S.; Fan, H.; Rowell, N.; Ripmeester, J. A.; Renoud, R.; Bian, F.; Zeng, J.; Yu, K. Probing Intermediates of the Induction Period Prior to Nucleation and Growth of Semiconductor Quantum Dots. *Nat. Commun.* **2017**, *8*, 1–12.

- (93) Kwon, Y.; Oh, J.; Lee, E.; Lee, S. H.; Agnes, A.; Bang, G.; Kim, J.; Kim, D.; Kim, S. Evolution from Unimolecular to Colloidal-Quantum-Dot-like Character in Chlorine or Zinc Incorporated InP Magic Size Clusters. *Nat. Commun.* **2020**, *11*, 1–15.
- (94) Zhang, B.; Zhu, T.; Ou, M.; Rowell, N.; Fan, H.; Han, J.; Tan, L.; Dove, M. T.; Ren, Y.; Zuo, X.; Han, S.; Zeng, J.; Yu, K. Thermally-Induced Reversible Structural Isomerization in Colloidal Semiconductor CdS Magic-Size Clusters. *Nat. Commun.* **2018**, *9*, 2499.
- (95) Capek, R. K.; Lambert, K.; Dorfs, D.; Smet, P. F.; Poelman, D.; Eychmu, A. Synthesis of Extremely Small CdSe and Bright Blue Luminescent CdSe / ZnS Nanoparticles by a Prefocused Hot-Injection Approach. *Chem. Mater.* **2009**, *21*, 1743–1749.
- (96) Zhang, L.; Shen, X.; Liang, H.; Yao, J. Multiple Families of Magic-Sized ZnSe Quantum Dots via Noninjection One-Pot and Hot-Injection Synthesis. *J. Phys. Chem. C* **2010**, *114*, 21921–21927.
- (97) Chen, H. S.; Kumar, R. V. Discontinuous Growth of Colloidal CdSe Nanocrystals in the Magic Structure. *J. Phys. Chem. C* **2009**, *113*, 31–36.
- (98) Chen, H.-S.; Kumar, R. V. RSC Advances Synthesis of Ultrasmall Quantum Dots by Redirecting Kinetics-Based Crystal Growth to Thermodynamics-Based Crystal Dissolution. *RSC Adv.* **2012**, *2*, 11586–11591.
- (99) Gao, D.; Hao, X.; Rowell, N.; Kreouzis, T.; Lockwood, D. J.; Han, S.; Fan, H.; Zhang, H.; Zhang, C.; Jiang, Y.; Zeng, J.; Zhang, M.; Yu, K. Formation of Colloidal Alloy Semiconductor CdTeSe Magic-Size Clusters at Room

- Temperature. *Nat. Commun.* **2019**, *10*, 1674.
- (100) Kudera, S.; Zanella, M.; Giannini, C.; Rizzo, A.; Li, Y.; Gigli, G.; Cingolani, R.; Ciccarella, G.; Spahl, W.; Parak, W. J.; Manna, L. Sequential Growth of Magic-Size CdSe Nanocrystals. *Adv. Mater.* **2007**, *19*, 548–552.
- (101) Li, L.; Zhang, J.; Zhang, M.; Rowell, N.; Zhang, C.; Wang, S.; Lu, J.; Fan, H.; Huang, W.; Chen, X.; Yu, K. Fragmentation of Magic-Size Cluster Precursor Compounds into Ultrasmall CdS Quantum Dots with Enhanced Particle Yield at Low Temperatures. *Angew. Chemie* **2020**, *132*, 12111–12119.
- (102) Ning, J.; Banin, U. Magic Size InP and InAs Clusters: Synthesis, Characterization and Shell Growth. *Chem. Commun.* **2017**, *53*, 2626–2629.
- (103) Yu, K.; Ouyang, J.; Leek, D. M. In-Situ Observation of Nucleation and Growth of PbSe Magic-Sized Nanoclusters and Regular Nanocrystals. *Small* **2011**, *7*, 2250–2262.
- (104) Beecher, A. N.; Yang, X.; Palmer, J. H.; Lagrassa, L.; Juhas, P.; Billinge, S. J. L.; Owen, J. S. Atomic Structures and Gram Scale Synthesis of Three Tetrahedral Quantum Dots. *J. Am. Chem. Soc.* **2014**, *136*, 10645–10653.
- (105) Gary, D. C.; Flowers, S. E.; Kaminsky, W.; Petrone, A.; Li, X.; Cossairt, B. M. Single-Crystal and Electronic Structure of a 1.3 Nm Indium Phosphide Nanocluster. *J. Am. Chem. Soc.* **2016**, *138*, 1510–1513.
- (106) Sun, M.; Yang, X. Phosphine-Free Synthesis of High-Quality CdSe Nanocrystals in Noncoordination Solvents: “Activating Agent” and “Nucleating Agent” Controlled Nucleation and Growth. *J. Phys. Chem. C* **2009**, *113*, 8701–8709.

- (107) Jiang, Z. J.; Kelley, D. F. Role of Magic-Sized Clusters in the Synthesis of CdSe Nanorods. *ACS Nano* **2010**, *4*, 1561–1572.
- (108) Evans, C. M.; Love, A. M.; Weiss, E. A. Surfactant-Controlled Polymerization of Semiconductor Clusters to Quantum Dots through Competing Step-Growth and Living Chain-Growth Mechanisms. *J. Am. Chem. Soc.* **2012**, *134*, 17298–17305.
- (109) Wang, Y.; Zhang, Y.; Wang, F.; Giblin, D. E.; Hoy, J.; Rohrs, H. W.; Loomis, R. A.; Buhro, W. E. The Magic-Size Nanocluster (CdSe)₃₄ as a Low-Temperature Nucleant for Cadmium Selenide Nanocrystals; Room-Temperature Growth of Crystalline Quantum Platelets. *Chem. Mater.* **2014**, *26*, 2233–2243.
- (110) Green, M. Solution Routes to III - V Semiconductor Quantum Dots. *Curr. Opin. Solid State Mater. Sci.* **2002**, *6*, 355–363.
- (111) Yarema, M.; Kovalenko, M. V. Colloidal Synthesis of InSb Nanocrystals with Controlled Polymorphism Using Indium and Antimony Amides. *Chem. Mater.* **2013**, *25*, 1788–1792.
- (112) Montie, E. A.; Van Gurp, G. J. Photoluminescence of Zn-Diffused and Annealed InP. *J. Appl. Phys.* **1989**, *66*, 5549–5553.
- (113) Adam, S.; Talapin, D. V.; Borchert, H.; Lobo, A.; McGinley, C.; De Castro, A. R. B.; Haase, M.; Weller, H.; Möller, T. The Effect of Nanocrystal Surface Structure on the Luminescence Properties: Photoemission Study of HF-Etched InP Nanocrystals. *J. Chem. Phys.* **2005**, *123*, 084706–1.
- (114) Stasiuk, G. J.; Tamang, S.; Imbert, D.; Gateau, C.; Reiss, P.; Fries, P.; Mazzanti, M. Optimizing the Relaxivity of Gd(III) Complexes Appended to InP/ZnS

- Quantum Dots by Linker Tuning. *Dalt. Trans.* **2013**, *42*, 8197–8200.
- (115) Li, D.; Kristal, B.; Wang, Y.; Feng, J.; Lu, Z.; Yu, G.; Chen, Z.; Li, Y.; Li, X.; Xu, X. Enhanced Efficiency of InP-Based Red Quantum Dot Light-Emitting Diodes. *ACS Appl. Mater. Interfaces* **2019**, *11*, 34067–34075.
- (116) Stasiuk, G. J.; Tamang, S.; Imbert, D.; Poillot, C.; Giardiello, M.; Tisseyre, C.; Barbier, E. L.; Fries, P. H.; De Waard, M.; Reiss, P.; Mazzanti, M. Cell-Permeable Ln(III) Chelate-Functionalized InP Quantum Dots as Multimodal Imaging Agents. *ACS Nano* **2011**, *5*, 8193–8201.
- (117) Fan, G.; Wang, C.; Fang, J. Solution-Based Synthesis of III-V Quantum Dots and Their Applications in Gas Sensing and Bio-Imaging. *Nano Today* **2014**, *9*, 69–84.
- (118) Mushonga, P.; Onani, M. O.; Madiehe, A. M.; Meyer, M. Indium Phosphide-Based Semiconductor Nanocrystals and Their Applications. *J. Nanomater.* **2012**, *2012*, 869284–869295.
- (119) Heath, J. R.; Shiang, J. J. Covalency in Semiconductor Quantum Dots. *Chem. Soc. Rev.* **1998**, *27*, 65–71.
- (120) Wells, R. L.; Aubuchon, S. R.; Kher, S. S.; Lube, M. S.; White, P. S. Synthesis of Nanocrystalline Indium Arsenide and Indium Phosphide from Indium(III) Halides and Tris (Trimethylsilyl)Pnicogens. Synthesis, Characterization, and Decomposition Behavior of I3In.P(SiMe₃)₃. *Chem. Mater.* **1995**, *7*, 793–800.
- (121) Wells, R. L.; Pitt, C. G.; Mcphail, A. T.; Purdy, A. P.; Shafieezad, S.; Hallock, R. B. Use of Tris(Trimethylsilyl)arsine To Prepare Gallium Arsenide and

- Indium Arsenide. *Chem. Mater.* **1989**, *1*, 4–6.
- (122) Mičić, O. I.; Curtis, C. J.; Jones, K. M.; Sprague, J. R.; Nozik, A. J. Synthesis and Characterization of InP Quantum Dots. *J. Phys. Chem.* **1994**, *98*, 4966–4969.
- (123) Joung, S.; Yoon, S.; Han, C.-S.; Kim, Y.; Jeong, S. Facile Synthesis of Uniform Large-Sized InP Nanocrystal Quantum Dots Using Tris(Tert-Butyldimethylsilyl)Phosphine. *Nanoscale Res. Lett.* **2012**, *7*, 1–8.
- (124) Franke, D.; Harris, D. K.; Xie, L.; Jensen, K. F.; Bawendi, M. G. The Unexpected Influence of Precursor Conversion Rate in the Synthesis of III-V Quantum Dots. *Angew. Chemie - Int. Ed.* **2015**, *54*, 14299–14303.
- (125) Gary, D. C.; Glassy, B. A.; Cossairt, B. M. Investigation of Indium Phosphide Quantum Dot Nucleation and Growth Utilizing Triarylsilylphosphine Precursors. *Chem. Mater.* **2014**, *26*, 1734–1744.
- (126) Thuy, U. T. D.; Huyen, T. T. T.; Liem, N. Q.; Reiss, P. Low Temperature Synthesis of InP Nanocrystals. *Mater. Chem. Phys.* **2008**, *112*, 1120–1123.
- (127) Liu, Z.; Kumbhar, A.; Xu, D.; Zhang, J.; Sun, Z.; Fang, J. Coreduction Colloidal Synthesis of III-V Nanocrystals: The Case of InP. *Angew. Chemie - Int. Ed.* **2008**, *47*, 3540–3542.
- (128) Li, L.; Protière, M.; Reiss, P. Economic Synthesis of High Quality InP Nanocrystals Using Calcium Phosphide as the Phosphorus Precursor. *Chem. Mater.* **2008**, *20*, 2621–2623.
- (129) Tamang, S.; Beaune, G.; Texier, I.; Reiss, P. Aqueous Phase Transfer of InP/ZnS Nanocrystals Conserving Fluorescence and High Colloidal Stability. *ACS Nano*

2011, 5, 9392–9402.

- (130) Jun, K. W.; Khanna, P. K.; Hong, K. B.; Baeg, J. O.; Suh, Y. D. Synthesis of InP Nanocrystals from Indium Chloride and Sodium Phosphide by Solution Route. *Mater. Chem. Phys.* **2006**, 96, 494–497.
- (131) Allen, P. M.; Walker, B. J.; Bawendi, M. G. Mechanistic Insights into the Formation of InP Quantum Dots. *Angew. Chemie - Int. Ed.* **2010**, 49, 760–762.
- (132) Cros-Gagneux, A.; Delpech, F.; Nayral, C.; Cornejo, A.; Coppel, Y.; Chaudret, B. Surface Chemistry of InP Quantum Dots: A Comprehensive Study. *J. Am. Chem. Soc.* **2010**, 132, 18147–18157.
- (133) Tamang, S.; Lee, S.; Choi, H.; Jeong, S. Tuning Size and Size Distribution of Colloidal InAs Nanocrystals via Continuous Supply of Prenucleation Clusters on Nanocrystal Seeds. *Chem. Mater.* **2016**, 28, 8119–8122.

Chapter II

*Preparation of precursor of CQDs
synthesis*

2.1. Introduction.

The commonly used metal precursor in almost all the synthetic procedures for colloidal semiconductor NCs involving the hot injection method is the metal salt of fatty acids (MFAs) or metal carboxylates.¹⁻⁴ MFAs are the salts of metal (halide, nitrate, acetate, etc.) and long-chain fatty acids with a general formula of $M(C_nH_{2n+1}COO)_x$; where M could be any metal and x its valency.^{5,6} MFAs are ideal for the synthesis of NCs due to the following attributes:

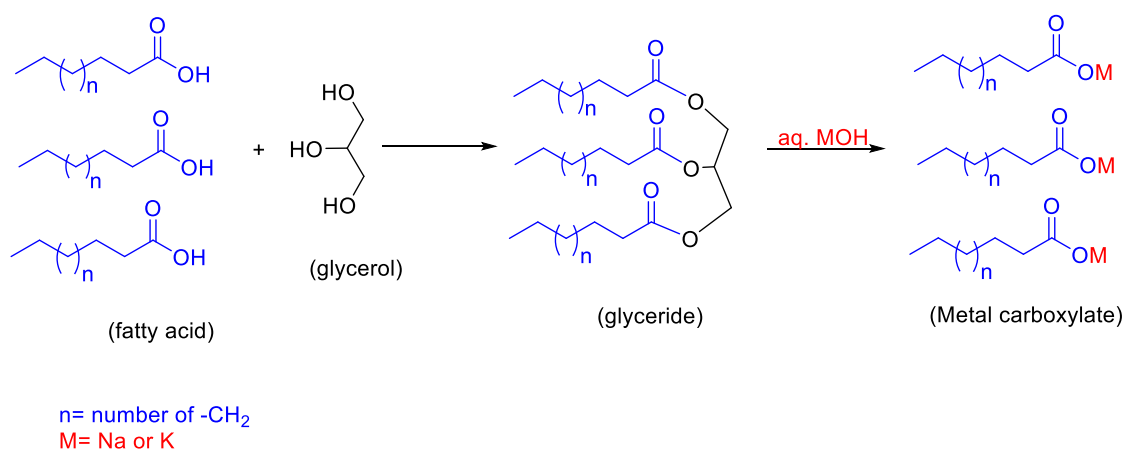
- (a) MFAs have good solubility in a non-coordinating solvent (1-ODE), especially at high temperatures.^{3,7-13}
- (b) MFAs release fatty acids during the reaction which are attached to the surface of the NCs as a stable ligand/surfactant.^{1,4,14-17}
- (c) MFAs play a decisive role in nucleation and growth processes and have a direct bearing on the evolution of size^{7,8}, shape^{18,19}, crystal phase^{13,20} and assembly of NCs.^{18,21}

In addition to the enormous applicability of MFAs in CQDs, MFAs also have varied applications in industrial and commercial processes. For instance, MFAs comprising zinc and calcium metals have been used as active processing additives (APA) in the rubber industry.²² In addition, calcium salts of fatty acids display notable bactericidal properties against *Staphylococcus aureus*.²³ Apart from this, MFAs are also used as lubricating agents²⁴⁻²⁶ in the production of biofuels^{27,28}, in the preparation of catalysts with mesoporous structure²⁹, and act as an active catalyst for the esterification of lauric acid³⁰, etc. Furthermore, they are also used in waterproofing agents³¹, cosmetics³², polyolefin acid scavenger³³, mould release agents in polymers³⁴, anticaking agents in pharmaceuticals³⁵, and fuel additives.³⁶

Its academic and industrial importance has motivated the scientific community to develop an efficient method for the synthesis of metal carboxylate of higher fatty acids. The common methods for preparing MFAs are as follows:

2.1.1. Saponification method: The method involves the reaction of fatty acid with an alkali metal hydroxide (NaOH, KOH, etc.) in presence of water as a solvent.^{37,38} Initially, the fatty acid combines with glycerol to form triglyceride (an ester of fatty acid and glycerol) which undergoes hydrolysis in presence of an alkali to yield MFAs of sodium and potassium.³⁷⁻⁴⁰ Scheme 2.1 is given as an example of the formation of alkali metal carboxylate by saponification reaction based on the work from Wang *et al.*³⁷

Scheme 2.1. Preparation of alkali metal carboxylates through saponification reaction.

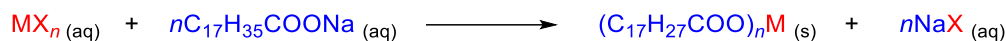


Although this is an excellent method to prepare the MFAs, its limited substrate scope implies that the applicability remains confined only to alkali metals like sodium and potassium.

2.1.2. Double decomposition or precipitation method: This is a very common industrial and commercial method for the preparation of MFAs. Typically, alkali metal carboxylates are treated with water-soluble metal salts yielding the

desired metal salt of fatty acids.^{34,36,39,41} Scheme 2.2 gives an overview of the double decomposition method.

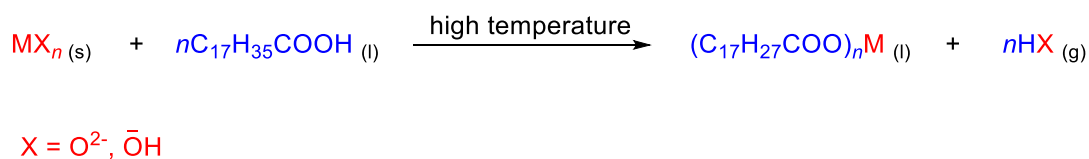
Scheme 2.2. Preparation of metal stearate through double decomposition method.



In this method, the desired product is precipitated out in the reaction mixture and hence the name.⁴² The industrial applicability of this method is enormous as the substrate scope is diverse.⁴³ However, its production cost is high and an excess amount of water is contaminated during the purification.⁴⁴

2.1.3. Fusion method: The MFAs are prepared by direct reaction of molten fatty acid with metal oxides or hydroxides.³⁶ This method requires extremely high temperatures (~250 °C or above).⁴⁵⁻⁴⁹ A representative example of the formation of metal stearate using the fusion method based on the seminal work of John Blachford⁵⁰ is illustrated in scheme 2.3.

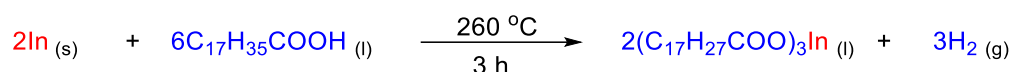
Scheme 2.3. Formation of metal stearate by fusion method.



The limited substrate scope is the major drawback of the fusion method. Furthermore, as the reaction occurs at a very high temperature there is a possibility of the formation of undesired side products. Additionally, the reaction does not occur completely leaving behind the starting material which needs to be removed from post reaction thus increasing the production cost.^{34,36,42,44}

2.1.4. Direct reaction of fatty acid with metal: Along with the fusion method John Blachford first introduced this method in 1982.⁵⁰ Again, the molten fatty acid is reacted with metal directly instead of its oxide or hydroxide.⁵¹⁻⁵⁴ Ming Ng and coworkers⁵⁵ prepared indium stearate using this method as demonstrated in Scheme 2.4.

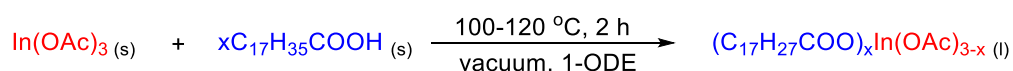
Scheme 2.4. Preparation of indium stearate by direct reaction of indium metal with stearic acid.



The reaction is carried out in a solvent-free condition which is an advantage.^{54,55} However, the limited substrate scope (all metals do not react readily with fatty acids) and the byproduct (hydrogen gas) exceeding the explosive limits are a few disadvantages of this method.⁵⁶ Furthermore, the atom economy is poor as a large quantity of fatty acid is used in the reaction process.³⁴

2.1.5. Vacuum method: The vacuum method is invariably the most widely employed method for the preparation of MFAs in the colloidal synthesis of NCs based on the hot injection method.^{7,8,11,13,15} Scheme 2.5 outlines the vacuum method or degassing method for the preparation of indium stearate by mixing indium acetate with stearic acid in 1-ODE.

Scheme 2.5. Formation of indium stearate from a vacuum method.



The metal salts and desired fatty acid are mixed in a non-coordinating solvent like 1-octadecene (1-ODE) and vacuumed at high temperatures (100- 120 °C) for an hour or

until an optically “clear solution” is obtained.^{4,7,8,15} The reaction proceeds further to form CQDs with *in situ* generated MFA. Unfortunately, in this method, there is no consensus on the reaction time, temperature, and pressure required for the degassing process. Furthermore, except for a few cases^{10,57-59}, the purity and composition of *in situ* generated MFAs are unknown. These insufficiencies lead to batch-to-batch variations in the properties of CQDs.

In this chapter, we review the vacuum method of preparation of MFAs. Secondly, we explore saponification and double decomposition (trans saponification method) methods to prepare high-purity MFAs and CQDs. Finally, we introduce a novel generalized method for the preparation of almost any MFA. Since the properties of CQDs are extremely sensitive to the purity and reactivity of the precursor, this chapter will eventually address all the key issues about the synthesis of high-quality MFAs, which is important for batch-to-batch reproducibility of the CQDs.

2.2. Determination of purity of MFAs prepared by vacuum method.

To investigate the purity of MFAs prepared by vacuum method indium salt of stearic acid was prepared. In a typical synthetic method^{8,60,61} indium acetate was mixed with stearic acid in 1-ODE and vacuumed at 120 °C until a clear solution was observed (Figure 2.1a). The isolated indium stearate was characterized by TGA (Figure 2.1b).

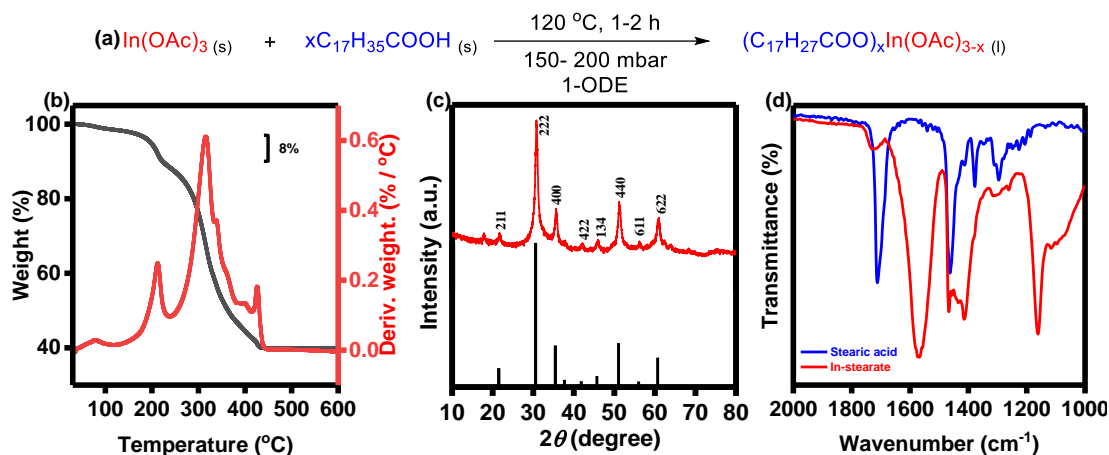


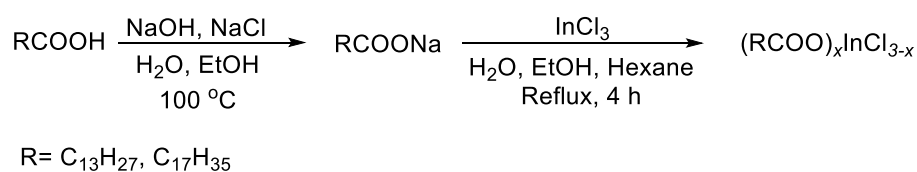
Figure 2.1. Characterization of indium stearate prepared through vacuum method. (a) Scheme for preparation of indium stearate through vacuum method. (b) TGA analysis depicts the loss of ~8% consistent with one acetate group. (c) PXRD of the residual mass obtained from TGA (red) compared with the standard In_2O_3 (black, JCPDS card no.: 01-088-2160) (d) FTIR shows the impurity peak at 1726 cm^{-1} .

In the literature, it is presumed that the vacuum method invariably forms pure $\text{In}(\text{OCC}_{17}\text{H}_{27})_3$ *in situ*.^{8,60,61} In the TGA thermogram the initial loss of 8% (which is equivalent to the loss of one acetate group) cannot be accounted for by assuming the structure of MFA as $\text{In}(\text{OCC}_{17}\text{H}_{27})_3$. The product is either $\text{In}(\text{OCC}_{17}\text{H}_{27})_2(\text{OAc})$ or related mixed carboxylate complex instead of assumed $\text{In}(\text{OCC}_{17}\text{H}_{27})_3$. Although we do concede that the vacuum used in our case may be lower compared to the literature report, it is important to be sure about the actual composition of the MFA for reproducibility. The 40% residue of the MFA in TGA is consistent with the mass of indium oxide, which is confirmed by PXRD (figure 2.1c). Furthermore, a prominent peak at 1728 cm^{-1} in FTIR reveals the presence of a free carbonyl group. The results show that the purity and final composition of assumed indium stearate prepared by the vacuum method are ambiguous.

2.3. Preparation of MFAs from combined saponification and double decomposition methods.

The uncertainty in the purity and composition of MFA prepared by the vacuum method instigated the need for an alternative method to generate pure MFA. A strategy involving the combination of saponification and double decomposition method based on the preparation of iron-oleate by Hyeon and coworkers⁶² was employed as a model reaction for preparing indium carboxylate (precisely myristate) as depicted in scheme 2.6.

Scheme 2.6. Preparation of indium salt of fatty acid by the combination of saponification of double decomposition method.



Initially, sodium myristate was prepared from myristic acid and sodium hydroxide in presence of sodium chloride (Scheme 2.6) which is subsequently reacted with InCl₃ to obtain indium myristate.^{37,63} The product was characterized by FTIR, NMR, HRMS, and TGA. The FTIR spectrum confirmed the formation of indium myristate as the carbonyl peak of myristic acid at 1710 cm⁻¹ is absent and a peak at 1558 cm⁻¹ ascribed to carbonyl stretching of indium myristate is present (figure 2.2a). NMR further confirmed the successful formation of indium myristate (section 2.7).

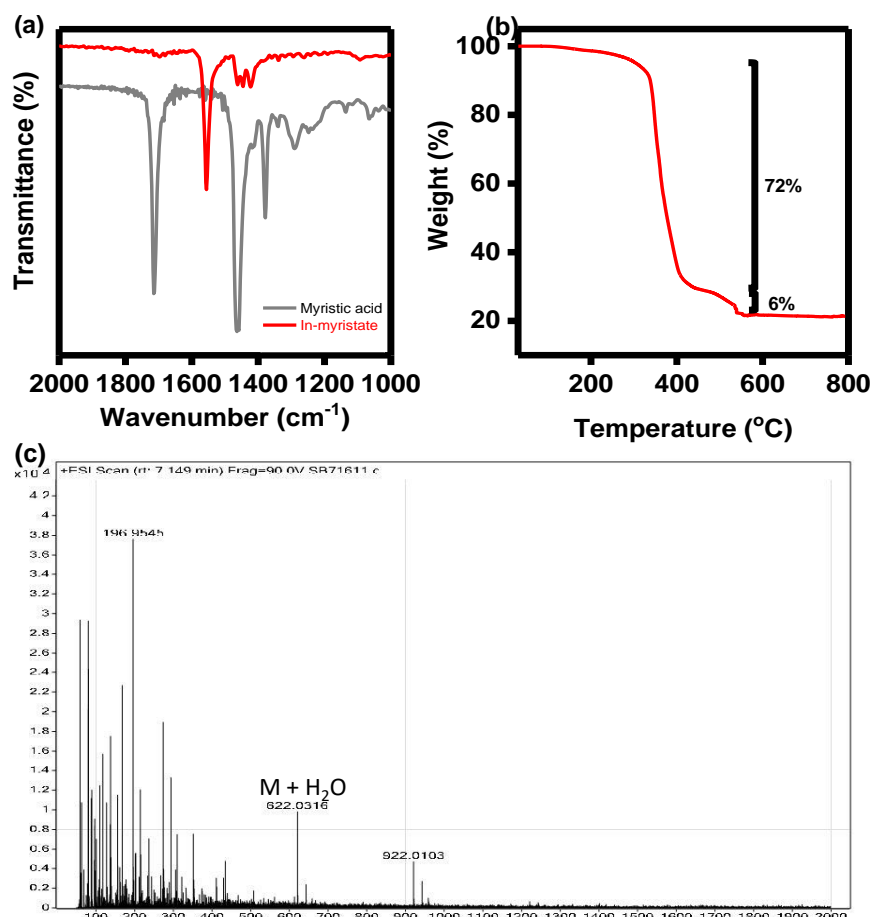
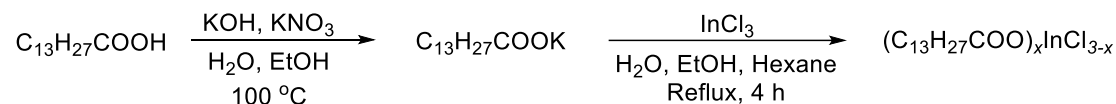


Figure 2.2. (a) FTIR to myristic acid (grey), and indium myristate (red) shows the major carbonyl shift of myristic acid with the addition of respective metals. (b) TGA of indium myristate depicting an initial loss of ~72% consistent with two myristate groups (75%) and a final loss of ~6% consistent with one chloride group. (c) ESIMS of as-synthesized indium myristate shows the molecular ion peak at 622 which accounts for $\text{In}(\text{OCOC}_{13}\text{H}_{27})_2\text{Cl} + \text{H}_2\text{O}$ ($\text{M} + \text{H}_2\text{O}$).

However, TGA and HRMS results revealed that only two chloride ions are substituted by the myristate group in this method. The TGA thermogram (figure 2.2b) shows a weight loss of ~72% at around 232 – 477 °C and ~6% around 480-580 °C attributed to two myristates and one chloride respectively. The formation of $\text{In}(\text{OCOC}_{13}\text{H}_{27})_2\text{Cl}$ was corroborated by its ESIMS (figure 2.2c). It is noteworthy that this method works perfectly for more ionic metal salts like Pb (II) and Cd (II). The partial reaction of sodium myristate with indium chloride in our case is attributed to the lower reactivity

of indium salt with sodium myristate.⁶⁴ We noted that using the more reactive potassium myristate instead of sodium myristate solved the problem of partial substitution. Potassium lies above sodium in an electrochemical series⁶⁴⁻⁶⁶ and is expected to react with indium chloride more strongly (Scheme 2.7).

Scheme 2.7. Preparation of indium myristate from potassium myristate.



The formation of the product was confirmed by FTIR (figure 2.3). The carbonyl peak of free acid shifts from 1710 cm^{-1} to 1555 cm^{-1} in indium myristate confirming its formation. NMR results are also consistent with indium myristate (section 2.7) Furthermore, TGA shows an initial loss of $\sim 57\%$ at a temperature range of $\sim 135\text{-}300^\circ\text{C}$ consistent with two myristate groups followed by the subsequent loss of $\sim 28\%$ at temperature range $300\text{-}450^\circ\text{C}$ consistent with one myristate group. The complete substitution of three chlorides with three myristates was confirmed by mass spectroscopy. The molecular ion peak related to $\text{In}(\text{OCOC}_{13}\text{H}_{27})_3$ was detected at $m/z = 795\text{ (M-H)}^+$.

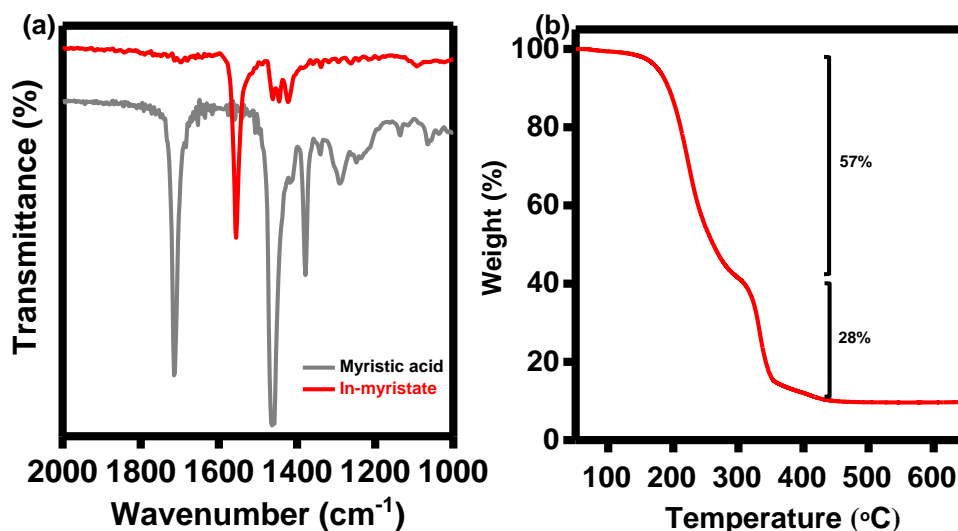
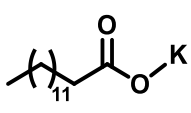
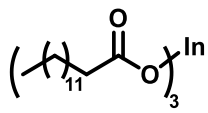
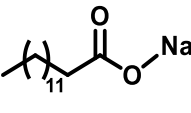
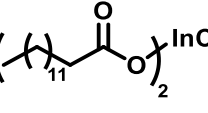
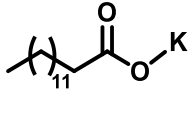
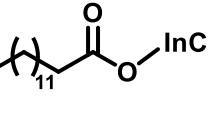


Figure 2.3. (a) Comparative FTIR spectrum of myristic acid (grey), and indium myristate (red) showing the significant shift in carbonyl peak (1710 cm^{-1}) of myristic acid confirming the addition of metal. (b) TGA thermogram of as-synthesized indium myristate with total loss of $\sim 85\%$ consistent with three myristate groups.

The indium carboxylates prepared using this method are summarised in table 2.1.

Table 2.1. Indium carboxylates prepared from the combination of saponification and double decomposition method.

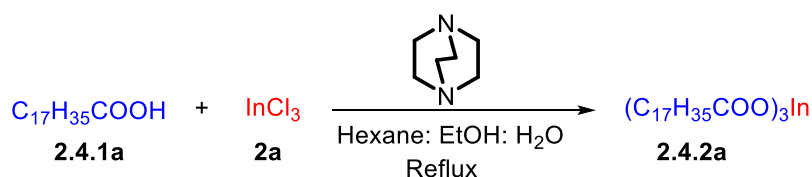
Entry	In-source	Fatty acid source	Product	Yield (%)
1.	InCl_3 (2a)	 (2.3.1a)	 (2.3.2a)	67
2.	InCl_3 (2a)	 (2.3.1b)	 (2.3.2b)	64
3.	InCl_3 (2a)	 (2.3.1a)	 (2.3.2c)	52

The method described above works remarkably well for the production of ionic MFAs (Na, K, Cd, Pb, Zn, etc.) but for covalent MFAs (Al, Ga, In, etc.) the yield is comparatively low.^{1,43} The atom economy of the process is also poor due to the multiple steps involved in the synthetic approach. Furthermore, the hydroxyl anion of inorganic bases of NaOH and KOH competes with the other intended metal ions perturbing the formation of desired metal carboxylates.⁶⁷ Therefore, a single-step synthetic approach using a non-ionic and non-coordinating organic base with a low affinity towards metal ions is highly desirable.

2.4. DBU-catalysed synthesis of MFAs.

In pursuit of a more efficient method for the preparation of MFAs, we explored an organic base as the catalyst. The premise on which the organic base was chosen was, they do not have counter-ions competing with metal ions for the carboxylate group. Initially, an inexpensive, commercially available, and environment-friendly benign base^{68,69} 1,4-diazabicyclo[2.2.2]octane (DABCO, pK_a conjugate acid~8.7)^{70,71} was used to prepare the indium stearate (**2.4.2a**) from indium chloride (**2a**) and stearic acid (**2.4.1a**). Refluxing 1 equivalent indium chloride with 3 equivalent stearic acids in presence of DABCO formed indium stearate (Scheme 2.8). The higher amount of base ensured the complete deprotonation of stearic acid.

Scheme 2.8. Preparation of indium stearate from indium chloride and stearic acid in presence of DABCO.



The reaction yield of 72% (**2.4.2a**) is relatively higher than the method discussed in section 2.3. The formation of the product is confirmed by the shift of the carbonyl peak in FTIR (figure 2.4a). The displacement of sharp C=O stretching frequency at 1712 cm^{-1} in free stearic acid to 1525 cm^{-1} in indium stearate confirms the formation of the product. Furthermore, the absence of bending -OH frequency at 1296 cm^{-1} for indium stearate (**2.4.2a**) suggests its formation.⁵² TGA thermogram (figure 2.4b) depicts the loss of ~85% at a temperature range of 150-500 °C which is consistent with three stearate groups in indium stearate. The structural purity of the as-synthesized product (1 mmol) was further confirmed by its ^1H NMR (figure 2.4c) in presence of internal standard (1,3,5- trimethoxybenzene, TMB, 1 mmol). The red outlined peak in figure 2.4c is for the three methoxy groups of TMB and the blue outlined peak is for the methyl group of as-synthesized indium stearate. The relative ratio of integration of proton of both of these groups is 1:3 which confirms three methyl groups attached with one indium.

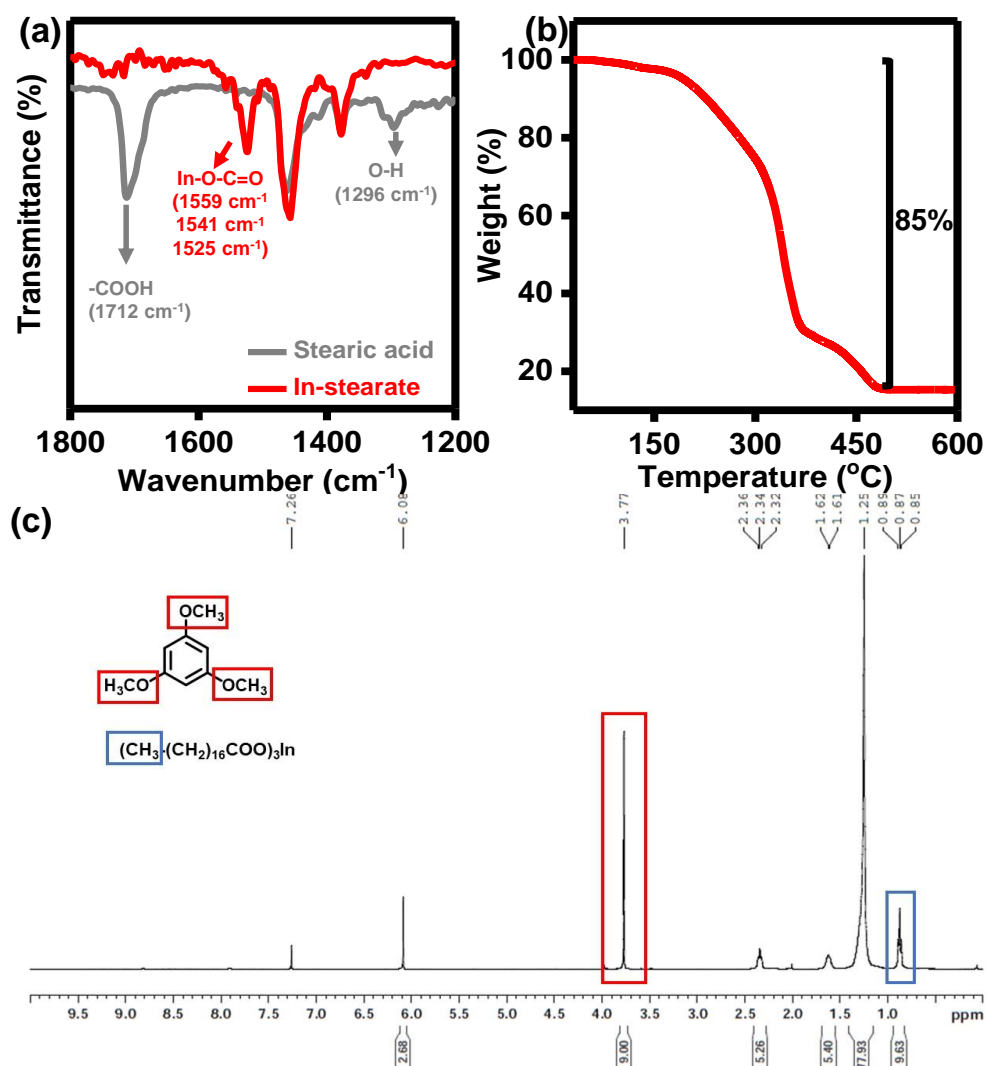
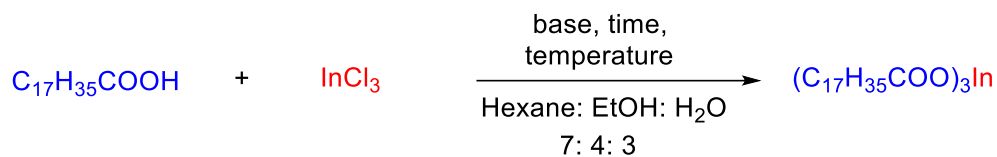


Figure 2.4. Characterization of as-synthesized indium stearate (2.4.2a). (a) FTIR of stearic acid (grey) and indium stearate (red) showing some signature stretching and bending peaks. (b) TGA thermogram of indium stearate with the loss of 85% weight consistent with three stearates. (c) ^1H NMR in presence of internal standard 1,3,5-trimethoxybenzene (1 mmol) suggesting the presence of three stearates (1 mmol).

2.4.1. Optimization studies.

The initial success with DABCO opened up the possibility of the reaction occurring with other non-nucleophilic nitrogenous bases. We explored a variety of organic bases under different reaction conditions with stearic acid and indium chloride as model substrates. Table 2.2 summarizes the optimization studies.

Table 2.2. Optimization studies for novel one-pot synthesis of indium stearate.

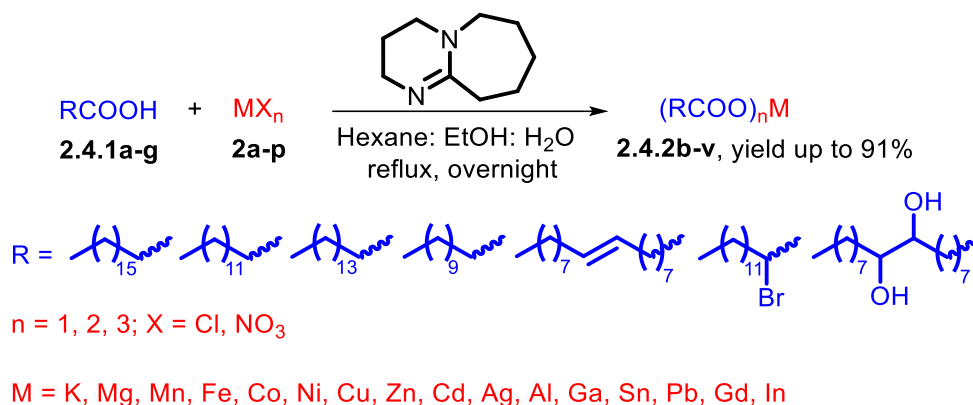
Entry	Base	Equivalent	Temperature (°C)	Time (h)	Yield (%)
1.	DABCO	4.0	Reflux	Overnight	72
2.	Pyridine	4.0	Reflux	Overnight	66
3.	Triethylamine	4.0	Reflux	Overnight	32
4 ^a .	DBU	4.0	Reflux	Overnight	78
5 ^b .	DBU	3.0	Reflux	Overnight	80
6^c.	DBU	1.0	Reflux	Overnight	85
7 ^d .	DBU	0.5	Reflux	Overnight	66
8 ^e .	DBU	1.0	25	Overnight	nr
9 ^f .	DBU	1.0	40	Overnight	22
10 ^g .	DBU	1.0	60	Overnight	60
11.	DBU	1.0	Reflux	6	60
12	DBU	1.0	Reflux	8	58
13	DBN	1.0	Reflux	Overnight	82

^aUnless noted otherwise, all reactions were carried out with 4.0 equivalent (with respect to a fatty acid) of the base under reflux condition. ^bThe reaction was performed with 3.0 equivalent of the base. ^cThe reaction was performed with 1.0 equivalent of the base. ^dThe reaction was performed with 0.5 equivalent of the base. ^enr denotes no reaction. ^fThe reaction was performed at 40 °C. ^gThe reaction was performed at 60 °C.

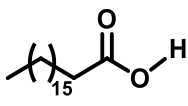
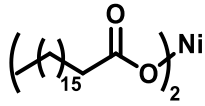
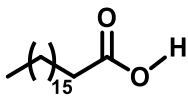
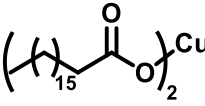
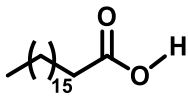
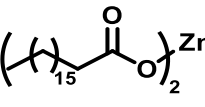
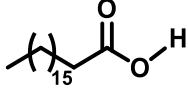
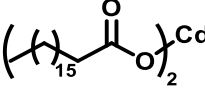
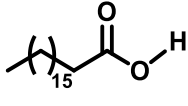
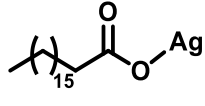
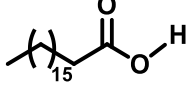
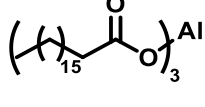
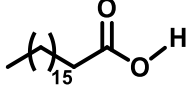
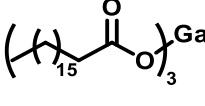
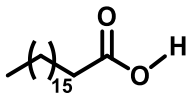
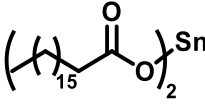
In this context, pyridine (aromatic base), triethylamine (aliphatic base), and DBU (sterically hindered bicyclic amidine base) were screened (entries 1-4, table 2.2). The use of pyridine and triethylamine gives the desired product at a relatively lower yield of 66% and 32% respectively compared to DABCO proving that the sterically hindered base is more effective for indium stearate preparation. DBU (entry 4, table 2.2) on the other hand yields the highest 78% of indium stearate. The fact that DBU yields more product than DABCO is attributed to its higher basicity (pK_a conjugate \sim 13.5)⁷² compared to that of DABCO (pK_a conjugate acid \sim 8.7). Our optimization results show that DBU is the most efficient. The concentration of base DBU was further optimized (entries 4-7, table 2.2). Initially, the concentration of the DBU was 4.0 equivalent (entry 4, table 2.2). The yield of the reaction increased from 78% in the 4.0 equivalent (entry 4, table 2.2) to 80% in the 3.0 equivalent (entry 5, table 2.2). The best result (85 %) was obtained when 1.0 equivalent of DBU was used (entry 6, table 2.2). Next, the effect of temperature on the reaction yield was studied (using 1 equivalent of DBU). At room temperature (25 °C, entry 8) the reaction does not occur. At 40 °C (entry 9, 22%) and 60 °C (entry 10, 60 %) the reaction yields are comparatively lower than the reaction carried under refluxing conditions (entry 6, 85%). Next, the reaction time was optimized (entries 11-12). Interestingly, the five-membered analogue of DBU, 1,5-diazabicyclo[4.3.0]non-5-ene (DBN) also (entry 13, table 2.2) produced a comparative product yield of 82%. In summary, the non-ionic, inexpensive, non-toxic stable amidine base DBU^{73,74} when used in a catalytic amount under reflux conditions produced pure indium stearate at a high reaction yield (85%).

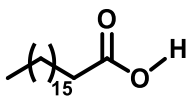
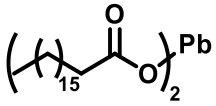
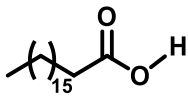
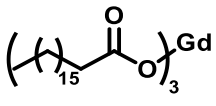
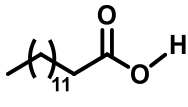
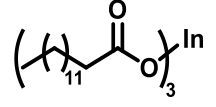
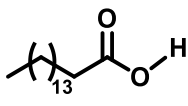
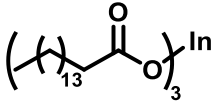
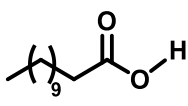
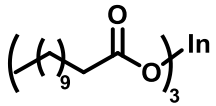
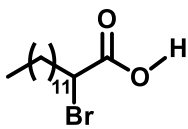
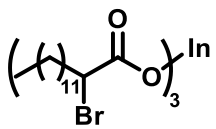
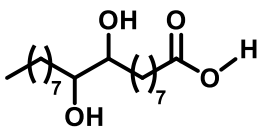
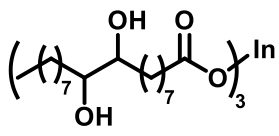
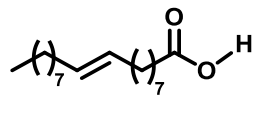
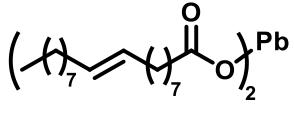
2.4.2. Substrate scope.

We prepared a diverse range of MFAs with various metal salts with fatty acids. Table 2.3 depicts the substrate scope studies of the novel reaction scheme.

Table 2.3. Synthesis of metal carboxylates from fatty acid and a metal salt.

Entry	Metal salt	Fatty acid	Product	Yield (%)
1.	KNO_3 (2b)	 (2.4.1a)	 (2.4.2b)	85
2.	$\text{Mg}(\text{NO}_3)_2$ (2c)	 (2.4.1a)	 (2.4.2c)	88
3.	$\text{MnCl}_2 \cdot 4\text{H}_2\text{O}$ (2d)	 (2.4.1a)	 (2.4.2d)	70
4.	FeCl_3 (2e)	 (2.4.1a)	 (2.4.2e)	90
5.	CoCl_2 (2f)	 (2.4.1a)	 (2.4.2f)	75

6.	NiCl ₂ .6H ₂ O (2g)	 (2.4.1a)	 (2.4.2g)	87
7.	CuCl ₂ .H ₂ O (2h)	 (2.4.1a)	 (2.4.2h)	91
8.	ZnCl ₂ (2i)	 (2.4.1a)	 (2.4.2i)	87
9.	CdCl ₂ (2j)	 (2.4.1a)	 (2.4.2j)	81
10.	AgNO ₃ (2k)	 (2.4.1a)	 (2.4.2k)	91
11.	AlCl ₃ (2l)	 (2.4.1a)	 (2.4.2l)	35
12.	GaCl ₃ (2m)	 (2.4.1a)	 (2.4.2m)	90
13.	SnCl ₂ .2H ₂ O (2n)	 (2.4.1a)	 (2.4.2n)	90

14.	Pb(NO ₃) ₂ (2o)			73
		(2.4.1a)	(2.4.2o)	
15.	GdCl ₃ .6H ₂ O (2p)			45
		(2.4.1a)	(2.4.2p)	
16.	InCl ₃ (2a)			90
		(2.4.1b)	(2.4.2q)	
17.	InCl ₃ (2a)			60
		(2.4.1c)	(2.4.2r)	
18.	InCl ₃ (2a)			75
		(2.4.1d)	(2.4.2s)	
19.	InCl ₃ (2a)			89
		(2.4.1e)	(2.4.2t)	
20.	InCl ₃ (2a)			72
		(2.4.1f)	(2.4.2u)	
21.	Pb(NO ₃) ₂ (2o)			90
		(2.4.1g)	(2.4.2v)	

All the substrates were well tolerated under optimized conditions. The products were obtained in high yields (up to ~91%, table 2.3). The synthetic versatility of the reaction is evident from the fact that each type of metal in the periodic table was considered and corresponding MFAs were prepared from them. For example, from the alkali metal group, K-stearate was prepared (**2.4.2.b**). Similarly, alkaline earth metal Mg-stearate (**2.4.2.c**), first row transitional metals: Mn-stearate (**2.4.2.d**), Fe-stearate (**2.4.2.e**), Co-stearate (**2.4.2.f**), Ni-stearate (**2.4.2.g**), Cu-stearate (**2.4.2.h**), Zn-stearate (**2.4.2.i**); second-row transitional metals: Cd-stearate (**2.4.2.j**), Ag-stearate (**2.4.2.k**), post-transition metals (triels): Al-stearate (**2.4.2.l**), Ga-stearate (**2.4.2.m**), indium stearate (**2.4.2.a**); post-transition metals (tetrels): Sn-stearate (**2.4.2.n**), Pb-stearate (**2.4.2.o**) and lanthanide Gd-stearate (**2.4.2.p**) were all successfully synthesized. The method also works with different types of fatty acids (**2.4.1a-g**). The formation of MFAs (**2.4.2b-v**) was confirmed by -COO^- stretching frequency⁷⁵ in FTIR ranging from 1510 to 1650 cm^{-1} (Annexure A2). For some of the MFAs, two stretching frequencies were detected attributing to asymmetric and symmetric stretching arising from the different types of bonding between metal and oxygen of fatty acids.⁷⁶⁻⁷⁸ For a free acid, typically the C=O stretching⁵⁵ is observed around 1700 cm^{-1} which is absent in as-prepared MFAs (**2.4.2b-v**) indicating the high purity of the products. The TGA thermogram of MFAs (**2.4.2b-v**) depicts the weight loss which is consistent with the number of carboxylate groups attached to each metal in the products (**2.4.2b-v**, Annexure I). Furthermore, ^1H NMR and ^{13}C NMR were used for the characterization of MFAs containing diamagnetic metal ions (Annexure A2). Additionally, the melting point of MFAs was also determined for representative examples. To conclude, the developed method exhibited a high substrate scope.

2.4.3. Mechanism.

The DBU is highly efficient when a catalytic amount is used (entry 6, table 2.2). Unprotonated DBU shows C=N stretching at 1608 cm^{-1} (Figure 2.5a and b). This peak shifts to 1608 cm^{-1} due to the protonation and formation of intermediate **A**. The C=O stretching of free stearic acid at 1712 cm^{-1} also shifts to 1557 cm^{-1} in intermediate **A**. Next, the anion exchange between intermediate **A** and metal salt takes place resulting in desired product and intermediate **B**. The driving force for this exchange is the high oxyphilic nature of metal ions.^{79,80} Formation of **B** is evident in FTIR as C=N⁺ stretching at 1608 cm^{-1} appears in the water extract. This FTIR is consistent with the literature report where commercially available fatty acid bio-based dimer Pripol 1009 protonated DBU.⁸¹ Finally, the catalytic cycle is complete as intermediate **B** releases HX.

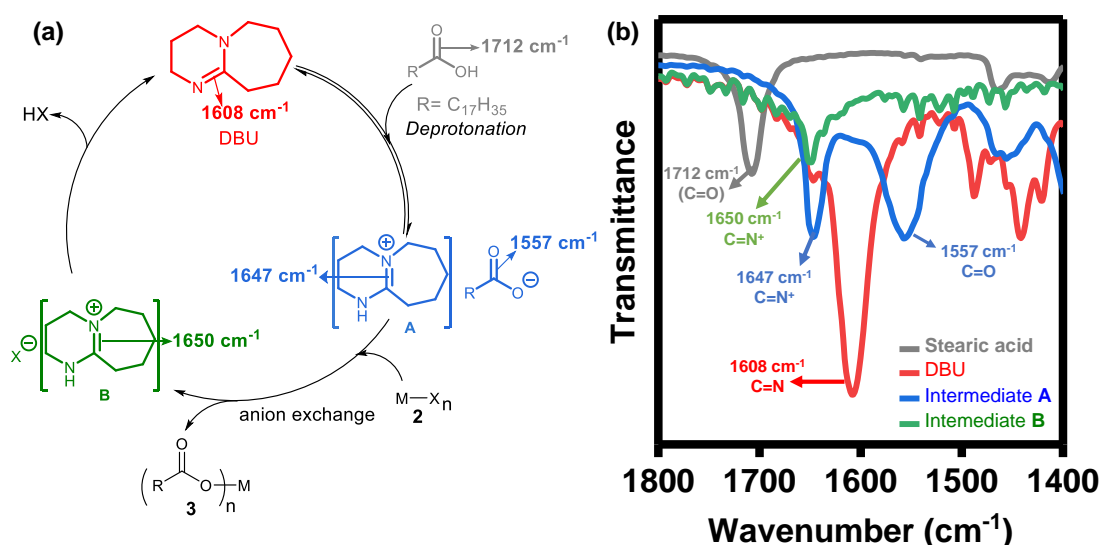


Figure 2.5. (a) A plausible mechanism for the formation of MFAs in presence of DBU as a catalyst. The substrate and intermediates are colours in grey, red, blue and green for co-relating them with their corresponding FTIR. (b) FTIR of stearic acid (grey) with signature carbonyl stretching frequency at 1712 cm^{-1} , pristine DBU (red) with signature C=N stretching at 1608 cm^{-1} , intermediate **A** (blue) formed after deprotonation of stearic acid by DBU and intermediate **B** (green) formed at the end of the reaction.

2.4.4. Multi-gram scale synthesis.

A multi-gram synthesis of zinc stearate was performed (figure 2.6a). 20.0 g of stearic acid was reacted with 5.0 g of zinc chloride in presence of DBU under optimized conditions to obtain 19.7 g of zinc stearate (figure 2.6a, 86% yield). The product was characterized using FTIR (C=O stretching $\sim 1537\text{ cm}^{-1}$) and NMR. Furthermore, the loss of $\sim 86\%$ weight in TGA at a temperature range of 170-500 $^{\circ}\text{C}$ is consistent with the two stearate groups. The melting point of the product is $\sim 128\text{--}130\text{ }^{\circ}\text{C}$ which is consistent with its literature value ($130\text{ }^{\circ}\text{C}$).⁸²

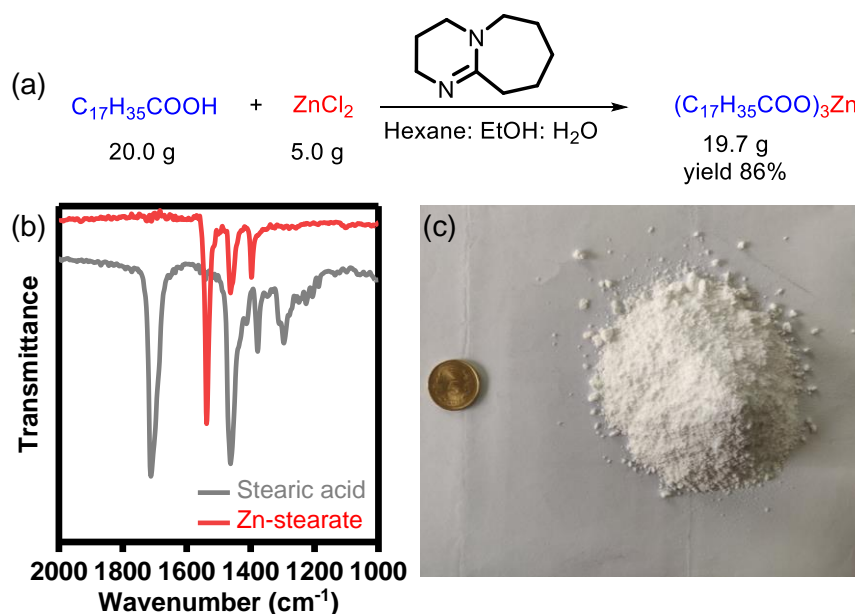


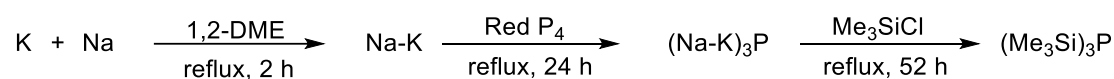
Figure 2.6. (a) Scheme for preparing zinc stearate from zinc chloride and stearic acid in presence of DBU catalyst. (b) A comparative FTIR of as-prepared zinc stearate (red) and stearic acid (grey) showing a shift in the carbonyl peak of acid from 1712 cm^{-1} to 1537 cm^{-1} . (c) A visual description of as-prepared zinc stearate and ₹5 coin (Diameter: 23 mm) for relative assimilation.

2.5. Preparation of group V precursors.

2.5.1. Tris(trimethylsilyl) group V.

Tris(trimethylsilyl) group V compounds have been widely used as group V precursors in III-V semiconductor synthesis. These reactive compounds containing labile Si-V (V=P or As etc.) bonds are excellent precursors for the synthesis of many III-V semiconductor^{59,83,84} The common group V precursor used in the preparation of III-V semiconductor nanocrystals are tris(trimethylsilyl)phosphine (PTMS). Due to its pyrophoric nature,^{16,85,86} it is difficult to obtain commercially. We prepared PTMS using the standard procedure^{16,59,85,86} (Scheme 2.9).

Scheme 2.9. Preparation of tris(trimethylsilyl)phosphine.



Its formation was confirmed with ¹H NMR and ¹³C {¹H} NMR (Figure 2.7). With the help of NMR data, the purity of as-synthesized PTMS was determined to be 83%.

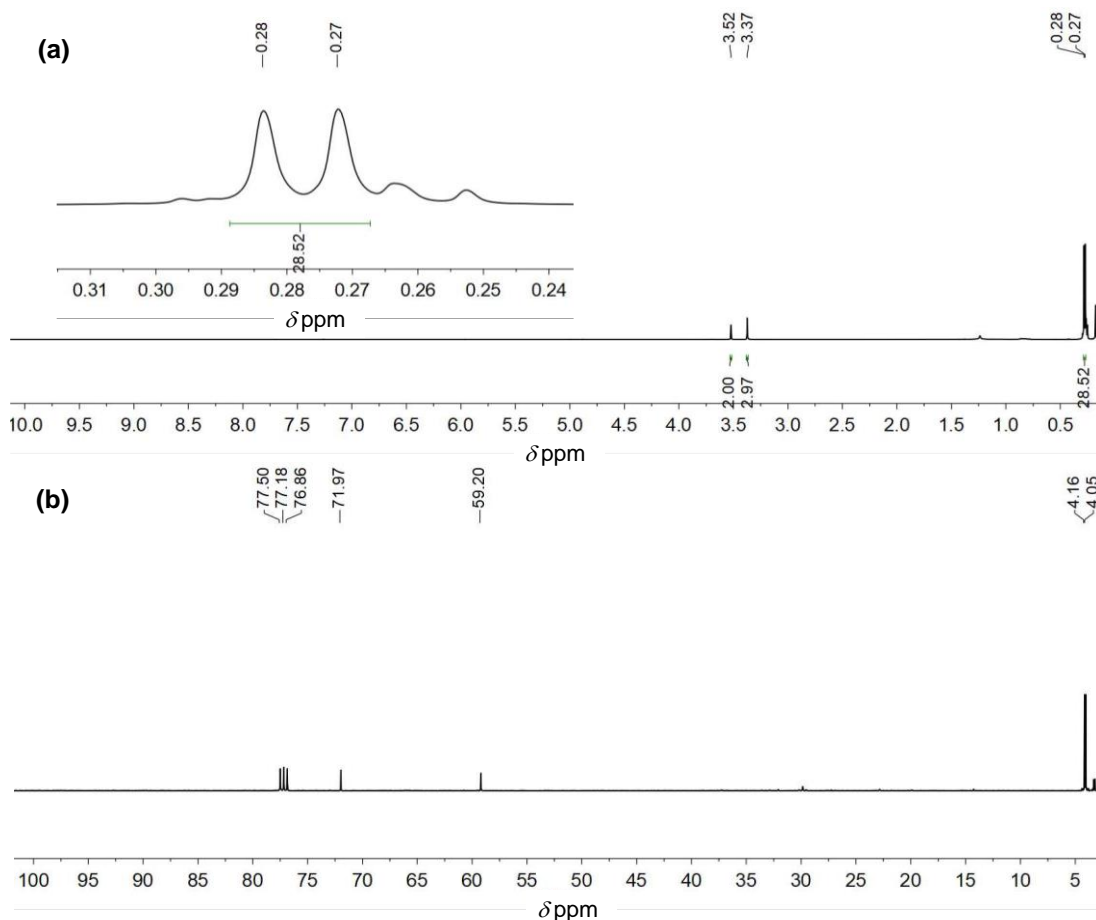
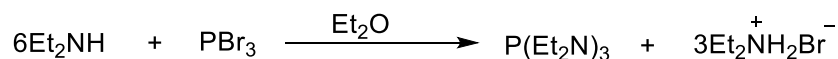


Figure 2.7. Characterization of PTMS with NMR in presence of CDCl_3 as solvent. (a) ^1H NMR peak with a signature methyl chemical shift at 0.27 and 0.28 ppm. The peaks at 3.37 and 3.52 ppm are a peak for the 1,2-DME present as an impurity. Inset: expansion of ^1H NMR between 0.31 to 0.24 ppm showing a distinct doublet of methyl hydrogen from PTMS. (b) ^{13}C { ^1H } NMR of PTMS with methyl carbon chemical shift at 4.16 and 4.05 ppm. The two peaks at 59.2 and 71.97 ppm are for $-\text{CH}_3$ and $-\text{CH}_2$ respectively of 1,2-DME.

2.5.2. Tris(dialkylamino) group V.

In addition, alternative group V precursors such as tris(diethylamino)phosphine ($\text{P}(\text{NEt}_2)_3$) were also prepared. $\text{P}(\text{NEt}_2)_3$ or related amides are of interest because of their stability as compared to tris(trimethylsilyl) phosphine counterparts. In our study, we have prepared $\text{P}(\text{NEt}_2)_3$ (Scheme 2.10)

Scheme 2.10. Preparation of tris(diethylamino)phosphine.



2.6. Conclusion.

The evaluation of purity for ascertaining the exact composition of any material is highly indispensable and scheming the facile strategy for the synthesis of a pristine form of materials is equally noteworthy. The purity of the MFA prepared by vacuum method for CQDs synthesis is highly ambiguous. In this context, we have successfully prepared MFA using a combination of saponification and double decomposition (also known as trans saponification). However, due to its lower substrate scope, an alternative method was highly desirable. In this regard, a novel cost-effective and efficient strategy for the collection of MFA precursors via a one-step nucleophilic substitution reaction of fatty acids with metal salts in the presence of DBU as a base catalyst in pure forms was devised. The generality of the strategy has been successfully evaluated by procuring the library of MFA precursors in excellent yields under mild optimized reaction conditions. Furthermore, group V precursor has also been explored by synthesizing commercially unavailable tris(trimethylsilyl)phosphine and tris(diethylamino)phosphine.

2.7. Experimental section.

2.7.1. General method.

2.7.1.1. Materials and general consideration.

In(OAc)₃ (99%), InCl₃ (99.99%), GaCl₃ (99.99%), lauric acid (98%), palmitic acid (99%), GdCl₃.6H₂O (99.9%), PBr₃ (97%), sodium (99.9%), potassium (98%), red phosphorous (≥97%), chlorotrimethylsilane (99%), pentane (99%), phenylisothiocyanate (98%), 1-ODE (technical grade), 1, 2-DME (99.5%), were all

purchased from Sigma Aldrich, India. Aniline (99%) was purchased from TCI, India. KOH (85%), $\text{Pb}(\text{NO}_3)_2$ (99%), FeCl_3 (96%), $\text{CoCl}_2 \cdot 6\text{H}_2\text{O}$ (98%), NiCl_2 (97%), MnCl_2 (99%), $\text{Mg}(\text{NO}_3)_2$ (99%), KMnO_4 (99%), $\text{Na}_2\text{S}_2\text{O}_3$ (97%), NaHSO_3 , diethyl amine (99%), oleic acid (65-88%), toluene ($\geq 99\%$) were purchased from Merck, India. $\text{CuCl}_2 \cdot 2\text{H}_2\text{O}$ (99%), ZnCl_2 (97%), $\text{CdCl}_2 \cdot \text{H}_2\text{O}$ (98%), KNO_3 (99%), $\text{SnCl}_2 \cdot 2\text{H}_2\text{O}$, Stearic acid (90%) were purchased from Thomas Baker, India. NaOH (99.9%), NaCl (99.9%) and AgNO_3 (99.8%) were purchased from Rankem. Myristic acid (95%) and AlCl_3 (96%) were purchased from SRL and Finar respectively. The deuterated solvent used for NMR analysis was purchased from Sigma Aldrich India.

2.7.1.2. Characterization method.

Fourier Transform Infrared Spectroscopy (FTIR): FTIR spectra were obtained using Bruker ALPHA E, 200396. The solution-based FTIR was performed by placing a thin film of solution on the Attenuated total reflectance (ATR) of the instrument. The solid-state FTIR was performed by preparing a pellet with KBr purchased from Merck, India.

Nuclear magnetic resonance (NMR): ^1H NMR, ^{13}C NMR spectra were recorded on a Bruker ASCENDTM (400 MHz) spectrometer using CDCl_3 solvent as an internal reference. Multiplicity was indicated as follows: s (singlet), d (doublet), t (triplet), q (quartet), and m (multiplet).

Thermogravimetric analysis (TGA): TGA data were collected from TA Instruments, TGA Q50 Analyzer using the platinum pan.

Mass spectroscopy: The mass spectroscopy was studied on Agilent Technologies, Accurate Mass Q-TOF LC/MS G65208.

X-ray Diffractometer (XRD): The X-ray diffraction studies were run under a PANalytical X-ray diffractometer using Cu K α ($\lambda = 1.54 \text{ \AA}$) as the incident radiation (40 kV and 30 mA).

2.7.2. Preparation of indium stearate by vacuum method.

2.7.2.1. Synthesis: For the determination of purity of indium stearate prepared by vacuum method a typical synthetic method was followed.^{7,8,60,61} Briefly, 0.2 g (0.685 mmol) of In(OAc)₃ and 0.584 g (2.055 mmol) of stearic acid were mixed in a 25 mL three-necked round-bottom flask along with 5 mL of 1-ODE. The reaction mixture was degassed at 120 °C until the solution turned transparent. The solution was brought down to room temperature.

2.7.2.2. Purification: In each centrifuge tube 2 mL of the reaction mixture was taken out and then 8 mL of dry acetone was added. The white precipitate was formed which was further washed again with 8 mL of acetone. This process was repeated four times. The precipitate was dried under a vacuum overnight.

2.7.3. Preparation of MFAs from combined saponification and double decomposition methods.

2.7.3.1. Preparation of potassium myristate (2.3.1a).

It was prepared according to the earlier reports.^{32,37} Briefly, a 50% KOH solution was prepared by dissolving 0.35 g of KOH pellets in 2.8 mL of ethanol and distilled water (1:1) mixture. 8.7 mmol (2 g) of myristic acid was added to the mixture and stirred for 15 min at room temperature. Subsequently, the reaction mixture was refluxed for 45 min. Separately, 25 wt% of KNO₃ was prepared by dissolving 0.0875 g of KNO₃ in 2.8 mL of ethanol and distilled water (1:1) mixture. The refluxing reaction mixture was

poured into the KNO_3 solution and stirred vigorously for 20 min to obtain white precipitation. The obtained product is washed several times with distilled water and dried over a vacuum in presence of phosphorous pentoxide as a drying agent.

The purification was carried out by recrystallisation. Briefly, the as-synthesized product was dissolved in boiling methanol. The solution was then brought down to room temperature slowly. After a few minutes, the white crystals of potassium myristate were observed. It was filtered and dried over a vacuum. The product obtained in 61% yield. ^1H NMR (DMSO- d_6 , 400MHz): δ ppm 0.86 (t, 3H, $J= 8$ Hz), 1.23 (m, 28H), 1.45 (m, 2H), 2.14 (t, 2H, $J= 8$ Hz).

2.7.3.2. Preparation of sodium myristate (2.3.1b).

Sodium myristate was prepared according to earlier reports.^{32,37} Briefly, a 50% NaOH solution was prepared by dissolving 0.35 g of NaOH pellets in 2.8 mL of ethanol and distilled water (1:1) mixture. 8.7 mmol (2 g) of myristic acid was added to the mixture and stirred for 15 min at room temperature. Subsequently, the reaction mixture was refluxed for 45 min. Separately, 25 wt% of NaCl was prepared in 2.8 mL of ethanol and distilled water (1:1) mixture. The refluxing reaction mixture was poured into NaCl solution and stirred vigorously for 20 min to obtain white precipitation. The obtained product is washed several times with distilled water and dried over a vacuum in presence of phosphorous pentoxide as a drying agent.

The purification was carried out by recrystallisation. Briefly, the as-synthesized product was dissolved in boiling methanol. The solution was then brought down to room temperature slowly. After a few minutes, the white crystals of sodium myristate were observed. It was filtered and dried over a vacuum. The product obtained in 57% yield.

^1H NMR (CDCl_3 , 400MHz): δ ppm 0.84 (t, 3H, $J = 6.8$ Hz), 1.22 (m, 20H), 1.46 (m, 2H), 2.17 (t, $J = 7.3$ Hz, 2H).

2.7.3.3. A general method for preparation of different indium myristate (method A).

The methodology used to prepare different indium-myristate (**2.3.2a-d**) was similar to the one reported for iron-oleate.⁶² Briefly, 1 equivalent of indium chloride was mixed with 1-3 equivalent (depending upon the composition of the product) of potassium or sodium myristate. The reaction solvent was a mixture of hexane, water and ethanol (7:3:4). All of these components were mixed and stirred for 5 min at room temperature before being refluxed for 4 h. After 4 h the desired indium-myristate (**2.3.2a-d**) was extracted from hexane and dried over a vacuum overnight.

2.7.3.3.1. Preparation of indium (myristate)₃ (2.3.2a) from potassium myristate (2.3.1a).

It was prepared according to the general **method A** discussed above. 50 mg (0.23 mmol) of indium chloride and 186.4 mg (0.69 mmol) of potassium myristate were used. The product obtained was white solid with a yield of 67%. ^1H NMR (CDCl_3 , 400MHz): δ ppm 0.88 (t, 3H, $J = 6.8$ Hz), 1.25 (m, 20H), 1.63 (m, 2H) 2.35 (t, 2H, $J = 7.5$ Hz).

2.7.3.3.2. Preparation of indium (myristate)₂ (2.3.2b) from sodium myristate (2.3.1b).

It was prepared according to the general **method A** discussed above. 50 mg (0.23 mmol) of indium chloride and 175.2 mg (0.69 mmol) of sodium myristate were used. The product obtained was white solid with a yield of 64%. ^1H NMR (DMSO-d_6 ,

400MHz): δ ppm 0.85 (t, 3H, $J = 6.8$ Hz), 1.23 (m, 20H), 1.47 (m, 2H), 2.17 (t, 2H, $J = 7.4$ Hz).

2.7.3.3.3. Preparation of indium (myristate) (2.3.2c) from potassium myristate (2.3.1a).

It was prepared according to the general **method A** discussed above. 50 mg (0.23 mmol) of indium chloride and 61.2 mg (0.23 mmol) of potassium myristate were used. The product obtained was white solid with a yield of 52%. ^1H NMR (CDCl_3 , 400MHz): δ ppm 0.86 (t, 3H, $J = 7.2$ Hz), 1.21 (m, 20H), 1.48 (m, 2H), 2.19 (t, 2H, $J = 7.2$ Hz).

2.7.4. Preparation of MFA salts by DBU method.

2.7.4.1. Preparation of fatty acid precursors.

α -bromomyristic acid (2.4.1e): It was prepared in accordance with the earlier reports with slight modification.^{88,89} 5 g (21.93 mmol) of myristic acid and 5.98 g (22.1 mmol, 2.1 mL) of PBr_3 were dissolved in 50 mL CCl_4 under nitrogen atmosphere in a three-necked round bottom flask. The flask was fitted with a drying tube containing calcium chloride and a reflux condenser. The reaction mixture was brought down to 0 °C. 7.19 g (22.1 mmol, 2.3 mL) of Br_2 was slowly added in portions over the time of 2 h. Once the addition was completed the reaction mixture was refluxed overnight. The following day the reaction mixture was brought down to room temperature and poured into 20 mL of chloroform which was carefully poured into 100 mL of methanol and water. The solvent was dried in a rotary evaporator. The final product was extracted from the aqueous part using ethyl acetate. The product obtained in 43% yield. ^1H NMR (CDCl_3 , 400MHz): δ ppm 0.88 (s, 3H, $J = 8$ Hz), 1.26 (m, 18H), 1.62 (m, 2H), 2.33 (t, 2H $J =$

7.5 Hz), 4.22 (t, 1H, $J = 5.8$ Hz). ^{13}C {H} NMR (CDCl_3 , 100MHz): δ ppm 15.72, 22.32, 27.22, 28.85, 29.33, 29.41, 29.52, 29.74, 31.97, 34.64, 45.88, 175.69.

9,10- dihydroxy stearic acid (2.4.1f): The synthesis was carried out following the general method reported earlier.^{90,91} 1 g (3.54 mmol, 1.12 mL) of oleic acid was added to a solution of 0.5 g (8.91 mmol) of KOH in 20 mL distilled water and heated to 50 °C. Once the reaction mixture reached 50 °C, the second fraction of 0.5 g (8.91 mmol) of KOH in 20 mL distilled water was added. The reaction temperature was brought down to 5 °C by constantly adding crushed ice to it. 1 g (6.49 mmol) of potassium permanganate was added to the reaction mixture and stirred for 10 min maintaining the temperature at 5 °C. After 10 min the reaction was quenched by the addition of a saturated solution of sodium thiosulfate in distilled water. At this point, a brown colouration was observed. It was decolourised by adding 40% of sodium bisulfite and 37% hydrochloric acid. The resulting mixture was filtered and the crude residue was recrystallized from ethanol. The product was obtained in 76% yield with FTIR signature stretching at 3283 cm^{-1} for added -OH group. ^1H NMR (CD_3OD , 400MHz): δ ppm 0.87 (t, 3H, $J = 6.8$ Hz), 1.31 (m, 19H), 1.56 (m, 7H), 2.26 (t, 2H, $J = 7.6$ Hz), 3.32 (m, 2H). ^{13}C {H} NMR (CD_3OD , 100MHz): δ ppm 13.05, 22.03, 24.73, 25.57, 28.82, 29.05, 29.36, 29.48, 31.37, 32.19, 74.58.

General method (method B): In a typical synthesis 0.1 g of metal salt (1.0 equivalent) was taken in a round bottom flask and 3.0 equivalent of fatty acid and 1.0 equivalent of DBU were added to it. A mixture of hexane, ethanol and water (ratio 7:4:3) was added to the above mixture. It was then stirred for 2-3 min at room temperature. The reaction mixture was then refluxed overnight (13 h). The following day, the product was extracted from the non-polar hexane part and was dried under a vacuum.

2.7.4.2. Spectral (NMR) analyses, melting point and specification of experimental conditions.

Indium (stearate)₃ (2.4.2a): It was prepared according to the general procedure discussed in **method B**. Indium chloride was used as a metal precursor and stearic acid as a carboxylate precursor. The product was obtained as a white powder with an 85% yield. m.p. 145-148 °C; ¹H NMR (CDCl₃, 400MHz): δ ppm 0.88 (t, 3H, *J*= 8 Hz), 1.27 (m, 28H), 1.60 (m, 2H), 2.33 (t, 2H, *J*= 8 Hz). ¹³C {H} NMR (CDCl₃, 100MHz): δ ppm 14.12, 22.70, 24.72, 29.08, 29.26, 29.37, 29.45, 29.69, 31.93, 33.95, 179.35.

Potassium stearate (2.4.2b): It was prepared according to the general procedure discussed in **method B**. Potassium nitrate was used as a metal precursor and stearic acid as a carboxylate precursor. The product was obtained with an 85% yield. ¹H NMR (CDCl₃, DMSO-d₆, 3:1, 400MHz): δ ppm 0.78 (t, 3H, *J*= 8 Hz), 1.16 (m, 28H), 1.49 (m, 2H), 2.16 (t, 2H, *J*= 8 Hz). ¹³C {H} NMR (CDCl₃, DMSO-d₆, 3:1 100MHz): δ ppm 14.40, 22.76, 25.11, 29.26, 29.40, 29.43, 29.57, 29.73, 31.97, 34.39, 175.66.

Magnesium (stearate)₂ (2.4.2c): It was prepared according to the general procedure discussed in **method B**. Magnesium nitrate was used as a metal precursor and stearic acid as a carboxylate precursor. The product was obtained with an 88% yield. m.p. 118-122 °C ¹H NMR (CDCl₃, 400MHz): δ ppm 0.88 (t, 3H, *J*= 8 Hz), 1.29 (m, 28H), 1.62 (m, 2H), 2.34 (t, 2H, *J*= 8 Hz). ¹³C {H} NMR (CDCl₃, 100MHz): δ ppm 14.31, 22.88, 22.89, 24.89, 29.25, 29.44, 29.55, 29.63, 29.78, 29.86, 32.11, 34.15, 179.52.

Manganese (stearate)₂ (2.4.2d): It was prepared according to the general procedure discussed in **method B**. Manganese chloride was used as a metal precursor and stearic acid as a carboxylate precursor. The product was obtained in 70% yield. m.p. 108-111 °C

Ferric (stearate)₃ (2.4.2e): It was prepared according to the general procedure discussed in **method B**. Ferric chloride was used as a metal precursor and stearic acid as a carboxylate precursor. The product obtained in 90% yield.

Cobalt (stearate)₂ (2.4.2f): It was prepared according to the general procedure discussed in **method B**. Cobalt chloride was used as a metal precursor and stearic acid as a carboxylate precursor. The product obtained in 75% yield. m.p. 110-113 °C.

Nickel (stearate)₂ (2.4.2g): It was prepared according to the general procedure discussed previously. Zinc chloride was used as a metal precursor and stearic acid as a carboxylate precursor. The product was obtained with an 87% yield. m.p. 84-87 °C.

Copper (stearate)₂ (2.4.2h): It was prepared according to the general procedure discussed in **method B**. Copper chloride was used as a metal precursor and stearic acid as a carboxylate precursor. The product obtained in 91% yield. m.p. 248-251 °C.

Zinc (stearate)₂ (2.4.2i): It was prepared according to the general procedure discussed in **method B**. Zinc chloride was used as a metal precursor and stearic acid as a carboxylate precursor. The product was obtained with an 87% yield. m.p. 128-130 °C; ¹H NMR (CDCl₃, 400MHz): δ ppm 0.88 (t, 3H, *J*= 8 Hz), 1.30 (m, 28H), 1.62 (m, 2H), 2.35 (t, 2H, *J*= 8 Hz). ¹³C {H} NMR (CDCl₃, 100MHz): δ ppm 14.31, 22.88, 24.87, 29.24, 29.42, 29.55, 29.62, 29.77, 29.87, 32.11, 34.05, 179.21.

Cadmium (stearate)₂ (2.4.2j): It was prepared according to the general procedure discussed in **method B**. Cadmium chloride was used as a metal precursor and stearic acid as a carboxylate precursor. The product was obtained with an 81% yield. m.p. 132-135 °C; ¹H NMR (CDCl₃, 400MHz): δ ppm 0.88 (t, 3H, *J*= 8 Hz), 1.27 (m, 28H), 1.61

(m, 2H), 2.35 (t, 2H, $J=8$ Hz). ^{13}C {H} NMR (CDCl_3 , 100MHz): δ ppm 14.31, 22.88, 24.86, 29.24, 29.42, 29.54, 29.77, 29.87, 34.12, 179.62.

Silver stearate (2.4.2k): It was prepared according to the general procedure discussed in **method B**. Silver nitrate was used as a metal precursor and stearic acid as a carboxylate precursor. The product obtained in 91% yield. m.p. 204-207 °C; ^1H NMR (CDCl_3 , 400MHz): δ ppm 0.80 (m, 3H), 1.21 (m, 28H), 1.53 (m, 2H), 2.32 (m, 2H). ^{13}C {H} NMR (CDCl_3 , DMSO- d_6 , 3:1, 100MHz): δ ppm 14.31, 22.54, 24.95, 28.99, 29.14, 29.17, 29.34, 29.46, 31.74, 34.12, 174.94.

Aluminium (stearate) $_3$ (2.4.2l): It was prepared according to the general procedure discussed in **method B**. Aluminium chloride was used as a metal precursor and stearic acid as a carboxylate precursor. The product was obtained in a 35% yield. ^1H NMR (CDCl_3 , 400MHz): δ ppm 0.88 (t, 3H, $J=8$ Hz), 1.27 (m, 28H), 1.61 (m, 2H), 2.34 (t, 2H, $J=8$ Hz). ^{13}C {H} NMR (CDCl_3 , 100MHz): δ ppm 14.30, 22.88, 24.88, 29.26, 29.44, 29.55, 29.63, 29.79, 29.88, 30.02, 32.14, 34.23 179.98.

Gallium (stearate) $_3$ (2.4.2m): It was prepared according to the general procedure discussed in **method B**. Gallium chloride was used as a metal precursor and stearic acid as a carboxylate precursor. The product obtained in 90% yield. ^1H NMR (CDCl_3 , 400MHz): δ ppm 0.88 (t, 3H, $J=8$ Hz), 1.27 (m, 28H), 1.63 (m, 2H), 2.34 (t, 2H, $J=8$ Hz). ^{13}C {H} NMR (CDCl_3 , 100MHz): δ ppm 14.31, 22.88, 24.85, 29.24, 29.43, 29.56, 29.62, 29.79, 29.84, 32.11, 34.27, 180.46.

Tin (stearate) $_2$ (2.4.2n): It was prepared according to the general procedure discussed in **method B**. Tin (II) chloride was used as a metal precursor and stearic acid as a carboxylate precursor. The product obtained in 90% yield. ^1H NMR (CDCl_3 , 400MHz): δ ppm 0.88 (t, 3H, $J=8$ Hz), 1.28 (m, 28H), 1.63 (m, 2H), 2.34 (t, 2H, $J=8$ Hz). ^{13}C

{H} NMR (CDCl₃, 100MHz): δ ppm 14.12, 22.70, 24.68, 29.07, 29.25, 29.37, 29.44, 29.69, 31.93, 34.02, 179.84.

Lead (stearate)₂ (2.4.2o): It was prepared according to the general procedure discussed in **method B**. Lead nitrate was used as a metal precursor and stearic acid as a carboxylate precursor. The product obtained in 73% yield. ¹H NMR (CDCl₃, 400MHz): δ ppm 0.88 (t, 3H, $J= 8$ Hz), 1.25 (m, 28H), 1.63 (m, 2H), 2.35 (t, 2H, $J= 8$ Hz). ¹³C NMR (CDCl₃, 100MHz): δ ppm 14.31, 22.88, 24.87, 29.24, 29.42, 29.54, 29.61, 29.77, 29.87, 32.10, 34.08, 179.40.

Gadolinium (stearate)₃ (2.4.2p): It was prepared according to the general procedure discussed in **method B**. Gadolinium chloride was used as a metal precursor and stearic acid as a carboxylate precursor. The product was obtained with a 45% yield. m.p. 107-110 °C.

Indium (myristate)₃ (2.4.2q): It was prepared according to the general procedure discussed in **method B**. Indium chloride was used as a metal precursor and myristic acid as a carboxylate precursor. The product obtained in 90% yield. m.p. 142-145 °C; ¹H NMR (CDCl₃, 400MHz): δ ppm 0.88 (t, 3H, $J= 8$ Hz), 1.27 (m, 20H), 1.61 (m, 2H), 2.34 (t, 2H, $J= 8$ Hz). ¹³C {H} NMR (CDCl₃, 100MHz): δ ppm 14.28, 22.88, 24.94, 29.28, 29.47, 29.56, 29.66, 29.85, 32.11, 34.44, 180.93.

Indium (palmitate)₃ (2.4.2r): It was prepared according to the general procedure discussed in **method B**. Indium chloride was used as a metal precursor and palmitic acid as a carboxylate precursor. The product obtained in 60% yield. ¹H NMR (CDCl₃, 400MHz): δ ppm 0.88 (t, 3H, $J= 8$ Hz), 1.28 (m, 24H), 1.62 (m, 2H), 2.34 (t, 2H, $J= 8$ Hz). ¹³C {H} NMR (CDCl₃, 100MHz): δ ppm 14.31, 22.88, 24.85, 29.24, 29.43, 29.56, 29.62, 29.78, 29.87, 32.12, 34.30, 180.63.

Indium (laurate)₃ (2.4.2s): It was prepared according to the general procedure discussed in **method B**. Indium chloride was used as a metal precursor and lauric acid as a carboxylate precursor. The product obtained in 75% yield. ¹H NMR (CDCl₃, 400MHz): δ ppm 0.88 (t, 3H, *J*= 8 Hz), 1.27 (m, 16H), 1.61 (m, 2H), 2.34 (t, 2H, *J*= 8 Hz). ¹³C {H} NMR (CDCl₃, 100MHz): δ ppm 14.28, 22.87, 24.92, 29.26, 29.45, 29.53, 29.64, 29.79, 32.09, 34.40, 180.91.

Indium (α-bromomyristate)₃ (2.4.2t): It was prepared according to the general procedure discussed in **method B**. Indium chloride was used as a metal precursor and α-bromomyristic acid as a carboxylate precursor. The product was obtained with an 89% yield. ¹H NMR (CDCl₃, 400MHz): δ ppm 0.92 (t, 3H, *J* = 8 Hz), 1.26 (m, 18H), 1.65 (m, 2H), 2.34 (t, 2H, *J* = 7.5 Hz), 4.22 (t, 1H, *J* = 5.9 Hz). ¹³C {H} NMR (CDCl₃, 100MHz): δ ppm 14.14, 23.67, 27.20, 28.82, 29.30, 29.49, 29.64, 31.93, 34.66, 45.49, 175.90.

Indium (9, 10- dihydroxy stearate)₃ (2.4.2u): It was prepared according to the general procedure discussed in **method B**. Indium chloride was used as a metal precursor and 9, 10- hydroxystearic acid as a carboxylate precursor. The product was obtained in 72% yield. ¹H NMR (CD₃OD, 400MHz): δ ppm 0.89 (t, *J* = 6.8 Hz, 3H), 1.31 (m, 20H), 1.56 (m, 6H), 2.27 (t, *J* = 7.5 Hz, 2H), 3.30 (t, *J* = 2.6 Hz, 2H). ¹³C {H} NMR (CD₃OD, 100MHz): δ ppm 13.05, 21.48, 24.72, 25.64, 28.82, 29.06, 29.36, 29.49, 31.68, 32.21, 74.53, 182.92.

Lead (oleate)₂ (2.4.2v): It was prepared according to the general procedure discussed in **method B**. Lead nitrate was used as a metal precursor and oleic acid as a carboxylate precursor. The product obtained in 90% yield. m.p. 91-94 °C; ¹H NMR (CDCl₃, 400MHz): δ ppm 0.87 (t, 3H, *J*= 8 Hz), 1.27 (m, 18H), 1.62 (m, 2H), 2.01 (m, 1H), 2.34

(t, 2H, $J= 8$ Hz), 5.34 (dd, 1H, $J= 4$ Hz). ^{13}C {H} NMR (CDCl_3 , 100MHz): δ ppm 14.29, 22.86, 25.00, 27.35, 29.20, 29.30, 29.39, 29.50, 29.70, 29.87, 32.08, 35.17, 129.88, 130.16, 180.67.

2.7.5. Preparation of group-V precursor.

2.7.5.1. Preparation of tris(trimethylsilyl)phosphine ($\text{P}(\text{SiMe}_3)_3$).

The synthetic procedure was similar to the previous reports.^{16,59,85,86} Briefly, 4.825 g (0.21 mol) of sodium and 11.361 g (0.29 mol) of potassium was cut into small pieces in a glove box and mixed with 250 mL of 1,2-dimethoxyethane in a three-necked round bottom flask. It was sealed properly and brought out of the glove box. The mixture was refluxed at 80 °C for 2 h under a nitrogen atmosphere during which the solution formed blue colouration. After 2 h the reaction mixture was brought down to room temperature. Separately, 5 g (0.16 mol) of red phosphorous was weighed inside the glove box. It was added to the reaction mixture at room temperature with the help of a solid addition funnel. As soon as red phosphorous was added the colour of the reaction mixture changed to red. It was refluxed for 24 h until the colour of the solution turned black. After 24 h the reaction mixture was slowly brought down to room temperature and placed in an ice bath. One of the necks on the round bottom flask was exchanged with a dropping funnel containing 56.12 g (0.52 mmol, 66 mL) of chlorotrimethylsilane. It was slowly added to the reaction mixture dropwise over a time of 2-3 h. After the addition of chlorotrimethylsilane was completed the reaction mixture was again refluxed for 72 h (the colour changed from black to grey during this period). The round bottom flask was carefully wrapped in aluminium foil during this period so that the external light does not reach the reaction as it tends to interfere in the reaction. After 72 h the reaction was brought down to room temperature, and all the openings were sealed

with electric tape and brought into the glove box. Inside the glove box, a celite pad was prepared and the reaction mixture was vacuum filtered through the celite pad and washed with anhydrous pentane 3-4 times. The residue was properly neutralised with ethanol and discarded. The filtrate was brought out of the glove box and vacuum distilled. At first, washing solvents were collected and during the second distillation, the desired product of tris(trimethylsilyl) phosphine was obtained. The yield of the product was around 44%. ^1H NMR (CDCl_3 , 400MHz): δ ppm 0.275 (d, 27H, $J= 4$ Hz). ^{13}C {H} NMR (CDCl_3 , 100MHz): δ ppm 4.1.

2.7.5.2. Preparation of tris(diethylamino)phosphine ($\text{P}(\text{NEt}_2)_3$).

It was prepared in accordance with the previous reports with slight modifications.⁹²⁻⁹⁴ Briefly, 6.77 g (25 mmol, 2.5 mL) of phosphorus tribromide was mixed with 7.13 g (96.19 mmol, 10 mL) of diethyl ether under a nitrogen atmosphere. The solution was slowly brought down to 0 °C. A solution of 10.97 g (150 mmol, 15.5 mL) of diethyl amine in 35.65 g (481 mmol, 50 mL) diethyl ether was added dropwise to the former reaction solution ensuring the temperature does not exceed 10 °C. Once all the solution of diethyl amine was added the reaction mixture was brought up to room temperature and stirred overnight (13 h). The following day the mixture was filtered and washed with anhydrous diethyl ether and dried under vacuum. The yield of the product was around 52%. ^1H NMR (CDCl_3 , 400MHz): δ ppm 1.017 (t, 18H, $J= 7.2$ Hz), 2.957 (m, 12H). ^{13}C {H} NMR (CDCl_3 , 100MHz): δ ppm 13.95, 39.06.

2.7.6. Preparation of thiourea precursor.

It was prepared according to the previous reports.¹⁰ Briefly, 0.676 g (5 mmol, 0.6 mL) of phenylisothiocyanate was mixed with 3 mL of toluene. Separately, 0.466 g (5 mmol, 0.46 mL) of aniline was mixed with 3 mL of toluene. The solution of aniline in toluene

was added to the solution of phenylisothiocyanate in toluene and stirred for 5 min. A white-coloured precipitate was observed after five minutes. Excess toluene was evaporated in a rotary evaporator and dried overnight in a vacuum. The product obtained in 91% yield. ^1H NMR (DMSO- d_6 , 400 MHz) δ 7.17 (t, 1H, $J = 7.3$ Hz), 7.33 (t, 2H, $J = 7.8$ Hz), 7.40 (d, 2H, $J = 8.2$ Hz), 10.16 (s, 1H). ^{13}C {H} NMR (DMSO- d_6 , 100MHz): δ ppm 125.30, 125.83, 129.20, 140.33, 179.58.

2.8. References.

- (1) Tamang, S.; Lincheneau, C.; Hermans, Y.; Jeong, S.; Reiss, P. Chemistry of InP Nanocrystal Syntheses. *Chem. Mater.* **2016**, *28*, 2491–2506.
 - (2) Murray, C. B.; Norris, D. J.; Bawendi, M. G. Synthesis and Characterization of Nearly Monodisperse CdE (E = S, Se, Te) Semiconductor Nanocrystallites. *J. Am. Chem. Soc.* **1993**, *115*, 8706–8715.
 - (3) Reiss, P.; Protière, M.; Li, L. Core/Shell Semiconductor Nanocrystals. *Small* **2009**, *5*, 154–168.
 - (4) Reiss, P.; Carrière, M.; Lincheneau, C.; Vaure, L.; Tamang, S. Synthesis of Semiconductor Nanocrystals, Focusing on Nontoxic and Earth-Abundant Materials. *Chem. Rev.* **2016**, *116*, 10731–10819.
 - (5) Amos, O.; Odetoye, T. E.; Ogunniyi, D. S. Preparation and Characterization of Zinc Metal Soap from Shea Butter (*Vitellaria Paradoxa*). *J. Niger. Soc. Phys. Sci.* **2021**, *3*, 340–343.
 - (6) Ek, O. Preparation and Characterization of Metal Soaps of Cocos Nucifera Seed Oil. *J. Appl. Sci. Environ. Manag.* **2014**, *18*, 359–363.
 - (7) Yu, W. W.; Peng, X. Formation of High-Quality CdS and Other II-VI
-

- Semiconductor Nanocrystals in Noncoordinating Solvents: Tunable Reactivity of Monomers. *Angew. Chemie - Int. Ed.* **2002**, *41*, 2368–2371.
- (8) Battaglia, D.; Peng, X. Formation of High Quality InP and InAs Nanocrystals in Noncoordinating Solvent. *Nano Lett.* **2002**, *2*, 1027–1030.
- (9) Protesescu, L.; Yakunin, S.; Bodnarchuk, M. I.; Krieg, F.; Caputo, R.; Hendon, C. H.; Yang, R. X.; Walsh, A.; Kovalenko, M. V. Nanocrystals of Cesium Lead Halide Perovskites (CsPbX₃, X = Cl, Br, and I): Novel Optoelectronic Materials Showing Bright Emission with Wide Color Gamut. *Nano Lett.* **2015**, *15*, 3692–3696.
- (10) Hendricks, M. P.; Campos, M. P.; Cleveland, G. T.; Plante, I. J. La; Owen, J. S. A Tunable Library of Substituted Thiourea Precursors to Metal Sulfide Nanocrystals. *Science.* **2015**, *348*, 1226–1230.
- (11) Akkerman, Q. A.; Martínez-Sarti, L.; Goldoni, L.; Imran, M.; Baranov, D.; Bolink, H. J.; Palazon, F.; Manna, L. Molecular Iodine for a General Synthesis of Binary and Ternary Inorganic and Hybrid Organic-Inorganic Iodide Nanocrystals. *Chem. Mater.* **2018**, *30*, 6915–6921.
- (12) Imran, M.; Caligiuri, V.; Wang, M.; Goldoni, L.; Prato, M.; Krahne, R.; De Trizio, L.; Manna, L. Benzoyl Halides as Alternative Precursors for the Colloidal Synthesis of Lead-Based Halide Perovskite Nanocrystals. *J. Am. Chem. Soc.* **2018**, *140*, 2656–2664.
- (13) Thapa, S.; Bhardwaj, K.; Basel, S.; Pradhan, S.; Eling, C. J.; Adawi, A. M.; Bouillard, J. S. G.; Stasiuk, G. J.; Reiss, P.; Pariyar, A.; Tamang, S. Long-Term Ambient Air-Stable Cubic CsPbBr₃ Perovskite Quantum Dots Using Molecular

- Bromine. *Nanoscale Adv.* **2019**, *1*, 3388–3391.
- (14) Calvin, J. J.; Brewer, A. S.; Alivisatos, A. P. The Role of Organic Ligand Shell Structures in Colloidal Nanocrystal Synthesis. *Nat. Synth.* **2022**, *1*, 127–137.
- (15) Li, L.; Reiss, P. One-Pot Synthesis of Highly Luminescent InP / ZnS Nanocrystals without Precursor Injection. *J. Am. Chem. Soc.* **2008**, *130*, 11588–11589.
- (16) Gary, D. C.; Cossairt, B. M. Role of Acid in Precursor Conversion During InP Quantum Dot Synthesis. *Chem. Mater.* **2013**, *25*, 2463–2469.
- (17) Thanh, N. T. K.; Maclean, N.; Mahiddine, S. Mechanisms of Nucleation and Growth of Nanoparticles in Solution. *Chem. Rev.* **2014**, *114*, 7610–7630.
- (18) Almeida, G.; Goldoni, L.; Akkerman, Q.; Dang, Z.; Khan, A. H.; Marras, S.; Moreels, I.; Manna, L. Role of Acid-Base Equilibria in the Size, Shape, and Phase Control of Cesium Lead Bromide Nanocrystals. *ACS Nano* **2018**, *12*, 1704–1711.
- (19) Kim, D.; Park, J.; An, K.; Yang, N.-K.; Park, J.-G.; Hyeon, T. Synthesis of Hollow Iron Nanoframes. *J. Am. Chem. Soc.* **2007**, *129*, 5812–5813.
- (20) Pradhan, S.; Bhujel, D.; Gurung, B.; Sharma, D.; Basel, S.; Rasaily, S.; Thapa, S.; Borthakur, S.; Ling, W. L.; Saikia, L.; Reiss, P.; Pariyar, A.; Tamang, S. Stable Lead-Halide Perovskite Quantum Dots as Efficient Visible Light Photocatalysts for Organic Transformations. *Nanoscale Adv.* **2021**, *3*, 1464–1472.
- (21) Schliehe, C.; Juarez, B. H.; Pelletier, M.; Jander, S.; Greshnykh, D.; Nagel, M.;

- Meyer, A.; Foerster, S.; Kornowski, A.; Klinke, C.; Weller, H. Ultrathin PbS Sheets by Two-Dimensional Oriented Attachment. *Science* (80-.). **2010**, 329, 550–553.
- (22) Rakhmatullina, A. P.; Akhmed'yanova, R. A.; Liakumovich, A. G.; Portnoi, T. B.; Mokhnatkina, E. G.; Il'yasov, R. S. Active Processing Additives Based on Zinc and Calcium Salts of Stearic and Oleic Acids and Their Mixtures. *Int. Polym. Sci. Technol.* **2004**, 31, 29–32.
- (23) Yamamoto, Y.; Kijima, T.; Morikawa, T.; Nonomura, Y. Lubricant and Bactericidal Properties of Calcium Salts of Fatty Acids: Effect of Degree of Unsaturation. *J. Oleo Sci.* **2015**, 64, 1095–1100.
- (24) Gregory, J. N.; Spink, J. A. Lubricating Properties of Molecular Layers of Stearic Acid and Calcium Stearate on Metal Surfaces. *Nature* **1947**, 4038, 403.
- (25) Sahoo, R. R.; Biswas, S. K. Frictional Response of Fatty Acids on Steel. *J. Colloid Interface Sci.* **2009**, 333, 707–718.
- (26) Li, J.; Wu, Y. Lubricants in Pharmaceutical Solid Dosage Forms. *Lubricants* **2014**, 2, 21–43.
- (27) Lappi, H.; Alén, R. Pyrolysis of Vegetable Oil Soaps - Palm, Olive, Rapeseed and Castor Oils. *J. Anal. Appl. Pyrolysis* **2011**, 91, 154–158.
- (28) Pratiwi, M.; Neonufa, G. F.; Prakoso, T.; Soerawidjaja, T. H. The Synthesis of Magnesium Soaps as Feed for Biohydrocarbon Production. *MATEC Web Conf.* **2018**, 156, 1–5.
- (29) Kim, Y.; Kim, P.; Kim, C.; Yi, J. A Novel Method for Synthesis of a Ni/Al₂O₃

- Catalyst with a Mesoporous Structure Using Stearic Acid Salts. *J. Mater. Chem.* **2003**, *13*, 2353–2358.
- (30) Lisboa, F. D. S.; Gardolinski, J. E. F. D. C.; Cordeiro, C. S.; Wypych, F. Layered Metal Laurates as Active Catalysts in the Methyl/Ethyl Esterification Reactions of Lauric Acid. *J. Braz. Chem. Soc.* **2012**, *23*, 46–56.
- (31) Whitmore, W. F.; Lauro, M. Metallic Soaps-Their Uses, Preparation, and Properties. *Ind. Eng. Chem.* **1930**, *22*, 646–649.
- (32) Bivash Ranjan, D.; Lei, H.; Sanzgiri, V. R.; Sethna, S. D.; Shah, P. C. Novel Cosmetic Cream Composition Comprising C12-C20 Fatty Acid. WO 2008/104591 A3, 2008.
- (33) Mennicken, M.; Stolz, H. J.; Gmbh, P. G. Selecting Metal Soaps for Optimum Acid Scavenging Performance in Polyolefin. In *Polyolefin additives 2018 Conference- Cologne (Germany)*; 2018.
- (34) Hwu, H.-D.; Hsu, H. Y.; Chen, J.-H.; Jiang, S.-F. Improved Metallic Soaps of Fatty Acids for Use as Photolyzing Agents for Photodegradable Polymerfilms. US005434277A, 1995.
- (35) Wendt, R. E.; Wagner, E. F. Applications of Fatty Acids in Metallic Soaps. *J. Am. Oil Chem. Soc.* **1954**, *31*, 590–593.
- (36) Gönen, M.; Balköse, D.; Inal, F.; Ülkü, S. Zinc Stearate Production by Precipitation and Fusion Processes. *Ind. Eng. Chem. Res.* **2005**, *44*, 1627–1633.
- (37) Phanstiel IV, O.; Dueno, E.; Wang, Q. X. Synthesis of Exotic Soaps in the Chemistry Laboratory. *J. Chem. Educ.* **1998**, *75*, 612–614.

- (38) Evans, D. C. Experimental Soap Making. *J. Chem. Educ.* **1937**, *14*, 534–536.
- (39) Wolfgang, S. M.; Heider, T. P. Stearate Composition and Method of Production Thereof. USOO74563 06B2, 2008.
- (40) Hill, J. W.; Solberg, S. J.; Hill, C. S. A Catalyst for the Synthesis of Soap. *J. Chem. Educ.* **1982**, *52*, 788.
- (41) Preston, W. C. The Modern Soap Industry. *J. Chem. Educ.* **1925**, *2*, 1130–1139.
- (42) Gönen, M.; Öztürk, S.; Balköse, D.; Okur, S.; Ülkü, S. Preparation and Characterization of Calcium Stearate Powders and Films Prepared by Precipitation and Langmuir-Blodgett Techniques. *Ind. Eng. Chem. Res.* **2010**, *49*, 1732–1736.
- (43) Akanni, M. S.; Okoh, E. K.; Burrows, H. D.; Ellis, H. A. The Thermal Behaviour of Divalent and Higher Valent Metal Soaps: A Review. *Thermochim. Acta* **1992**, *208*, 1–41.
- (44) Neonufa, G. F.; Pratiwi, M.; Purwadi, R.; Prakoso, T.; Soerawidjaja, T. H.; Elizabeth, L. Production and Characterization of the Basic Soaps Obtained by Double Decomposition and Direct Process of Palm Stearin Oils. *IOP Conf. Ser. Mater. Sci. Eng.* **2018**, *543*, 1–7.
- (45) Sakai, H.; Umemura, J. Evaluation of Molecular Structure in Langmuir Monolayers of Zinc Stearate and Zinc 12-Hydroxystearate by IR External Reflection Spectroscopy. *Colloid Polym. Sci.* **2002**, *280*, 316–321.
- (46) Kato, Y. Process for Preparing Aqueous Dispersion of Higher Fatty Acid Zinc Salt. US006162836A, 2000.

- (47) Schultes, K.; Suefke, T.; Mueller, R.; Schikowsky, H.; Hoess, W. Process for Preparing Aqueous Dispersions. US008119734B2, 2012.
- (48) Hudson, C. R.; Nelson, E. N. Process for Production of Granular Metal Soap. US005164523A, 1992.
- (49) Yu, W. W.; Falkner, J. C.; Yavuz, C. T.; Colvin, V. L. Synthesis of Monodisperse Iron Oxide Nanocrystals by Thermal Decomposition of Iron Carboxylate Salts. *Chem. Commun.* **2004**, 2306–2307.
- (50) John Blachford. Manufacture of Metallic Soaps. 4316852, 1982.
- (51) Luo, S.; Yang, D.; Zhuang, J.; Ng, K. M. Synthesis and Characterization of Nearly Monodisperse Deltoidal Icositrahedral In₂O₃ Nanocrystals via One-Pot Pyrolysis Reaction. *CrystEngComm* **2013**, *15*, 8065–8068.
- (52) Luo, S.; Feng, J.; Ng, K. M. Large Scale Synthesis of Nearly Monodisperse, Variable-Shaped In₂O₃ Nanocrystals via a One-Pot Pyrolysis Reaction. *CrystEngComm* **2014**, *16*, 9236–9244.
- (53) Simons, M. J. Preparation of Silver Salt of Fatty Acid. 3839049, 1974.
- (54) Ross, R. A.; Takacs, A. M. Surface Reactions of Ethyl Stearate and Stearic Acid with Zinc, Manganese and Their Oxides. *Surf. Technol.* **1984**, *21*, 361–377.
- (55) Dou, Q.; Ng, K. M. Synthesis of Various Metal Stearates and the Corresponding Monodisperse Metal Oxide Nanoparticles. *Powder Technol.* **2016**, *301*, 949–958.
- (56) Gonen, M. Process Development For Metal Soaps, Izmir Institute of Technology, Izmir, Turkey, 2003.

- (57) Franke, D.; Harris, D. K.; Xie, L.; Jensen, K. F.; Bawendi, M. G. The Unexpected Influence of Precursor Conversion Rate in the Synthesis of III-V Quantum Dots. *Angew. Chemie - Int. Ed.* **2015**, *54*, 14299–14303.
- (58) Wang, F.; Yu, H.; Li, J.; Hang, Q.; Zemlyanov, D.; Gibbons, P. C.; Wang, L.-W.; Janes, D. B.; Buhro, W. E. Spectroscopic Properties of Colloidal Indium Phosphide Quantum Wires. *J. Am. Chem. Soc.* **2007**, *129*, 14327–14335.
- (59) Harris, D. K.; Bawendi, M. G. Improved Precursor Chemistry for the Synthesis of III-V Quantum Dots. *J. Am. Chem. Soc.* **2012**, *134*, 20211–20213.
- (60) Nightingale, A. M.; Demello, J. C. Improving the Ensemble Optical Properties of InP Quantum Dots by Indium Precursor Modification. *J. Mater. Chem. C* **2016**, *4*, 8454–8458.
- (61) Grigel, V.; Dupont, D.; De Nolf, K.; Hens, Z.; Tessier, M. D. InAs Colloidal Quantum Dots Synthesis via Aminopnictogen Precursor Chemistry. *J. Am. Chem. Soc.* **2016**, *138*, 13485–13488.
- (62) Park, J.; An, K.; Hwang, Y.; Park, J. E. G.; Noh, H. J.; Kim, J. Y.; Park, J. H.; Hwang, N. M.; Hyeon, T. Ultra-Large-Scale Syntheses of Monodisperse Nanocrystals. *Nat. Mater.* **2004**, *3*, 891–895.
- (63) Sutrisno, S.; Wijaya, H. W.; Sukarianingsih, D.; Santiaji, M. N. D. Synthesis and Characterization of Metal Soap (Zn-, Al-, and Mg-Soap) from Sunflower Oil and Its Potential as Sunscreen. In *AIP Conference Proceedings*; 2021; Vol. 2349, pp 020042-1-020042–020048.
- (64) Bard, A. J.; Parsons, R.; Jordan, J. *Standard Potentials in Aqueous Solution*, 1st editio.; M. Dekker, New York: New York, 1985.

- (65) Bratsch, S. G. Standard Electrode Potentials and Temperature Coefficients in Water at 298.15 K. *J. Phys. Chem. Ref. Data* **1989**, *18*, 1–21.
- (66) Vanysek, P. Electrochemical Series. In *CRC handbook of chemistry and physics*; 2000; p 8.
- (67) Al-Sogair, F. M.; Operschall, B. P.; Sigel, A.; Sigel, H.; Schnabl, J.; Sigel, R. K. O. Probing the Metal-Ion-Binding Strength of the Hydroxyl Group. *Chem. Rev.* **2011**, *111*, 4964–5003.
- (68) Bitá, B. 1,4-Diazabicyclo[2.2.2]Octane (DABCO) as a Useful Catalyst in Organic Synthesis. *Eur. J. Chem.* **2010**, *1*, 54–60.
- (69) Pimenta, L. S.; Gusevskaya, E. V.; Alberto, E. E. Intermolecular Halogenation/Esterification of Alkenes with N-Halosuccinimide and Acetic Acid Catalyzed by DABCO. *Adv. Synth. Catal.* **2017**, *359*, 2297–2303.
- (70) Aggarwal, V. K.; Emme, I.; Fulford, S. Y. Correlation between PKa and Reactivity of Quinuclidine-Based Catalysts in the Baylis-Hillman Reaction: Discovery of Quinuclidine as Optimum Catalyst Leading to Substantial Enhancement of Scope. *J. Org. Chem.* **2003**, *68*, 692–700.
- (71) Faltin, C.; Fleming, E. M.; Connon, S. J. Acrylamide in the Baylis - Hillman Reaction: Expanded Reaction Scope and the Unexpected Superiority of DABCO over More Basic Tertiary Amine Catalysts. *J. Org. Chem.* **2004**, *69*, 6496–6499.
- (72) Kaupmees, K.; Trummal, A.; Leito, I. Basicities of Strong Bases in Water: A Computational Study. *Croat. Chem. Acta* **2014**, *87*, 385–395.

- (73) Shieh, W. C.; Lozanov, M.; Loo, M.; Repič, O.; Blacklock, T. J. DABCO- and DBU-Accelerated Green Chemistry for N-, O-, and S-Benzoylation with Dibenzyl Carbonate. *Tetrahedron Lett.* **2003**, *44*, 4563–4565.
- (74) Shekouhy, M.; Khalafi-Nezhad, A. Polyethylene Glycol-Bonded 1,8-Diazabicyclo[5.4.0]Undec-7-Ene (PEG-DBU) as a Surfactant-Combined Base Catalyst for the Application of Nucleosides as Reagents in Multi-Component Syntheses of 8-Substituted Pyrido[2,3-d]Pyrimidine-6-Carbonitriles in Water. *Green Chem.* **2015**, *17*, 4815–4829.
- (75) Bronstein, L. M.; Huang, X.; Retrum, J.; Schmucker, A.; Pink, M.; Stein, B. D.; Dragnea, B. Influence of Iron Oleate Complex Structure on Iron Oxide Nanoparticle Formation. *Chem. Mater.* **2007**, *19*, 3624–3632.
- (76) Gönen, M.; Egbuchunam, T. O.; Balköse, D.; Inal, F.; Ülkü, S. Preparation and Characterization of Magnesium Stearate, Cobalt Stearate, and Copper Stearate and Their Effects on Poly(Vinyl Chloride) Dehydrochlorination. *J. Vinyl Addit. Technol.* **2015**, *21*, 235–244.
- (77) Jóna, E.; Ondrušová, D.; Pajtášová, M.; Šimon, P.; Michálek, J. A Study of Curative Interactions in the Presence of Cobalt(II) Stearate. *J. Appl. Polym. Sci.* **2001**, *81*, 2936–2943.
- (78) Roy, P. K.; Surekha, P.; Rajagopal, C.; Choudhary, V. Effect of Cobalt Carboxylates on the Photo-Oxidative Degradation of Low-Density Polyethylene. Part-I. *Polym. Degrad. Stab.* **2006**, *91*, 1980–1988.
- (79) Bunting, J. W.; Thong, K. M. Stability Constants for Some 1 : 1 Metal-Carboxylate Complexes. *Can. J. Chem.* **1970**, *48*, 1654–1656.

- (80) Bala, T.; Prasad, B. L. V.; Sastry, M.; Kahaly, M. U.; Waghmare, U. V. Interaction of Different Metal Ions with Carboxylic Acid Group: A Quantitative Study. *J. Phys. Chem. A* **2007**, *111*, 6183–6190.
- (81) Torron, S.; Hult, D.; Pettersson, T.; Johansson, M. Tailoring Soft Polymer Networks Based on Sugars and Fatty Acids toward Pressure Sensitive Adhesive Applications. *ACS Sustain. Chem. Eng.* **2017**, *5*, 2632–2638.
- (82) Lide, D. R.; Baysinger, G. Physical Constants of Inorganic Compounds. In *CRC handbook of chemistry and physics*; 2007; pp 4–43.
- (83) Joung, S.; Yoon, S.; Han, C.-S.; Kim, Y.; Jeong, S. Facile Synthesis of Uniform Large-Sized InP Nanocrystal Quantum Dots Using Tris(Tert-Butyldimethylsilyl)Phosphine. *Nanoscale Res. Lett.* **2012**, *7*, 1–8.
- (84) Gary, D. C.; Glassy, B. A.; Cossairt, B. M. Investigation of Indium Phosphide Quantum Dot Nucleation and Growth Utilizing Triarylsilylphosphine Precursors. *Chem. Mater.* **2014**, *26*, 1734–1744.
- (85) Becker, G.; Schmidt, H.; Uhl, G.; Uhl, W.; Regitz, M.; Rösch, W.; Vogelbacher, U.-J. Tris(Trimethylsilyl)Phosphine and Lithium Bis(Trimethylsilyl)Phosphide. Bis-(Tetrahydrofuran). *Inorg. Synth.* **1990**, *27*, 243–249.
- (86) Wells, R. L.; Self, M. F.; Johansen, J. D.; Laske, J. A.; Aubuchon, S. R.; Jones, L. J. Tris(Trimethylsilyl)Arsine and Lithium Bis(Trimethylsilyl)Arsenide. *Inorg. Synth.* **1997**, *31*, 150–158.
- (87) Atkinson, J. G.; Csakvary, J. J.; Herbert, G. T.; Stuart, R. S. Exchange Reactions of Carboxylic Acid Salts. A Facile Preparation of α -Deuteriocarboxylic Acids.

- J. Am. Chem. Soc.* **1968**, *90*, 498–499.
- (88) Little, J. C.; Sexton, A. R.; Tong, Y.-L. C.; Zurawic, T. E. Chlorination. II Free Radical vs. Hell-Volhard-Zelinsky Chlorination of Cyclohexanecarboxylic Acid. *J. Am. Chem. Soc.* **1969**, *91*, 7098–7103.
- (89) Stasiuk, G. J.; Tamang, S.; Imbert, D.; Poillot, C.; Giardiello, M.; Tisseyre, C.; Barbier, E. L.; Fries, P. H.; De Waard, M.; Reiss, P.; Mazzanti, M. Cell-Permeable Ln(III) Chelate-Functionalized InP Quantum Dots as Multimodal Imaging Agents. *ACS Nano* **2011**, *5*, 8193–8201.
- (90) Coleman, J. E.; Ricciuti, C.; Swern, D. Improved Preparation of 9(10),10(9)-Keto-hydroxystearic Acids by Oxidation of Oleic Acid with Potassium Permanganate in Neutral Solution. *J. Am. Chem. Soc.* **1956**, *78*, 5342–5345.
- (91) Julien-David, D.; Geoffroy, P.; Marchioni, E.; Raul, F.; Aoudé-Werner, D.; Miesch, M. Synthesis of Highly Pure Oxyphytosterols and (Oxy)Phytosterol Esters. Part II. (Oxy)-Sitosterol Esters Derived from Oleic Acid and from 9,10-Dihydroxystearic Acid [1]. *Steroids* **2008**, *73*, 1098–1109.
- (92) Mark, V. Nucleophilic Reactions of Trivalent Phosphorus Compounds: A New Synthesis of Epoxides. *J. Am. Chem. Soc.* **1963**, *85*, 1884–1885.
- (93) Burg, A. B.; Jr Slota, P. J. Dimethylaminodimethylphosphine. *J. Am. Chem. Soc.* **1958**, *80*, 1107–1109.
- (94) Stuebe, C.; Lankelma, H. P. Preparation of Some Hexaalkyl-Phosphorous, Phosphoric and Phosphorothioic Triamides. *J. Am. Chem. Soc.* **1956**, *78*, 976–977.

Chapter III

*Role of metal precursors on size
and size distribution*

3.1. Introduction.

The colloidal route is one of the most energy-efficient ways to prepare high-quality QDs since the size and size distribution can be controlled by tuning precursor chemistry and reaction conditions.^{1,2} Additionally, the surface of these CQDs can be modified to meet the specific requirements for a wide range of applications.³⁻¹⁰ As far as size-tunable syntheses are concerned, there has been tremendous advancement achieved in the synthesis of sulphides and selenides of Pb and Cd.¹¹⁻¹³ (Size distributions below 5% for CdSe QDs and PbS QDs.)^{14,15} However, in the past few years, there has been a growing concern about the toxicity of these heavy metal (Cd, Pb) inclusive QDs and more interest toward non-toxic heavy metal free QDs.¹ In this context, III-V semiconductors provide a promising alternative. They are binary compounds formed by combining group IIIA (13) and group VA (15) elements of the periodic table.^{1,2,16} In bulk form they are used for high-performance optoelectronic devices due to their unique properties such as high electron mobility (78000 cm²/V.s InSb vs 1400 cm²/V.s for Si), direct band gap, the low exciton binding energy and bulk band gap values covering a wide range of spectra from ultraviolet to infrared region.^{2,17-20} Despite their gamut of application, III-V semiconductors have been outperformed by II-VI and IV-VI semiconductor-based CQDs mainly due to synthetic challenges.^{21,22} III-V semiconductors have more covalent bonds as reflected in their fractional ionic character (42% for InP) compared to 70% in CdSe and 77% in PbSe.²³ The formation of covalent bonds requires stringent reaction conditions, reactive precursors, higher reaction temperature, and longer reaction time which makes controlling precursor reaction, nucleation and growth of the NCs extremely difficult.^{2,23} As a consequence controlling the size and size distribution of the III-V NCs becomes a major challenge.^{1,24,25} The

formation process of NCs based on the works of Bawendi *et al.*²⁶, Alivisatos *et al.*²⁷ and Hens *et al.*²⁸, can be described in figure 3.1.

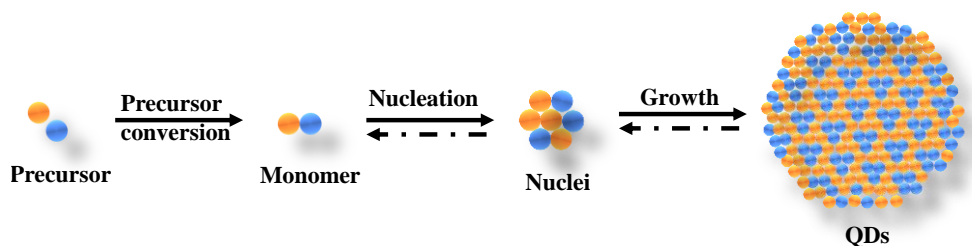


Figure 3.1. Schematic representation of the formation of QDs.

In the “classical model,” the first step is the chemical reaction of precursors leading to the formation of “monomer”, the smallest hypothetical unit of the solute. Above critical super-saturation, the accretion of these monomers results in the nucleation of the NCs, which is then followed by the growth step.^{29–31} Conventionally, precursor reactivity is carefully tuned to control reaction yield, size and size distribution. While this approach has been extremely successful with II-VI²⁷ and IV-VI²⁶ NCs, recent studies suggest that the strategy has failed to achieve the same degree of size and size distribution control with III-V semiconductors.²⁸

Amongst III-V semiconductors, InP NCs are one of the most widely studied NCs in colloidal form and are the benchmark of III-V NCs synthesis. Due to its suitable band gap (1.35 eV), under strong quantum confinement, its emission can be tuned in the entire visible region up to NIR (~750 nm) by varying sizes. It is an attractive alternative material to CdSe for biological imaging and optoelectronics, especially for lighting and displays.¹ Further, synthetic methods developed for InP can be used as a prototype for the synthesis of various other III-V semiconductors. It is typically synthesized by following a method developed by Peng and co-workers.³² Typically, In(III) precursor [InCl₃ or In(OAc)₃] is reacted with tris(trimethylsilyl)-phosphine (P(SiMe₃)₃) in a non-

coordinating solvent (1-ODE) in the presence of a ligand (myristic acid or palmitic acid). Although the synthesis of InP in a non-coordinating solvent is much faster and more efficient compared to earlier synthetic schemes developed by Nozik and co-workers²⁰, the size-tunability and monodispersity are still poorer compared to CdSe NCs. For example, the narrowest fluorescence line widths obtained for InP NCs are about ~45–50 nm, whereas with CdSe QDs emitting in the same wavelength range values below 30 nm can be achieved.² Based on the works of several research groups around the world we now have a basic understanding of (a) the mechanism of InP formation from In(III) and P(SiMe₃)₃^{33,34}; (b) the role of solvent,³² (c) the role of Zinc(II) salt² (d) the role of amine^{2,35–37} (e) the role of water³⁸ (f) surface chemistry including ligand passivation³⁸ and surface oxidation³⁹ and (g) acid precursor.⁴⁰ Furthermore, the current efforts are focused on improving size distribution with a better understanding of the crystallization process. Bawendi and co-workers using NMR spectroscopy showed that the precursor, P(SiMe₃)₃ depletes instantly in the reaction, therefore, concluding that the molecular precursor is not available for the growth of the NCs.³⁷ Classical studies of LaMer predict that the temporal separation of nucleation and growth is necessary for obtaining colloidal solutions of NCs showing narrow size distribution.⁴¹ Short “burst” of nucleation results in a sudden drop of monomer concentration below a critical value, thus terminating further nucleation. Subsequently, the slow growth of the NCs follows with no separate nuclei being formed, resulting in monodispersity. PTMS depletion was identified as a possible reason for polydispersity InP NCs. Several attempts have been made to address the issue of group V precursor depletion in III-V NCs synthesis. Cossairt and co-workers combined P(SiMe₃)₃ with more stable P(SiPh₃)₃ to achieve temporal separation of nucleation and growth.⁴² More reactive P-precursor, (P(SiMe₃)₃) supplies monomers for the initial “burst” of

nucleation, while more stable $(\text{P}(\text{SiPh}_3)_3)$ supplies monomers during the growth stages. Despite implementing LaMer like separation of nucleation and growth, there was no improvement in size distribution. The authors concluded that, separation of nucleation and growth is not the sufficient condition to achieve monodispersity in InP NCs. To solve the problem of rapid precursor depletion in $\text{P}(\text{SiMe}_3)_3$ based methods, phosphorus precursors with higher stability have been synthesized. Jeong and co-workers substituted one of the methyl groups bound to silicon with a sterically bulkier tertiary butyl group resulting in $\text{P}(\text{SiMe}_2(\text{t-Bu}))_3$.⁴³ With this strategy, access to larger-sized InP QDs was possible without sacrificing a narrow size distribution, shifting the emission wavelength from 600 to 640 nm. However, the overall size dispersion was still poor compared to CdSe QDs. Similarly, Bawendi *et al.* introduced other more stable phosphorus precursors, $\text{X}(\text{YMe}_3)_3$ (where $\text{X}=\text{As}$ or P and $\text{Y}=\text{Ge}$ or Sn), replacing the Si by Ge or Sn bonds.⁴⁴ Due to decrease in polarity, Ge-X or Sn-X bond is stronger than Si-X bond, thus results in slower precursor conversion rates. Although, they achieved improvement in size distribution in the case of InAs QDs, no significant improvement in the size distribution was obtained with InP QDs. The same group studied the effect of precursor reactivity on the size and size distribution using precursors of 2-3 order of reactivity differences.⁴⁵ They conclude that precursor conversion rates have weaker potential to improve the size tunability in III-V NCs synthesis, thus opening up a debate about whether or not classical nucleation and growth theory holds for III-V NCs. Many reports have suggested the replacement of toxic silyl based phosphorous precursor. For example: white phosphorous,⁴⁶ Na_3P ,⁴⁷ PCl_3 ⁴⁸ and gaseous phosphine.^{49,50} However, the size distribution of NCs obtained from these precursors did not improve in a significant way. Therefore, the translation of synthesis methods and mechanistic insights to other III-V NCs is not straightforward.²

For example, the stability order of group V precursor is as follows $P(\text{SiMe}_3)_3 > \text{As}(\text{SiMe}_3)_3 > \text{Sb}(\text{SiMe}_3)_3$; $\text{PH}_3 > \text{AsH}_3 > \text{SbH}_3$. Consequently, size-tunable synthesis of InSb is difficult due to diminished precursor stability. The most successful synthesis of InSb is not a direct translation from InP NCs synthesis procedures. Talapin and co-workers obtain InSb QDs simultaneous co-reduction of $\text{Sb}(\text{N}(\text{SiMe}_3)_2)_3$ and InCl_3 in oleylamine in the presence of a strong reducing agent, LiEt_3BH .¹⁹ In another report, Kovalenko and co-workers have reacted two amido precursors, namely $\text{In}(\text{N}(\text{SiMe}_3)_2)_3$ and $\text{Sb}(\text{NMe}_2)_3$ yielding sub 10 nm InSb NCs.⁵¹

It is clear that III-V NCs formation is more complex than the formation of II-VI and IV-VI NCs due to the more covalent nature of the III-V bonds and the involvement of reactive precursors which makes controlling nucleation and growth processes difficult. The existing literature on mechanistic studies of III-V semiconductor nanocrystals in colloidal form can be summarised as follows:

- The temporal separation of nucleation and growth is not a sufficient criterion for monodispersity.²
- The precursor conversion kinetics cannot predict the reaction outcome reliably.⁴⁵
- The surface oxidation appears to influence even the final size of the NCs.
- The direct translation of the synthesis of InP NCs to other III-V NCs is not straightforward.
- All previous works on mechanistic studies of III-V semiconductor NCs have focused on only a special type of group V precursor while completely

undermining the role of group III precursor or the concomitant role of both group III and V precursors on the size evolution.

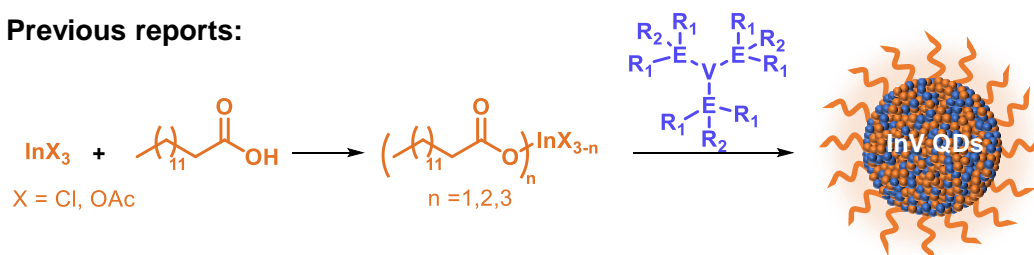
Against this background, this chapter studies the role of indium precursor on the size and size distribution of the III-V NCs in colloidal form.

3.2. Rationally resigned indium carboxylates for the study.

While most recent studies focus on the conversion kinetics of the phosphorus precursor, no experimental studies address the role of indium precursor on the size and size distribution. Theoretical studies reported by Xie *et al.* reveal that indium precursor reactivity does influence the energetics of the reaction pathways of InP formation.⁵²

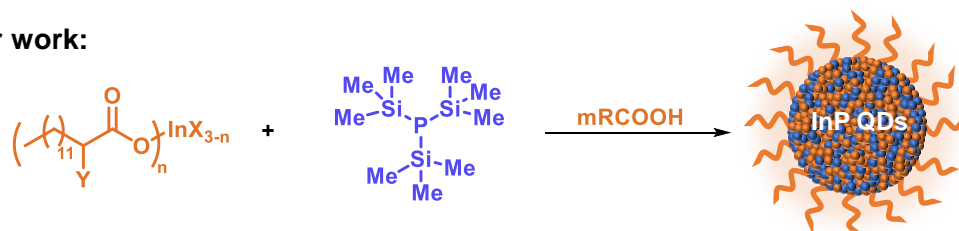
Figure 3.2 compares precursor modification in previous studies with our project.

Previous reports:



- | | |
|--|--|
| 1. V = P; E = Si; R ₁ = R ₂ = Ph | 6. V = P or As; E = Ge; R ₁ = R ₂ = Et |
| 2. V = P; E = Si; R ₁ = Me; R ₂ = t-Bu or Ph | 7. V = P; E = P |
| 3. V = P or As; E = Ge or Sn; R ₁ = R ₂ = Me | 8. V = P; E = Na |
| 4. V = P; E = Si; R ₁ = Me R ₂ = i-Pr | 9. V = P; E = Cl |
| 5. V = P or As; E = Si or Ge; R ₁ = R ₂ = Me | 10. V = P; E = H |

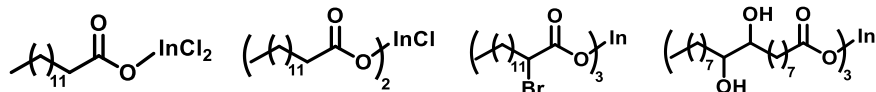
Our work:



- | | |
|---|---|
| R = C₁₃H₂₇ | 5. n = 1; m = 0; X = Cl; Y = H (Complex 3.3) |
| 1. n = 0; m = 3; X = OAc; Y = H (Complex 3.1) | 6. n = 2; m = 0; X = Cl; Y = H (Complex 3.4) |
| 2. n = 3; m = 0; Y = H (Complex 3.2) | 7. n = 1; m = 2; X = Cl; Y = H (Complex 3.3 + ROOH) |
| 3. n = 3; m = 0.5; Y = H (Experiment 2) | 8. n = 2; m = 1; X = Cl; Y = H (Complex 3.4 + ROOH) |
| 4. n = 3; m = 1.0; Y = H (Experiment 3) | 9. n = 3; m = 0; Y = Br (Complex 3.5) |

Figure 3.2. Overview of previous work and the studies carried out in this chapter.

Attention is drawn to the following metal precursors:



where the reactivity of the metal precursors has been systematically altered using methods described in the previous chapter. These precursors will have a crucial role in understanding the effect of metal-precursor reactivity on the size and size distribution of the III-V semiconductor NCs. In fact, the precursor conversion chemistry of both indium and phosphorus precursors will be important. We have used group III precursors of different reactivities to synthesize InP NCs (figure 3.2). The correlation between the evolution of particle size and precursor reactivity has been studied using UV-VIS-NIR spectroscopy.

3.3. Optimization of reaction temperature of InP NCs synthesis.

For the synthesis of InP NCs, we followed a hot-injection method in a non-coordinating solvent developed by Peng *et al.*³² (figure 3.3a) albeit using our phosphorus and indium precursors synthesized in the laboratory. As expected, a lower injection temperature (250 °C) results in relatively smaller sizes ($\lambda_{\text{max}}=547$ nm) compared to those prepared at a higher injection temperature (270 °C, $\lambda_{\text{max}}=583$ nm, figure 3.3b).⁵³⁻⁵⁵ Since the size distribution (as reflected in HWHM of the absorption peak at 270 °C (figure 3.3c) was better, we used this reaction for the rest of the studies.

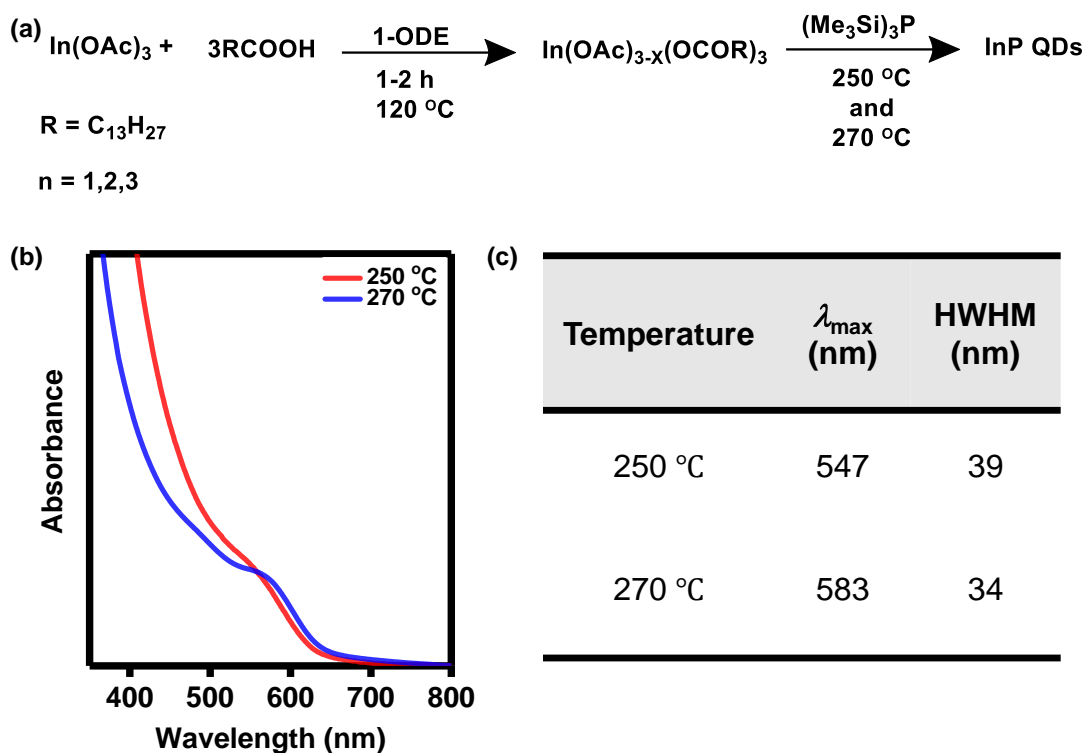


Figure 3.3. (a) Scheme for preparation of InP QDs using the typical hot injection method. (b). UV-Visible spectra of InP QDs taken at the end of growth time (3600 s) at two different injection temperatures. (c) Tabular description of λ_{max} (indicative of size) and HWHM (indicative of size distribution) observed from UV-Visible spectra of InP QDs at 250 °C and 270 °C injection temperature.

3.4. Effect of indium precursors.

For investigating the effect of indium precursors on the formation of InP QDs we initially prepared the QDs under air and moisture-free conditions with the as-synthesized pure indium myristate complex (Figure 3.4a). The temporal evolution of size and size distribution was monitored by collecting the aliquots at regular time intervals and studying their absorption feature in absorption spectra (Figure 3.4b). The TEM image shows quasi-spherical particles with an average size of $\sim 3.25 \pm 0.33$ nm (figure 3.4c).

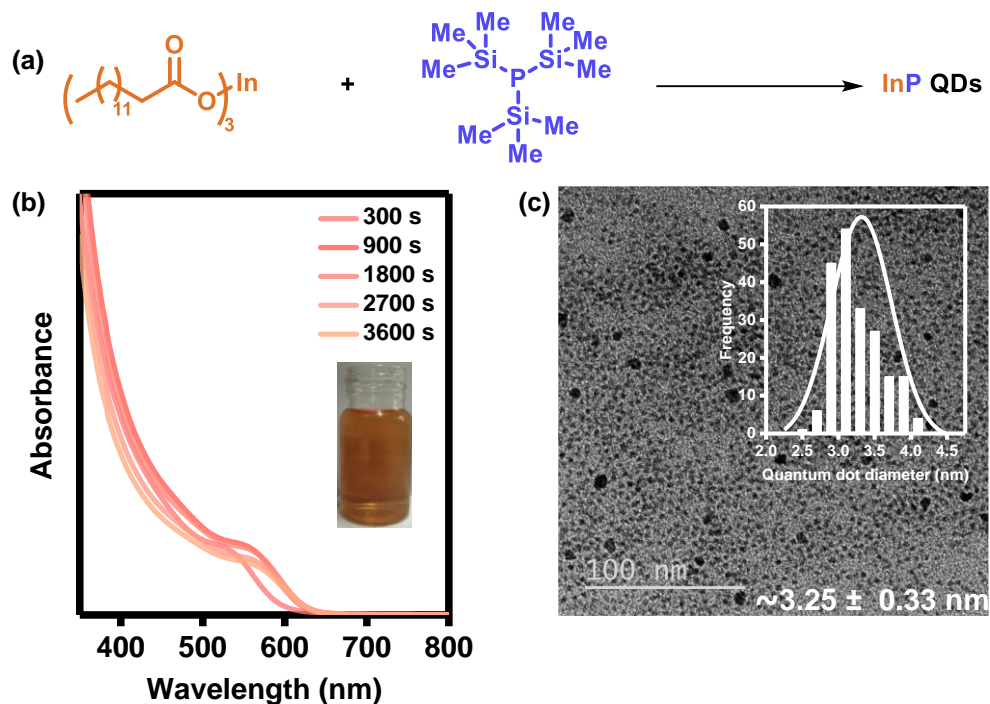


Figure 3.4. (a) Scheme for preparation of InP QDs from pure indium myristate (complex **3.2**) (b) Temporal evolution of InP QDs formation monitored using UV-Visible spectroscopy. (Inset: Image of a colloidal dispersion of InP QDs in hexane under normal light). (c) TEM micrograph of the InP QDs (Inset: size distribution graph).

The growth profiles of the InP NCs obtained from both the typical “vacuum method” (complex **3.1**) and pure indium myristate (complex **3.2**) were compared using UV–Visible absorption spectroscopy. To obtain insight into the mechanism of NCs formation three parameters were closely monitored. First, the energy of the lowest energy electronic transition (LEET), also known as the first excitonic peak ($1S_h-1S_e$). The energy (or wavelength) of LEET is directly related to the size of QDs: smaller-sized QDs absorb at higher energy and vice versa.^{40,44,56} Second parameter of interest is the full-width at half maximum (FWHM). The FWHM is related to the size distribution of the QDs: poor size distribution is reflected as larger FWHM in absorption spectroscopy^{40,57,58} The last parameter we monitored is the absorbance (or optical density) at high photon energy i.e., at 310 nm (A_{310}).^{56,59} Absorbance is related

to the concentration of the QDs.^{40,56} Figure 3.5a shows the comparative LEET at different growth times for complex **3.1** and **3.2**. It is evident from the figure that complex **3.2** crystallizes into smaller sizes as compared to complex **3.1**. This is attributed to the presence of free acids in complex **3.1** confirmed using FTIR (*c.f.* Section 2.2, Chapter II). The H⁺ from the free ligand reacts with PTMS to form a more stable H_{3-n}P(SiMe₃)_n precursor *in situ*, leading to larger-sized NCs.⁴⁰ The detailed discussion on the effect of free acid is provided in the next *section 3.4.1*. The FWHM (figure 3.5b) indicates similar size distribution of the QDs with both complexes. Similarly, the concentration of QDs at a different time (absorbance at 310 nm) is also comparable with both complexes (Figure 3.5c). A representative absorption spectrum of InP QDs obtained from complex **3.1** and **3.2** for an aliquot collected at 45 min is provided in figure 3.5d.

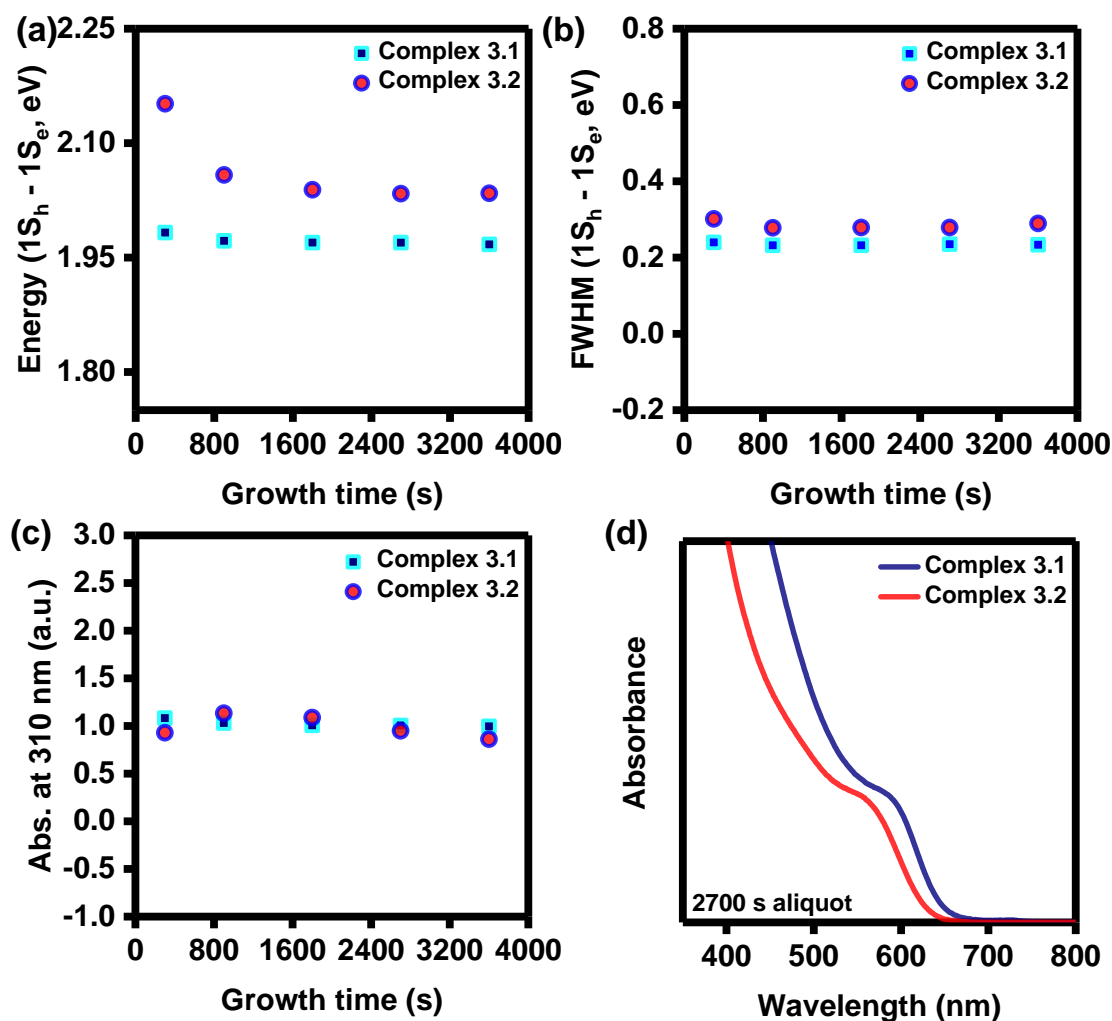


Figure 3.5. Data extracted from the UV-Visible absorption spectra of InP QDs growth using complex 3.1 and 3.2. (a) LEET vs. growth time; (b) FWHM at different times; (c) Evolution of absorbance at 310 nm (A_{310}); (d) Representative absorption spectra (measured with 45 min aliquots).

3.4.1. Effect of free acid on InP QDs synthesis and growth.

To understand the effect of free acid on the size of the InP NCs, we varied the free ligand concentration (externally added) and monitored the absorption parameters *viz.*, LEET and FWHM during the synthesis.

Table 3.1. Study of the effect of free acid on InP QDs synthesis and growth.

Experiment	In-precursor	Additional ligand (Molar equivalent)
1	Complex 3.2	0
2	Complex 3.2	0.5
3	Complex 3.2	1.0

Figure 3.6a depicts the schematic representation of the reaction involved. The evolution of LEET during the course of the reaction shows the increase in the size of the NCs as the concentration of an additional free ligand is increased (Figure 3.6b). This result is consistent with the literature report.³² In fact, Peng *et al.* studied the effect of free ligands on CdS, CdSe and ZnS QDs in detail.¹¹ They reported that in a non-coordinating solvent like 1-ODE, the concentration of ligands is crucial in achieving the balance between the nucleation and growth stages.^{11,60} Their studies suggest that the higher concentration of free ligands stabilises or decreases the reactivity of the monomers leading to a decrease in the availability of the active monomers which can be converted to nuclei.^{11,61–65} This phenomenon will decrease the nucleation rate resulting in the formation of larger sized QDs. However, Cossairt *et al.* showed that a trace amount (up to 0.6 equivalent) of the free ligand is indeed beneficial for size distribution. They attributed this observation to the formation of less reactive intermediate precursor $H_{3-n}P(SiMe_3)_n$. In several studies, it has been confirmed that poor stability and high reactivity of $P(SiMe_3)_3$ leads to depletion of monomer concentration during the growth stage, triggering the Ostwald ripening.^{66,67} In our case, using trace amount of free ligand (Experiment 2, table 3.1, figures 3.6b and c) led to the increase in size without decreasing the size distribution. However, the presence of excess free ligands (Experiment 3, table 3.1, figures 3.6c) resulted in poor size distribution. The excess of

free ligands can result in poor distribution due to prolonging the nucleation event. In fact, a short nucleation event well separated from the growth stage is a prerequisite to monodispersity according to LaMer and Dinger's model.⁴¹ Similar results have been reported elsewhere for InP QDs.³²

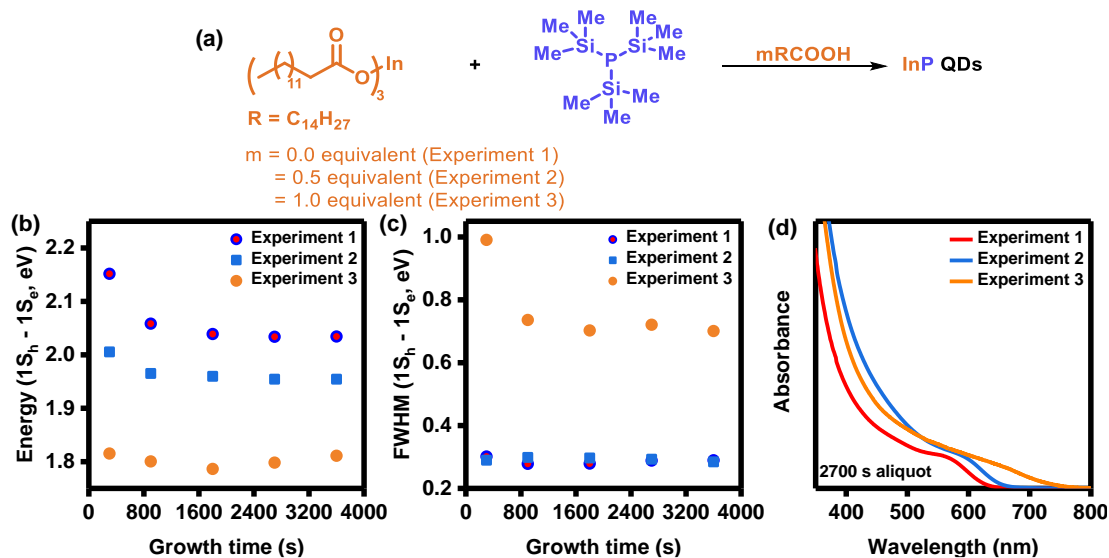
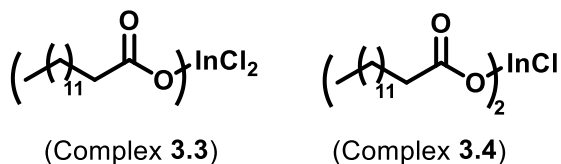


Figure 3.6. Data extracted from the UV-Visible absorption spectra of InP QDs growth under various concentrations of free ligand (a) Reaction scheme (b) LEET vs. reaction time; (c) FWHM of absorption peak against reaction time; (d) Representative absorption traces for 45 min aliquots of experiment 1, 2 and 3.

3.4.2. Partially substituted indium precursor.

As discussed in chapter II, due to the lack of agreement on reaction time, temperature, and pressure needed for the degassing process in the vacuum method, the purity and composition of *in situ* generated MFAs remain unknown, resulting in inconsistencies in the properties of CQDs from batch to batch. Our experiments (Chapter II, section 2.2) and some other reports^{2,68} confirmed that the partial acid substitution in indium precursor is common. We synthesized two partially acid-substituted indium precursors *viz.*, complex **3.3** and **3.4** and carried out the synthesis of InP QDs under optimized reaction conditions (Figure 3.7a).



With both the complexes, no distinguishable absorption peak (LEET) was observed indicating the broad size distribution of the NCs (figure 3.7b and c). This is attributed to the higher reactivity of these partially substituted ligands and uncontrolled nucleation and growth processes,^{66,69–73} which showed slight improvement when free acid ligands are externally added (Figure 3.7d). However, the improvement was not dramatic. This can be explained based on the presence of halide ion which increases the reactivity of the precursor.

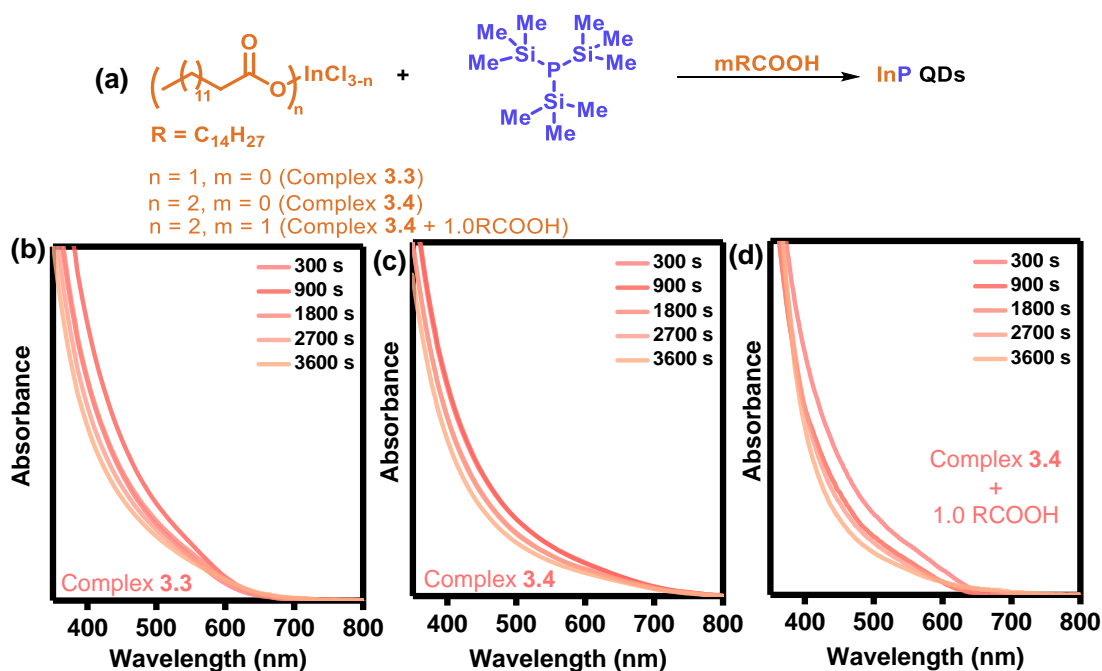


Figure 3.7. (a) Scheme for preparation of InP QDs from acid substituted InCl_3 . (b) Temporal evolution of absorption spectra with (b) complex 3.3 and (c) complex 3.4 and (d) complex 3.4 + 1.0 myristic acid.

3.4.3. Increasing reactivity of indium precursor

Previous research on the mechanistic studies of III-V semiconductor NCs has exclusively focussed on group V precursor, disregarding the significance of the group III precursor or the joint contribution of both group III and V precursors to the nucleation and growth.⁴²⁻⁵⁰ We synthesized an alpha bromo-substituted indium myristate (complex **3.5**) and compared its precursor reactivity-size relationship to that of unsubstituted indium myristate (complex **3.2**). DFT calculation shows that the indium-oxygen bond length in complex **3.5** is longer than in complex **3.2**, signifying more reactivity. The value of Mullikan charge distribution of the central indium atom is also higher for complex **3.5** (+1.591) compared to that of complex **3.2** (+1.540) due to the presence of highly electronegative bromine atom in the alpha carbon atom (Table 3.2, Annexure A3).

Table 3.2. Summary of DFT studies.

Entry	Bond	Bond length(Å)	
		Complex 3.2	Complex 3.5
1	In-O1	1.968	1.928
2	In-O3	2.007	2.030
3	In-O4	2.113	2.122
4	In-O6	2.184	2.190
5	In-O7	2.192	2.135
6	In-O8	2.166	2.195
7	In	+1.540	+1.591

Note: 1-6: bond length determination from DFT, 7: Value of Mullikan charge distribution of central indium atom

The comparative study of size evolution with complex **3.2** and complex **3.5** are presented in figure 3.8. The effect of reactivity of indium precursor was clearly evident in size and size distribution. More reactive complex **3.5** led to larger-sized NCs and poor size distribution as reflected in LEET (Figure 3.8b) and FWHM (Figure 3.8c). Our results reveal that not only the reactivity of the group V precursor but the higher reactivity of the group III precursor also results in the formation of larger-sized NCs with poor size distribution. The absorption spectra with two complexes are compared in figure 3.8d. Clearly, the sharper first excitonic peak is visible for complex **3.2** which is more stable compared to complex **3.5**. This result is further confirmed by TEM (figure 3.8e). Complex **3.5** formed larger-sized and more polydisperse NCs ($\sim 5.04 \pm 1.06$ nm) as shown in figure 3.8e compared to complex **3.2**.

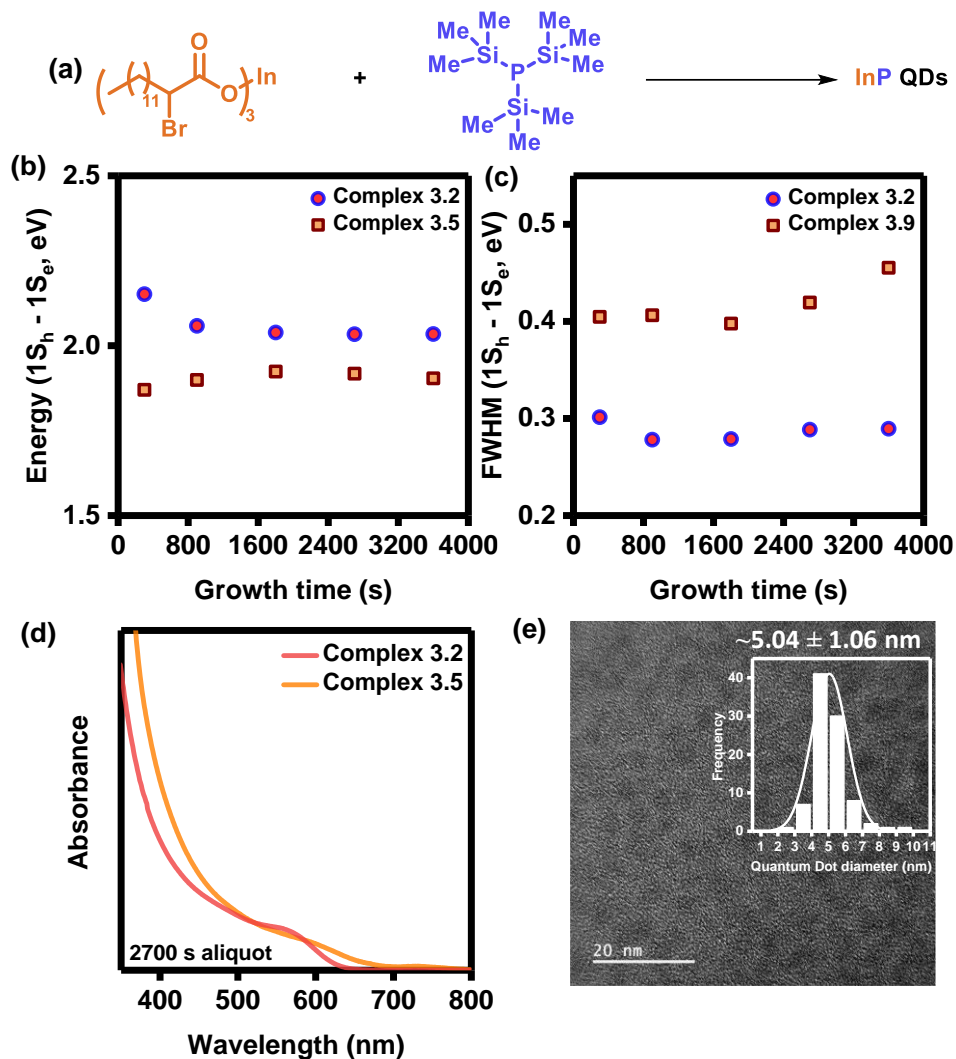


Figure 3.8. Data extracted from the UV-Visible spectra of InP QDs growth using complex 3.2 and 3.5. (a) Reaction scheme for the preparation of InP QDs from complex 3.5. (b) Energy of LEET vs. reaction time; (c) FWHM of the absorption peak vs. reaction time; (d) Representative absorption spectra for two complexes (45 min aliquots); (f) TEM image of InP QDs prepared from complex 3.5. Inset: Size distribution obtained from TEM data.

In summary, the presence of a bromide group increases the reactivity of complex 3.5 (electronegativity value of Br: 3.219) compared to the non-substituted one (complex 3.2, electronegativity value of H: 2.592)⁷⁴⁻⁷⁶ which results in larger sized NCs and broader size distribution. Furthermore, the ¹H NMR studies confirmed that more reactive complex 3.5 promotes faster depletion of PTMS precursor (figure 3.9c).

Molecular precursors completely vanished in the reaction mixture within a short span of time (~300 seconds, figure 3.8a and b). Non-molecular ripening stage, which results in broad size distribution, has been proposed for such a scenario in the literature.²

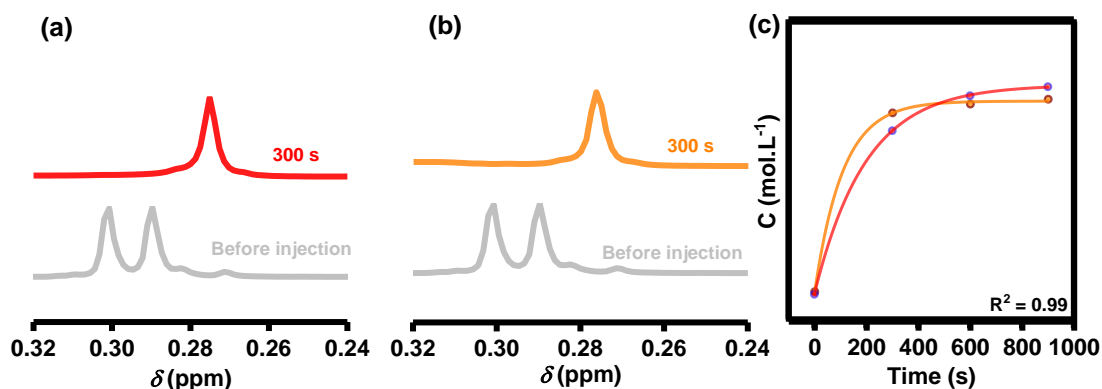


Figure 3.9. *In situ* ^1H NMR studies of the reaction of indium precursor with PTMS. (a) *In situ* ^1H NMR for InP NCs synthesis from complex **3.2**. The peaks are for PTMS before injection and 5 min after injection. (b) *In situ* ^1H NMR for InP NCs synthesis from complex **3.5**. The peaks are for PTMS before injection and 5 min after injection. (c) concentration (C) profiles of TMS-MA protons determined at 5 min time intervals from the integration of spectra represented in figures 3.9a and b.

Additionally, we also prepared InP QDs from highly polar indium salt of 9,10-dihydroxystearic acid (complex **3.6**).

Scheme 3.1. Preparation of InP QDs from complex **3.6**.



Figure 3.10 depicts the absorption spectra of NCs prepared using complex **3.6** in comparison with the indium stearate (complex **3.7**). The results show that highly polydisperse InP NCs are formed if the polarity of indium precursor is increased *via* hydroxylation of olefinic bond in oleic acid.

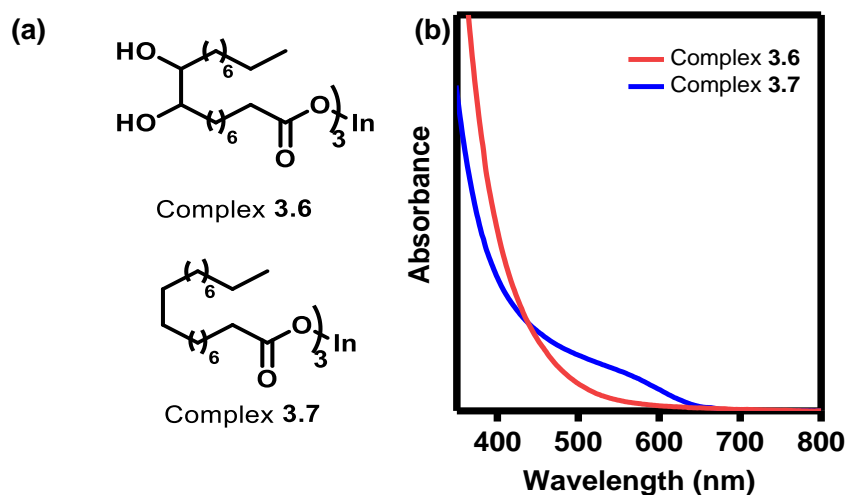


Figure 3.10. (a) The structural difference between complex 3.6 and complex 3.7. (b) Comparative absorption spectra of complex 3.6 and complex 3.7. A distinct absorption peak is observed for complex 3.7 at 550 nm which is absent in complex 3.6.

3.5. Conclusion.

Previous studies that have studied the mechanisms of III-V semiconductor NCs have solely focused on the group V precursor, neglecting the importance of the group III precursor and the combined influence of both group III and V precursors on size development. This chapter explored the impact of the indium precursor on the size and size distribution of III-V nanocrystals in colloidal form while considering the previous context. The methods used in the previous chapter were applied to systematically modify the reactivity of the metal precursors.

To examine the effect of the reactivity of indium precursor on InP QDs formation, we first synthesized QDs using the pure indium myristate complex under air- and moisture-free conditions. The results indicate that the pure complex yields smaller sizes than the indium precursor complex prepared using the vacuum method, which contains free acids. Similar results were observed when trace amounts of free ligand were added along with the pure indium myristate complex. This was attributed to the formation of

a less reactive intermediate precursor, $\text{H}_{3-n}\text{P}(\text{SiMe}_3)_n$, in the presence of trace acid. However, an excess of free ligands resulted in poor size distribution by prolonging the nucleation event.

Furthermore, partially substituting group III precursors with 1 or 2 equivalents of long-chain fatty acid led to poor size distribution. This was due to the higher reactivity of the partially substituted precursor, which in turn caused uncontrolled nucleation and growth processes. The bromide substitution at the alpha position of the long-chain fatty acid also increased the reactivity of the indium precursor, resulting in larger-sized nanocrystals and broader size distribution. ^1H NMR studies confirmed that more reactive bromo-substituted indium precursors promoted faster depletion of PTMS precursor. Lastly, highly polydisperse InP nanocrystals were formed when the polarity of the indium precursor was increased.

3.6. Experimental Section.

3.6.1. General information.

3.6.1.1. Materials and general consideration.

1-ODE (technical grade), $\text{In}(\text{OAc})_3$ (99.99% trace metals basis) were all purchased from Sigma Aldrich, India. Oleic acid (65-88%) was purchased from Merck, India. Myristic acid was purchased from SRL. The deuterated solvent used for NMR analysis was purchased from Sigma Aldrich India.

3.6.1.2. Characterization method.

UV-Visible spectrophotometer: The UV-Visible absorption spectra were collected using Perkin Elmer (Model: LS 55) spectrophotometer (scan rate: 480 nm/s) and Agilent Technologies Cary 100 UV-Visible.

Transmission electron microscopy (TEM): TEM images were taken in JEOL-JEM-F200 and Tecnai G2 20 S-TWIN electron microscope. Samples were prepared by drop-casting of NC solution in anhydrous toluene on a carbon-coated copper grid purchased from EMS, the grids were kept overnight in a vacuum desiccator. The analysis of average size was performed with ImageJ software.

Nuclear magnetic resonance (NMR): ^1H NMR, ^{13}C NMR spectra were recorded on a Bruker ASCENDTM (400 MHz) spectrometer using CDCl_3 solvent

X-ray Diffractometer (XRD): The purified NCs in hexane were drop-casted on a clean and dry glass slide. The film on the glass slide was run under PANalytical X-ray diffractometer using $\text{Cu K}\alpha$ ($\lambda = 1.54 \text{ \AA}$) as the incident radiation (40 kV and 30 mA).

3.6.2. Preparation of InP QDs.

3.6.2.1. Preparation of InP QDs using vacuum method for optimization studies.

3.6.2.1.1. Synthesis of 250 °C sample.

InP QDs were synthesized following the reported method with slight modification.^{32,40} Briefly, 0.029 g (0.1 mmol) of indium acetate and 0.069 g (0.3 mmol) of myristic acid were mixed in 3.945 g (15.6 mmol, 5 mL) of 1-ODE. The mixture was transferred to three-necked round bottom flask (A) was vacuumed at 120 °C until an optically clear solution was obtained (1-2 h). The flask A was backfilled with nitrogen and the solution was heated to 250 °C. Separately 0.0126 g (0.05 mmol, 14.6 μL) of tris(trimethylsilyl)phosphine was mixed with 0.5 mL of 1-ODE inside the glove box. This solution was slowly brought out of the glove box and rapidly injected into the heated solution of flask A and reacted for 1 h. After 1 h the reaction was brought down to room temperature naturally. The as-synthesized InP QDs were purified through a

centrifugation method. 4 mL of the reaction solution was mixed with 2 mL of anhydrous hexane and 8 mL of anhydrous ethanol. The mixture was centrifuged at 5000 rpm for 10 min. The supernatant was discarded and the solid residue was washed again with a 1:4 mixture of anhydrous hexane and anhydrous ethanol at 5000 rpm for 10 min. The purified NCs were dispersed in hexane. UV-Visible absorption peak (λ_{max}) = 547 nm

3.6.2.1.2. Synthesis of 270 °C sample.

Synthesized as above (250 °C sample), except the injection temperature was 270 °C. UV-Visible absorption peak (λ_{max}) = 583 nm

3.6.2.2. Preparation of InP QDs using typical vacuum method (complex 3.1) for mechanistic studies.

InP QDs were synthesized following the reported method with slight modification.^{32,40} Briefly, 0.029 g (0.1 mmol) of indium acetate and 0.069 g (0.3 mmol) of myristic acid were mixed in 3.945 g (15.6 mmol, 5 mL) of 1-ODE. The mixture was transferred to three-necked round bottom flask (A) was vacuumed at 120 °C until an optically clear solution was obtained (1-2 h). The flask A was backfilled with nitrogen and the solution was heated to 270 °C. Separately 0.0125 g (0.05 mmol, 14.6 μL) of tris(trimethylsilyl)phosphine was mixed with 0.5 mL of 1-ODE inside the glove box. This solution was slowly brought out of the glove box and rapidly injected into the heated solution of flask A. At 5 min first aliquots (200 μL) were withdrawn from the reaction mixture and dispersed in 1 mL of anhydrous hexane to immediately quench its growth. Similarly, other aliquots were collected at 15, 30, 45 and 60 min respectively and dispersed in anhydrous hexane and correspondingly the UV-Visible absorption spectra were collected. The purification step was performed in a similar way as described for 250 and 270 °C samples.

3.6.2.3. Preparation of InP QDs using pure indium myristate (complex 3.2) for mechanistic studies.

0.079 g (0.1 mmol) of complex **3.2** were mixed in 3.945 g (15.6 mmol, 4 mL) of 1-ODE in a three-necked round bottom flask (A) and vacuumed at 120 °C for 1 h. The flask A was backfilled with nitrogen and the solution was heated to 270 °C. Separately 0.0125 g (0.05 mmol, 14.6 µL) of tris(trimethylsilyl)phosphine was mixed with 0.5 mL of 1-ODE inside the glove box. This solution was rapidly injected into the heated reaction solution of flask A. At 5 min first aliquots (200 µL) were withdrawn from the reaction mixture and dispersed in 1 mL anhydrous hexane to immediately quench its growth. Similarly, other aliquots were collected at 15, 30, 45 and 60 min respectively and dispersed in anhydrous hexane and correspondingly the UV-Visible absorption spectra were collected. The purification step was performed in a similar way as described for 250 and 270 °C samples.

3.6.2.4. Preparation of InP QDs using complex 3.3 for mechanistic studies.

The synthetic approach was the same as discussed above for complex **3.2**. However, the major difference here was the addition of 0.011 g (0.05 mmol) of myristic acid initially along with pure indium myristate.

3.6.2.5. Preparation of InP QDs using complex 3.4 for mechanistic studies.

It was prepared in the same way as discussed for complex **3.2**, one major difference being the addition of 0.023 (0.1 mmol) of myristic acid initially along with pure indium myristate.

3.6.2.6. Preparation of InP QDs using complex 3.5.

It was prepared similarly as discussed above for complex **3.2**. 0.041 g (0.1 mmol) of complex **3.5** was utilised.

3.6.2.7. Preparation of InP QDs using complex 3.6.

The NCs were prepared with a similar approach as employed for preparing InP QDs using complex **3.2**. 0.061 g (0.1 mmol) of complex **3.6** was used.

3.6.2.8. Preparation of InP QDs using complex 3.7.

It was prepared similarly as discussed above for complex **3.5**. 0.041 g (0.1 mmol) of complex **3.5** was used along with 0.046 g (0.2 mmol) of myristic acid.

3.6.2.9. Preparation of InP QDs using complex 3.8.

The NCs were prepared in the same way as discussed above for complex **3.6**. 0.061 g (0.1 mmol) of complex **3.6** was used along with 0.023 g (0.1 mmol) of myristic acid.

3.6.2.10. Preparation of InP QDs using complex 3.9 for mechanistic studies.

The synthetic method was similar to the one discussed for complex **3.2**. The amount of complex **3.9** used for the reaction was 0.103 g (0.1 mmol).

3.6.2.11. Preparation of InP QDs using complex 3.10.

It was prepared according to the method discussed above for complex **3.2**. The major difference in this procedure was the replacement of complex **3.2** with complex **3.10** for which 0.106 g (0.1 mmol) of complex **3.10** was utilised.

3.6.2.12. Preparation of InP QDs using complex 3.11.

It was prepared according to the method discussed above for complex **3.10**. The major difference in this procedure is the replacement of complex **3.10** with 0.097 g (0.1 mmol) of complex **3.10**.

3.6.3. *In situ* ^1H NMR studies for the reaction of complex 3.2 and complex 3.9 with PTMS.

0.78 mg (0.003 mmol, 0.9 μL) of tris(trimethylsilyl)phosphine was mixed with 0.4 mL of CDCl_3 inside the glove box in an NMR tube. Two batches of this tube (A1 and A2) were prepared. Both of these tubes were sealed properly and transferred out of the glove box. ^1H NMR was determined for tube A1. After the completion of the run solution of 4.8 mg (0.006 mmol) of complex **3.2** in 0.2 mL of CDCl_3 was injected into it and a temporal ^1H NMR was determined. Similarly, ^1H NMR was determined for tube A2 after the completion of which a solution of 6.2 mg (0.006 mmol) of complex **3.9** in 0.2 mL of CDCl_3 was injected into it and a temporal ^1H NMR was determined.

3.6.4. DFT calculations.

DFT studies were performed on Gaussian 09 and GaussView 6.0 suite of software programs. The optimization and vibrational frequencies calculation were performed by applying B3LYP functional and LanL2DZ as a basis set.⁷⁹ The optimized ground states with local minima were confirmed by the absence of negative frequency value. The studies were carried out for reducing the carbon chain of carboxylates with a simple phenyl group.^{77,78} Under the study of two different sets of In-salts used as precursor, the comparative results based on bond length between the central atom indium and oxygen atom was determined.

3.7. References.

- (1) Reiss, P.; Carrière, M.; Lincheneau, C.; Vaure, L.; Tamang, S. Synthesis of Semiconductor Nanocrystals, Focusing on Nontoxic and Earth-Abundant Materials. *Chem. Rev.* **2016**, *116*, 10731–10819.
- (2) Tamang, S.; Lincheneau, C.; Hermans, Y.; Jeong, S.; Reiss, P. Chemistry of InP Nanocrystal Syntheses. *Chem. Mater.* **2016**, *28*, 2491–2506.
- (3) Frecker, T.; Bailey, D.; Arzeta-Ferrer, X.; McBride, J.; Rosenthal, S. J. Quantum Dots and Their Application in Lighting, Displays, and Biology. *J. Solid State Sci. Technol.* **2015**, *5*, R3019--R3031.
- (4) Tang, R.; Xue, J.; Xu, B.; Shen, D.; Sudlow, G. P.; Achilefu, S. Tunable Ultrasmall Visible-to-Extended near-Infrared Emitting Silver Sulfide Quantum Dots for Integrin-Targeted Cancer Imaging. *ACS Nano* **2015**, *9*, 220–230.
- (5) Liu, M.; Voznyy, O.; Sabatini, R.; García De Arquer, F. P.; Munir, R.; Balawi, A. H.; Lan, X.; Fan, F.; Walters, G.; Kirmani, A. R.; Hoogland, S.; Laquai, F.; Amassian, A.; Sargent, E. H. Hybrid Organic-Inorganic Inks Flatten the Energy Landscape in Colloidal Quantum Dot Solids. *Nat. Mater.* **2017**, *16*, 258–263.
- (6) Wu, Y.; Zhou, B.; Yang, C.; Liao, S.; Zhang, W. H.; Li, C. CuFeS₂ Colloidal Nanocrystals as an Efficient Electrocatalyst for Dye Sensitized Solar Cells. *Chem. Commun.* **2016**, *52*, 11488–11491.
- (7) Harris, C.; Kamat, P. V. Photocatalytic Events of CdSe Quantum Dots in Confined Media. Electrode Behavior of Coupled Platinum Nanoparticles. *ACS Nano* **2010**, *4*, 7321–7330.

- (8) Yuan, S.; Wang, Z. K.; Zhuo, M. P.; Tian, Q. S.; Jin, Y.; Liao, L. S. Self-Assembled High Quality CsPbBr₃ Quantum Dot Films toward Highly Efficient Light-Emitting Diodes. *ACS Nano* **2018**, *12*, 9541–9548.
- (9) Li, D.; Kristal, B.; Wang, Y.; Feng, J.; Lu, Z.; Yu, G.; Chen, Z.; Li, Y.; Li, X.; Xu, X. Enhanced Efficiency of InP-Based Red Quantum Dot Light-Emitting Diodes. *ACS Appl. Mater. Interfaces* **2019**, *11*, 34067–34075.
- (10) Stasiuk, G. J.; Tamang, S.; Imbert, D.; Poillot, C.; Giardiello, M.; Tisseyre, C.; Barbier, E. L.; Fries, P. H.; De Waard, M.; Reiss, P.; Mazzanti, M. Cell-Permeable Ln(III) Chelate-Functionalized InP Quantum Dots as Multimodal Imaging Agents. *ACS Nano* **2011**, *5*, 8193–8201.
- (11) Yu, W. W.; Peng, X. Formation of High-Quality CdS and Other II-VI Semiconductor Nanocrystals in Noncoordinating Solvents: Tunable Reactivity of Monomers. *Angew. Chemie - Int. Ed.* **2002**, *41*, 2368–2371.
- (12) Schliehe, C.; Juarez, B. H.; Pelletier, M.; Jander, S.; Greshnykh, D.; Nagel, M.; Meyer, A.; Foerster, S.; Kornowski, A.; Klinke, C.; Weller, H. Ultrathin PbS Sheets by Two-Dimensional Oriented Attachment. *Science*. **2010**, *329*, 550–553.
- (13) Hendricks, M. P.; Campos, M. P.; Cleveland, G. T.; Plante, I. J. La; Owen, J. S. A Tunable Library of Substituted Thiourea Precursors to Metal Sulfide Nanocrystals. *Science*. **2015**, *348*, 1226–1230.
- (14) Peng, X.; Manna, L.; Yang, W.; Wickham, J.; Scher, E.; Kadavanich, A.; Alivisatos, A. P. Shape Control of CdSe Nanocrystals. *Nature* **2000**, *404*, 59–61.
- (15) Mourdikoudis, S.; Liz-Marza, L. M. Oleylamine in Nanoparticle Synthesis. *Chem. Mater.* **2016**, *25*, 1465–1476.

- (16) Reiss, P.; Protière, M.; Li, L. Core/Shell Semiconductor Nanocrystals. *Small* **2009**, *5*, 154–168.
- (17) Montie, E. A.; Van Gorp, G. J. Photoluminescence of Zn-Diffused and Annealed InP. *J. Appl. Phys.* **1989**, *66*, 5549–5553.
- (18) Green, M. Solution Routes to III - V Semiconductor Quantum Dots. *Curr. Opin. Solid State Mater. Sci.* **2002**, *6*, 355–363.
- (19) Liu, W.; Chang, A. Y.; Schaller, R. D.; Talapin, D. V. Colloidal InSb Nanocrystals. *J. Am. Chem. Soc.* **2012**, *134*, 20258–20261.
- (20) Mičić, O. I.; Curtis, C. J.; Jones, K. M.; Sprague, J. R.; Nozik, A. J. Synthesis and Characterization of InP Quantum Dots. *J. Phys. Chem.* **1994**, *98*, 4966–4969.
- (21) Fan, G.; Wang, C.; Fang, J. Solution-Based Synthesis of III-V Quantum Dots and Their Applications in Gas Sensing and Bio-Imaging. *Nano Today* **2014**, *9*, 69–84.
- (22) Mushonga, P.; Onani, M. O.; Madiehe, A. M.; Meyer, M. Indium Phosphide-Based Semiconductor Nanocrystals and Their Applications. *J. Nanomater.* **2012**, *2012*, 869284–869295.
- (23) Heath, J. R.; Shiang, J. J. Covalency in Semiconductor Quantum Dots. *Chem. Soc. Rev.* **1998**, *27*, 65–71.
- (24) Ren, A.; Yuan, L.; Xu, H.; Wu, J.; Wang, Z. Recent Progress of III-V Quantum Dot Infrared Photodetectors on Silicon. *J. Mater. Chem. C* **2019**, *7*, 14441–14453.
- (25) Zhao, T.; Oh, N.; Jishkariani, D.; Zhang, M.; Wang, H.; Li, N.; Lee, J. D.; Zeng,

- C.; Muduli, M.; Choi, H. J.; Su, D.; Murray, C. B.; Kagan, C. R. General Synthetic Route to High-Quality Colloidal III-V Semiconductor Quantum Dots Based on Pnictogen Chlorides. *J. Am. Chem. Soc.* **2019**, *141*, 15145–15152.
- (26) Steckel, J. S.; Yen, B. K. H.; Oertel, D. C.; Bawendi, M. G. On the Mechanism of Lead Chalcogenide Nanocrystal Formation. *J. Am. Chem. Soc.* **2006**, *128*, 13032–13033.
- (27) Liu, H.; Owen, J. S.; Alivisatos, A. P. Mechanistic Study of Precursor Evolution in Colloidal Group II-VI Semiconductor Nanocrystal Synthesis. *J. Am. Chem. Soc.* **2007**, *129*, 305–312.
- (28) Abe, S.; Čapek, R. K.; De Geyter, B.; Hens, Z. Tuning the Postfocused Size of Colloidal Nanocrystals by the Reaction Rate: From Theory to Application. *ACS Nano* **2012**, *6*, 42–53.
- (29) Chatani, E.; Yamamoto, N. Recent Progress on Understanding the Mechanisms of Amyloid Nucleation. *Biophys. Rev.* **2018**, *10*, 527–534.
- (30) Thanh, N. T. K.; Maclean, N.; Mahiddine, S. Mechanisms of Nucleation and Growth of Nanoparticles in Solution. *Chem. Rev.* **2014**, *114*, 7610–7630.
- (31) Zhang, J.; Hao, X.; Rowell, N.; Kreouzis, T.; Han, S.; Fan, H.; Zhang, C.; Hu, C.; Zhang, M.; Yu, K. Individual Pathways in the Formation of Magic-Size Clusters and Conventional Quantum Dots. *J. Phys. Chem. Lett.* **2018**, *9*, 3660–3666.
- (32) Battaglia, D.; Peng, X. Formation of High Quality InP and InAs Nanocrystals in Noncoordinating Solvent. *Nano Lett.* **2002**, *2*, 1027–1030.

- (33) Wells, R. L.; Aubuchon, S. R.; Kher, S. S.; Lube, M. S.; White, P. S. Synthesis of Nanocrystalline Indium Arsenide and Indium Phosphide from Indium(III) Halides and Tris (Trimethylsilyl)Phosphenes. Synthesis, Characterization, and Decomposition Behavior of $\text{In}_3\text{P}_2\text{S}_6$. *Chem. Mater.* **1995**, *7*, 793–800.
- (34) Healy, M. D.; Laibinis, P. E.; Stupik, P. D.; Barron, A. R. The Reaction of Indium(III) Chloride with Tris(trimethylsilyl)phosphine: A Novel Route to Indium Phosphide. *J. Chem. Soc. Chem. Commun.* **1989**, *6*, 359–360.
- (35) Xie, R.; Battaglia, D.; Peng, X. Colloidal InP Nanocrystals as Efficient Emitters Covering Blue to Near-Infrared. *J. Am. Chem. Soc.* **2007**, *129*, 15432–15433.
- (36) Protière, M.; Reiss, P. Amine-Induced Growth of an In_2O_3 Shell on Colloidal InP Nanocrystals. *Chem. Commun.* **2007**, 2417–2419.
- (37) Allen, P. M.; Walker, B. J.; Bawendi, M. G. Mechanistic Insights into the Formation of InP Quantum Dots. *Angew. Chemie - Int. Ed.* **2010**, *49*, 760–762.
- (38) Xie, L.; Harris, D. K.; Bawendi, M. G.; Jensen, K. F. Effect of Trace Water on the Growth of Indium Phosphide Quantum Dots. *Chem. Mater.* **2015**, *27*, 5058–5063.
- (39) Cros-Gagneux, A.; Delpech, F.; Nayral, C.; Cornejo, A.; Coppel, Y.; Chaudret, B. Surface Chemistry of InP Quantum Dots: A Comprehensive Study. *J. Am. Chem. Soc.* **2010**, *132*, 18147–18157.
- (40) Gary, D. C.; Cossairt, B. M. Role of Acid in Precursor Conversion During InP Quantum Dot Synthesis. *Chem. Mater.* **2013**, *25*, 2463–2469.

- (41) LaMer, V. K.; Dinegar, R. H. Theory, Production and Mechanism of Formation of Monodispersed Hydrosols. *J. Am. Chem. Soc.* **1950**, *72*, 4847–4854.
- (42) Gary, D. C.; Glassy, B. A.; Cossairt, B. M. Investigation of Indium Phosphide Quantum Dot Nucleation and Growth Utilizing Triarylsilylphosphine Precursors. *Chem. Mater.* **2014**, *26*, 1734–1744.
- (43) Joung, S.; Yoon, S.; Han, C.-S.; Kim, Y.; Jeong, S. Facile Synthesis of Uniform Large-Sized InP Nanocrystal Quantum Dots Using Tris(Tert-Butyldimethylsilyl)Phosphine. *Nanoscale Res. Lett.* **2012**, *7*, 1–8.
- (44) Harris, D. K.; Bawendi, M. G. Improved Precursor Chemistry for the Synthesis of III-V Quantum Dots. *J. Am. Chem. Soc.* **2012**, *134*, 20211–20213.
- (45) Franke, D.; Harris, D. K.; Xie, L.; Jensen, K. F.; Bawendi, M. G. The Unexpected Influence of Precursor Conversion Rate in the Synthesis of III-V Quantum Dots. *Angew. Chemie* **2015**, *127*, 14507–14511.
- (46) Thuy, U. T. D.; Huyen, T. T. T.; Liem, N. Q.; Reiss, P. Low Temperature Synthesis of InP Nanocrystals. *Mater. Chem. Phys.* **2008**, *112*, 1120–1123.
- (47) Jun, K. W.; Khanna, P. K.; Hong, K. B.; Baeg, J. O.; Suh, Y. D. Synthesis of InP Nanocrystals from Indium Chloride and Sodium Phosphide by Solution Route. *Mater. Chem. Phys.* **2006**, *96*, 494–497.
- (48) Liu, Z.; Kumbhar, A.; Xu, D.; Zhang, J.; Sun, Z.; Fang, J. Coreduction Colloidal Synthesis of III-V Nanocrystals: The Case of InP. *Angew. Chemie - Int. Ed.* **2008**, *47*, 3540–3542.
- (49) Li, L.; Protière, M.; Reiss, P. Economic Synthesis of High Quality InP

- Nanocrystals Using Calcium Phosphide as the Phosphorus Precursor. *Chem. Mater.* **2008**, *20*, 2621–2623.
- (50) Tamang, S.; Beaune, G.; Texier, I.; Reiss, P. Aqueous Phase Transfer of InP/ZnS Nanocrystals Conserving Fluorescence and High Colloidal Stability. *ACS Nano* **2011**, *5*, 9392–9402.
- (51) Yarema, M.; Kovalenko, M. V. Colloidal Synthesis of InSb Nanocrystals with Controlled Polymorphism Using Indium and Antimony Amides. *Chem. Mater.* **2013**, *25*, 1788–1792.
- (52) Xie, L.; Zhao, Q.; Jensen, K. F.; Kulik, H. J. Direct Observation of Early-Stage Quantum Dot Growth Mechanisms with High-Temperature Ab Initio Molecular Dynamics. *J. Phys. Chem. C* **2016**, *120*, 2472–2483.
- (53) Narayanaswamy, A.; Feiner, L. F.; Van Der Zaag, P. J. Temperature Dependence of the Photoluminescence of InP/ZnS Quantum Dots. *J. Phys. Chem. C* **2008**, *112*, 6775–6780.
- (54) Narayanaswamy, A.; Feiner, L. F.; Meijerink, A.; Van Der Zaag, P. J. The Effect of Temperature and Dot Size on the Spectral Properties of Colloidal InP/ZnS Core-Shell Quantum Dots. *ACS Nano* **2009**, *3*, 2539–2546.
- (55) Ramasamy, P.; Kim, N.; Kang, Y. S.; Ramirez, O.; Lee, J. S. Tunable, Bright, and Narrow-Band Luminescence from Colloidal Indium Phosphide Quantum Dots. *Chem. Mater.* **2017**, *29*, 6893–6899.
- (56) Mičić, O. I.; Cheong, H. M.; Fu, H.; Zunger, A.; Sprague, J. R.; Mascarenhas, A.; Nozik, A. J. Size-Dependent Spectroscopy of InP Quantum Dots. *J. Phys. Chem. B* **1997**, *101*, 4904–4912.

- (57) Yu, W. W.; Qu, L.; Guo, W.; Peng, X. Experimental Determination of the Extinction Coefficient of CdTe, CdSe, and CdS Nanocrystals. *Chem. Mater.* **2003**, *125*, 2854–2860.
- (58) Kashyap, V.; Kumar, C.; Chaudhary, N.; Goyal, N.; Saxena, K. The Correlation of Resistivity with the Crystal Size Present in Silicon Nanowires through Confinement Based Models. *Mater. Lett.* **2021**, *301*, 130312.
- (59) Yu, P.; Beard, M. C.; Ellingson, R. J.; Fernere, S.; Curtis, C.; Drexler, J.; Luiszer, F.; Nozik, A. J. Absorption Cross-Section and Related Optical Properties of Colloidal InAs Quantum Dots. *J. Phys. Chem. B* **2005**, *109*, 7084–7087.
- (60) Peng, X.; Wickham, J.; Alivisatos, A. P. Kinetics of II-VI and III-V Colloidal Semiconductor Nanocrystal Growth: “Focusing” of Size Distributions. *J. Am. Chem. Soc.* **1998**, *120*, 5343–5344.
- (61) Yu, W. W.; Falkner, J. C.; Yavuz, C. T.; Colvin, V. L. Synthesis of Monodisperse Iron Oxide Nanocrystals by Thermal Decomposition of Iron Carboxylate Salts. *Chem. Commun.* **2004**, 2306–2307.
- (62) Meledandri, C. J.; Stolarczyk, J. K.; Ghosh, S.; Brougham, D. F. Nonaqueous Magnetic Nanoparticle Suspensions with Controlled Particle Size and Nuclear Magnetic Resonance Properties. *Langmuir* **2008**, *24*, 14159–14165.
- (63) Demortière, A.; Panissod, P.; Pichon, B. P.; Pourroy, G.; Guillon, D.; Donnio, B.; Bégin-Colin, S. Size-Dependent Properties of Magnetic Iron Oxide Nanocrystals. *Nanoscale* **2011**, *3*, 225–232.
- (64) Baaziz, W.; Pichon, B. P.; Fleutot, S.; Liu, Y.; Lefevre, C.; Greneche, J. M.; Toumi, M.; Mhiri, T.; Bégin-Colin, S. Magnetic Iron Oxide Nanoparticles:

- Reproducible Tuning of the Size and Nanosized-Dependent Composition, Defects, and Spin Canting. *J. Phys. Chem. C* **2014**, *118*, 3795–3810.
- (65) Sharifi Dehsari, H.; Halda Ribeiro, A.; Ersöz, B.; Tremel, W.; Jakob, G.; Asadi, K. Effect of Precursor Concentration on Size Evolution of Iron Oxide Nanoparticles. *CrystEngComm* **2017**, *19*, 6694–6702.
- (66) Marqusee, J. A.; Ross, J. Theory of Ostwald Ripening: Competitive Growth and Its Dependence on Volume Fraction. *J. Chem. Phys.* **1984**, *80*, 536–543.
- (67) Marqusee, J. A.; Ross, J. Kinetics of Phase Transitions: Theory of Ostwald Ripening. *J. Chem. Phys.* **1983**, *79*, 373–378.
- (68) Narayanaswamy, A.; Xu, H.; Pradhan, N.; Kim, M.; Peng, X. Formation of Nearly Monodisperse In₂O₃ Nanodots and Oriented-Attached Nanoflowers: Hydrolysis and Alcoholysis vs Pyrolysis. *J. Am. Chem. Soc.* **2006**, *128*, 10310–10319.
- (69) Sugimoto, T. Preparation of Monodispersed Colloidal Particles. *Adv. Colloid Interface Sci.* **1987**, *28*, 65–108.
- (70) Clark, M. D.; Kumar, S. K.; Owen, J. S.; Chan, E. M. Focusing Nanocrystal Size Distributions via Production Control. *Nano Lett.* **2011**, *11*, 1976–1980.
- (71) Yu, W. W.; Wang, Y. A.; Peng, X. Formation and Stability of Size-, Shape-, and Structure-Controlled CdTe Nanocrystals: Ligand Effects on Monomers and Nanocrystals. *Chem. Mater.* **2003**, *15*, 4300–4308.
- (72) Elimelech, O.; Aviv, O.; Oded, M.; Banin, U. A Tale of Tails: Thermodynamics of CdSe Nanocrystal Surface Ligand Exchange. *Nano Lett.* **2020**, *20*, 6396–

6403.

- (73) Calvin, J. J.; Brewer, A. S.; Alivisatos, A. P. The Role of Organic Ligand Shell Structures in Colloidal Nanocrystal Synthesis. *Nat. Synth.* **2022**, *1*, 127–137.
- (74) Aitken, E. J.; Bahl, M. K.; Bomben, K. D.; Gimzewski, J. K.; Nolan, G. S.; Thomas, T. D. Electron Spectroscopic Investigations of the Influence of Initial- and Final-State Effects on Electronegativity. *J. Am. Chem. Soc.* **1980**, *102*, 4873–4879.
- (75) Pauling, L. The Nature of the Chemical Bond. IV. The Energy of Single Bonds and the Relative Electronegativity of Atoms. *J. Am. Chem. Soc.* **1932**, *54*, 3570–3582.
- (76) Sanderson, R. T. Electronegativity and Bond Energy. *J. Am. Chem.* **1983**, *105*, 2259–2261.
- (77) Gary, D. C.; Flowers, S. E.; Kaminsky, W.; Petrone, A.; Li, X.; Cossairt, B. M. Single-Crystal and Electronic Structure of a 1.3 nm Indium Phosphide Nanocluster. *J. Am. Chem. Soc.* **2016**, *138*, 1510–1513.
- (78) Churakov, A. V.; Vinokurov, A. A.; Znamekov, K. O.; Mordvinova, N. E.; Gippius, A. A.; Zhurenko, S. V.; Baenitz, M.; Istomin, S. Y. In(CH₃COO)₃: The First Example of Group 13 Elements Triacetate with an Infinite Chain Crystal Structure. *Polyhedron* **2019**, *160*, 42–45.
- (79) Gaussian 09, Revision A.02, M. J. Frisch, G. W. Trucks, H. B. Schlegel, G. E. Scuseria, M. A. Robb, J. R. Cheeseman, G. Scalmani, V. Barone, G. A. Petersson, H. Nakatsuji, X. Li, M. Caricato, A. Marenich, J. Bloino, B. G. Janesko, R. Gomperts, B. Mennucci, H. P. Hratchian, J. V. Ortiz, A. F. Izmaylov,

J. L. Sonnenberg, D. Williams-Young, F. Ding, F. Lipparini, F. Egidi, J. Goings, B. Peng, A. Petrone, T. Henderson, D. Ranasinghe, V. G. Zakrzewski, J. Gao, N. Rega, G. Zheng, W. Liang, M. Hada, M. Ehara, K. Toyota, R. Fukuda, J. Hasegawa, M. Ishida, T. Nakajima, Y. Honda, O. Kitao, H. Nakai, T. Vreven, K. Throssell, J. A. Montgomery, Jr., J. E. Peralta, F. Ogliaro, M. Bearpark, J. J. Heyd, E. Brothers, K. N. Kudin, V. N. Staroverov, T. Keith, R. Kobayashi, J. Normand, K. Raghavachari, A. Rendell, J. C. Burant, S. S. Iyengar, J. Tomasi, M. Cossi, J. M. Millam, M. Klene, C. Adamo, R. Cammi, J. W. Ochterski, R. L. Martin, K. Morokuma, O. Farkas, J. B. Foresman, and D. J. Fox, Gaussian, Inc., Wallingford CT, 2016.

Chapter IV

*Effect of intermediate clusters on
size*

4.1. Introduction.

Recent observations of clusters at the very early stages of the reaction have led several research groups to question the correctness of classical single nucleation events i.e., the assembly of monomers directly from the solution in III-V NCs formation.¹⁻³ Cossairt *et al.* have proposed two-step nucleation involving MSCs, where the first nucleation is the formation of clusters followed by a second nucleation event where accretion or dissolution of clusters contributes to NCs nucleation and growth. The clusters containing a well-defined number of atoms with high thermodynamic stability are known MSCs.⁴⁻¹² They exhibit a very narrow size distribution accounting for them undergoing a quantised growth (heterogenous growth) as opposed to continuous growth (homogenous growth) with preference to a specific size in ultrasmall or larger NCs.^{2,13-15} Cossairt *et al.* have recently isolated, purified and characterized the InP magic-sized pre-nucleation clusters.¹⁶ These clusters are important intermediate and our understanding of these intermediate clusters has held the key to improving the size-tunability and size distribution in III-V NCs.^{4,17}

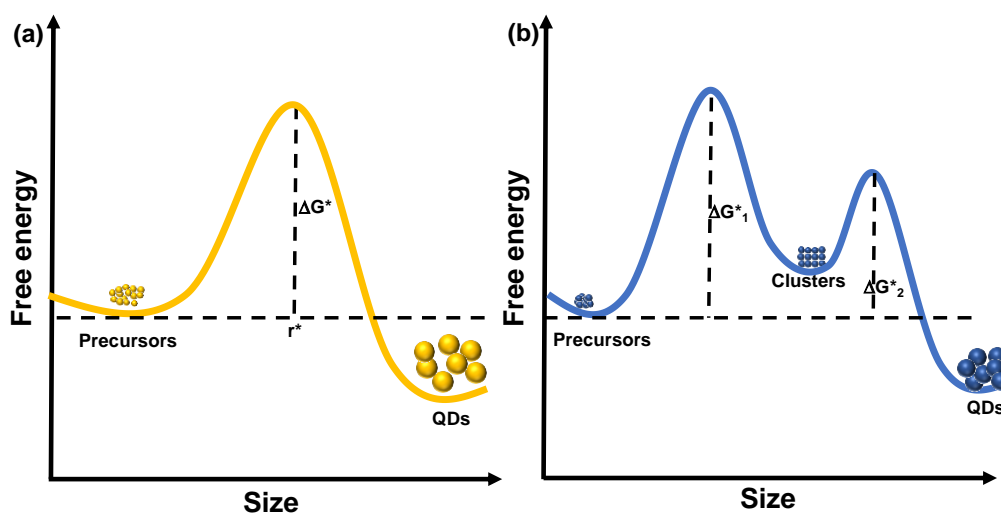


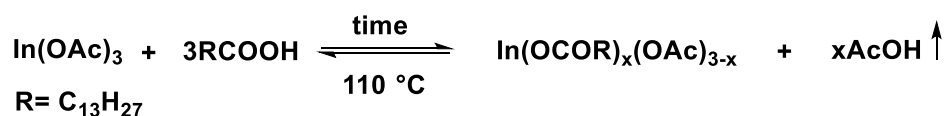
Figure 4.1. Graphical representation of (a) classical and (b) non-classical nucleation models.

Classical nucleation and growth theory have been remarkably successful in predicting the size evolution in II-VI and IV-VI NCs. However, the approach has failed to achieve the same degree of size and size distribution control with III-V semiconductor NCs. The intermediate clusters appear to be involved in rate-determining steps of the crystallization.^{3,18}

With this vital consideration, the chapter examines the reactivity and stability of the intermediate clusters and their correlation with the size evolution of the NCs. MSCs have been prepared/isolated under different conditions and used as the direct single-source precursor for NC growth.

4.2. Preparation and isolation of intermediate clusters.

Before synthesizing and studying intermediate clusters, we prepared indium carboxylate precursors using the vacuum method (*cf.* Chapter II, section 2.1.5 and 2.2), which is a widely employed technique in III-V QDs synthesis. Typically¹⁹⁻²¹ indium acetate was mixed with myristic acid in 1-ODE and vacuumed at 110 °C until a clear solution was observed. The substitution of acetate with myristate is thermodynamically driven by the vaporization of acetic acid under vacuum (Le Chatelier's principle).^{22,23}



Clearly, the extent of substitution and composition of the product depends on strength of the vacuum, time and temperature. It is presumed in the literature that the vacuum method forms pure In(OOCC₁₇H₂₇)₃ *in situ*¹⁹⁻²¹ which is not true as we have seen in chapter II. Depending on the vacuum time, the product is either In(OOCC₁₇H₂₇)₂(OAc) or related mixed carboxylate complex instead of assumed In(OOCC₁₇H₂₇)₃. For the

synthesis of MSCs, we synthesized indium-myristate complex (In-My) at three different vacuum times *viz.*, 1 h (designated as In-My1), 6 h (In-My2) and 12 h (In-My3). These precursors were then subsequently employed to synthesize MSCs following the known literature procedure.^{2,16,24,25} The MSCs are typically designated with their absorption characteristics or the number of atoms.¹⁵ Henceforth, we identify MSCs prepared using In-My2 and In-My3 as 386-InP MSCs2 and 386-InP MSCs3 respectively. According to the literature, MSCs absorbing at 386 nm are expected to contain 37 indium atoms and 20 phosphorus and 51 carboxylates.¹⁶

The method for preparing MSCs was initially developed by Peng *et al.*²⁶ and progressively standardized by other groups.^{9,27-31} However, in the existing pool of literature reports^{2,3,16,25,32,33} there is no consensus on the reaction time for InP MSCs. We found that 30 minutes is the optimum reaction time for the preparation of 386-InP MSCs (Figure 4.2). Figure 4.2b shows the temporal evolution MSCs of InP from 30 s to 1 h of reaction time. As the reaction time increased from 30 s to 1 h, the absorption peak gradually becomes narrower up to 30 minutes. However, as the time increases above 30 min (1800 s) the peak gradually broadens. Figure 4.2c shows the change in the width of the absorption peak as the reaction time progresses.

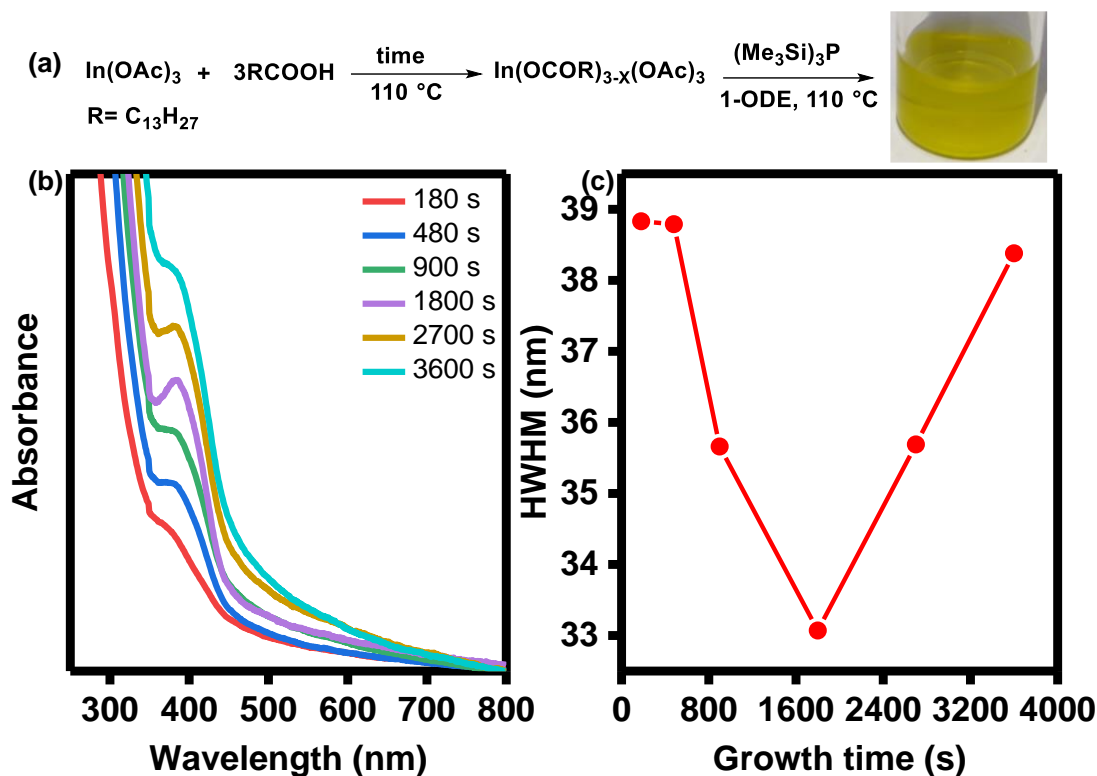


Figure 4.2. (a) Preparation of MSCs of InP. The picture in the scheme is the colloidal dispersion of MSCs in hexane. (b) Temporal evolution of MSCs of InP studied through UV-Visible absorption spectroscopy by collecting aliquots at respective time intervals. (c) A graphical representation of the evolution of HWHM with growth time.

Partially substituted In-My1 did not form MSCs (Annexure A4), while In-My2 and In-My3 formed stable MSCs with distinct absorption at 386 nm (Figure 4.3a and 4.3b respectively). This result exemplified the importance of the purity and composition of the indium precursor for forming InP MSCs. MSCs are characterized by typical absorption features in the UV region. This absorption feature marks its high thermodynamic stability and unique size. In our case, both In-My2 and In-My3 formed MSCs exhibiting a distinct absorption feature at 386 nm. The carbonyl asymmetric and symmetric stretching for indium-bound carboxylates in MSCs were observed at 1645 and 1463 cm^{-1} in FTIR spectroscopy (figure 4.3c) suggesting the presence of ligands on the surface of MSCs.³⁴ The PXRD studies illustrate the amorphous nature of as-

synthesized MSCs (figure 4.3d). Typically, the crystal structure of MSCs does not match with the zinc blende phase of bulk InP.^{24,35}

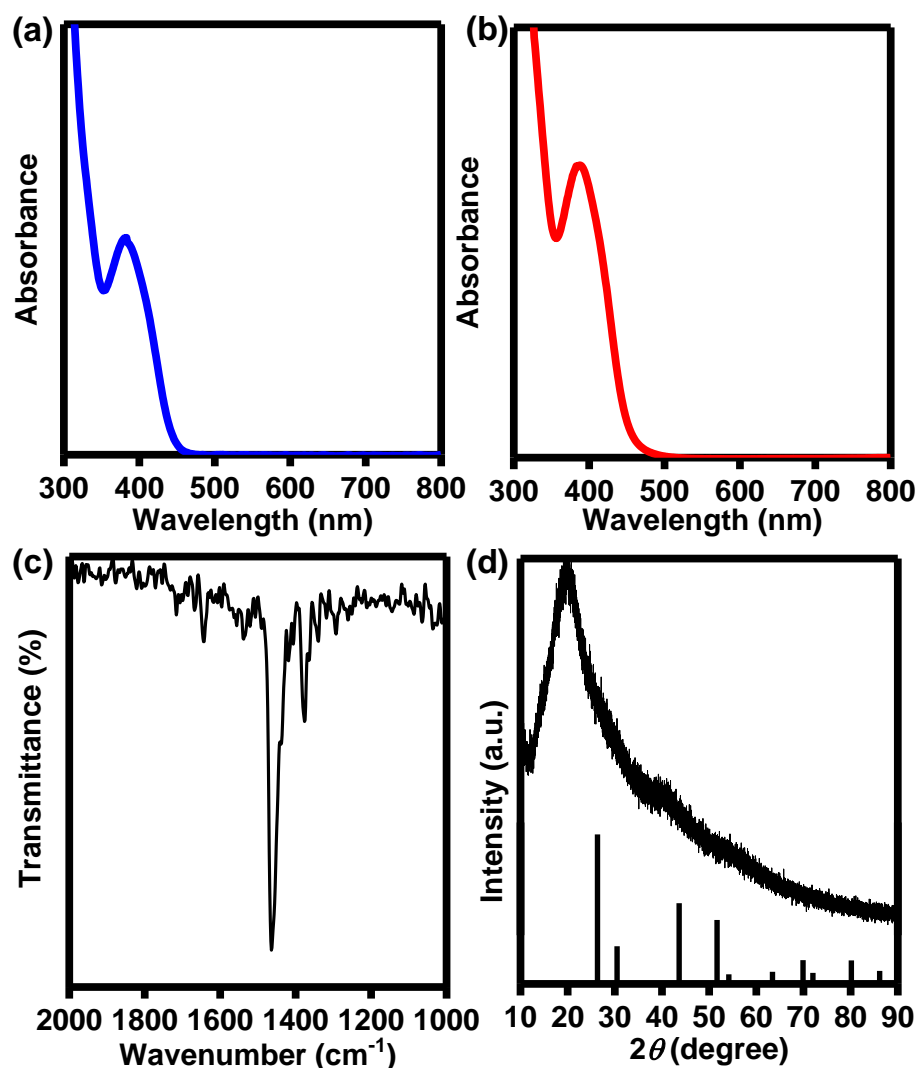


Figure 4.3. (a) The absorption spectrum of 386-InP MSCs2. (b) Absorption spectrum of 386-InP MSCs3. (c) FTIR spectra of 386-InP MSCs indicating the symmetric and asymmetric stretching of carbonyl bonds of indium bound myristate groups. (d) PXRD of as-synthesized MSCs (red) compared with standard zinc blende structure of bulk InP (PDF number: 96-101-0147, black).

4.3. MSCs as a single source to InP QDs synthesis.

MSCs have been isolated and employed as single-source precursors for various QDs.^{2,17,36-41} The formation of MSCs before the formation of NCs *in situ* is the

foundation of their potential use as a single-source precursor in the synthesis of various QDs in colloidal form.^{15,25,42,43} We carried out the preparation of InP QDs from 386-InP MSCs in accordance with the scheme represented in figure 4.4a employing the hot-injection method. QDs prepared from 386-InP MSCs2 and 386-InP MSCs3 are designated as QD2 and QD3 respectively. QD2 displays a first excitonic peak at 615 nm (figure 4.4b) while QD3 shows absorption maxima at 620 nm (figure 4.4c). The difference in excitonic peak position suggests that the size of the InP QDs prepared from 386-InP MSCs2 and 386-InP MSCs3 are comparatively different. The higher asymmetry in the absorption peak observed for QD2 indicates its broader size distribution compared to QD3 (figure 4.4d). The PXRD of both QD2 and QD3 are consistent with the zinc blende phase of bulk InP (figure 4.4e). The TEM image (figure 4.4f and g) confirmed that QD2 is slightly polydisperse (Average size $\sim 3.92 \pm 0.91$ nm) compared to QD3 (4.7 ± 0.44 nm).

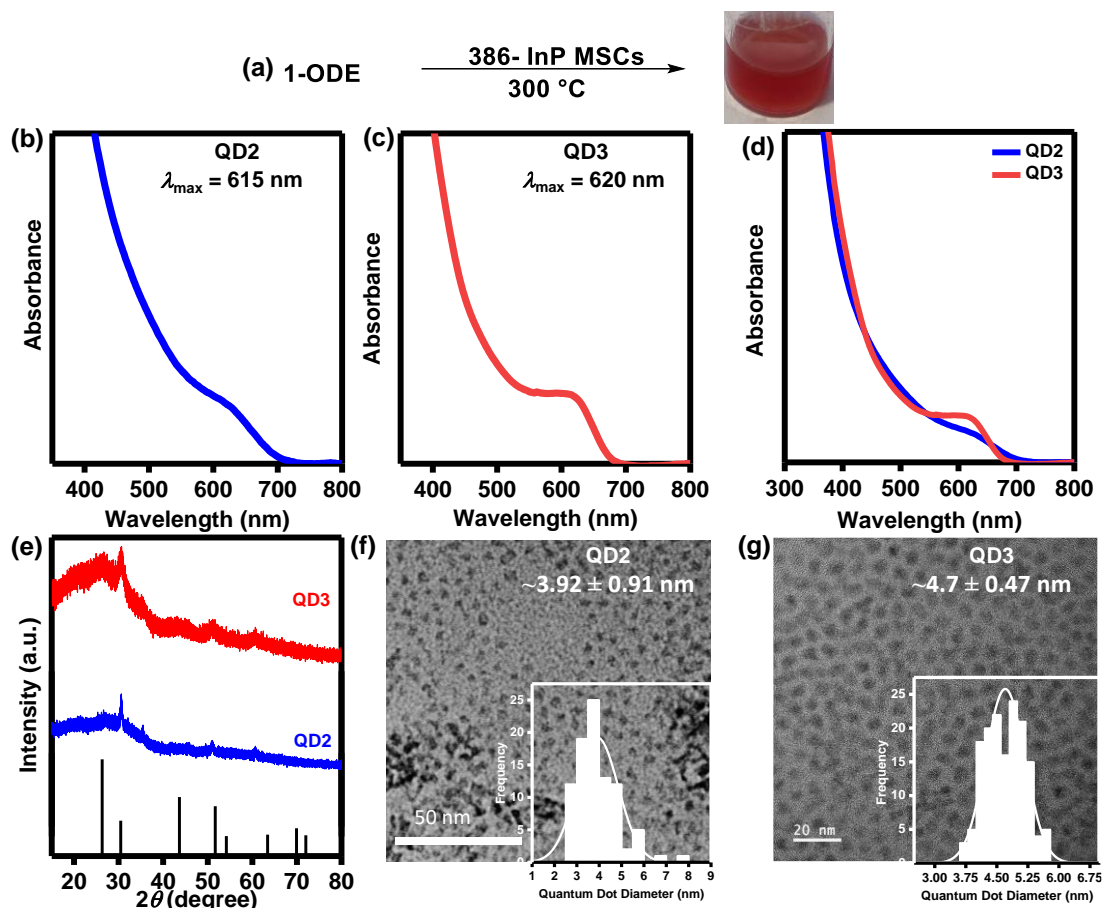


Figure 4.4. (a) Scheme for the synthesis of InP QDs from 386-InP MSCs. The picture in the scheme is a colloidal dispersion of QDs in hexane. (b). The UV-Visible absorption spectrum of QD2. (c) The UV-Visible absorption spectrum QD3. (d) A comparative representation of the absorption spectrum of QD2 and QD3. (e) PXRD of as-synthesized QD2 (blue) and QD3 (red) compared with standard zinc blende structure of bulk InP (PDF number: 96-101-0147, black) (f) TEM image QD2 indicating a size of $\sim 3.92 \pm 0.91$ nm (Inset: size distribution graph). (g) TEM image QD3 indicates a size of $\sim 4.7 \pm 0.47$ nm (Inset: size distribution graph).

All the parameters for conversion of MSCs to QDs (For In-My2 and In-My3) were the same, yet we observe the difference in size and size distribution. In fact, with precursor In-My1 no MSCs formation was detected. This led us to investigate the compositional purity of In-My1, In-My2 and In-My3 precursors in further detail.

4.3.1. In-My1, In-My2 and In-My3 precursors.

In order to study their compositional purity, the precursors were isolated from the reaction mixture and precipitated in acetone. FTIR is a useful spectroscopic tool to detect the difference in chemical structure or the presence of impurities.^{34,44-48} Figure 4.5a shows the FTIR spectra of In-My1, In-My2 and In-My3. As expected in In-My1 the substitution of acetate with the myristate group is incomplete (figure 4.5b). The FTIR of In-My1 shows unreacted myristic acid carbonyl stretching at 1712 cm^{-1} . Furthermore, we compared the FTIR spectra of In-My2 (reaction time: 6 h) with In-My3 (reaction time: 12 h) precursors. The formation of indium myristate in both cases is confirmed by the presence of a peak at 1555 cm^{-1} which is attributed to the carbonyl group of myristate bound to a metal ion. However, closer inspection revealed the presence of a peak at 1712 cm^{-1} which corresponds to the carbonyl stretching frequency of free myristic acid. The intensity of the peak was prominent in the case of In-My2 indicating the substantial presence of free acid. Comparatively, in In-My3 the peak is less intense. These results confirmed the incomplete substitution of acetate by myristic acid when the degassing time is low i.e., 1 h (In-My1), and the substantial presence of unreacted free myristic acid even when the degassing time was 6 h (In-My2). Only when the mixture was degassed for 12 h, the substitution is near completion with only a trace amount of unreacted free myristic acid. The presence of free acid in In-My2 explains the polydispersity in QD2. Similarly, complexes In-My1, In-My2 and In-My3 were subjected to TGA to detect any compositional variance between them (figure 4.5b, 4.5c and 4.5d respectively). The weight loss of $\sim 1.5\%$ for the In-My2 complex at a temperature range of $85\text{-}130\text{ }^{\circ}\text{C}$ is accounted for by the constituent impurities (free acid and acetic acid).

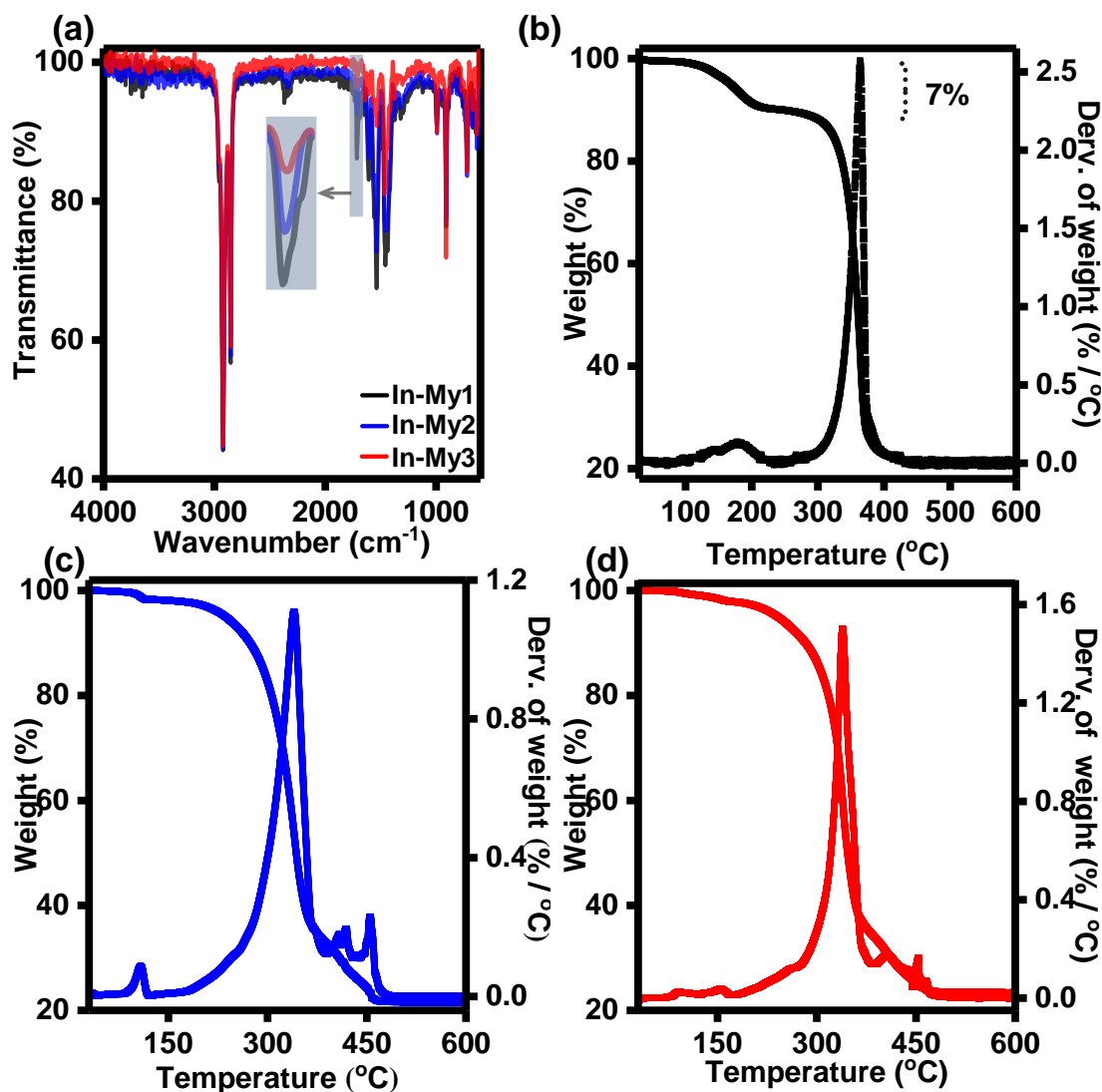


Figure 4.5. (a) FTIR spectra of indium precursors In-My1 (black), In-My2 (blue) and In-My3 (red). (b) TGA thermogram of In-My1 precursor depicting the weight loss of ~7% at temperature 130-200 °C for one acetate group. (c) TGA thermogram of In-My2 precursor depicting the weight loss of ~1.5% at temperature 85-130 °C and ~78% at a temperature range of 180- 510 °C. (d) TGA thermogram of In-My3 precursor showing a weight loss of ~78% at a temperature range of 180- 510 °C.

We performed Differential Scanning Calorimetry (DSC) analysis of In-My2 and In-My3 (figure 4.6a). The results observed for the melting point temperature range of In-My2 and In-My3 are presented in the inset of figure 4.6a. The expansion of the temperature range during melting indicates a widening of the peaks in In-My2 (160.6 – 177.7 °C) compared to 169.8 – 175.5 °C in In-My3. The broadening of melting

temperature peaks for In-My2 in DSC is attributed to the presence of constituents impurity.⁴⁹⁻⁵¹

Furthermore, when we carried out a solubility test (using DMF as solvent) on both of the precursors, we obtained a small amount of undissolved part in precursor In-My2, which was absent in In-My3. A powder X-ray diffractogram of the undissolved part (figure 4.6b, blue) hydroxides of indium.⁵² When degassing time is low the reaction mixture thus contains unreacted acid and some other impurities.

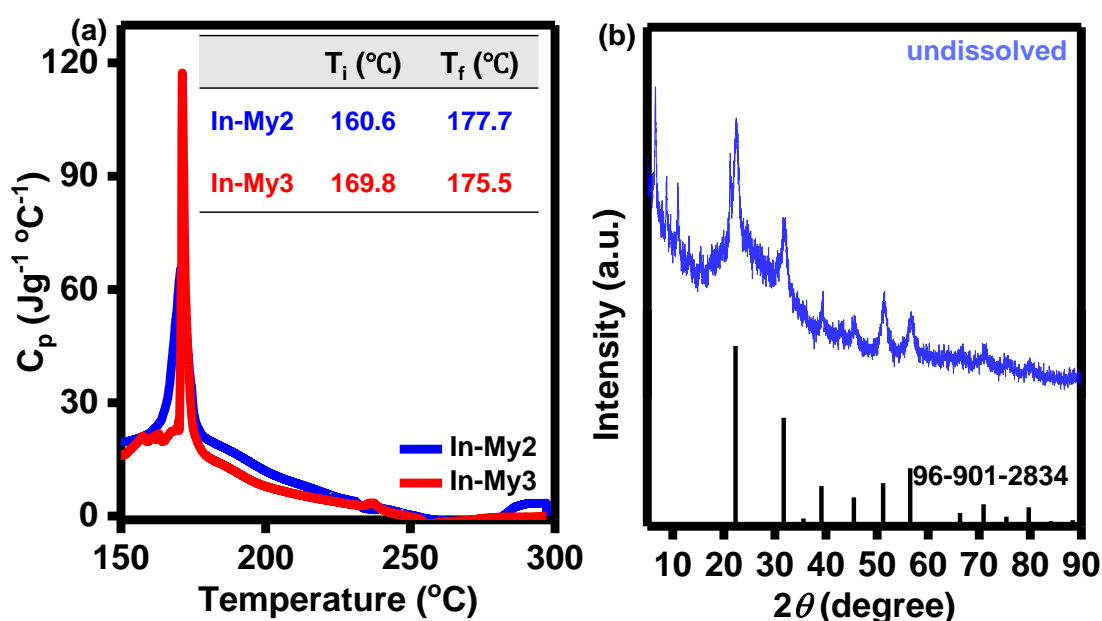


Figure 4.6 (a) DSC plot of indium precursors In-My2 (blue) and In-My3 (red). Inset: melting point analysis where T_i is the initial temperature and T_f is the final temperature. (b) PXRD of undissolved part of In-My2 (blue) indexed with a standard file of indium hydroxide (PDF no.: 96-901-2825, black).

4.3.2. Mechanism of conversion of MSCs to QDs.

In general, the formation of NCs from MSCs occurs through either of the two pathways: (i) aggregation and (ii) dissolution.^{9,15,25,53-55} The aggregation mechanism of conversion of MSCs to NCs involves the coalescence of small clusters into larger ones which eventually form crystalline structures.⁵⁶⁻⁵⁸ Liu and co-workers studied the MSCs-

mediated formation of CdS NCs occurring through aggregation mechanism pathway. They detected the aggregation of MSCs to NCs through UV-Visible absorption spectroscopy where multiple absorption peaks were observed during conversion.³⁰ The dissolution mechanism of conversion of MSCs to NCs involves the dissolution of initial clusters followed by the formation of new NCs. This process can be initiated by a change in temperature, the concentration of reactants, or pH. When initial clusters dissolve, the atoms or molecules that make up the clusters become available for new crystal growth.⁵⁹⁻⁶² Kelly *et al.* reported the dissolution mechanism for the formation of CdSe nanorods through MSCs by studying the decrease of the peak of MSCs and the growth of the nanorod's peak through UV-Visible absorption spectroscopy.⁹ We observed a similar result in our study. Figure 4.7a shows a temporal evolution of the conversion of 386-InP MSCs to InP QDs monitored through UV-Visible absorption spectroscopy. The peak of MSCs at 386 nm gradually decreases over time as the absorption maxima at 620 nm increases simultaneously, and there is no other absorption peak detected during the reaction, indicating a dissolution mechanism. Furthermore, a quantitative representation of the time-dependent depletion of the MSC peak at 386 nm and evolution of the QDs peak at 620 nm is represented in figure 4.7b. The difference in absorbance of peak and underlying baseline indicates the steady dissolution of MSCs (temporal decrease of absorbance at 386 nm) and progressive growth of QDs (temporal increase in absorbance at 620 nm).

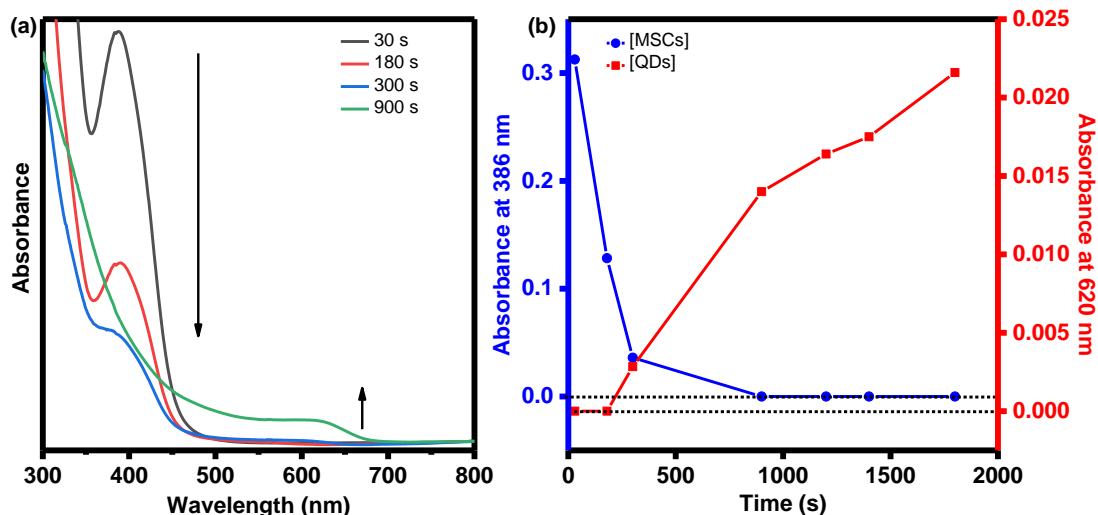


Figure 4.7. (a) Temporal evolution of conversion of 386-InP MSCs to InP QDs. The absorption maxima of MSCs decrease concurrently with the increase in absorption peak of QDs whilst no other peaks are detected. (b) A graphical representation of change in absorbance at 386 nm (blue) and 620 nm (red) subtracting the underlying baseline. The black dotted line indicates the range of zero values for respective absorbances.

It may be noted that MSCs and QDs discussed in the section are all prepared using indium myristate complex formed *in situ* by vacuum method. Our results show that they are not perfectly pure. In the next section, we attempted to synthesise MSCs and QDs using pure $\text{In}(\text{My})_3$ prepared from the method discussed in Chapter II.

4.4. MSCs and QDs from pure $\text{In}(\text{My})_3$.

It is noteworthy that $\text{In}(\text{My})_3$ exhibited only partial solubility in 1-ODE at 110 °C. On the other hand, In-My_2 and In-My_3 formed transparent solutions in ODE at the same temperature. Even though FTIR and TGA results confirmed the formation of indium-myristate bonds in all cases, the exact structures of In-My_2 and In-My_3 remain unclear. Solubility tests indicate that In-My_2 and In-My_3 are structurally or compositionally distinct from pure $\text{In}(\text{My})_3$. The FTIR and TGA data (as shown in Figure 4.5) reveal the presence of additional species in In-My_2 and In-My_3 , such as free acid and indium hydroxide. In contrast, $\text{In}(\text{My})_3$ is a pure compound consisting of three myristate groups

and one indium atom per molecule (confirmed with NMR and TGA), and is free from any impurities of free acid (confirmed with FTIR and TGA).

The pure $\text{In}(\text{My})_3$ dissolved in 1-ODE at a much higher temperature (165-170 °C). This temperature is much higher than required for stabilizing MSCs (<150 °C), therefore it was not possible to prepare 386-InP MSCs with pure $\text{In}(\text{My})_3$. Higher temperatures (>150 °C) favour the direct formation of QDs over the growth of small clusters.^{2,3} As expected, at a temperature of 170 °C when phosphorus precursor (PTMS) is injected ultra-small InP QDs were formed directly. The QDs exhibited a distinct absorption feature at 502 nm. From TEM data, the size of the QDs was calculated to be $\sim 2.8 \pm 0.44$ nm.

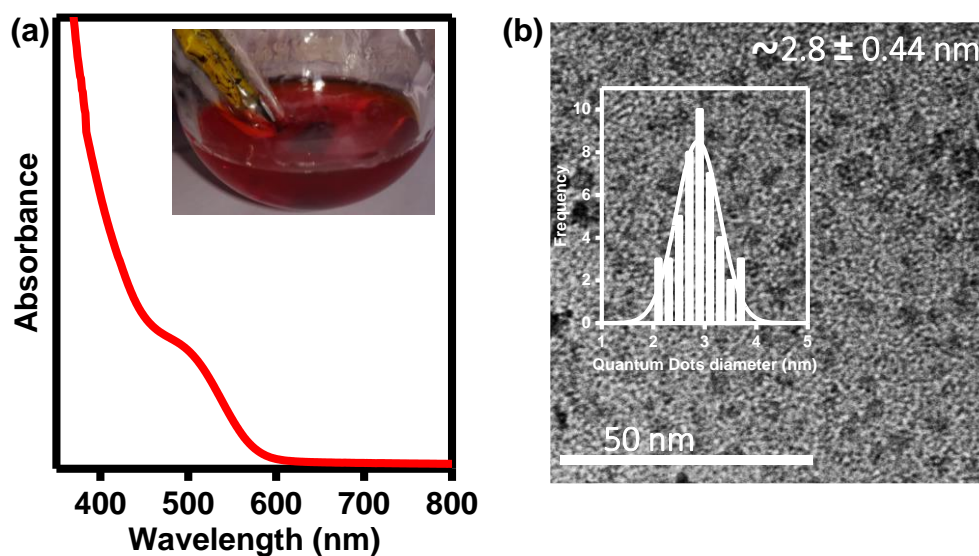


Figure 4.8. (a) The UV-Visible absorption spectrum of QDs prepared from pure indium myristate complex at an injection temperature of 170 °C. Inset: The reaction mixture at the end of growth time (30 min). (b) TEM image of as-synthesized InP QDs with a diameter of $\sim 2.8 \pm 0.44$ nm (Inset: size distribution graph).

4.5. Effect of carbon chain length on MSCs and QDs

The length fatty acid group in the indium precursor is crucial for controlling nucleation and growth.⁶³⁻⁶⁵ We studied the effect of alkyl fatty acid chain length on InP MSCs and

InP QDs. Figure 4.9a shows the absorption spectra of MSCs obtained using indium laurate (C_{12} , LA), myristate (C_{14} , MA) and stearate (C_{18} , SA). All of these precursors form a stable MSC with a sharp absorption at ($\lambda_{\max} = 386$ nm) confirming the same number of constituent indium, phosphorous and carboxylate groups in the cluster. Nonetheless, when employed as a singular source precursor for the synthesis of InP QDs, they produced NCs of varying sizes (as shown in Figure 4.9b) as indicated by the location of their excitonic peaks (laurate, $\lambda_{\max} = 630$ nm; myristate, $\lambda_{\max} = 620$ nm; and stearate, $\lambda_{\max} = 586$ nm). Furthermore, we determined the size distribution of InP QDs by measuring absorption half width at half maximum, HWHM (44 nm, 40 nm and 46 nm for laurate, myristate and stearate respectively). In other words, longer fatty acids resulted in smaller QDs. The size distribution was optimum when myristate was employed as an indium precursor.

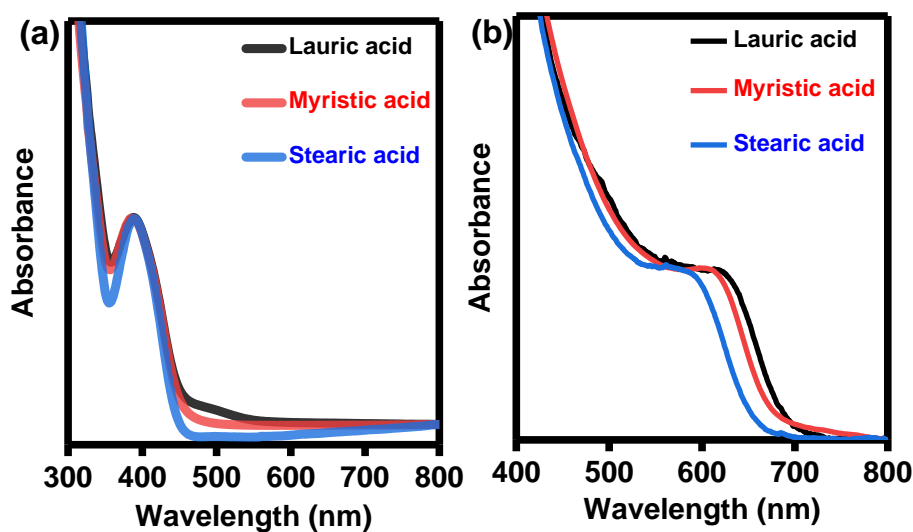


Figure 4.9. (a) A comparable representation of the absorption spectrum of InP MSCs prepared by using different capping ligands. (b) The UV-Visible absorption spectra of InP QDs prepared from InP MSCs capped with fatty acid ligands of different chain lengths.

These results reveal that although similarly constituted 386-InP MSCs are formed even when different fatty acids are used, their stability and reactivity are different from each

other due to the chain length. The longer the chain length, the less stable the MSCs as reflected in size variation. This observation is also confirmed by the thermal stability test of MSCs (Figure 4.10). MSCs prepared with longer chain stearate completely decompose within 150 °C compared to those with myristates. Furthermore, intermediate chained ligand i.e., myristate formed highly monodisperse QDs. This shows that the optimum stability of MSCs is important for balancing the rate of nucleation and growth and achieving monodispersity.^{4,19}

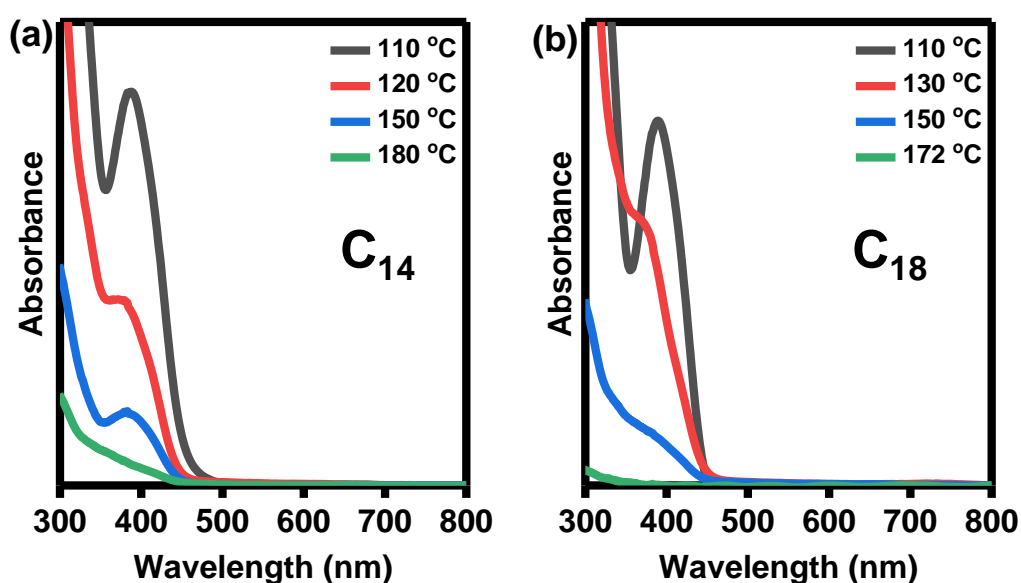


Figure 4.10. A study of thermal stability (a) 386-InP MSCs (C₁₄). (b) 386-InP MSCs (C₁₈) was obtained by tuning the chain length of capping ligands through absorption spectroscopy by collected aliquots at different temperature intervals.

4.6. Effect of additives on MSCs and QDs synthesis.

The effect of additives on the properties of NCs is significant.⁴ There are reports of additives influencing the dynamics of NCs as well as the properties of intermediate clusters.^{66–69} In this section, we discuss a study conducted on the effect of additives (specifically amines and phosphines) on MSCs and QDs.

4.6.1. Effect of primary amine

The effect of primary alkylamine on InP QDs is widely studied.^{43,70–72} It is reported that using amine can drastically reduce the reaction temperature.⁴ We attempted to synthesise InP MSCs in the presence of amine at 110 °C but to no avail. We propose that oleylamine destabilizes the MSCs. This hypothesis also explains why QDs are formed at lower temperatures when the amine is present.

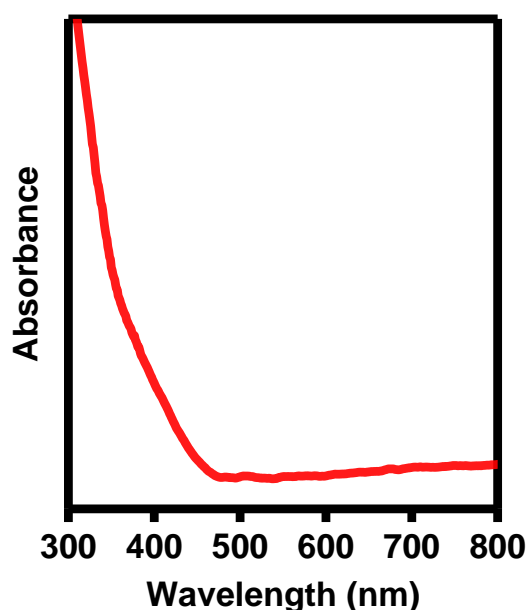


Figure 4.11. The UV-Visible absorption spectrum of MSCs prepared in presence of oleylamine as additives with no distinct excitonic peak.

4.6.2. Effect of phosphines

The phosphines are extensively used in CQDs synthesis both as stabilizing ligands and coordinating solvents.^{73–77} To understand the effect of phosphine additives on the synthesis of InP MSCs and its consequent conversion to InP QDs we added trioctylphosphine (TOP) during the preparation of MSCs. Figure 4.12a shows the board absorption peak around 386 nm. FTIR studies reveal that these clusters have TOP ligands instead of acid. The characteristic indium-carboxylate carbonyl stretching at

1537 cm^{-1} is absent. Instead, a distinct peak at 1463 cm^{-1} is observed which is due to the C-P bond stretching. Phosphines (L-type ligands) are known to be stronger coordinating ligands compared to fatty acids (X-type ligands).⁷⁸

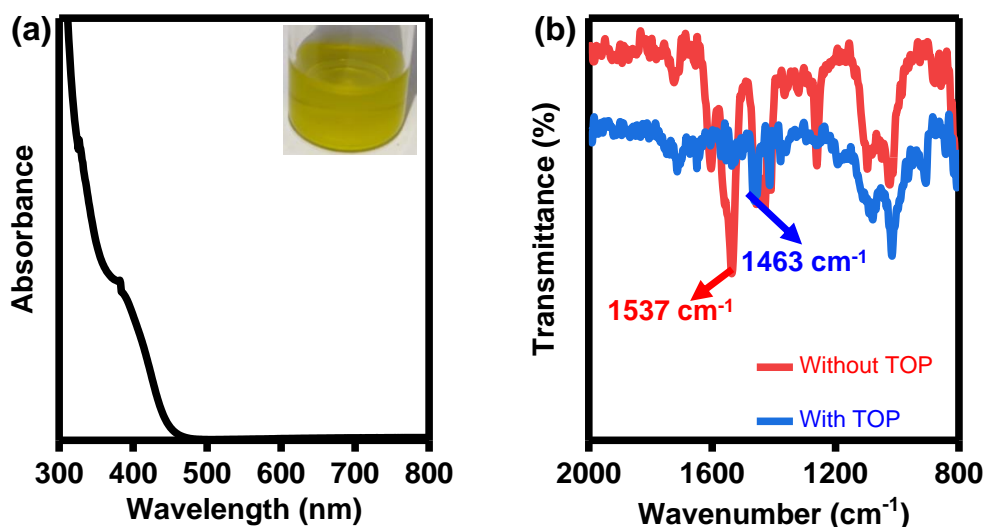


Figure 4.12. (a) The UV-Visible absorption spectrum of clusters prepared in presence of TOP as additive. (Inset: colloidal dispersion of cluster in hexane prepared in presence of TOP additive). (b) Comparative analysis of FTIR spectra of precursor used for preparing InP MSCs in absence of TOP (red) and in presence of TOP (blue).

These clusters were isolated and used as single source precursors for InP QDs synthesis. Compared with the typical carboxylate-terminated MSCs ($\lambda_{\text{max}} = 620\text{ nm}$), TOP-capped clusters formed smaller NCs ($\lambda_{\text{max}} = 586$ under the same condition. This result is attributed to the stronger coordinating nature of the phosphine group as a capping ligand.

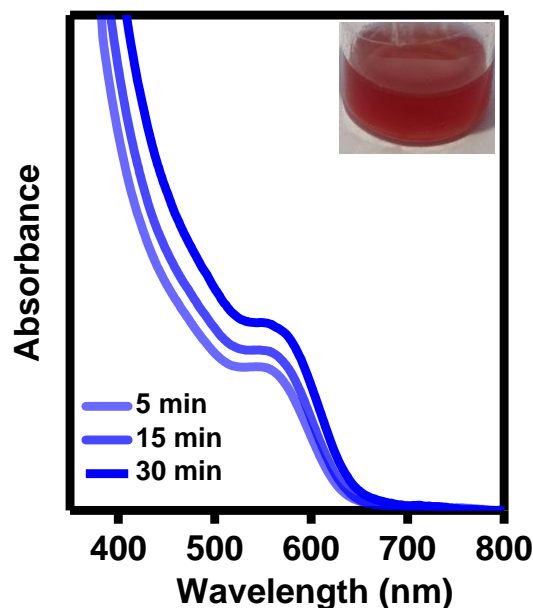


Figure 4.13. Temporal evolution of first excitonic peak of InP QDs prepared from an as-synthesized cluster. (Inset: colloidal dispersion of QDs in hexane prepared from former clusters).

4.7. Size-focusing growth of InP and InAs QDs.

One of the important traits of diffusion-controlled growth of NCs is its dependency on the size of the NCs as represented by the equation.^{79,80}

$$\frac{dr}{dt} = DV_m \left(\frac{1}{r} + \frac{1}{\delta} \right) (C_b - C_e) \quad (4.1)$$

Where r is the particle size, δ is the thickness of the diffusion layer, C_b is bulk concentration and C_e is the solubility of particles. If sufficient monomers are present, the smaller NCs grow at a faster rate compared to the larger ones. Consequently, smaller NCs catch up with larger particles to result in monodispersity. This is known as size-focusing growth.⁸¹ Size-focusing growth can take place only when the monomer concentration does not drop below the solubility limit in which case Oswald ripening takes place.⁸² In Oswald ripening larger sized NCs grow at the expense of smaller NCs due to solubility difference.⁸³ Therefore, maintaining higher monomer concentration

during the growth stage is a necessity for preparing QDs with narrow size distribution.^{80,81,83} This can be achieved through secondary injection of precursors during the growth stage as observed experimentally by Alivisatos and co-workers for CdSe and InAs CQDs.⁸¹ Tamang *et al.* have also injected pre-nucleation clusters instead of precursors to maintain the optimum concentration of the monomers during the growth phase.⁸⁴

In our case, we found a completely different result with InP and InAs NCs. InP and InAs MSCs were first prepared and isolated. These clusters were then injected continuously into a growing InP and InAs NCs solution at 300 °C. The absorption spectra of InAs QDs progressively became narrower as the clusters were continuously injected, demonstrating a successful size-focusing growth just as predicted by equation 4.1. (figure 4.14, black to green).

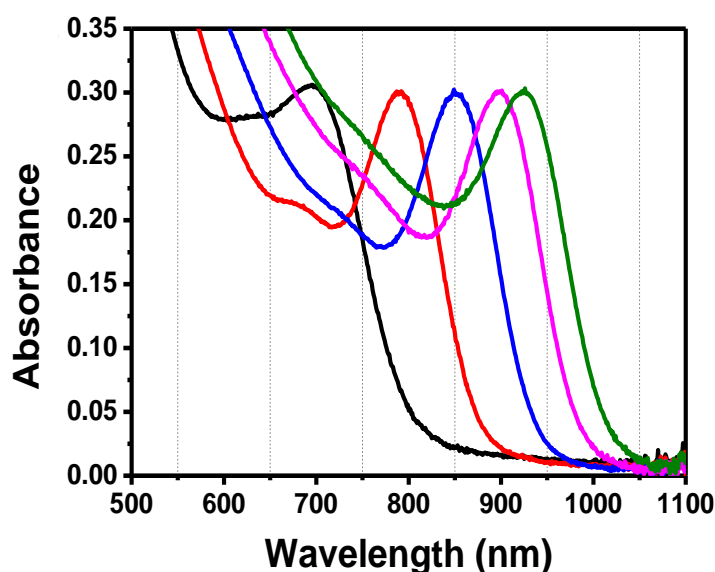


Figure 4.14. Absorption spectra of the evolution of size distribution in InAs QDs prepared by a continuous supply of InAs nanoclusters externally.

The TEM micrograph confirmed the (a) growth of the InAs NCs from 3.4 to 4.3 nm. (b) improvement of size distribution from 14.2% to 10.2% over time (figures 4.15a and

b). These observations strongly confirmed the diffusion-controlled growth mechanism in the formation of colloidal InAs NCs.

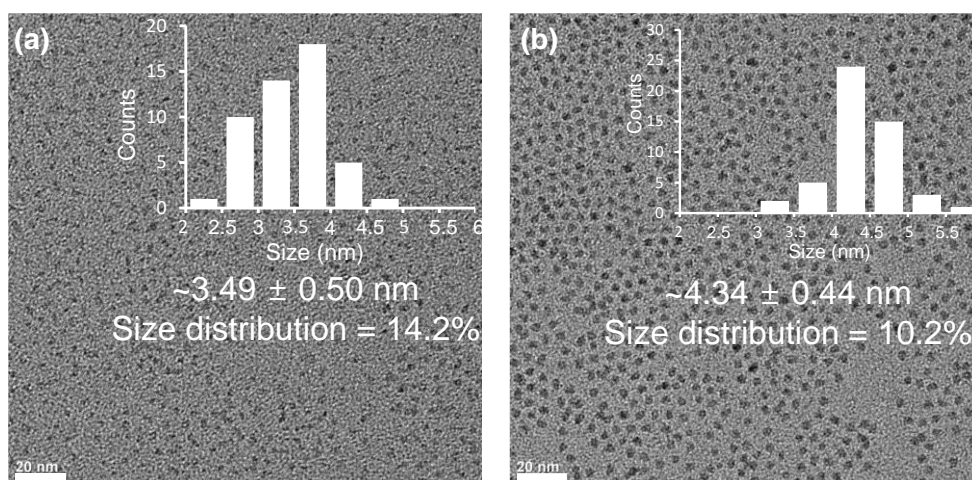


Figure 4.15. TEM image of InAs QDs (a) before cluster injection and (b) after cluster injection.

A similar study was performed on InP QDs. 386-InP MSCs were injected into InP NCs during the growth stage at 300 °C to maintain the optimum monomer concentration required for size-focussing growth. However, we observed the peak broadening in absorption spectroscopy with time and also a decrease in average size (figure 4.16).

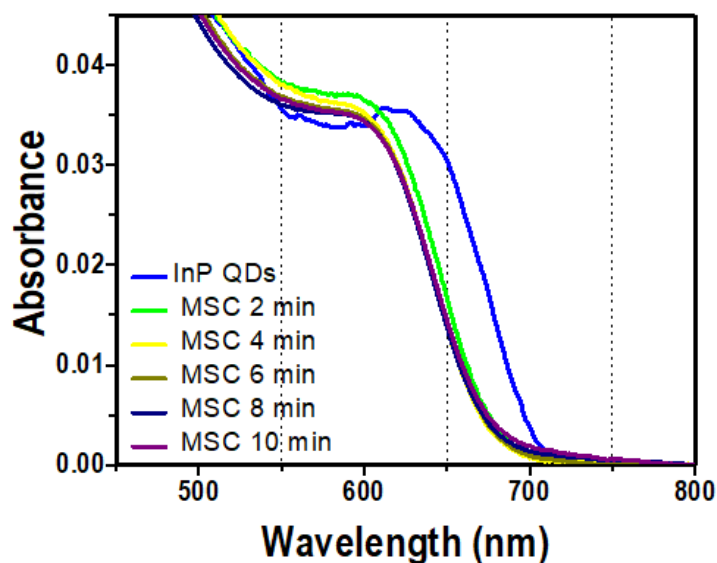


Figure 4.16. Absorption spectra of the evolution of size distribution in InP QDs prepared by a continuous supply of 386-InP MSCs externally.

The observation from absorption spectra was further confirmed by the TEM image of InP NCs before and after injection (figure 4.17a and b). The size distribution increased from 10% to 12.6%. These results reveal that InP NCs do not undergo growth under prevailing circumstances. We hypothesise that the InP NCs surface is more prone to oxidation at 300 °C impeding the growth. At the high-temperature formation of oxide on the surface is well known in InP NCs.^{43,71,85,86}

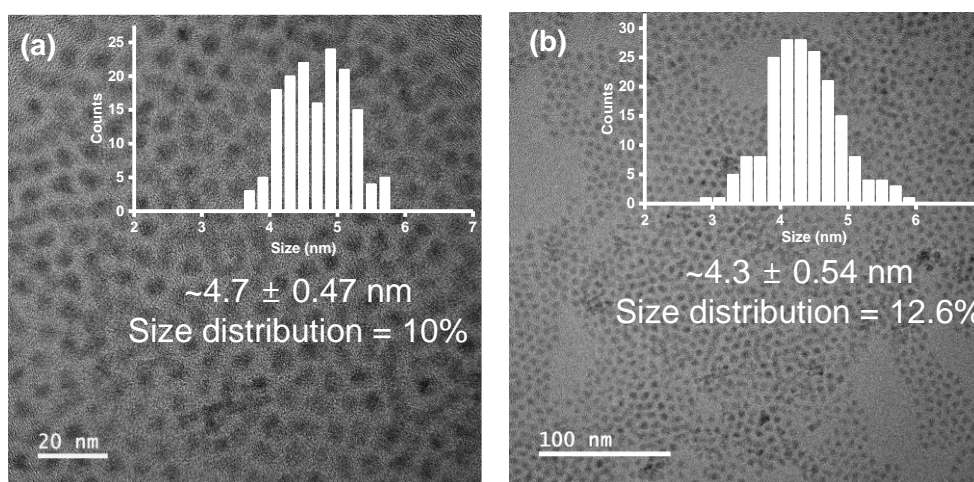


Figure 4.17. TEM image of InP QDs (a) before cluster injection and (b) after cluster injection.

4.8. Conclusion.

We investigated the formation of InP MSCs and their conversion into InP QDs. The reactivity of the precursor and additives such as amine and phosphine are crucial for the stability of MSCs and consequently the size distribution of the QDs. The di-substituted indium myristate did not form MSCs, unlike its tri-substituted analogue, indicating the strong role of surface myristate in stabilizing the MSCs. Furthermore, precursors containing longer chain carboxylates led to less stable MSCs. For instance, MSCs prepared from myristate (C₁₄) indium precursor were stable up to 150 °C, while MSCs prepared from stearate (C₁₈) were destroyed at the same temperature. The higher

stability of MSCs also influenced the size and size distribution of the QDs. More stable MSCs led to larger-sized NCs with improved size distribution.

The primary amine (oleylamine) exhibited a destabilizing effect on MSCs. In the case of TOP as a reaction additive, the TOP ligand was detected on the surface of MSCs instead of acid, which is due to the stronger coordination of the phosphine group (L-type) compared to acetates (X-type) to the surface of MSCs.

Finally, we monitored the growth of pre-synthesized InP QDs and InAs QDs with the continuous addition of MSCs. In InAs, size-focused growth leading to highly monodispersed QDs was observed, whereas InP QDs did not grow in size, indicating different surface chemistry of the two III-V QDs. These results clearly established the decisive role of group III precursor in the stability and reactivity of the intermediate cluster and subsequently on the final size and size distribution.

4.9. Experimental Section.

4.9.1. General information.

4.9.1.1. Materials and general consideration.

In(OAc)₃ (99.99%, trace metal basis), lauric acid (98%), oleylamine (technical grade), 1-ODE (technical grade), trioctylphosphine (97%), were all purchased from Sigma Aldrich, India. Stearic acid (90%) was purchased from Thomas Baker, India. Myristic acid was purchased from SRL.

4.9.1.2. Characterization method.

UV-Visible spectrophotometer: The UV-Visible absorption spectra were collected using Perkin Elmer (Model: LS 55) spectrophotometer (scan rate: 480 nm/s) and Agilent Technologies Cary 100 UV-vis.

Transmission electron microscopy (TEM): TEM images were taken in JEOL-JEM-F200 and Tecnai G2 20 S-TWIN electron microscope. Samples were prepared by drop-casting of nanocrystal solution in anhydrous toluene on a carbon-coated copper grid purchased from EMS, the grids were kept overnight in a vacuum desiccator. The analysis of average size was performed with ImageJ software.

Fourier Transform Infrared Spectroscopy (FTIR): FTIR spectra were obtained using Bruker ALPHA E, 200396. The solution-based FTIR was performed by placing a thin film of solution on the Attenuated total reflectance (ATR) of the instrument. The solid-state FTIR was performed by preparing a pellet with KBr purchased from Merck, India.

Thermogravimetric analysis (TGA): TGA data were collected from TA Instruments, TGA Q50 Analyzer using the platinum pan.

Differential Scanning Calorimetry (DSC): DSC data was collected from TA Instruments, TGA Q2000 Analyzer.

X-ray Diffractometer (XRD): The purified NCs in hexane were drop-casted on a clean and dry glass slide. The film on the glass slide was run under PANalytical X-ray diffractometer using Cu K α ($\lambda = 1.54 \text{ \AA}$) as the incident radiation (40 kV and 30 mA).

4.9.2. Preparation of InP Magic-Sized Clusters.

4.9.2.1. General method (method A): It was prepared according to the previous method with slight modifications.^{2,16,24} All the glassware required for the preparation was heated overnight in an oven at 160 °C to ensure the complete exclusion of moisture. 0.684 g (3 mmol) of myristic acid was degassed at 110 °C in a three-necked round-bottom flask (flask A) equipped with a thermometer well, reflux condenser and septum. After 2 h the molten acid was slowly brought down to room temperature under nitrogen.

0.292 g (1 mmol) of $\text{In}(\text{OAc})_3$ was added to the solidified acid under counterflow of nitrogen. Flask A was vacuumed for the second time at 110 °C overnight (12-13 h) to facilitate the formation of indium salt of fatty acid and also to ensure the complete removal of volatile impurities. The following day flask A was backfilled with nitrogen. 3.945 g (15.6 mmol, 5 mL) of anhydrous 1-ODE was added into it and stirred for 30 min under nitrogen at 110 °C. Separately, in a nitrogen-filled glovebox, 0.126 g (0.5 mmol, 146 μL) of PTMS was dissolved in 0.2 mL of 1-ODE. This PTMS solution was rapidly injected into flask A. The growth of InP MSCs was monitored through UV-Visible absorption spectroscopy over a time of 30 min. After 30 min it was slowly cooled to room temperature and the MSC solution was stored inside a nitrogen-filled glovebox for future use.

4.9.2.2. Preparation of InP MSCs for assessment of growth time.

It was prepared according to general **method A**. However, the MSCs growth was monitored through absorption spectroscopy over a time of 1 h by collecting timed aliquots of 200 μL in 1 mL anhydrous hexane.

4.9.2.3. Preparation of InP MSCs for PXRD and FTIR analysis.

The synthetic procedure was followed according to **method A**. However, at the end of growth time (30 min) the as-synthesized MSCs were purified using the centrifugation technique. 4 mL of MSC solution was diluted with 2 mL of anhydrous hexane and initially centrifuged at 2000 rpm for 3 min to remove any undissolved impurities. The supernatant was then mixed with 8 mL butanol and centrifuged at 10000 rpm for 10 min. The process was repeated three times. The resulting residue of MSCs was vacuum-dried overnight and characterized with FTIR and PXRD the following day.

4.9.2.4. Preparation of 386-InP MSCs at two different degassing times.

It was prepared according to general **method A**. The only difference was the second degassing time which was 6 h for In-My2 and 12 for In-My3.

4.9.2.4.1. Isolation of complexes In-My2 and In-My3.

After the addition of 1-ODE and stirring for 30 min under nitrogen (**method A**) the solution was slowly cooled down to room temperature. 4 mL respective solution of complexes In-My2 and In-My3 were mixed with 16 mL of anhydrous acetone in a centrifuge tube and centrifuged for 10 min. A transparent supernatant was discarded and a white precipitate was mixed again with 16 mL of anhydrous acetone and centrifuged. The process was repeated three times and the residue was dried overnight under a vacuum.

4.9.2.5. Preparation of InP MSCs using pure indium myristate complex.

It was prepared according to general **method A** except for the first step of degassing of free myristic acid was omitted. 0.796 g (1 mmol) of the indium myristate complex was used and the addition of 1-ODE after overnight degassing gave a white hazy white solution. In the second process same method was followed. However, the hazy white solution of the indium myristate complex was heated to 170 °C which resulted in QDs instead of MSCs. For purification 4 mL of this solution was mixed with 1:4 anhydrous hexane and ethanol and centrifuged at 5000 rpm for 10 min. The transparent supernatant was discarded and the purification step was repeated two times. The as-synthesized QDs were dispersed in anhydrous hexane.

4.9.2.6. Preparation of InP MSCs with a fatty acid of different chain lengths.

The procedure followed for preparing MSCs of InP with different fatty acid chain lengths was similar to general **method A**. The only difference was the use of 0.601 g (3 mmol) of lauric acid and 0.854 g (3 mmol) of stearic acid instead of myristic acid.

4.9.2.6.1. Determination of thermal stability of 386-InP MSCs with a fatty acid of different chain lengths.

In order to determine the thermal stability of 386-InP MSCs prepared with different fatty acid chain lengths we heated all the corresponding MSCs above their growth time of 110 °C. With increasing temperature, we collected 200 µL aliquots of MSCs in 1 mL of hexane to monitor the evolution of its absorption peak. Along with this, we also observed the optical evolution of MSCs from their characteristics of yellow colour to transparent.

4.9.2.7. Preparation of InP MSCs in presence of additives.

The synthetic procedure was followed according to **method A**. However, along with 1-ODE, added after overnight degassing, 0.5 mL of additives were also added.

4.9.2.7.1. Isolation of TOP-infused indium precursor.

After the addition of 1-ODE and TOP, the reaction mixture was stirred for 30 min (**method A**, section 4.8.2.7). After 30 min it was cooled down to room temperature. 4 mL of the reaction mixture was centrifuged with 16 mL of anhydrous acetone for 10 min. The supernatant was discarded and the residue was washed three times with anhydrous acetone through centrifugation. The resulting residue was vacuum-dried overnight.

4.9.3. Preparation of InP QDs from MSCs.

4.9.3.1 General method (method B): 3.945 g (15.6 mmol, 5 mL) of 1-ODE was a vacuum in a three-necked round bottom flask equipped with thermometer well, condenser and septum for 1.5 h at 120 °C. After 1.5 h the flask was slowly heated to 300 °C under a nitrogen atmosphere. 3 mL of InP MSCs were withdrawn from a nitrogen-filled glove box and rapidly injected into this flask. The InP QDs were grown for 30 min. After 30 min the QDs solution was cooled and purified by mixing 4 mL of the colloidal solution with 2 mL of anhydrous hexane and 8 mL of anhydrous ethanol. The mixture was centrifuged at 5000 rpm for 10 min. The supernatant was discarded and the solid residue was washed again with a 1:4 mixture of anhydrous hexane and anhydrous ethanol at 5000 rpm for 5 min. The purified NCs were dispersed in hexane.

All the InP QDs synthesized in this study were prepared from corresponding clusters according to general **method B**.

4.9.4. Size-focusing growth of InP and InAs QDs.

A similar methodology was adopted as reported earlier.⁸⁴ 386-InP MSC solution and InAs nanoclusters were drawn in a syringe and respectively injected into InP QDs solution and InAs QDs solution at a rate of 0.05 mmol min⁻¹ at a temperature of 300 °C. 200 µL of aliquots were collected in 1 mL of anhydrous hexane and monitored through UV-Visible absorption spectroscopy.

4.10. References.

- (1) Alivisatos, A. P. Semiconductor Clusters, Nanocrystals, and Quantum Dots. *Science*. **1996**, 271, 933–937.
- (2) Gary, D. C.; Terban, M. W.; Billinge, S. J. L.; Cossairt, B. M. Two-Step

- Nucleation and Growth of InP Quantum Dots via Magic-Sized Cluster Intermediates. *Chem. Mater.* **2015**, *27*, 1432–1441.
- (3) Kwon, Y.; Kim, S. Indium Phosphide Magic-Sized Clusters: Chemistry and Applications. *NPG Asia Mater.* **2021**, *13*, 1–16.
- (4) Tamang, S.; Lincheneau, C.; Hermans, Y.; Jeong, S.; Reiss, P. Chemistry of InP Nanocrystal Syntheses. *Chem. Mater.* **2016**, *28*, 2491–2506.
- (5) Kudera, S.; Zanella, M.; Giannini, C.; Rizzo, A.; Li, Y.; Gigli, G.; Cingolani, R.; Ciccarella, G.; Spahl, W.; Parak, W. J.; Manna, L. Sequential Growth of Magic-Size CdSe Nanocrystals. *Adv. Mater.* **2007**, *19*, 548–552.
- (6) Singh, V.; Priyanka; More, P. V.; Hemmer, E.; Mishra, Y. K.; Khanna, P. K. Magic-Sized CdSe Nanoclusters: A Review on Synthesis, Properties and White Light Potential. *Mater. Adv.* **2021**, *2*, 1204–1228.
- (7) Wang, Y.; Zhang, Y.; Wang, F.; Giblin, D. E.; Hoy, J.; Rohrs, H. W.; Loomis, R. A.; Buhro, W. E. The Magic-Size Nanocluster (CdSe)₃₄ as a Low-Temperature Nucleant for Cadmium Selenide Nanocrystals; Room-Temperature Growth of Crystalline Quantum Platelets. *Chem. Mater.* **2014**, *26*, 2233–2243.
- (8) Cossairt, B. M.; Owen, J. S. CdSe Clusters: At the Interface of Small Molecules and Quantum Dots. *Chem. Mater.* **2011**, *23*, 3114–3119.
- (9) Jiang, Z. J.; Kelley, D. F. Role of Magic-Sized Clusters in the Synthesis of CdSe Nanorods. *ACS Nano* **2010**, *4*, 1561–1572.
- (10) Sun, M.; Yang, X. Phosphine-Free Synthesis of High-Quality CdSe Nanocrystals in Noncoordination Solvents: “Activating Agent” and “Nucleating

- Agent” Controlled Nucleation and Growth. *J. Phys. Chem. C* **2009**, *113*, 8701–8709.
- (11) Evans, C. M.; Guo, L.; Peterson, J. J.; Maccagnano-Zacher, S.; Krauss, T. D. Ultrabright PbSe Magic-Sized Clusters. *Nano Lett.* **2008**, *8*, 2896–2899.
- (12) Liu, Z. Low Temperature Fragmentation of Magic-Size Cluster Precursor Compounds into Ultrasmall Cds Quantum Dots with Enhanced Particle Yield. *Wuli Huaxue Xuebao/ Acta Physico - Chimica Sinica*. 2020, pp 1–3.
- (13) McBride, J. R.; Dukes, A. D.; Schreuder, M. A.; Rosenthal, S. J. On Ultrasmall Nanocrystals. *Chem. Phys. Lett.* **2010**, *498*, 1–9.
- (14) Harrell, S. M.; McBride, J. R.; Rosenthal, S. J. Synthesis of Ultrasmall and Magic-Sized CdSe Nanocrystals. *Chem. Mater.* **2013**, *25*, 1199–1210.
- (15) Palencia, C.; Yu, K.; Boldt, K. The Future of Colloidal Semiconductor Magic-Size Clusters. *ACS Nano* **2020**, *14*, 1227–1235.
- (16) Gary, D. C.; Flowers, S. E.; Kaminsky, W.; Petrone, A.; Li, X.; Cossairt, B. M. Single-Crystal and Electronic Structure of a 1.3 Nm Indium Phosphide Nanocluster. *J. Am. Chem. Soc.* **2016**, *138*, 1510–1513.
- (17) Lee, J.; Yang, J.; Kwon, S. G.; Hyeon, T. Nonclassical Nucleation and Growth of Inorganic Nanoparticles. *Nat. Rev. Mater.* **2016**, *1*.
- (18) Gary, D. C.; Glassy, B. A.; Cossairt, B. M. Investigation of Indium Phosphide Quantum Dot Nucleation and Growth Utilizing Triarylsilylphosphine Precursors. *Chem. Mater.* **2014**, *26*, 1734–1744.
- (19) Battaglia, D.; Peng, X. Formation of High Quality InP and InAs Nanocrystals in

- Noncoordinating Solvent. *Nano Lett.* **2002**, 2, 1027–1030.
- (20) Nightingale, A. M.; Demello, J. C. Improving the Ensemble Optical Properties of InP Quantum Dots by Indium Precursor Modification. *J. Mater. Chem. C* **2016**, 4, 8454–8458.
- (21) Grigel, V.; Dupont, D.; De Nolf, K.; Hens, Z.; Tessier, M. D. InAs Colloidal Quantum Dots Synthesis via Aminopnictogen Precursor Chemistry. *J. Am. Chem. Soc.* **2016**, 138, 13485–13488.
- (22) Knox, K. Le Chatelier's Principle. *J. Chem. Educ.* **1985**, 62, 863.
- (23) Lin, W.; Murphy, C. J. A Demonstration of Le Chatelier's Principle on the Nanoscale. *ACS Cent. Sci.* **2017**, 3, 1096–1102.
- (24) Park, N.; Monahan, M.; Ritchhart, A.; Friedfeld, M. R.; Cossairt, B. M. Synthesis of $\text{In}_{37}\text{P}_{20}(\text{O}_2\text{CR})_{51}$ Clusters and Their Conversion to InP Quantum Dots. *J. Vis. Exp.* **2019**, 1–8.
- (25) Friedfeld, M. R.; Johnson, D. A.; Cossairt, B. M. Conversion of InP Clusters to Quantum Dots. *Inorg. Chem.* **2019**, 58, 803–810.
- (26) Peng, Z. A.; Peng, X. Nearly Monodisperse and Shape-Controlled CdSe Nanocrystals via Alternative Routes: Nucleation and Growth. *J. Am. Chem. Soc.* **2002**, 124, 3343–3353.
- (27) Soloviev, V. N.; Eichhöfer, A.; Fenske, D.; Banin, U. Size-Dependent Optical Spectroscopy of a Homologous Series of CdSe Cluster Molecules. *J. Am. Chem. Soc.* **2001**, 123, 2354–2364.
- (28) Landes, C.; Braun, M.; Burda, C.; El-Sayed, M. A. Observation of Large

- Changes in the Band Gap Absorption Energy of Small CdSe Nanoparticles Induced by the Adsorption of a Strong Hole Acceptor. *Nano Lett.* **2001**, *1*, 667–670.
- (29) Xia, Y.-S.; Zhu, C.-Q. Aqueous Synthesis of Luminescent Magic Sized CdSe Nanoclusters. *Mater. Lett.* **2008**, *62*, 2103–2105.
- (30) Yu, Q.; Liu, C. Y. Study of Magic-Size-Cluster Mediated Formation of CdS Nanocrystals: Properties of the Magic-Size Clusters and Mechanism Implication. *J. Phys. Chem. C* **2009**, *113*, 12766–12771.
- (31) Dukes, A. D.; McBride, J. R.; Rosenthal, S. J. Synthesis of Magic-Sized CdSe and CdTe Nanocrystals with Diisooctylphosphinic Acid. *Chem. Mater.* **2010**, *22*, 6402–6408.
- (32) Ning, J.; Banin, U. Magic Size InP and InAs Clusters: Synthesis, Characterization and Shell Growth. *Chem. Commun.* **2017**, *53*, 2626–2629.
- (33) Stein, J. L.; Steimle, M. I.; Terban, M. W.; Petrone, A.; Billinge, S. J. L.; Li, X.; Cossairt, B. M. Cation Exchange Induced Transformation of InP Magic-Sized Clusters. *Chem. Mater.* **2017**, *29*, 7984–7992.
- (34) Leger, J. D.; Friedfeld, M. R.; Beck, R. A.; Gaynor, J. D.; Petrone, A.; Li, X.; Cossairt, B. M.; Khalil, M. Carboxylate Anchors Act as Exciton Reporters in 1.3 Nm Indium Phosphide Nanoclusters. *J. Phys. Chem. Lett.* **2019**, *10*, 1833–1839.
- (35) Friedfeld, M. R.; Johnson, D. A.; Cossairt, B. M. Conversion of InP Clusters to Quantum Dots. *Inorg. Chem.* **2019**, *58*, 803–810.
- (36) Ou, X.; Sietsma, J.; Santofimia, M. J. Fundamental Study of Nonclassical

- Nucleation Mechanisms in Iron. *Acta Mater.* **2022**, 226, 117655–117664.
- (37) Jun, Y. S.; Zhu, Y.; Wang, Y.; Ghim, D.; Wu, X.; Kim, D.; Jung, H. Classical and Nonclassical Nucleation and Growth Mechanisms for Nanoparticle Formation. *Annu. Rev. Phys. Chem.* **2022**, 73, 453–477.
- (38) Gebauer, D.; Cölfen, H. Prenucleation Clusters and Non-Classical Nucleation. *Nano Today* **2011**, 6, 564–584.
- (39) Sarkies, K. W.; Frankel, N. E. Nonclassical Nucleation Theory. *Phys. Rev. A* **1975**, 11, 1724–1731.
- (40) Karthika, S.; Radhakrishnan, T. K.; Kalaichelvi, P. A Review of Classical and Nonclassical Nucleation Theories. *Cryst. Growth Des.* **2016**, 16, 6663–6681.
- (41) Vekilov, P. G. Nonclassical Nucleation. In *ACS Symposium Series*; 2020; Vol. 1358, pp 19–46.
- (42) Wurmbrand, D.; Wolfram, J.; Anselm, F.; Rosenberg, R.; Boldt, K. Morphogenesis of Anisotropic Nanoparticles: Self-Templating via Non-Classical, Fibrillar Cd₂Se Intermediates. *Chem. Commun.* **2018**, 54, 7358–7361.
- (43) Gary, D. C.; Petrone, A.; Li, X.; Cossairt, B. M. Investigating the Role of Amine in InP Nanocrystal Synthesis: Destabilizing Cluster Intermediates by Z-Type Ligand Displacement. *Chem. Commun.* **2017**, 53, 161–164.
- (44) Algozeeb, W.; Raja, P. M. V.; Barron, A. R. Determination of Coordination Geometry by IR Spectroscopy. In *Physical Methods in Chemistry and Nano Science*; 2015.
- (45) Stuart, B. H. *Infrared Spectroscopy: Fundamentals and Applications*; 2004.

- (46) Komiya, S. *Synthesis of Organometallic Compounds: A Practical Guide*; 1997.
- (47) Deacon, G. B.; Phillips, R. J. Relationships between the Carbon-Oxygen Stretching Frequency of Carboxylato Complexes and the Type of Carboxylate Coordination. *Coord. Chem. Rev.* **1980**, *33*, 227–250.
- (48) Nakamoto, K. *Infrared and Raman Spectra of Inorganic Coordination Compounds Part A: Theory and Applications in Inorganic Chemistry*; 2009.
- (49) Blaine, R. L.; Blaine, R. L.; Schoff, C. K. *Purity Determinations by Thermal Methods: A Symposium*; American Society for Testing and Materials, 1984.
- (50) Haines, P. J. *Principles of Thermal Analysis and Calorimetry*; 2002.
- (51) Gabbott, P. *Principles and Applications of Thermal Analysis*; 2008.
- (52) Mullica, D. F.; Beall, G. W.; Milligan, W. O.; Korp, J. D.; Bernal, I. The Crystal Structure of Cubic $\text{In}(\text{OH})_3$ by X-Ray and Neutron Diffraction Methods. *J. Inorg. Nucl. Chem.* **1979**, *41*, 277–282.
- (53) Siddhanta, S.; Barman, I.; Narayana, C. Revealing the Trehalose Mediated Inhibition of Protein Aggregation through Lysozyme-Silver Nanoparticle Interaction. *Soft Matter* **2015**, *11*, 7241–7249.
- (54) Evans, C. M.; Love, A. M.; Weiss, E. A. Surfactant-Controlled Polymerization of Semiconductor Clusters to Quantum Dots through Competing Step-Growth and Living Chain-Growth Mechanisms. *J. Am. Chem. Soc.* **2012**, *134*, 17298–17305.
- (55) Thanh, N. T. K.; Maclean, N.; Mahiddine, S. Mechanisms of Nucleation and Growth of Nanoparticles in Solution. *Chem. Rev.* **2014**, *114*, 7610–7630.

- (56) Meakin, P. Models for Colloidal Aggregation. *Annu. Rev. Phys. Chem.* **1988**, *39*, 237–267.
- (57) Lee, J. H. E.; Ribeiro, C.; Longo, E.; Leite, E. R. Oriented Attachement: An Effective Mechanism in Formation of Anisotropic Nanocrystals. *Chem. Phys.* **2005**, *109*, 20842–20846.
- (58) Lee, E. J. H.; Ribeiro, C.; Longo, E.; Leite, E. R. Growth Kinetics of Tin Oxide Nanocrystals in Colloidal Suspensions under Hydrothermal Conditions. *Chem. Phys.* **2006**, *328*, 229–235.
- (59) Owen, J. S.; Chan, E. M.; Liu, H.; Alivisatos, A. P. Precursor Conversion Kinetics and the Nucleation of Cadmium Selenide Nanocrystals. *J. Am. Chem. Soc.* **2010**, *132*, 18206–18213.
- (60) Steckel, J. S.; Yen, B. K. H.; Oertel, D. C.; Bawendi, M. G. On the Mechanism of Lead Chalcogenide Nanocrystal Formation. *J. Am. Chem. Soc.* **2006**, *128*, 13032–13033.
- (61) Rempel, J. Y.; Bawendi, M. G.; Jensen, K. F. Insights into the Kinetics of Semiconductor Nanocrystal Nucleation and Growth. *J. Am. Chem. Soc.* **2009**, *131*, 4479–4489.
- (62) Ott, F. D.; Riedinger, A.; Ochsenbein, D. R.; Knüsel, P. N.; Erwin, S. C.; Mazzotti, M.; Norris, D. J. Ripening of Semiconductor Nanoplatelets. *Nano Lett.* **2017**, *17*, 6870–6877.
- (63) Taylor, R. M.; Monson, T. C.; Gullapalli, R. R. Influence of Carbon Chain Length on the Synthesis and Yield of Fatty Amine-Coated Iron-Platinum Nanoparticles. *Nanoscale Res. Lett.* **2014**, *9*, 1–12.

- (64) Dey, A.; Purkait, M. K. Effect of Fatty Acid Chain Length and Concentration on the Structural Properties of the Coated CoFe₂O₄ Nanoparticles. *J. Ind. Eng. Chem.* **2015**, *24*, 181–187.
- (65) Nakamura, T. Influence of Fatty Acid Alkyl Chain Length on Anisotropy of Copper Nitride Nano-Crystallites. *Inorganics* **2017**, *5*, 1–13.
- (66) Liu, Y.; Zhang, B.; Fan, H.; Rowell, N.; Willis, M.; Zheng, X.; Che, R.; Han, S.; Yu, K. Colloidal CdSe 0-Dimension Nanocrystals and Their Self-Assembled 2-Dimension Structures. *Chem. Mater.* **2018**, *30*, 1575–1584.
- (67) Liu, Y.; Willis, M.; Rowell, N.; Luo, W.; Fan, H.; Han, S.; Yu, K. Effect of Small Molecule Additives in the Prenucleation Stage of Semiconductor CdSe Quantum Dots. *J. Phys. Chem. Lett.* **2018**, *9*, 6356–6363.
- (68) Kirkwood, N.; Boldt, K. Protic Additives Determine the Pathway of CdSe Nanocrystal Growth. *Nanoscale* **2018**, *10*, 18238–18248.
- (69) Yu, K. CdSe Magic-Sized Nuclei, Magic-Sized Nanoclusters and Regular Nanocrystals: Monomer Effects on Nucleation and Growth. *Adv. Mater.* **2012**, *24*, 1123–1132.
- (70) Mourdikoudis, S.; Liz-Marza, L. M. Oleylamine in Nanoparticle Synthesis. *Chem. Mater.* **2016**, *25*, 1465–1476.
- (71) Protière, M.; Reiss, P. Amine-Induced Growth of an In₂O₃ Shell on Colloidal InP Nanocrystals. *Chem. Commun.* **2007**, 2417–2419.
- (72) Allen, P. M.; Walker, B. J.; Bawendi, M. G. Mechanistic Insights into the Formation of InP Quantum Dots. *Angew. Chemie - Int. Ed.* **2010**, *49*, 760–762.

- (73) Mičić, O. I.; Curtis, C. J.; Jones, K. M.; Sprague, J. R.; Nozik, A. J. Synthesis and Characterization of InP Quantum Dots. *J. Phys. Chem.* **1994**, *98*, 4966–4969.
- (74) Murray, C. B.; Norris, D. J.; Bawendi, M. G. Synthesis and Characterization of Nearly Monodisperse CdE (E = S, Se, Te) Semiconductor Nanocrystallites. *J. Am. Chem. Soc.* **1993**, *115*, 8706–8715.
- (75) Beberwyck, B. J.; Alivisatos, A. P. Ion Exchange Synthesis of III-V Nanocrystals. *J. Am. Chem. Soc.* **2012**, *134*, 19977–19980.
- (76) Nozik, A. J.; Micic, O. I. Synthesis and Characterization of Binary and Ternary III-V Quantum Dots. *J. Lumin.* **1996**, *70*, 95–107.
- (77) Guzelian, A. A.; Banin, U.; Kadavanich, A. V.; Peng, X.; Alivisatos, A. P. Colloidal Chemical Synthesis and Characterization of InAs Nanocrystal Quantum Dots. *Appl. Phys. Lett.* **1996**, *69*, 1432–1434.
- (78) Heuer-Jungemann, A.; Feliu, N.; Bakaimi, I.; Hamaly, M.; Alkilany, A.; Chakraborty, I.; Masood, A.; Casula, M. F.; Kostopoulou, A.; Oh, E.; Susumu, K.; Stewart, M. H.; Medintz, I. L.; Stratakis, E.; Parak, W. J.; Kanaras, A. G. The Role of Ligands in the Chemical Synthesis and Applications of Inorganic Nanoparticles. *Chem. Rev.* **2019**, *119*, 4819–4880.
- (79) Sugimoto, T. Underlying Mechanisms in Size Control of Uniform Nanoparticles. *J. Colloid Interface Sci.* **2007**, *309*, 106–118.
- (80) Sugimoto, T. Preparation of Monodispersed Colloidal Particles. *Adv. Colloid Interface Sci.* **1987**, *28*, 65–108.
- (81) Peng, X.; Wickham, J.; Alivisatos, A. P. Kinetics of II-VI and III-V Colloidal

- Semiconductor Nanocrystal Growth: “Focusing” of Size Distributions. *J. Am. Chem. Soc.* **1998**, *120*, 5343–5344.
- (82) Talapin, D. V.; Rogach, A. L.; Haase, M.; Weller, H. Evolution of an Ensemble of Nanoparticles in a Colloidal Solution: Theoretical Study. *J. Phys. Chem. B* **2001**, *105*, 12278–12285.
- (83) Marqusee, J. A.; Ross, J. Theory of Ostwald Ripening: Competitive Growth and Its Dependence on Volume Fraction. *J. Chem. Phys.* **1984**, *80*, 536–543.
- (84) Tamang, S.; Lee, S.; Choi, H.; Jeong, S. Tuning Size and Size Distribution of Colloidal InAs Nanocrystals via Continuous Supply of Prenucleation Clusters on Nanocrystal Seeds. *Chem. Mater.* **2016**, *28*, 8119–8122.
- (85) Cros-Gagneux, A.; Delpech, F.; Nayral, C.; Cornejo, A.; Coppel, Y.; Chaudret, B. Surface Chemistry of InP Quantum Dots: A Comprehensive Study. *J. Am. Chem. Soc.* **2010**, *132*, 18147–18157.
- (86) Virieux, H.; Le Troedec, M.; Cros-Gagneux, A.; Ojo, W. S.; Delpech, F.; Nayral, C.; Martinez, H.; Chaudret, B. InP/ZnS Nanocrystals: Coupling NMR and XPS for Fine Surface and Interface Description. *J. Am. Chem. Soc.* **2012**, *134*, 19701–19708.

Chapter V

*Synthesis of diverse CQDs using
MFA as precursors.*

5.1. Introduction.

In recent years, the chemistry of CQDs has garnered tremendous recognition in the field of material science due to their tunable optoelectronic properties in the quantum confinement regime. The size-dependent properties of QDs have introduced a paradigm shift in this domain.¹⁻⁵ The unique optical properties of these QDs have been widely exploited in the field of optoelectronics⁶, photovoltaics⁷, bio-molecular imaging^{8,9} and photocatalysis^{10,11}. Since, MFAs have been widely employed as the metal precursor for various CQDs such as III-V¹², II-VI¹³, IV-VI¹⁴, perovskite¹⁵ and other semiconductor materials¹⁶, the designing and developing of more sophisticated protocols for the synthesis of a library of MFAs, followed by its subsequent transformation to high-quality QDs is crucial. In this chapter, we will demonstrate the use of MFAs by synthesizing different types of high-quality colloidal NCs (III-V, II-VI, IV-VI, I-VI, chalcopyrite and perovskites) with a wide range of optical properties.

5.2. Preparation of different colloidal NCs from as-synthesized MFAs.

For the practical applicability of MFAs prepared using DBU (discussed in chapter II), we carried out the synthesis of CsPbBr₃, PbS, CdSe, CuFeS₂, Ag₂S and InP. Literature shows that these materials have been extensively researched and utilized for a broad range of purposes. For example, PbS¹⁷ and CuFeS₂¹⁸ are widely explored for photovoltaics; CdSe¹⁹, InP²⁰, and CsPbBr₃²¹ for light emitting diodes; InP²² and Ag₂S²³ for visible and near-infrared bio-imaging; and CsPbBr₃²⁴, CdSe²⁵ and InP²⁶ for organic transformation photocatalysis.

Table 5.1. Details of the MFAs used for the synthesis of various NCs.

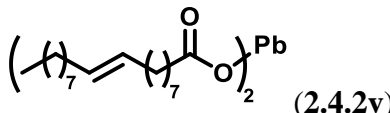
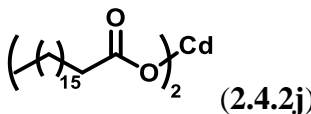
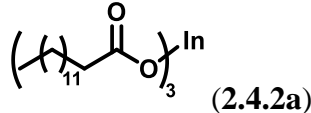
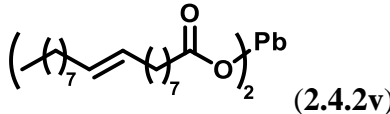
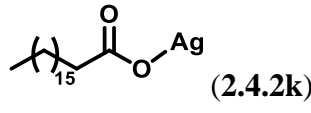
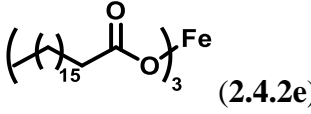
Entry	MFA precursor	Semiconductor type	Colloidal NCs
1.	 (2.4.2v)	Perovskite	CsPbBr ₃
2.	 (2.4.2j)	II-VI	CdSe
3.	 (2.4.2a)	III-V	InP
4.	 (2.4.2v)	IV-VI	PbS
5.	 (2.4.2k)	I-VI	Ag ₂ S
6.	and  (2.4.2h)	I-III-VI	CuFeS ₂

Figure 5.1 and Figure 5.2 show the optical properties of visible (CsPbBr₃, CdSe and InP) and near-infrared (PbS and Ag₂S) active and CuFeS₂ NCs respectively prepared using corresponding MFAs (Table 5.1). These materials exhibited distinct absorption and emission properties. For example, CsPbBr₃ perovskite NCs prepared using Pb(oleate)₂ (2.4.2v) show the first excitonic peak at 507 nm and a strong green emission peak at 515 nm.

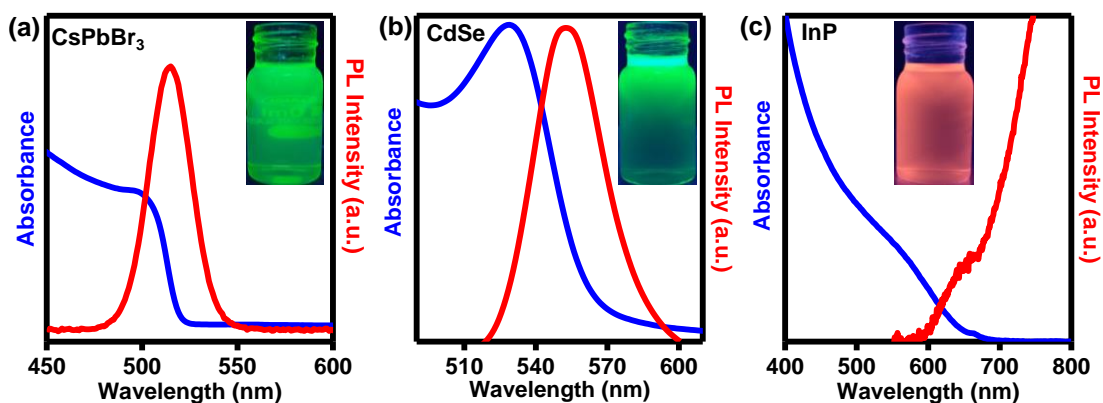


Figure 5.1. Optical studies of visible emitting colloidal NCs. (a) Absorption (blue) and emission spectrum (red) of CsPbBr₃ perovskite NCs (excited at 400 nm). Inset: Photograph of a colloidal dispersion of CbPbBr₃ NCs in hexane under a UV lamp. (b) Absorption (blue) and emission spectrum (red) of CdSe NCs (excited at 480 nm). Inset: Photograph of a colloidal dispersion of CdSe NCs in hexane under a UV lamp. (c) Absorption (blue) and emission (red) of InP NCs (excited at 500 nm). Inset: Photograph of a colloidal dispersion of InP NCs in hexane under a UV lamp.

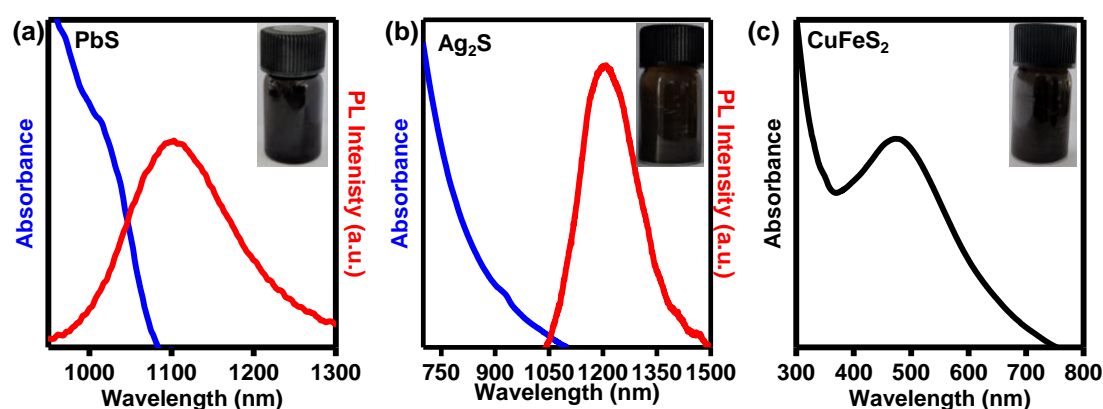


Figure 5.2. Optical studies of NIR emitting and CuFeS₂ NCs. (a) Absorption spectrum of PbS NCs (excited at 950 nm). Inset: Photograph of a colloidal dispersion of PbS NCs in hexane. (b) Absorption (blue) and emission spectrum (red) Ag₂S NCs (excited at 800 nm). Inset: Photograph of a colloidal dispersion of Ag₂S NCs in hexane, and (c) surface plasmon resonance band (black) of CuFeS₂ of NCs. Inset: Photograph of a colloidal dispersion of CuFeS₂ NCs in hexane.

The crystal structure and phase purity of these NCs were confirmed using PXRD (figure 5.3). CsPbBr₃, CdSe, InP, PbS, Ag₂S, and CuFeS₂ NCs crystallized in orthorhombic

(Pnma), zinc blende ($\bar{F}43m$), zinc blende ($\bar{F}43m$), rock salt (Fm-3m), monoclinic (P21/c), and tetragonal ($\bar{I}42d$) structures respectively.

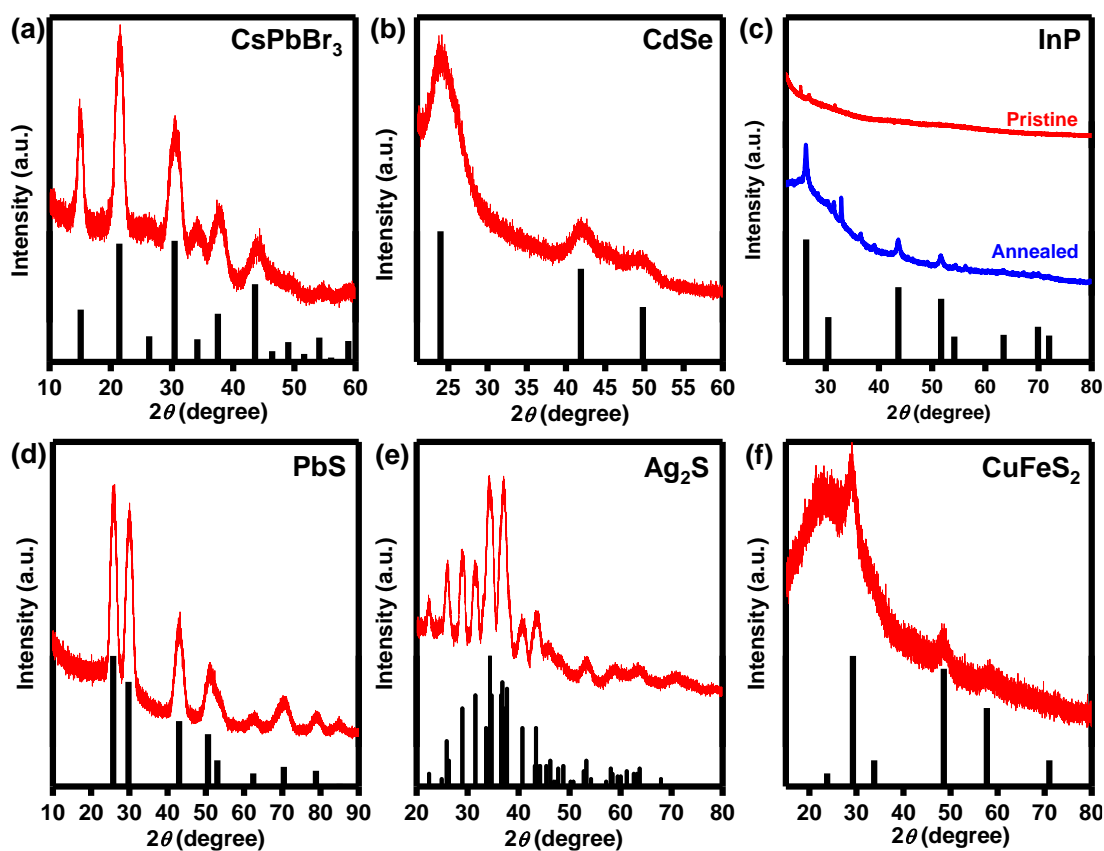


Figure 5.3. Powder X-ray diffraction studies of (a) CsPbBr₃ NCs (red) indexed with standard PDF 00-054-0752 (black). (b) CdSe NCs (red) indexed with standard PDF 65-2891 (black). (c) InP NCs (red and blue) indexed with standard PDF 96-101-0147 (black). (d) PbS NCs (red) indexed with standard PDF 05-0592 (black). (e) Ag₂S NCs (red) indexed with standard PDF 00-014-0072 (black) and (f) CuFeS₂ NCs (red) indexed with standard PDF 00-037-0471 (black).

For a representative purpose, we also performed a PLE study of green-emitting CsPbBr₃ NCs (figure 5.4). The green fluorescent emission in CsPbBr₃ NCs exhibits excitation spectra that closely resemble the absorption spectra with a maximum wavelength (λ_{\max}) of 497 nm (figure 5.4). Therefore, to excite electrons in CsPbBr₃, it is necessary to optically excite them with light having sufficient photon energy above 500 nm.

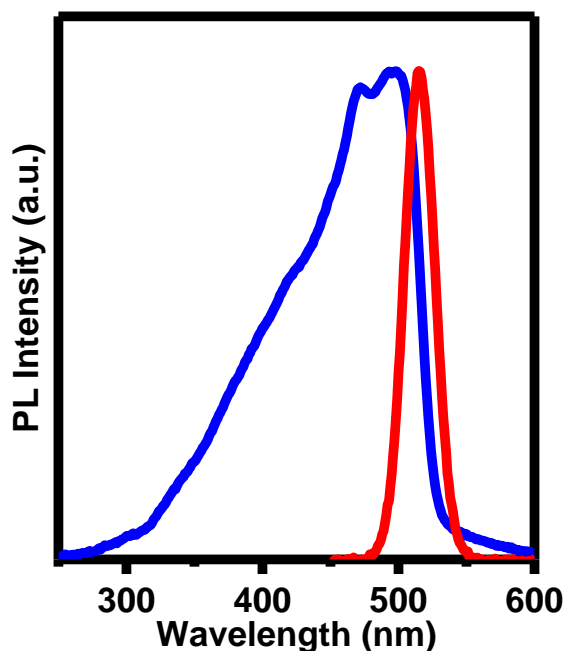


Figure 5.4. Photoluminescence excitation (PLE, blue line) spectrum of CsPbBr₃ NCs in hexane, $\lambda_{\text{ex}} = 497$ nm (emission wavelength 515 nm). The corresponding photoluminescence (PL, red line) emission spectrum exhibits emission maximum (λ_{em}) at 515 nm (excitation: 400 nm).

5.3. Conclusion

In chapter 2, we discussed a novel method for the preparation of MFAs in the presence of a DBU catalyst. The synthetic scheme provided access to a library of MFAs, which can be used for various colloidal NCs syntheses. In this chapter, we demonstrated a practical application of these MFAs by synthesizing different types of high-quality colloidal NCs (III-V, II-VI, IV-VI, I-VI, chalcopyrite and perovskites) with a wide range of optical properties.

5.4. Experimental section.

5.4.1. General information.

5.4.1.1. Material and general consideration.

Br₂ (≥99%), 1, 2-dimethoxyethane (99.5%), oleylamine (technical grade), 1-ODE (technical grade), sulphur (99.98%), selenium (≥99.5%), and trioctylphosphine (97%) were all bought from Sigma Aldrich, India. 1-dodecanthiol (98%) was bought from Loba Chemie.

5.4.1.2. Characterization method.

UV-Visible spectrophotometer: The UV-Visible absorption spectra were studied using Perkin Elmer (Model: LS 55) spectrophotometer (scan rate: 480 nm/s) and Agilent Technologies Cary 100 UV-vis.

PL spectrofluorometer: HORIBA Scientific spectrophotometer (Model: PTI-QM 510) was utilized for collecting the PL spectra of colloidal NCs.

X-ray Diffractometer (XRD): The purified NCs in hexane were drop-casted on a clean and dry glass slide. The film on the glass slide was run under PANalytical X-ray diffractometer with incident radiation (40 kV and 30 mA) using Cu K α ($\lambda = 1.54 \text{ \AA}$).

5.4.2. Preparation of colloidal NCs.

5.4.2.1. Synthesis of colloidal CsPbBr₃ NCs from as-prepared lead oleate (2.4.2v)

Colloidal CsPbBr₃ NCs were prepared following the reported method.^{24,27} Briefly, 0.077 g (0.1 mmol) of Pb-oleate and 30 μ L (0.6 mmol) of bromine were mixed with 0.407 g (1.52 mmol, 0.5 mL) of oleylamine in 3.156 g (12.5 mmol, 4 mL) of 1-ODE in a three-necked round bottom flask. The mixture was vacuumed at room temperature for

30 min and at 120 °C for 30 min. The round-bottom flask was back-filled with N₂ and slowly heated to 200 °C. 0.4 mL of caesium oleate solution was injected. The reaction was immediately quenched by immersing the flask in an ice bath. For purification 4 mL of crude colloidal solution was mixed with 4 mL anhydrous toluene and centrifuged for 10 min at 5000 rpm. The residue was purified again with 4 mL anhydrous toluene for 5 min at 5000 rpm. The purified NCs were dispersed in hexane.

5.4.2.2. Synthesis of colloidal CdSe NCs from as-prepared cadmium stearate (2.4.2j).

The colloidal synthesis of CdSe NCs was performed according to the reported method with minor modifications.^{13,28} Briefly, 0.068 g (0.1 mmol) cadmium stearate and 0.12 g (0.5 mmol, 0.147 mL) oleylamine were mixed with 4.73 g (18.75 mmol, 6 mL) of 1-ODE in a round bottom flask and degassed for 1 h at 120 °C. The flask was slowly heated to 150 °C after 1 h under N₂. In a separate flask, a solution of 0.15 g (1.9 mmol) selenium powder in 1.66 g (4.48 mmol, 2 mL) of trioctylphosphine was prepared. The as-prepared solution was rapidly injected into previously prepared cadmium stearate solution at 150 °C resulting in CdSe NCs. The purification was carried out by centrifugation of 5 mL crude NCs solution in a 1:4 mixture of anhydrous toluene and ethanol at 5000 rpm for 10 min. The same process was repeated two times, each time discarding the supernatant. The purified NCs were dispersed in anhydrous hexane.

5.4.2.3. Synthesis of colloidal InP NCs from as-prepared using indium stearate (2.4.2a).

The colloidal synthesis of InP NCs has been carried out following earlier reports with minor modifications.^{12,29} In brief, 0.097 g (0.1 mmol) indium stearate and 3.156 g (12.5 mmol, 4 mL) of 1-ODE were mixed in a three-necked flask and vacuumed for 1 h at

120 °C. After 1 h the reaction flask was backfilled with N₂ and the temperature was slowly raised to 270 °C. Separately, inside a nitrogen-filled glove box 12.5 mg (0.05 mmol, 14.5 μL) of PTMS was dissolved in 0.395 g (1.5 mmol, 0.5 mL) 1-ODE. This solution was swiftly injected into indium stearate solution and NCs were grown for another 1 h. For the annealing process to improve its PXRD, the as-synthesized InP NCs were heated beyond 1 h (2.5- 3 h). The reaction mixture was allowed to slowly cool down to room temperature. For the purification, a mixture of 1:4 anhydrous hexane and anhydrous ethanol was mixed and added to 4 mL of crude NCs solution and centrifuged for 10 min at 5000 rpm. The process of purification was repeated three times discarding the supernatant each time. The purified NCs were dispersed in hexane.

5.4.2.4. Synthesis of colloidal PbS from as-prepared lead oleate (2.4.2v).

Colloidal synthesis of PbS NCs was performed following the reported method with slight modifications.¹⁴ In brief, 0.030 g (0.0389 mmol) lead oleate was mixed with 3.95 g (15.6 mmol, 5 mL) of 1-ODE in a three-necked round bottom flask and vacuumed at 120 °C for 30 min. After 30 min the temperature was brought down to 80 °C under N₂. In a separate flask 1,3-diphenyl thiourea and 1, 2-dimethoxyethane were dissolved into a solution which was injected into the lead oleate mixture. A black colouration was observed at the end of growth time (15 min). The purification was carried out by precipitation of 4 mL crude colloidal solution with a mixture of 4 mL anhydrous toluene and 16 mL anhydrous ethanol and centrifuging for 10 min at 5000 rpm. The process was repeated 3 times with each time discarding the supernatant. The colloidal NCs were dispersed in hexane.

5.4.2.5. Synthesis of colloidal Ag₂S NCs from as-prepared silver stearate (2.4.2k).

Ag₂S NCs were synthesized following the method from earlier reports with minor modifications.^{30,31} In brief, 0.039 g (0.1 mmol) silver stearate was added to a three-necked flask with 2.37 g (9.37 mmol, 3 mL) of 1-ODE and degassed at room temperature for 1 h. The temperature was raised to 100 °C after 1 h and the process was continued for another 30 min. N₂ was back-filled in the flask and the temperature was slowly raised to 140 °C. In a separate flask, 0.023 g (0.1 mmol) 1,3-diphenyl thiourea was mixed with 0.25 g (1.25 mmol, 0.3 mL) of 1-DDT and degassed at room temperature for 1 h. The solution was rapidly injected into the as-prepared silver stearate solution. The reaction was continued for 5 min at 140 °C after which was slowly brought down to room temperature. For the purification of colloidal NCs, 3 mL of anhydrous ethanol was added to 3 mL of crude solution in a centrifuge tube. It was centrifuged for 5 min at 5000 rpm. The residue was purified again with 3 mL of anhydrous ethanol. The process of purification was repeated two times each time using 3 mL of anhydrous ethanol. A mixture of 3:1 anhydrous ethanol to anhydrous hexane was used for the final two purifications through centrifugation for 5 min at 5000 rpm. Finally, Ag₂S NCs in their pure form were dispersed in hexane.

5.4.2.6. Synthesis of colloidal CuFeS₂ NCs from as-prepared iron stearate (2.4.2e) and copper stearate (2.4.2h)

The preparative method for colloidal CuFeS₂ NCs was similar to earlier reports with slight modification.¹⁶ Briefly, 0.006 g (0.2 mmol) sulphur and 2.033 g (7.6 mmol, 2.5 mL) of oleylamine were mixed with 0.789 g (3.12 mmol, 1 mL) of 1-ODE in a three-necked round bottom flask. The flask was vacuumed at 120 °C for 30 min. The temperature was slowly increased to 160 °C under N₂. 0.090 g (0.1 mmol) iron stearate

along with 0.063 g (0.1 mmol) copper stearate were mixed in 2.367 g (9.37 mmol, 3 mL) of 1-ODE. The mixture was vacuumed at 120 °C for 1 h. The flask was back-filled with N₂ and 1.27 g (6.26 mmol, 1.5 mL) of 1-dodecanethiol was added. The temperature of the flask was increased to 180 °C after which sulphur solution was slowly injected dropwise. Once sulphur was added, the NCs were grown for 10 min and cold water was used to quench the growth. 4 mL of crude NCs solution was mixed with 4 mL of anhydrous toluene and 16 mL of anhydrous ethanol was centrifuged for 10 min at 5000 rpm. The supernatant was discarded and the residue was purified again with a 1:4 mixture of hexane and ethanol for 5 min at 5000 rpm. The process was repeated by the time of centrifugation was decreased to 3 min. The CuFeS₂ NCs were dispersed in anhydrous hexane.

5.5. References.

- (1) Reiss, P.; Carrière, M.; Lincheneau, C.; Vaure, L.; Tamang, S. Synthesis of Semiconductor Nanocrystals, Focusing on Nontoxic and Earth-Abundant Materials. *Chem. Rev.* **2016**, *116*, 10731–10819.
- (2) Tamang, S.; Lincheneau, C.; Hermans, Y.; Jeong, S.; Reiss, P. Chemistry of InP Nanocrystal Syntheses. *Chem. Mater.* **2016**, *28*, 2491–2506.
- (3) Reiss, P.; Protière, M.; Li, L. Core/Shell Semiconductor Nanocrystals. *Small* **2009**, *5*, 154–168.
- (4) Wise, F. W. Lead Salt Quantum Dots: The Limit of Strong Quantum Confinement. *Acc. Chem. Res.* **2000**, *33*, 773–780.
- (5) Luo, X.; Lai, R.; Li, Y.; Han, Y.; Liang, G.; Liu, X.; Ding, T.; Wang, J.; Wu, K. Triplet Energy Transfer from CsPbBr₃ Nanocrystals Enabled by Quantum Confinement. *J. Am. Chem. Soc.* **2019**, *141*, 4186–4190.

- (6) Talapin, D. V.; Lee, J. S.; Kovalenko, M. V.; Shevchenko, E. V. Prospects of Colloidal Nanocrystals for Electronic and Optoelectronic Applications. *Chem. Rev.* **2010**, *110*, 389–458.
- (7) Dayal, S.; Kopidakis, N.; Olson, D. C.; Ginley, D. S.; Rumbles, G. Photovoltaic Devices with a Low Band Gap Polymer and CdSe Nanostructures Exceeding 3% Efficiency. *Nano Lett.* **2010**, *10*, 239–242.
- (8) Michalet, X.; Pinaud, F. F.; Bentolila, L. A.; Tsay, J. M.; Doose, S.; Li, J. .; Sundaresan, G.; Wu, A. M.; Gambhir, S. S.; Weiss, S. Quantum Dots for Live Cells, in Vivo Imaging, and Diagnostics. *Science.* **2005**, *307*, 538–545.
- (9) Zhang, Y.; Hong, G.; Zhang, Y.; Chen, G.; Li, F.; Dai, H.; Wang, Q. Ag₂S Quantum Dot: A Bright and Biocompatible Fluorescent Nanoprobe in the Second Near-Infrared Window. *ACS Nano* **2012**, *6*, 3695–3702.
- (10) Li, X. B.; Tung, C. H.; Wu, L. Z. Semiconducting Quantum Dots for Artificial Photosynthesis. *Nat. Rev. Chem.* **2018**, *2*, 160–173.
- (11) Pal, A.; Ghosh, I.; Sapra, S.; König, B. Quantum Dots in Visible-Light Photoredox Catalysis: Reductive Dehalogenations and C-H Arylation Reactions Using Aryl Bromides. *Chem. Mater.* **2017**, *29*, 5225–5231.
- (12) Battaglia, D.; Peng, X. Formation of High Quality InP and InAs Nanocrystals in Noncoordinating Solvent. *Nano Lett.* **2002**, *2*, 1027–1030.
- (13) Murray, C. B.; Norris, D. J.; Bawendi, M. G. Synthesis and Characterization of Nearly Monodisperse CdE (E = S, Se, Te) Semiconductor Nanocrystallites. *J. Am. Chem. Soc.* **1993**, *115*, 8706–8715.
- (14) Hendricks, M. P.; Campos, M. P.; Cleveland, G. T.; Plante, I. J. La; Owen, J. S.

- A Tunable Library of Substituted Thiourea Precursors to Metal Sulfide Nanocrystals. *Science*. **2015**, *348*, 1226–1230.
- (15) Imran, M.; Caligiuri, V.; Wang, M.; Goldoni, L.; Prato, M.; Krahne, R.; De Trizio, L.; Manna, L. Benzoyl Halides as Alternative Precursors for the Colloidal Synthesis of Lead-Based Halide Perovskite Nanocrystals. *J. Am. Chem. Soc.* **2018**, *140*, 2656–2664.
- (16) Bhattacharyya, B.; Pandey, A. CuFeS₂ Quantum Dots and Highly Luminescent CuFeS₂ Based Core/Shell Structures: Synthesis, Tunability, and Photophysics. *J. Am. Chem. Soc.* **2016**, *138*, 10207–10213.
- (17) Liu, M.; Voznyy, O.; Sabatini, R.; García De Arquer, F. P.; Munir, R.; Balawi, A. H.; Lan, X.; Fan, F.; Walters, G.; Kirmani, A. R.; Hoogland, S.; Laquai, F.; Amassian, A.; Sargent, E. H. Hybrid Organic-Inorganic Inks Flatten the Energy Landscape in Colloidal Quantum Dot Solids. *Nat. Mater.* **2017**, *16*, 258–263.
- (18) Wu, Y.; Zhou, B.; Yang, C.; Liao, S.; Zhang, W. H.; Li, C. CuFeS₂ Colloidal Nanocrystals as an Efficient Electrocatalyst for Dye Sensitized Solar Cells. *Chem. Commun.* **2016**, *52*, 11488–11491.
- (19) Colvin, V. L.; Schlamp, M. C.; Alivisatos, A. P. Light-Emitting Diodes Made from Cadmium Selenide Nanocrystals and a Semiconducting Polymer. *Nature* **1994**, *370*, 354–357.
- (20) Li, D.; Kristal, B.; Wang, Y.; Feng, J.; Lu, Z.; Yu, G.; Chen, Z.; Li, Y.; Li, X.; Xu, X. Enhanced Efficiency of InP-Based Red Quantum Dot Light-Emitting Diodes. *ACS Appl. Mater. Interfaces* **2019**, *11*, 34067–34075.
- (21) Yuan, S.; Wang, Z. K.; Zhuo, M. P.; Tian, Q. S.; Jin, Y.; Liao, L. S. Self-

- Assembled High Quality CsPbBr₃ Quantum Dot Films toward Highly Efficient Light-Emitting Diodes. *ACS Nano* **2018**, *12*, 9541–9548.
- (22) Stasiuk, G. J.; Tamang, S.; Imbert, D.; Poillot, C.; Giardiello, M.; Tisseyre, C.; Barbier, E. L.; Fries, P. H.; De Waard, M.; Reiss, P.; Mazzanti, M. Cell-Permeable Ln(III) Chelate-Functionalized InP Quantum Dots as Multimodal Imaging Agents. *ACS Nano* **2011**, *5*, 8193–8201.
- (23) Tang, R.; Xue, J.; Xu, B.; Shen, D.; Sudlow, G. P.; Achilefu, S. Tunable Ultrasmall Visible-to-Extended near-Infrared Emitting Silver Sulfide Quantum Dots for Integrin-Targeted Cancer Imaging. *ACS Nano* **2015**, *9*, 220–230.
- (24) Pradhan, S.; Bhujel, D.; Gurung, B.; Sharma, D.; Basel, S.; Rasaily, S.; Thapa, S.; Borthakur, S.; Ling, W. L.; Saikia, L.; Reiss, P.; Pariyar, A.; Tamang, S. Stable Lead-Halide Perovskite Quantum Dots as Efficient Visible Light Photocatalysts for Organic Transformations. *Nanoscale Adv.* **2021**, *3*, 1464–1472.
- (25) Harris, C.; Kamat, P. V. Photocatalytic Events of CdSe Quantum Dots in Confined Media. Electrode Behavior of Coupled Platinum Nanoparticles. *ACS Nano* **2010**, *4*, 7321–7330.
- (26) Chakraborty, I. N.; Roy, S.; Devatha, G.; Rao, A.; Pillai, P. P. InP/ZnS Quantum Dots as Efficient Visible-Light Photocatalysts for Redox and Carbon-Carbon Coupling Reactions. *Chem. Mater.* **2019**, *31*, 2258–2262.
- (27) Thapa, S.; Bhardwaj, K.; Basel, S.; Pradhan, S.; Eling, C. J.; Adawi, A. M.; Bouillard, J. S. G.; Stasiuk, G. J.; Reiss, P.; Pariyar, A.; Tamang, S. Long-Term Ambient Air-Stable Cubic CsPbBr₃ Perovskite Quantum Dots Using Molecular Bromine. *Nanoscale Adv.* **2019**, *1*, 3388–3391.

- (28) Yu, W. W.; Peng, X. Formation of High-Quality CdS and Other II-VI Semiconductor Nanocrystals in Noncoordinating Solvents: Tunable Reactivity of Monomers. *Angew. Chemie - Int. Ed.* **2002**, *41*, 2368–2371.
- (29) Gary, D. C.; Cossairt, B. M. Role of Acid in Precursor Conversion During InP Quantum Dot Synthesis. *Chem. Mater.* **2013**, *25*, 2463–2469.
- (30) Jiang, P.; Tian, Z.-Q.; Zhu, C.-N.; Zhang, Z.-L.; Pang, D.-W. Emission-Tunable Near-Infrared Ag₂S Quantum Dots. *Chem. Mater.* **2012**, *24*, 3–5.
- (31) Ji, C.; Zhang, Y.; Zhang, X.; Wang, P.; Shen, H.; Gao, W.; Wang, Y.; Yu, W. W. Synthesis and Characterization of Ag₂S_xSe_{1-x} Nanocrystals and Their Photoelectrochemical Property. *Nanotechnology* **2017**, *28* (18), 065602.

Annexure A1

Instrumentation techniques

A1.1 Ultraviolet-visible (UV-Visible) spectroscopy.

UV-Visible absorption spectroscopy is a commonly used technique for studying the optical properties of QDs.^{1,2} When a QD is exposed to light, it absorbs some of the energy from the light and undergoes an electronic transition to a higher energy state. The amount of energy absorbed depends on the energy of the incident light and the band gap or the HOMO-LUMO gap.³ The absorption spectrum of a QD is typically measured by illuminating the sample with a broad range of wavelengths and measuring the intensity of the transmitted or reflected light. The intensity of the incident light and the intensity of the transmitted light are connected to its absorbance, A (Lambert-Beer's Law) as follows, $A = \varepsilon \times C \times l$ (where C is the concentration of the absorbing material, l is the path length and ε is the molar extinction coefficient). Typically, in the absorption spectroscopy of QDs, we analyze the absorbance vs. wavelength (or energy) plot. The absorbance at a given wavelength is related to the concentration of QDs and their absorption cross-section.

The absorption cross-section (cm^2) can be determined by using the Ricard equation⁴,

$$\sigma = \left(\frac{4\pi\omega r^3}{n_s c} \right) |f(\omega)|^2 2n_{QD} k_{QD} \quad (\text{A1.1})$$

Where, $f(\omega) = \frac{3\varepsilon_s}{\varepsilon_{QD} + 2\varepsilon_s}$

ω denotes the angular frequency, r is the radius of QDs, n_s denotes the refractive index of the solvent matrix, λ is the wavelength, ω denotes the angular frequency, n_{QD} denotes the real part of the refractive index of QDs and k_{QD} denotes the imaginary part of the refractive index of QDs and $f(\omega)$ is a local field factor, ε_s is the dielectric

constant of the solvent matrix and ϵ_{QD} is the dielectric constant of QDs.³⁻⁶ The σ can be converted into molar extinction coefficient (ϵ , $M^{-1}cm^{-1}$) using the equation

$$\sigma = \frac{2.303 \times \epsilon \times 1000}{N} \quad (A1.2)$$

where N is Avogadro's number.

At different wavelengths, the absorption spectrum typically shows well-defined peaks or humps, each corresponding to a specific electronic transition in the QD and formation of excitons (figure A1.1).⁷ From these peaks, the band gap or HOMO-LUMO gap can be determined. Smaller QDs have higher energy electronic transitions and absorb shorter wavelengths of light, while larger QDs absorb longer wavelengths of light due to the quantum confinement effect⁸⁻¹² (*c.f.* Chapter I). Furthermore, the width of the peak is strongly related to the size distribution. The polydisperse QDs will exhibit broader absorption peaks.^{2,13,14}

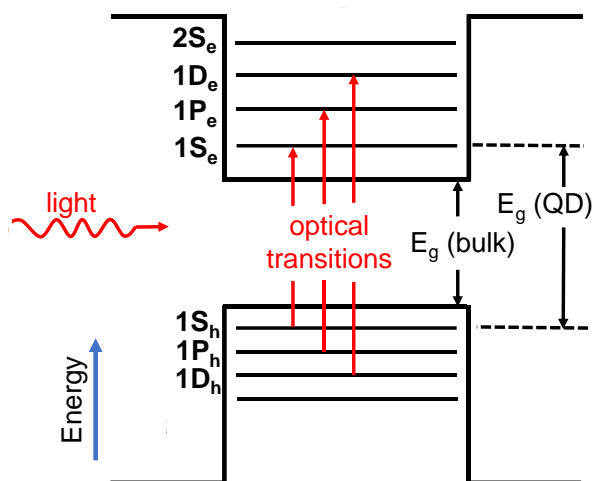


Figure A1.1. Allowed electronic transitions in QDs.

We used Perkin Elmer Lambda 25 spectrophotometer and Agilent Technologies Cary 100 UV-Visible spectrophotometer for our studies. Lambda 25 software was used to run the experiment and obtain the spectra. Two quartz or glass cuvettes having a path length

of 1 cm each were filled with the appropriate solvent (hexane) and autozero was performed for background corrections by placing each one of them in a reference holder and sample holder. Once the background correction is completed, the cuvette in the sample holder was replaced with a dilute solution of the sample. The absorption spectra were collected at 480 nm s⁻¹ from 800 to 200 nm. All the data were plotted in origin software with wave length on x-axis and normalized absorbance on y.

A1.2. Fourier Transform Infrared Spectroscopy (FTIR).

FTIR spectroscopy is a predominant analytical method used to determine the vibrational modes of molecules in the infrared region of the electromagnetic spectrum (2.5 to 25 μm).^{15,16} Its working principle is based on molecules absorbing infrared radiation at definite frequencies, which correspond to the energy levels of their vibrational modes. By measuring the absorbed radiation intensity (as a function of frequency), FTIR can provide information about the chemical structure and composition of a sample.^{17,18} Hooke's law is a fundamental principle of physics that describes the relationship between the force applied to a spring and the resulting displacement of the spring. In FTIR spectroscopy, Hooke's law is used to model the vibrational behaviour of molecules, which provides insights into the chemical composition and structure of a sample. The vibrational frequency relates to the force constant as described by an equation known as Hooke's law for a harmonic oscillator.¹⁹⁻

²² This equation is given by:

$$\bar{\nu} = \frac{1}{2\pi c} \sqrt{\frac{k}{\mu}} \quad (\text{A1.3})$$

where $\bar{\nu}$ is the vibrational frequency, c is the speed of light, k is the force constant, and μ is the reduced mass of the atoms in the molecule. This equation shows the

proportional relation of the square of the vibrational frequency with the force constant and the inversely proportional relation to reduced mass. In FTIR spectroscopy, the vibrational frequencies of the molecules in a sample are measured, and these frequencies are used to classify the functional groups and chemical bonds that are existing in the sample. By analysing the vibrational frequencies, one obtains information about the chemical composition.^{23,24} The principles of Hooke's law play an important role in the interpretation of FTIR spectra and the development of theoretical models for vibrational spectroscopy. In FTIR spectroscopy, the modes of vibration in a molecule that are detected correspond to the different types of chemical bonds present in the sample.²⁵ Here are some of the main types of bonds that can be detected by FTIR spectroscopy^{18,26,27}:

1. **Stretching Vibrations:** These vibrational modes correspond to the stretching of covalent bonds, such as the C-H, C=O, and O-H bonds. These modes occur at higher wavenumbers, typically above 1500 cm^{-1} . Furthermore, it can occur in two ways *viz.*, (a) symmetric and (b) asymmetric (figure A1.2).

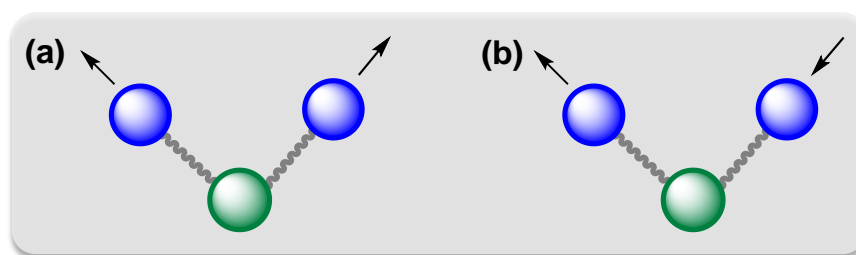


Figure A1.2. Representation of (a) symmetric and (b) asymmetric stretching vibrations.

2. **Bending Vibrations:** These vibrational modes correspond to the bending of covalent bonds, for example, the C-H and O-H bonds. These modes occur at lower wavenumbers, typically below 1500 cm^{-1} . Furthermore, there are four

different types of bending vibration modes: (a) scissoring (b) rocking (c) twisting and (d) wagging (figure A1.3).

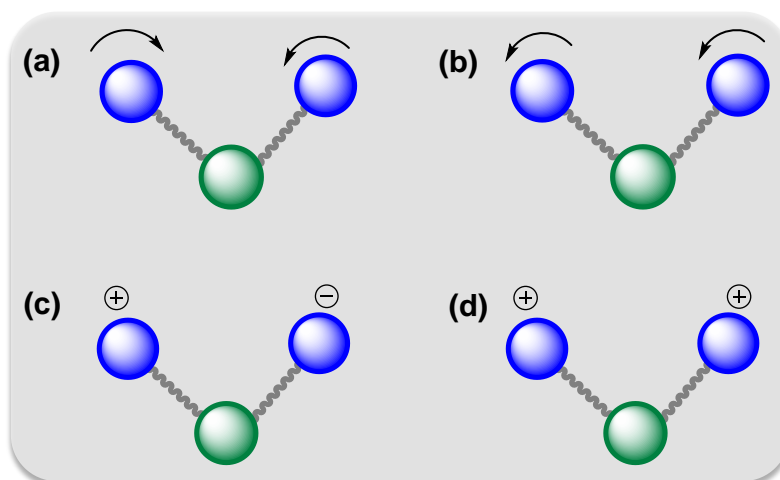


Figure A1.3. Representative of different types of bending vibrations (a) scissoring, (b) rocking, (c) twisting and (d) wagging.

3. **Combination Bands:** These are bands that correspond to a combination of stretching and bending modes of different bonds. For example, the C-H and C=O stretching vibrations can combine to produce a complex band in the region around 1700 cm^{-1} .
4. **Overtone and Combination Overtone:** These bands correspond to higher energy modes that are related to fundamental modes. They occur at higher wavenumbers and are typically weaker in intensity.

In addition to these main types of vibrational modes, other modes can be detected in FTIR spectroscopy, such as Fermi resonances, scissoring modes, and rocking modes. These modes can provide additional information about the molecular structure and dynamics of the sample in the study. The specific peaks and bands that are observed in an FTIR spectrum depend on the sample's chemical composition and structure. By analysing the peaks in the spectrum, the functional groups and chemical bonds existing

in the sample can be identified, and to gain insights into its chemical and physical properties.²⁸⁻³¹

All of our FTIR results were obtained on Bruker ALPHA E, 200396. The basic components of this spectrometer include a source of infrared radiation, an interferometer, a sample holder, and a detector (figure A1.4).

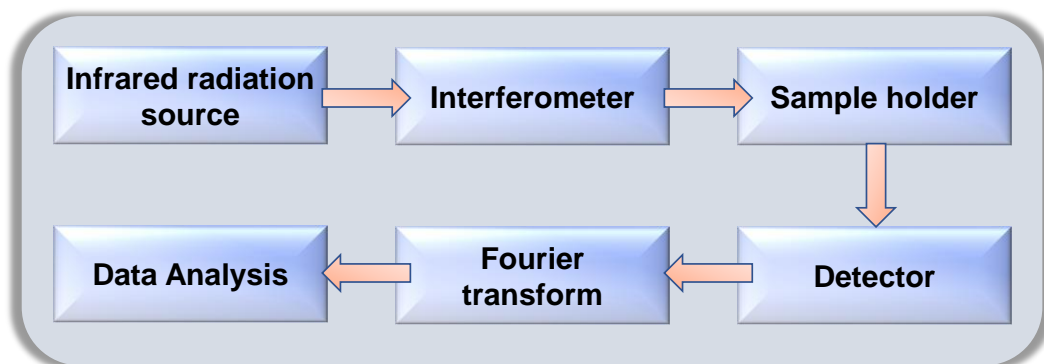


Figure A1.4. Basic components of FTIR spectroscopy.

The solution-based FTIR was performed by preparing a dilute solution of solid or liquid samples on a suitable solvent (hexane, chloroform or ethanol). This solution was carefully placed ATR crystal of the instrument to prepare a very thin layer of the sample. The FTIR of the as-prepared sample was determined subsequently. For solid un-dissolving samples, solid-state FTIR was performed. The pellet of solid sample and KBr was prepared and placed in the sample holder and FTIR was collected.

A1.3. Mass spectroscopy.

Mass spectroscopy has become an indispensable tool in modern analytical chemistry, allowing researchers to identify the molecular composition of an extensive range of samples with high precision and sensitivity.³² The basic principle of mass spectroscopy is to ionize a sample, separate the resulting ions based on their mass-to-charge ratio, and then detect and analyse these ions using various methods.³³ Mass spectroscopy is

commonly used in a variety of fields, including biochemistry, materials science, and environmental science, to name just a few. The basic components of a mass spectrometer include a sample inlet, an ionization source, a mass analyser, and a detector.³² The sample is placed in the sample inlet and then ionized by the ionization source. There are several different methods of ionization, including electron impact (EI), electrospray ionization (ESI), matrix-assisted laser desorption/ionization (MALDI), and others. The choice of ionization method depends on the properties of the sample being analysed and the desired level of sensitivity. Once the sample has been ionized, the resulting ions are separated based on their mass-to-charge ratio (m/z) using a mass analyzer.³⁴ There are several types of mass analysers, including magnetic sector, time-of-flight (TOF), quadrupole, and ion trap, among others. Each type of analyser has its strengths and weaknesses, and the choice of analyser depends on the specific application. After the ions are separated, they are detected and analysed using various methods. The most common method of detection is to measure the ion current as a function of m/z using a Faraday cup or an electron multiplier. This produces a mass spectrum, which is a plot of ion intensity versus m/z .³⁵ Mass spectra can provide information about the molecular weight, chemical composition, and structure of the sample being analysed.^{32,33} Mass spectroscopy has ample applications in chemistry. In drug discovery, mass spectroscopy is utilized to identify and characterize potential drug candidates, as well as to monitor the metabolism and pharmacokinetics of drugs *in vivo*. In biochemistry, mass spectroscopy is utilized to identify and characterize proteins, peptides, and other biomolecules, as well as to study protein-protein interactions and post-translational modifications. In materials science, mass spectroscopy is used to analyse the composition and structure of materials, including metals, semiconductors, and polymers.³⁴⁻³⁶

All of our mass spectroscopy was studied on Agilent Technologies, Accurate Mass Q-TOF LC/MS G65208. A dilute solution of the sample was prepared in HPLC-grade acetonitrile and placed in an autosampler inside an HPLC vial.

A1.4. X-ray diffraction (XRD).

Powder X-ray diffraction (PXRD) is a powerful tool for studying the structural properties of NCs. It can provide information about crystal size, shape, orientation, and composition, as well as lattice parameters, crystal symmetry, and crystallographic phase.^{37,38} The basic components of a powder X-ray diffractometer are an X-ray source, a sample holder, a goniometer, a detector, and a computer for data analysis. The X-ray source typically uses a copper or molybdenum anode to produce X-rays with a characteristic wavelength of around 1.54 Å or 0.71 Å, respectively.^{39,40}

Table A1.1. Different wavelengths used for X-ray

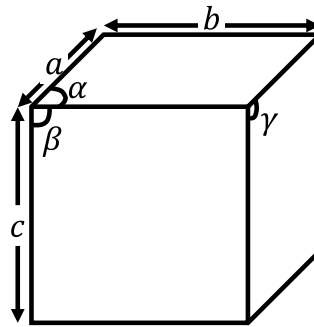
Target	K _{α1} (Å)	K _{α2} (Å)	Filter
Cr	2.289	2.293	V
Fe	1.936	1.939	Mn
Cu	1.540	1.544	Ni
Mo	0.710	0.713	Nb
Ag	0.559	0.563	Pd

The working principle of PXRD is based on the interaction of X-rays with the crystal structure of a powdered sample. The incident X-rays are diffracted by the crystal

structure of the sample, producing a characteristic diffraction pattern that can be analysed to obtain information about the crystal structure, properties, and composition.⁴¹⁻⁴³ Bragg's law is an important principle that helps to explain how the diffraction of X-rays occurs in a crystal lattice. Bragg's law states that when X-rays are diffracted by a crystal lattice, the diffraction peaks are produced when the path difference between the X-rays scattered by adjacent crystal planes is equal to an integer multiple of the X-ray wavelength.^{39,44} Mathematically, Bragg's law can be expressed as:

$$n\lambda = 2d\sin\theta \quad (\text{A1.4})$$

Where n is an integer, λ is the wavelength of the incident X-rays, d is the distance between adjacent crystal planes, and θ is the angle of incidence of the X-rays concerning the crystal plane. When the path difference between the scattered X-rays is equal to an integer multiple of the wavelength, the scattered X-rays will interfere constructively, producing a diffraction peak. This means that the intensity of the diffracted X-rays will be highest at specific angles, corresponding to the specific crystal planes that satisfy Bragg's law.^{39,45,46} The value of d , which is associated with a specific crystal plane in the $(h k l)$ set represented by Miller indices, depends on the type of crystal system (Table A1.2).

Table A1.2. Characteristics of different types of crystal systems.

En try	Crystal system	Axis system	Relation between d and h k l
1.	Cubic	$a = b = c$ $\alpha = \beta = \gamma = 90^\circ$	$\frac{1}{d^2} = \frac{h^2 + k^2 + l^2}{a^2}$
2.	Tetragonal	$a = b \neq c$ $\alpha = \beta = \gamma = 90^\circ$	$\frac{1}{d^2} = \frac{h^2 + k^2}{a^2} + \frac{l^2}{c^2}$
3.	Hexagonal	$a = b \neq c$ $\alpha = \beta = 90^\circ$ $\gamma = 120^\circ$	$\frac{1}{d^2} = \frac{4}{3} \left(\frac{h^2 + hk + k^2}{a^2} \right) + \frac{l^2}{c^2}$
4.	Rhombohedral	$a = b = c$ $\alpha = \beta = \gamma \neq 90^\circ$	$\frac{1}{d^2} = \frac{(h^2 + k^2 + l^2) \sin^2 \alpha + 2(hk + kl + hl)(\cos^2 \alpha - \cos \alpha)}{a^2(1 - 3 \cos^2 \alpha + 2 \cos^3 \alpha)}$
5.	Orthorhombic	$a \neq b \neq c$ $\alpha = \beta = \gamma = 90^\circ$	$\frac{1}{d^2} = \frac{h^2}{a^2} + \frac{k^2}{b^2} + \frac{l^2}{c^2}$
6.	Monoclinic	$a \neq b \neq c$ $\alpha = \gamma = 90^\circ$ $\beta \neq 90^\circ$	$\frac{1}{d^2} = \frac{1}{\sin^2 \beta} \left(\frac{h^2}{a^2} + \frac{k^2 \sin^2 \beta}{b^2} + \frac{l^2}{c^2} - \frac{2hl \cos \beta}{ac} \right)$
7.	Triclinic*	$a \neq b \neq c$ $\alpha \neq \beta \neq \gamma \neq 90^\circ$	$\frac{1}{d^2} = \frac{1}{V^2} (S_{11}h^2 + S_{22}k^2 + S_{33}l^2 + 2S_{12}hk + 2S_{23}kl + 2S_{13}hl)$

*In the equation: $V =$ Volume of unit cell, $S_{11} = b^2c^2\sin^2\alpha$, $S_{22} = a^2c^2\sin^2\beta$, $S_{33} = a^2b^2\sin^2\gamma$, $S_{12} = abc^2(\cos\alpha\cos\beta - \cos\gamma)$, $S_{23} = a^2bc(\cos\beta\cos\gamma - \cos\alpha)$, $S_{13} = ab^2c(\cos\gamma\cos\alpha - \cos\beta)$

Furthermore, by substituting the value of d from equation A1.4 in any one of the equations in table A1.2 we obtain a relation between h , k , l and θ for any crystal system. For example, for cubic crystal system by substitution d from A1.3 on the equation of cubic system (table A1.2, entry 1) we obtain,

$$\theta = \sin^{-1}\left(\frac{\lambda}{2a}\sqrt{h^2 + k^2 + l^2}\right) \quad (\text{A1.5})$$

In equation A1.5 the terms λ and a are constant which suggests that the change in θ dependent on h , k , and, l values. Since the Miller indices are whole numbers, the positions of the diffraction peaks are discrete, and the resulting diffraction pattern appears as a set of distinct peaks rather than a continuous spectrum. The intensity of these distinct peaks depends upon the structure factor which is represented mathematically as,

$$F(\theta) = \sum_i^n f_i e^{2\pi i(hx_i + ky_i + lz_i)} \quad (\text{A1.6})$$

Where n is the number of atoms per unit cell, f_i is the scattering factor and, x_i, y_i, z_i denotes lattice point coordinates. For example, the structure factor of InP QDs having a zinc blende crystal structure can be determined as

$$F(\theta) = [\sum_i^n f_i e^{2\pi i(hx_i + ky_i + lz_i)}]_{In} + [\sum_i^n f_i e^{2\pi i(hx_i + ky_i + lz_i)}]_P \quad (\text{A1.7})$$

Figure A1.5 shows a unit cell of zinc blende InP along with some parameters necessary for calculating its structure factors.⁴⁷⁻⁴⁹

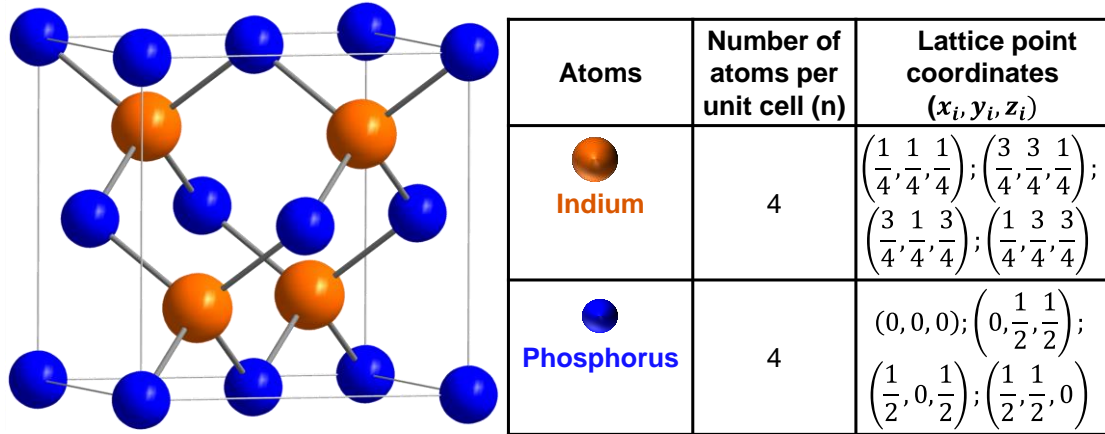


Figure A1.5. A unit cell of zinc blende InP and cell parameters of indium and phosphorus.

Substituting the values from figure A1.6 in equation A1.7 we obtained the structure factor of InP QDs as,

$$[F(\theta)]_{InP} = (f_P + f_{In} e^{\frac{i\pi}{2}(h+k+l)})(1 + e^{i\pi(k+l)} + e^{i\pi(l+h)} + e^{i\pi(h+k)}) \quad (A1.8)$$

Where, f_P and f_{In} are scattering factors of phosphorus and indium atoms.

In a PXRD experiment, the sample is typically prepared as a fine powder and placed in a sample holder. The X-rays are collimated and directed towards the sample holder, where the powder sample is mounted on a flat surface. The sample is typically rotated around an axis perpendicular to the X-ray beam using the goniometer, which allows diffraction patterns to be collected from multiple angles. The diffracted X-rays are collected by the detector, which is typically a scintillation counter or a semiconductor detector, and recorded as a series of peaks. The intensity of the diffracted X-rays is dependent on the crystal size, shape, orientation, and composition of the sample, as well as the wavelength and angle of incidence of the X-rays.^{40,44,50,51} The crystal size can be determined by analysing the width of the diffraction peaks using the Scherrer equation,

$$D = \frac{K\lambda}{\beta \cos \theta} \quad (\text{A1.9})$$

Where D denotes the crystallite size, K is the Scherrer constant also known as the shape factor, λ represents the wavelength of X-ray, β is the FWHM of PXRD peak at any given 2θ value.

Equation A1.9 relates the peak width to the crystal size, the wavelength of the X-rays, and the diffraction angle. Furthermore, crystal symmetry and phase can be determined by comparing the diffraction pattern to reference patterns from known crystal structures in a database, such as the International Centre for Diffraction Data (ICDD), Powder Diffraction File (PDF) and Joint Committee on Powder Diffraction Standards (JCPDS).^{45,52,53}

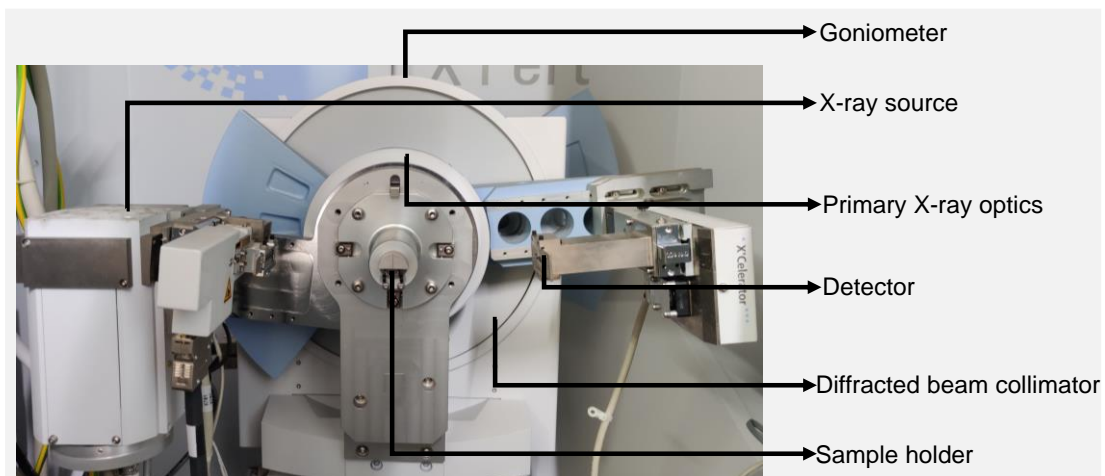


Figure A1.6. Different components of PANalytical powder X-ray diffractometer.

The diffraction patterns are analysed using various techniques, such as peak fitting, Rietveld refinement, or whole pattern fitting, to determine the crystal structure, properties, and composition of the sample. These analyses can provide information about the size, shape, orientation, and composition of NCs, as well as their lattice parameters, crystal symmetry, and crystallographic phase.^{40,52,54–56}

All of our PXRD studies were performed on a PANalytical X-ray diffractometer using Cu K α ($\lambda = 1.54 \text{ \AA}$) as the incident radiation at a voltage of 40 kV and a current of 30 mA. The colloidal samples were dispersed in a glass slide to prepare a thin film. High score plus software was used for analysing the diffractogram data.

A1.5. Photoluminescence (PL) spectroscopy.

Photoluminescence spectroscopy is a technique used to study the optical properties of materials by measuring the light that is emitted when the material is excited by a light source. The technique can be used to measure a variety of optical properties, such as the energy band gap, the presence of impurities, and the quality of the crystal lattice.^{57–59} The general working principle of PL spectroscopy involves exciting the material with a light source and measuring the emitted light. The light source can be a laser or a lamp, and the emitted light is typically collected using a spectrometer. The spectrometer is used to separate the emitted light into its constituent wavelengths, which can then be used to identify the specific optical properties of the material.^{57,58,60} The detailed working principle of PL spectroscopy can be broken down into several steps^{59,61}:

1. **Excitation:** The material is excited using a light source, which typically has a wavelength that is shorter than the wavelength of the emitted light. The excitation can be performed in two ways: continuous-wave excitation, which involves exposing the material to a constant stream of light, or pulsed excitation, which involves exposing the material to short bursts of light.
2. **Emission:** When the material is excited, it absorbs energy and enters an excited state. As the material returns to its ground state, it emits energy in the form of light. The wavelength of the emitted light depends on the energy band gap of the material and the nature of the excited state.

3. Collection: The emitted light is collected using a spectrometer, which separates the light into its constituent wavelengths. The spectrometer can be configured to measure either the intensity or the wavelength of the emitted light.
4. Analysis: The collected data can be analysed to extract information about the optical properties of the material. For example, the peak wavelength of the emitted light can be used to determine the energy band gap of the material, while the intensity of the emitted light can be used to determine the concentration of impurities in the material.

PL spectroscopy can be used to study a variety of materials, including semiconductors, organic compounds, and biological samples. The technique is non-destructive and can be used to study materials *in situ*, meaning that the material does not need to be removed from its environment to be studied.⁶²

All of our PL studies were performed on a HORIBA Scientific spectrophotometer (Model: PTI-QM 510). A dilute solution of the sample in the relevant solvent was prepared and placed in a quartz cuvette with a path length of 1 cm. The software used for determining the emission and excitation patterns of the sample was FelixGX.

A1.6. Transmission electron microscopy (TEM).

Transmission electron microscopy (TEM) is a high-resolution imaging technique that allows for the visualization and characterization of nanoscale structures, including QDs.⁶⁰ TEM uses a beam of electrons to image and analyse the internal structure and composition of materials at atomic resolution. The working principle of TEM involves passing a beam of electrons through a thin sample, which is typically less than 100 nm thick. The electrons interact with the sample, and the resulting electron-matter

interactions produce a transmitted electron signal, which is collected by an electron detector. The transmitted electrons that make it through the sample without being scattered or absorbed can be used to create an image of the sample's internal structure.⁶³⁻

65

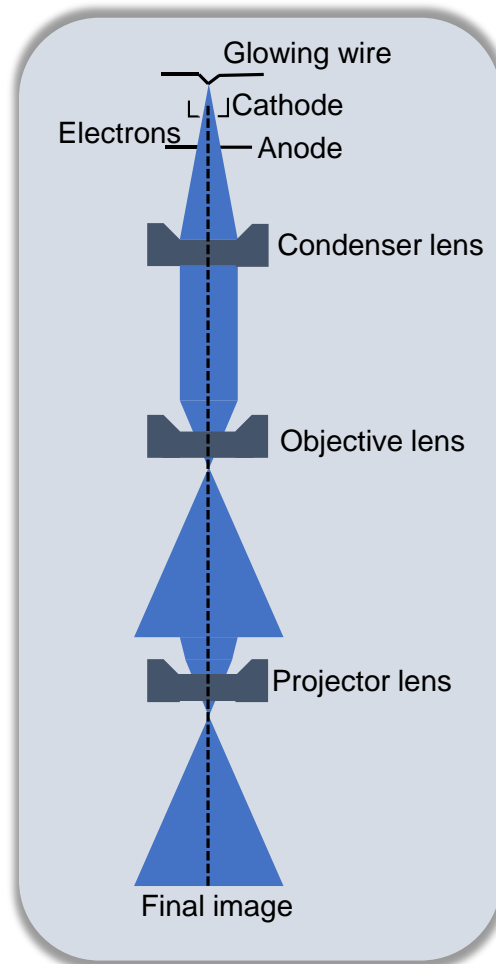


Figure A1.7. Various working components of TEM.

In addition to size, TEM can provide information about the crystal structure, composition, and defects of the QDs. High-resolution TEM (HRTEM) can be used to obtain detailed information about the atomic structure of the QDs, including the arrangement of atoms and the presence of defects or strain. Electron diffraction can be used to determine the crystal structure of the QDs, and energy-dispersive X-ray spectroscopy (EDX) can be used to determine the elemental composition of the

QDs.^{66,67} TEM is a powerful tool for studying QDs because it can provide information about their size, shape, structure, and composition with high resolution. This information is important for understanding the properties of QDs and for optimizing their use in a variety of applications, including bioimaging, photovoltaics, and optoelectronics.^{65,67,68}

All of our TEM was performed in JEOL-JEM-F200 and Tecnai G2 20 S-TWIN electron microscope. The samples were prepared by drop-casting a dilute solution of colloidal NCs in anhydrous toluene on a carbon-coated copper grid under a constant flow of nitrogen. They were stored under nitrogen before being loaded in the TEM instrument. The as-obtained data were analysed of average size with ImageJ software.

A1.7. Nuclear magnetic resonance (NMR).

Nuclear magnetic resonance (NMR) is a powerful analytical technique used to determine the physical and chemical properties of materials. The technique is based on the interaction of atomic nuclei with an external magnetic field, and it can be used to study a wide range of materials, including liquids, solids, and gases.^{32,69} The working principle of NMR involves applying a strong magnetic field to a sample containing atomic nuclei with a non-zero nuclear spin (such as hydrogen, carbon, or nitrogen).^{69,70} When placed in a magnetic field, the nuclei will align themselves with the magnetic field (figure A1.8). This alignment can be thought of as a "spin-up" or "spin-down" state, depending on the orientation of the nucleus with respect to the magnetic field. Next, a radio frequency (RF) pulse is applied to the sample. The RF pulse causes the aligned nuclei to temporarily flip into the opposite spin state, creating a net magnetic moment. As the nuclei relax back into their original spin state, they emit a signal that

can be detected and analysed. The signal emitted by the nuclei can be detected using a coil or antenna that is positioned around the sample.

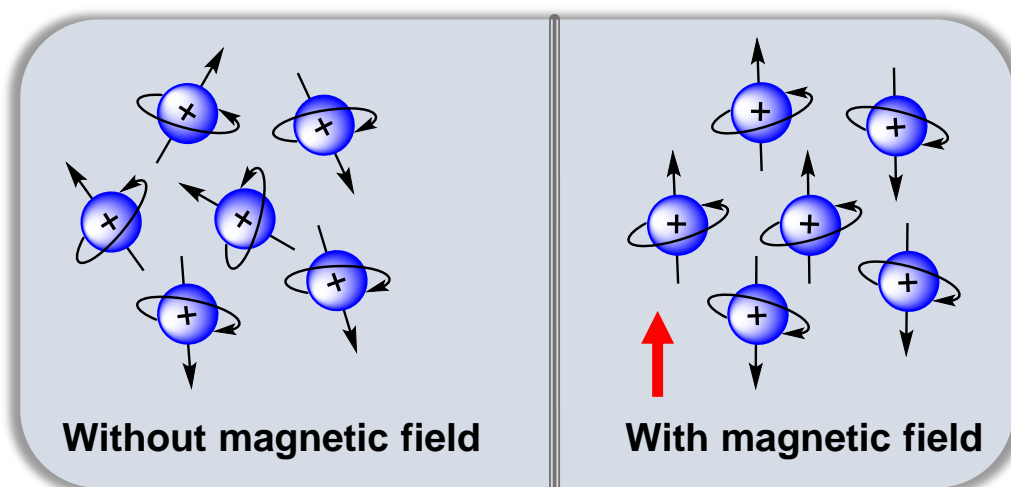


Figure A1.8. Schematic representation of arrangement of spins without and with magnetic field. Red arrow represents the direction of magnetic field.

The signal is typically measured as a function of time and is represented as a free induction decay (FID) signal. The FID signal is a complex exponential decay that contains information about the chemical and physical properties of the sample.^{69,71,72}

The NMR signal is influenced by the chemical and physical environment of the atomic nuclei, including factors such as the molecular structure, chemical composition, temperature, and pressure of the sample.^{33,73} By analysing the NMR signal, it is possible to obtain detailed information about the properties of the sample, such as the number and type of nuclei present, the molecular structure of the sample, and the dynamics of molecular motion within the sample.⁷¹ Several different NMR techniques can be used to study different properties of the sample. For example, ^1H NMR is used to study the behaviour of hydrogen atoms in the sample, while ^{13}C NMR is used to study the behaviour of carbon atoms in the sample.⁷⁰ Other techniques, such as 2D NMR, can be used to study the molecular structure and dynamics of the sample in more detail.^{69,72}

The results obtained on NMR are interpreted in terms of chemical shift which is fixed

for a different type of atom (figure A1.9). NMR is a valuable technique for studying a wide range of materials, including biomolecules, polymers, catalysts, and pharmaceuticals. It is non-destructive and non-invasive, making it ideal for studying samples *in situ*.⁷⁴

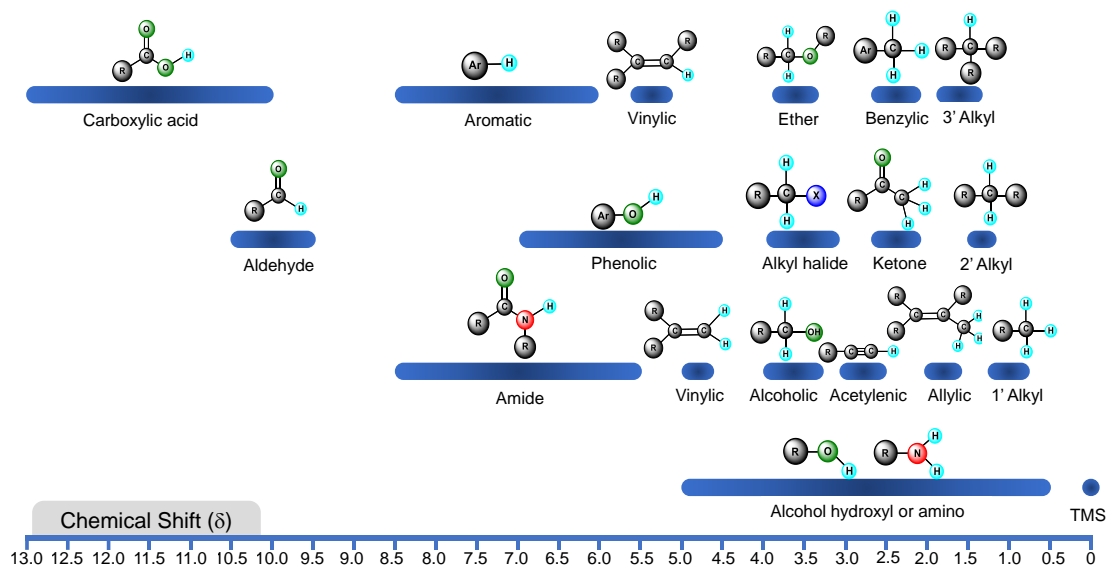


Figure A1.9. Signature ^1H NMR chemical shift values for different types of organic compounds.^{73,74}

In all of our experiments, we used the Bruker ASCENDTM NMR instrument. The sample was prepared by dissolving a small amount in 0.5-0.6 mL of suitable deuterated solvents like CDCl_3 , DMSO-d_6 etc. The software that was used for determining the NMR and its analysis was Topspin 4.0.1.

A1.8. Differential Scanning Calorimetry (DSC).

Differential scanning calorimetry (DSC) is a thermal analysis technique used to measure the heat flow and thermal behaviour of a sample as a function of temperature or time.⁷⁵ DSC is used to analyse the thermal properties of a wide variety of materials, including polymers, metals, ceramics, and pharmaceuticals.^{75,76} The working principle of DSC involves measuring the heat flow between a sample and a reference material as

they are heated or cooled under controlled temperature conditions. The sample and reference material are placed in two separate crucibles, which are then placed on a sample stage. The sample stage is placed in a furnace, which is heated or cooled at a constant rate, and the temperature is recorded as a function of time. During heating or cooling, the sample and reference material undergo various thermal events, such as phase transitions, melting, crystallization, or chemical reactions.⁷⁷⁻⁸⁰ The heat flow is measured by a highly sensitive differential thermocouple, which can detect changes in the heat flow as small as 1 μW . The change in heat flow is then plotted as a function of temperature or time to obtain a thermogram. DSC can be performed in two modes: isothermal and dynamic. In isothermal mode, the sample and reference material are held at a constant temperature for a specified period, and the heat flow is monitored until a steady state is reached. In dynamic mode, the sample and reference material is heated or cooled at a constant rate, and the heat flow is recorded continuously. Dynamic mode is preferred for most applications, as it provides more information about the thermal behaviour of the sample.^{81,82} The DSC instrument consists of a sample stage, a furnace, two thermocouples for temperature measurement, and a differential thermocouple for heat flow measurement. The sample stage is typically made of a high thermal conductivity material, such as aluminium or copper, and can accommodate two crucibles for the sample and reference material. The furnace is typically made of high-temperature materials such as ceramics and can be heated up to 1500 °C. The thermocouples are used to measure the temperature of the sample and the reference material, and the differential thermocouple is used to measure the heat flow between the sample and the reference material.^{83,84} The DSC thermogram provides valuable information about the thermal behaviour of the sample, including the heat capacity, enthalpy, phase transitions, and melting points. By comparing the thermograms of

different samples, it is possible to determine the thermal stability, composition, and purity of the materials. DSC is a highly versatile and widely used technique in many industries, including polymers, pharmaceuticals, materials science, and environmental science. It is particularly useful in the characterization of pharmaceuticals, where it can be used to evaluate the purity, stability, and polymorphic forms of drug substances.^{75,85,86}

All of our DSC experiments were performed on the TA instrument's Q2000 DSC analyser. TA universal analyser software was used for analysing the data obtained from DSC studies.

A1.9. Thermogravimetric Analysis (TGA).

Thermogravimetric analysis (TGA) is a thermal analysis technique that measures the change in weight of a sample as it is heated or cooled under controlled temperature conditions in a non-reactive or reactive environment.⁸⁷ TGA is used to analyse the thermal stability and composition of a wide variety of materials, including polymers, metals, ceramics etc.^{83,86} The working principle of TGA involves measuring the weight of the sample at different temperatures. The sample is heated at a constant rate, and the temperature is recorded as a function of time. During heating, the sample loses weight due to various thermal events, such as decomposition, oxidation, evaporation, or sublimation. The weight loss is measured by a highly sensitive microbalance, which can detect changes in the sample's mass as small as 0.1 µg. The weight change is then plotted as a function of temperature or time to obtain a thermogram.^{88,89} TGA can be performed in two modes: isothermal and dynamic. In isothermal mode, the sample is held at a constant temperature for a specified period, and the weight is monitored until a steady state is reached. In dynamic mode, the sample is heated at a constant rate, and

the weight is recorded continuously.⁸⁷ The TGA instrument consists of a sample holder, a furnace, a thermocouple for temperature measurement, and a microbalance for weight measurement. The sample holder is made of an inert material such as alumina, and it can be a pan or a crucible depending on the sample size and composition. The furnace is typically made of high-temperature materials such as ceramics and can be heated up to 1500 °C. The thermocouple is used to measure the temperature of the sample and the furnace, and the microbalance is used to measure the weight of the sample.^{81,84,89} The TGA thermogram provides valuable information about the thermal behaviour of the sample, including the onset temperature, the peak temperature, the rate of weight loss, and the total weight loss. By comparing the thermograms of different samples, it is possible to determine the thermal stability, composition, and purity of the materials. TGA is a highly versatile and widely used technique in many industries, including polymers, pharmaceuticals, materials science, and environmental science.^{83,84,88}

For all of our experiments involving TGA, we utilized TA instruments Q50 TGA analyser. The sample was loaded on a platinum pan. For analysing the data TA universal analyser software was used.

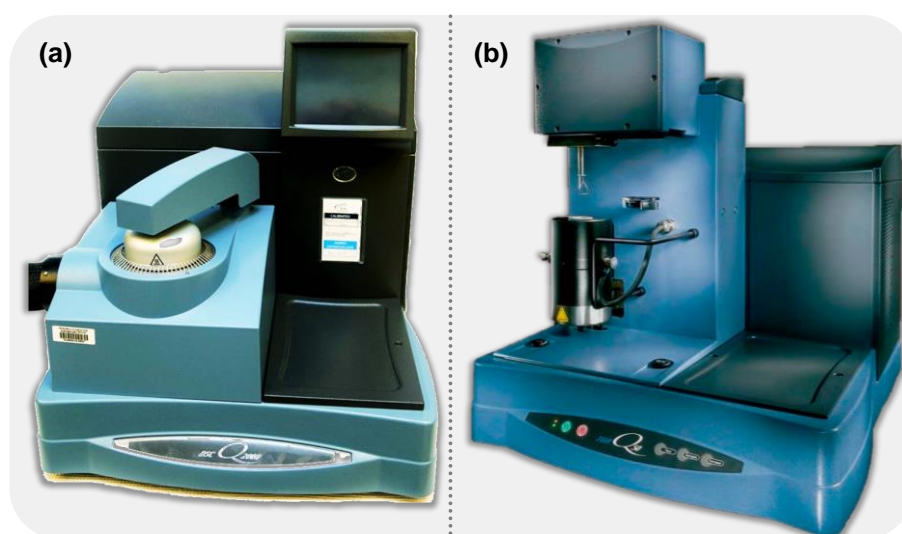


Figure A1.10. Image of TA instruments' (a) Q2000 DSC and (b) Q50 TGA.

A1.10 References.

- (1) Gary, D. C.; Cossairt, B. M. Role of Acid in Precursor Conversion During InP Quantum Dot Synthesis. *Chem. Mater.* **2013**, *25*, 2463–2469.
- (2) Battaglia, D.; Peng, X. Formation of High Quality InP and InAs Nanocrystals in Noncoordinating Solvent. *Nano Lett.* **2002**, *2*, 1027–1030.
- (3) Alivisatos, A. P. Perspectives on the Physical Chemistry of Semiconductor Nanocrystals. *J. Phys. Chem.* **1996**, *100*, 13226–13239.
- (4) Ricard, D.; Ghanassi, M.; Schanne-Klein, M. C. Dielectric Confinement and the Linear and Nonlinear Optical Properties of Semiconductor-Doped Glasses. *Opt. Commun.* **1994**, *108*, 311–318.
- (5) Klotz, I. M. Ultraviolet Absorption Spectroscopy. *J. Chem. Educ.* **1945**, *22*, 328–336.
- (6) Brus, L. E. A Simple Model for the Ionization Potential, Electron Affinity, and Aqueous Redox Potentials of Small Semiconductor Crystallites. *J. Chem. Phys.* **1983**, *79*, 5566–5571.
- (7) Efros, A. L.; Brus, L. E. Nanocrystal Quantum Dots: From Discovery to Modern Development. *ACS Nano* **2021**, *15*, 6192–6210.
- (8) Wise, F. W. Lead Salt Quantum Dots: The Limit of Strong Quantum Confinement. *Acc. Chem. Res.* **2000**, *33*, 773–780.
- (9) Kilina, S. V.; Kilin, D. S.; Prezhdo, O. V. Breaking the Phonon Bottleneck in PbSe and CdSe Quantum Dots: Time-Domain Density Functional Theory of Charge Carrier Relaxation. *ACS Nano* **2009**, *3*, 93–99.

- (10) Pietryga, J. M.; Park, Y. S.; Lim, J.; Fidler, A. F.; Bae, W. K.; Brovelli, S.; Klimov, V. I. Spectroscopic and Device Aspects of Nanocrystal Quantum Dots. *Chem. Rev.* **2016**, *116*, 10513–10622.
- (11) Yanhong, L.; Dejun, W.; Qidong, Z.; Min, Y.; Qinglin, Z. A Study of Quantum Confinement Properties of Photogenerated Charges in ZnO Nanoparticles by Surface Photovoltage Spectroscopy. *J. Phys. Chem. B* **2004**, *108*, 3202–3206.
- (12) Takagahara, T.; Takeda, K. Theory of the Quantum Confinement Effect on Excitons in Quantum Dots of Indirect-Gap Materials. *Phys. Rev. B* **1992**, *46*, 15578–15581.
- (13) Yu, W. W.; Peng, X. Formation of High-Quality CdS and Other II-VI Semiconductor Nanocrystals in Noncoordinating Solvents: Tunable Reactivity of Monomers. *Angew. Chemie - Int. Ed.* **2002**, *41*, 2368–2371.
- (14) Hendricks, M. P.; Campos, M. P.; Cleveland, G. T.; Plante, I. J. La; Owen, J. S. A Tunable Library of Substituted Thiourea Precursors to Metal Sulfide Nanocrystals. *Science*. **2015**, *348*, 1226–1230.
- (15) Coates, J. *Interpretation of Infrared Spectra, A Practical Approach*; 2000.
- (16) Perkins, W. D. Fourier Transform Infrared Spectroscopy. *J. Chem. Educ.* **1986**, *63*, 5–10.
- (17) Berthomieu, C.; Hienerwadel, R. Fourier Transform Infrared (FTIR) Spectroscopy. *Photosynth. Res.* **2009**, *101*, 157–170.
- (18) Silverstein, R. M.; Webster, F. X. *Spectrometric Identification Of Organic Compounds 6th Edition*; 1996.
- (19) Dutta, A. Fourier Transform Infrared Spectroscopy. In *Spectroscopic Methods*

for Nanomaterials Characterization; Elsevier Inc., 2017; Vol. 2, pp 73–93.

- (20) Bacsik, Z.; Mink, J.; Keresztury, G. FTIR Spectroscopy of the Atmosphere. I. Principles and Methods. *Appl. Spectrosc. Rev.* **2004**, *39*, 295–363.
- (21) Komiya, S. *Synthesis of Organometallic Compounds: A Practical Guide*; 1997.
- (22) Stuart, B. H. *Infrared Spectroscopy: Fundamentals and Applications*; 2004.
- (23) Algozeeb, W.; Raja, P. M. V.; Barron, A. R. Determination of Coordination Geometry by IR Spectroscopy. In *Physical Methods in Chemistry and Nano Science*; 2015.
- (24) Leger, J. D.; Friedfeld, M. R.; Beck, R. A.; Gaynor, J. D.; Petrone, A.; Li, X.; Cossairt, B. M.; Khalil, M. Carboxylate Anchors Act as Exciton Reporters in 1.3 Nm Indium Phosphide Nanoclusters. *J. Phys. Chem. Lett.* **2019**, *10*, 1833–1839.
- (25) Li, Q.; Chen, J.; Huyan, Z.; Kou, Y.; Xu, L.; Yu, X.; Gao, J. M. Application of Fourier Transform Infrared Spectroscopy for the Quality and Safety Analysis of Fats and Oils: A Review. *Crit. Rev. Food Sci. Nutr.* **2019**, *59*, 3597–3611.
- (26) Boccara, A. C.; Fournier, D.; Kumar, A.; Pandey, G. C. Nondestructive Evaluation of Carbon Fiber by Mirage–FTIR Spectroscopy. *J. Appl. Polym. Sci.* **1997**, *63*, 1785–1791.
- (27) Griffiths, P. R.; De Haseth, J. A. *Fourier Transform Infrared Spectrometry*; 2007.
- (28) Furutani, Y.; Shimizu, H.; Asai, Y.; Fukuda, T.; Oiki, S.; Kandori, H. ATR-FTIR Spectroscopy Revealing the Different Vibrational Modes of the Selectivity Filter Interacting with K⁺ and Na⁺ in the Open and Collapsed Conformations of the KcsA Potassium Channel. *J. Phys. Chem. Lett.* **2012**, *3*, 3806–3810.

- (29) Nan, C.; Yue, W.; Tao, L.; Yang, X. Fourier Transform Infrared Nano-Spectroscopy: Mechanism and Applications. *Appl. Spectrosc. Rev.* **2021**, *56* (7), 531–552.
- (30) Song, Y.; Cong, Y.; Wang, B.; Zhang, N. Applications of Fourier Transform Infrared Spectroscopy to Pharmaceutical Preparations. *Expert Opin. Drug Deliv.* **2020**, *17*, 551–571.
- (31) Baker, M. J.; Trevisan, J.; Bassan, P.; Bhargava, R.; Butler, H. J.; Dorling, K. M.; Fielden, P. R.; Fogarty, S. W.; Fullwood, N. J.; Heys, K. A.; Hughes, C.; Lasch, P.; Martin-Hirsch, P. L.; Obinaju, B.; Sockalingum, G. D.; Sulé-Suso, J.; Strong, R. J.; Walsh, M. J.; Wood, B. R.; Gardner, P.; Martin, F. L. Using Fourier Transform IR Spectroscopy to Analyze Biological Materials. *Nat. Protoc.* **2014**, *9*, 1771–1791.
- (32) Silverstein, R. M.; Webster, F. X.; Kiemle, D. J. *Spectrometric Identification of Organic Compounds*; 2005.
- (33) Pavia, D. L.; Lampman, G. M.; Kriz, G. S.; Vyvyan, J. R. *Introduction to Spectroscopy*; 2009.
- (34) Huheey, J. E.; Keiter, E. A.; Keiter, R. L. *Inorganic Chemistry: Principles of Structure and Reactivity*; 1993.
- (35) Gandhi, K.; Sharma, N.; Gautam, P. B.; Sharma, R.; Mann, B.; Pandey, V. *Advanced Analytical Techniques in Dairy Chemistry*; Springer, 2022.
- (36) Inghram, M. G. Modern Mass Spectroscopy. *Adv. Electron. Electron Phys.* **1948**, *1*, 219–268.
- (37) Černý, R. Crystal Structures from Powder Diffraction: Principles, Difficulties

- and Progress. *Crystals* **2017**, 7 (1–10).
- (38) Bayliss, P. X-Ray Diffraction Powder Data. *Am. Mineral.* **1976**, 61, 334–336.
- (39) Ryland, A. L. X-Ray Diffraction. *J. Chem. Educ.* **1958**, 35, 80–83.
- (40) Holder, C. F.; Schaak, R. E. Tutorial on Powder X-Ray Diffraction for Characterizing Nanoscale Materials. *ACS Nano* **2019**, 13, 7359–7365.
- (41) Harris, K. D. M.; Tremayne, M.; Kariuki, B. M. Contemporary Advances in the Use of Powder X-Ray Diffraction for Structure Determination. *Angew. Chemie - Int. Ed.* **2001**, 40, 1626–1651.
- (42) Andersen, H. L.; Christensen, M. In Situ Powder X-Ray Diffraction Study of Magnetic CoFe₂O₄ Nanocrystallite Synthesis. *Nanoscale* **2015**, 7, 3481–3490.
- (43) Christensen, A. N.; Broch, N. C.; von Heidenstam, O.; Nilsson, Å.; Theorell, H.; Blinc, R.; Paušak, S.; Ehrenberg, L.; Dumanović, J. Hydrothermal Investigation of the Systems In₂O₃-H₂O-Na₂O and In₂O₃-D₂O-Na₂O. The Crystal Structure of Rhombohedral In₂O₃ and of In(OH)₃. *Acta Chemica Scandinavica*. 1967, pp 1046–1056.
- (44) Ageev, E.; Pereverzev, A. X-Ray Diffraction Analysis of Products Sintered from Isostatically Pressed Leaded Bronze Powders. *MATEC Web Conf.* **2019**, 298, 00037.
- (45) Swanson, H. E.; Tatge, E. *Standard X-Ray Diffraction Powder Patterns*; 1953.
- (46) Moorhouse, S. J.; Wu, Y.; Buckley, H. C.; O'Hare, D. Time-Resolved in Situ Powder X-Ray Diffraction Reveals the Mechanisms of Molten Salt Synthesis. *Chem. Commun.* **2016**, 52, 13865–13868.

- (47) Frentrup, M.; Lee, L. Y.; Sahonta, S. L.; Kappers, M. J.; Massabuau, F.; Gupta, P.; Oliver, R. A.; Humphreys, C. J.; Wallis, D. J. X-Ray Diffraction Analysis of Cubic Zincblende III- Nitrides. *J. Phys. D. Appl. Phys.* **2017**, *50*, 1–13.
- (48) Tsuboi, M. Optically Active Lattice Vibrations of Zinc Blende Type and Wurtzite Type Crystals. *J. Chem. Phys.* **1964**, *40*, 1326–1335.
- (49) Birman, J. L. Simplified LCAO Method for Zincblende, Wurtzite, and Mixed Crystal Structures. *Phys. Rev.* **1959**, *115*, 1493–1505.
- (50) Bates, S.; Zografi, G.; Engers, D.; Morris, K.; Crowley, K.; Newman, A. Analysis of Amorphous and Nanocrystalline Solids from Their X-Ray Diffraction Patterns. *Pharm. Res.* **2006**, *23*, 2333–2349.
- (51) Bartos, A.; Lieb, K. P.; Uhrmacher, M.; Wiarda, D. Refinement of Atomic Positions in Bixbyite Oxides Using Perturbed Angular Correlation Spectroscopy. *Acta Crystallogr. Sect. B* **1993**, *49*, 165–169.
- (52) Calvin, J. J.; Kaufman, T. M.; Sedlak, A. B.; Crook, M. F.; Alivisatos, A. P. Observation of Ordered Organic Capping Ligands on Semiconducting Quantum Dots via Powder X-Ray Diffraction. *Nat. Commun.* **2021**, *12*, 1–8.
- (53) Hargreaves, J. S. J. Powder X-Ray Diffraction and Heterogeneous Catalysis. *Crystallogr. Rev.* **2005**, *11*, 21–34.
- (54) Martineau, C.; Fayon, F.; Legein, C.; Buzaré, J. Y.; Body, M.; Massiot, D.; Goutenoire, F. Structure Determination of β -Pb₂ZnF₆ by Coupling Multinuclear Solid State NMR, Powder XRD and Ab Initio Calculations. *Dalt. Trans.* **2008**, 6150–6158.
- (55) Harris, K. D. M. Powder Diffraction Crystallography of Molecular Solids. *Top*

Curr Chem **2012**, *315*, 133–178.

- (56) Bhadra, S.; Khastgir, D. Determination of Crystal Structure of Polyaniline and Substituted Polyanilines through Powder X-Ray Diffraction Analysis. *Polym. Test.* **2008**, *27*, 851–857.
- (57) Kutz, M. *Handbook of Measurement in Science and Engineering*; 2016.
- (58) Romani, A.; Clementi, C.; Miliani, C.; Favaro, G. Fluorescence Spectroscopy: A Powerful Technique for the Noninvasive Characterization of Artwork. *Acc. Chem. Res.* **2010**, *43*, 837–846.
- (59) Jain, A.; Blum, C.; Subramniam, V. Fluorescence Lifetime Spectroscopy and Imaging of Visible Fluorescent Proteins. In *Advances in Biomedical Engineering*; 2009; pp 145–174.
- (60) Borchert, H. *Solar Cells Based on Colloidal Nanocrystals*; Springer, 2014.
- (61) Abdi-Jalebi, M.; Ibrahim Dar, M.; Sadhanala, A.; Johansson, E. M. J.; Pazoki, M. Optical Absorption and Photoluminescence Spectroscopy. In *Characterization Techniques for Perovskite Solar Cell Materials*; 2020; pp 49–79.
- (62) Karoui, R.; Blecker, C. Fluorescence Spectroscopy Measurement for Quality Assessment of Food Systems-a Review. *Food Bioprocess Technol.* **2011**, *4*, 364–386.
- (63) Wen, J. G. Transmission Electron Microscopy. In *Practical Materials Characterization*; 2014; pp 189–229.
- (64) Akhtar, K.; Khan, S. A.; Khan, S. B.; Asiri, A. M. Scanning Electron Microscopy: Principle and Applications in Nanomaterials Characterization. In

Handbook of Materials Characterization; Springer, 2018; pp 113–145.

- (65) Fultz, B.; Howe, J. *Transmission Electron Microscopy and Diffractometry of Materials*; Springer, 2013.
- (66) Fan, Z.; Zhang, L.; Baumann, D.; Mei, L.; Yao, Y.; Duan, X.; Shi, Y.; Huang, J.; Huang, Y.; Duan, X. In Situ Transmission Electron Microscopy for Energy Materials and Devices. *Adv. Mater.* **2019**, *31*, 1–22.
- (67) Malac, M.; Hettler, S.; Hayashida, M.; Kano, E.; Egerton, R. F.; Beleggia, M. Phase Plates in the Transmission Electron Microscope: Operating Principles and Applications. *Microscopy* **2021**, *70*, 75–115.
- (68) Ma, H.; Shieh, K.-J.; Qiao, T. X. Study of Transmission Electron Microscopy (TEM) and Scanning Electron Microscopy (SEM). *Nat. Sci.* **2006**, *4*, 14–22.
- (69) Roberts, J. D. Nuclear Magnetic Resonance Spectroscopy. In *Proceedings of the California association of chemistry teachers*; 1961; Vol. 37, pp 581–584.
- (70) Balci, M. *Basic ¹H- and ¹³C-NMR Spectroscopy*; 2005.
- (71) Macomber, R. S. *A Complete Introduction To Modern NMR Spectroscopy*; John Wiley & Sons, Inc., 1998.
- (72) Kolonko, E. M.; Kolonko, K. J. Introducing NMR Spectroscopy Using Guided Inquiry and Partial Structure Templating. *J. Chem. Educ.* **2019**, *96*, 912–919.
- (73) Babij, N. R.; McCusker, E. O.; Whiteker, G. T.; Canturk, B.; Choy, N.; Creemer, L. C.; Amicis, C. V. D.; Hewlett, N. M.; Johnson, P. L.; Knobelsdorf, J. A.; Li, F.; Lorsbach, B. A.; Nugent, B. M.; Ryan, S. J.; Smith, M. R.; Yang, Q. NMR Chemical Shifts of Trace Impurities: Industrially Preferred Solvents Used in Process and Green Chemistry. *Org. Process Res. Dev.* **2016**, *20*, 661–667.

- (74) Gottlieb, H. E.; Kotlyar, V.; Nudelman, A. NMR Chemical Shifts of Common Laboratory Solvents as Trace Impurities. *J. Org. Chem.* **1997**, *62*, 7512–7515.
- (75) Chiu, M.; Prenner, E. Differential Scanning Calorimetry: An Invaluable Tool for a Detailed Thermodynamic Characterization of Macromolecules and Their Interactions. *J. Pharm. Bioallied Sci.* **2011**, *3*, 39–59.
- (76) Marti, E.; Kaisersberger, E.; Füglein, E. Multicycle Differential Scanning Calorimetry Thermophysical Procedures for Research, Development, and Quality Control of Substances and Materials. *J. Therm. Anal. Calorim.* **2010**, *101*, 1189–1197.
- (77) Knothe, G.; Dunn, R. O. A Comprehensive Evaluation of the Melting Points of Fatty Acids and Esters Determined by Differential Scanning Calorimetry. *JAOCs, J. Am. Oil Chem. Soc.* **2009**, *86*, 843–856.
- (78) Nassu, R. T.; Gonçalves, L. A. G. Determination of Melting Point of Vegetable Oils and Fats by Differential Scanning Calorimetry (DSC) Technique. *Grasas y Aceites* **1999**, *50*, 16–22.
- (79) Garidel, P.; Johann, C.; Mennicke, L. The Mixing Behaviour of Pseudobinary Phosphatidylcholine-Phosphatidylglycerol Mixtures as Function of PH and Chain Length. *Eur. Biophys. J* **1997**, *26*, 447–459.
- (80) Charsley, E. L.; Laye, P. G.; Palakollu, V.; Rooney, J. J.; Joseph, B. DSC Studies on Organic Melting Point Temperature Standards. *Thermochim. Acta* **2006**, *446*, 29–32.
- (81) Haines, P. J. *Principles of Thermal Analysis and Calorimetry*; 2002.
- (82) Smith, M. J. Using Differential Scanning Calorimetry to Explore the Phase

- Behavior of Chocolate. *J. Chem. Educ.* **2016**, 93, 898–902.
- (83) Menczel, J. D.; Prime, R. B. *Thermal Analysis of Polymers*; 2009.
- (84) Gabbott, P. *Principles and Applications of Thermal Analysis*; 2008.
- (85) D'Amelia, R.; Stracuzzi, V.; Nirode, W. F. Introduction of Differential Scanning Calorimetry in a General Chemistry Laboratory Course: Determination of Heat Capacity of Metals and Demonstration of Law of Dulong and Petit Ronald. *J. Chem. Educ.* **2008**, 85, 109–111.
- (86) Akash, M. S. H.; Rehman, K. *Essentials of Pharmaceutical Analysis*; 2019.
- (87) Coats, A. W.; Redfern, J. P. Thermogravimetric Analysis. *Analyst* **1963**, 88, 906–924.
- (88) Saadatkah, N.; Carillo Garcia, A.; Ackermann, S.; Leclerc, P.; Latifi, M.; Samih, S.; Patience, G. S.; Chaouki, J. Experimental Methods in Chemical Engineering: Thermogravimetric Analysis—TGA. *Can. J. Chem. Eng.* **2019**, 98, 34–43.
- (89) Thomas, S.; Thomas, R.; Zachariah, A. K.; Mishra, R. K. *Thermal and Rheological Measurement Techniques for Nanomaterials Characterization*; 2017.

Annexure A2

*Additional information for Chapter
II*

A2.1. Characterization of MFAs from combined saponification and double decomposition methods.

A2.1.1. Copies of FTIR spectra and TGA thermogram.

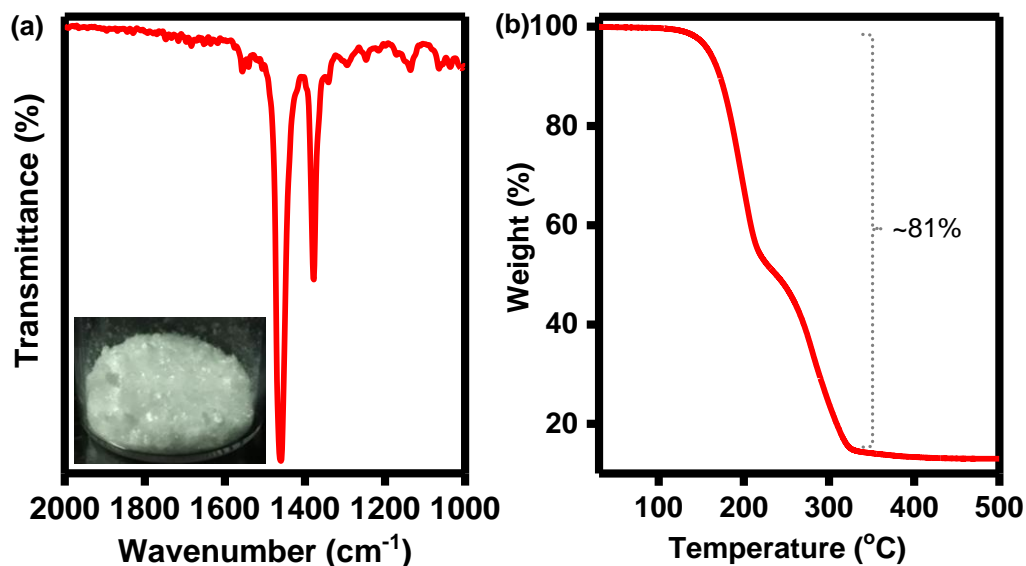


Figure A2.1. (a) FTIR spectrum of potassium myristate (**2.3.1a**) showing a shift in carbonyl stretching frequency. Inset: Photographic image of potassium myristate. (b) TGA thermogram of potassium myristate (**2.3.1a**) with weight loss of ~81% consistent with one myristate group.

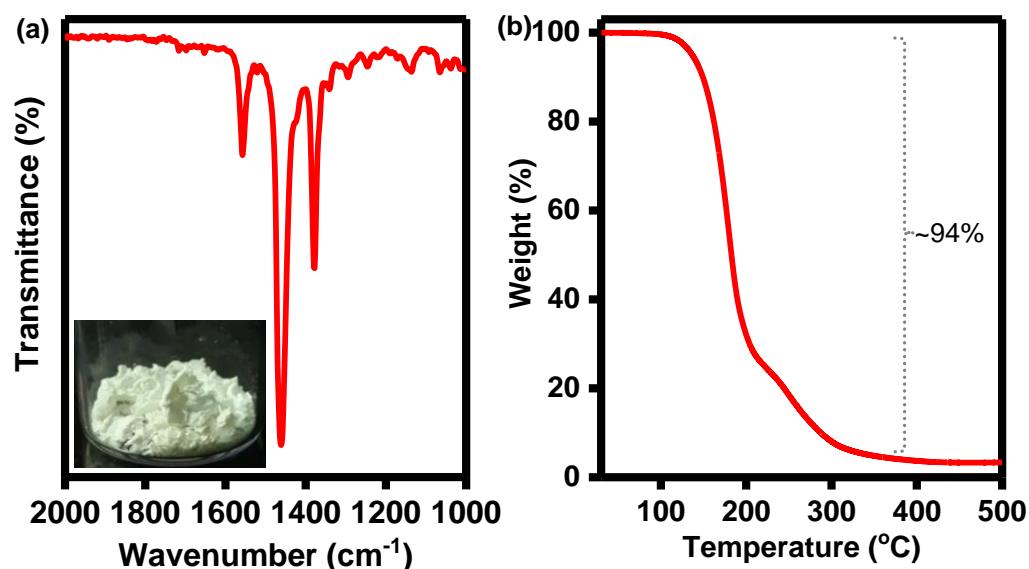


Figure A2.2. (a) FTIR spectrum of sodium myristate (**2.3.1b**) showing a shift in carbonyl stretching frequency. Inset: Photographic image of sodium myristate. (b) TGA thermogram of sodium myristate (**2.3.1b**) with weight loss of ~94% consistent with one myristate group.

thermogram of sodium myristate (**2.3.1b**) with weight loss of ~94% consistent with one myristate group.

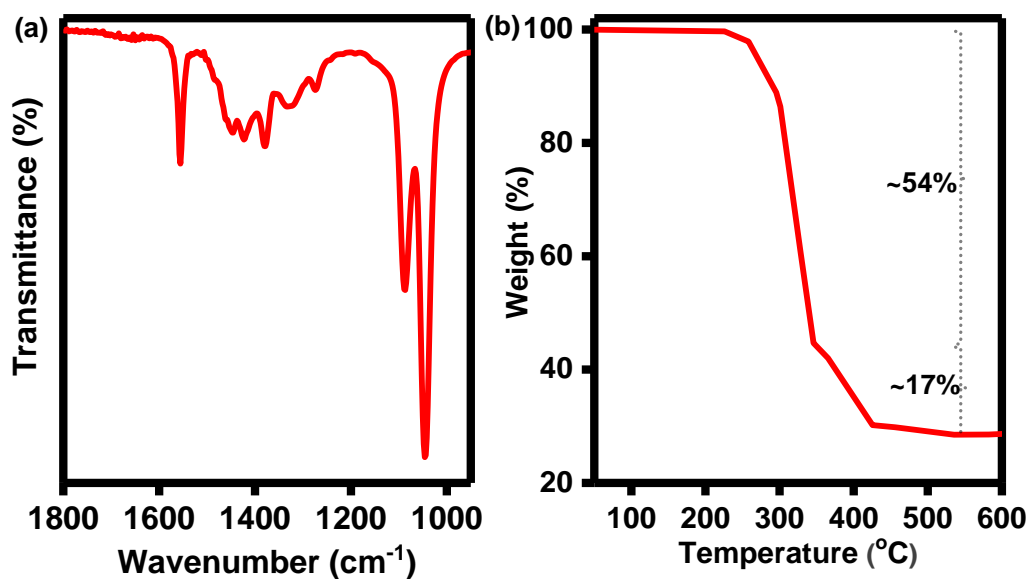


Figure A2.3. (a) FTIR spectrum of mono-substituted indium myristate (**2.3.2c**) showing a shift in carbonyl stretching frequency. (b) TGA thermogram of **2.3.1c** with initial weight loss of ~54% consistent with one myristate group and final weight loss of ~17% consistent with two chloride group.

A2.1.2. Copies of NMR spectra.

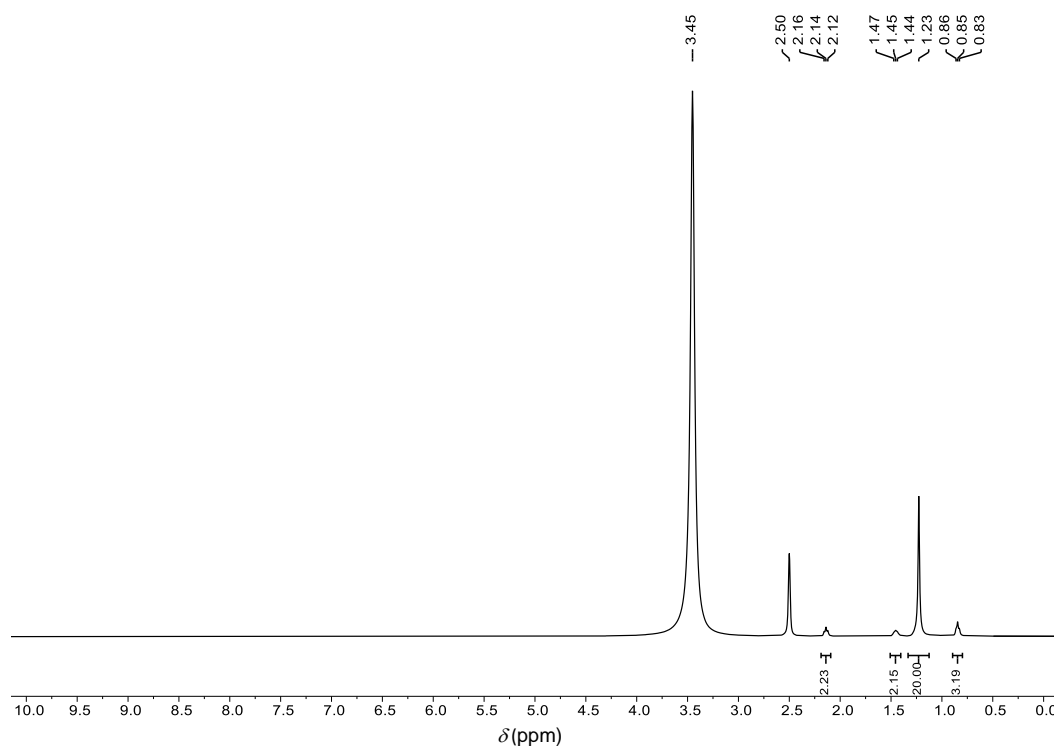


Figure A2.4: ^1H NMR spectrum of potassium myristate (**2.3.1a**) (DMSO- d_6 , 400 MHz)

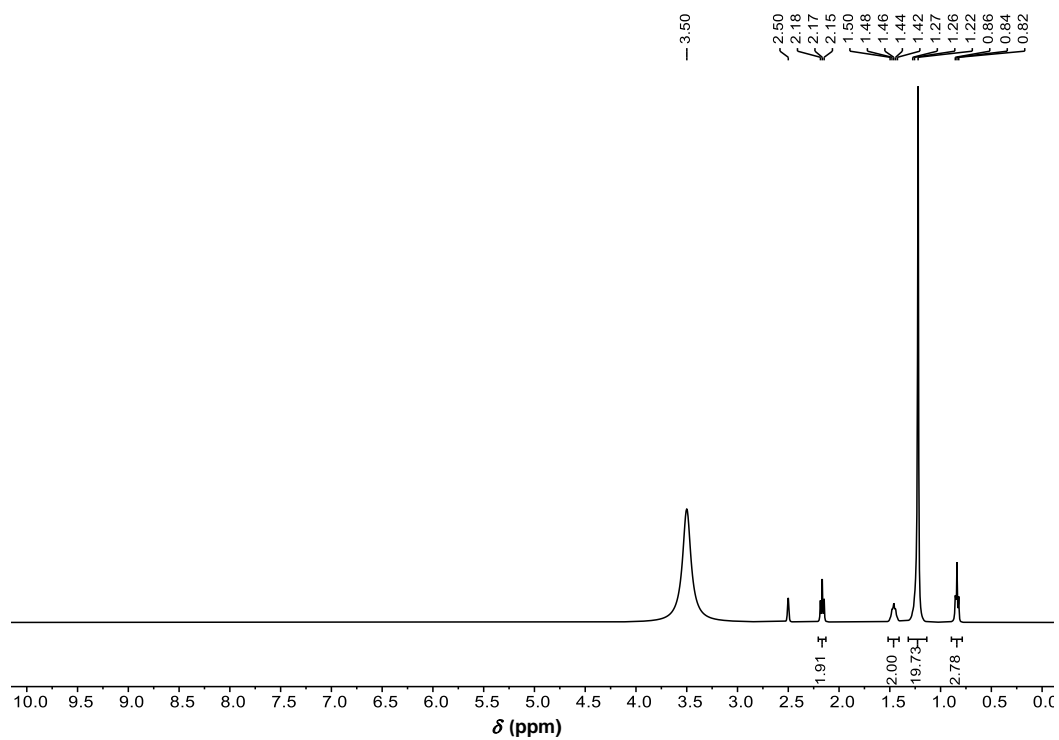


Figure A2.5: ^1H NMR spectrum of sodium myristate (**2.3.1b**) (DMSO- d_6 , 400 MHz)

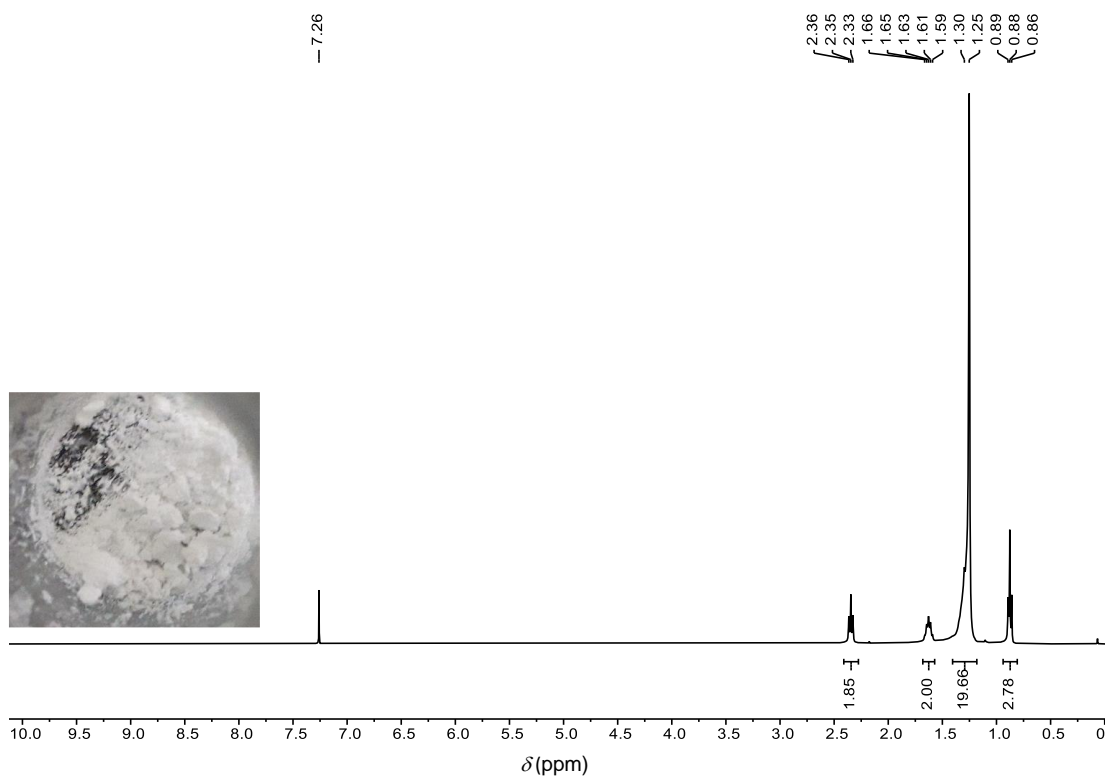


Figure A2.6: ^1H NMR spectrum of indium myristate (**2.3.2a**) (CDCl_3 , 400 MHz).

Inset: Photographic image of **2.3.2a**.

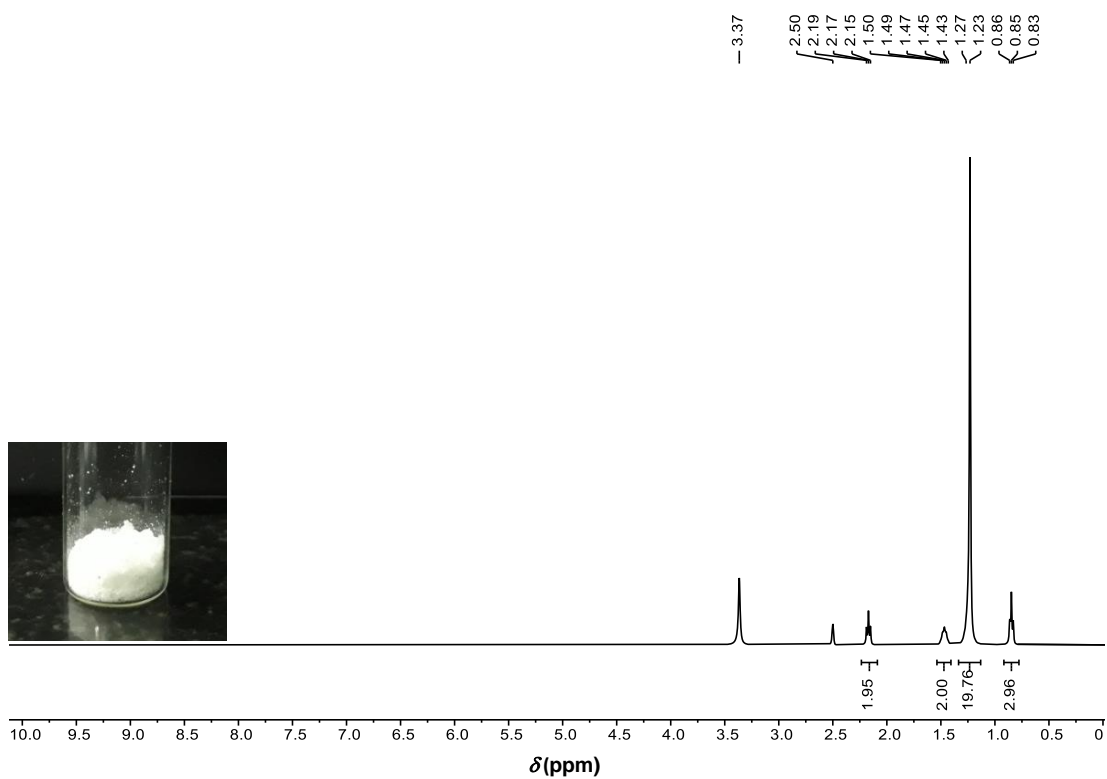


Figure A2.7: ^1H NMR spectrum of di-substituted indium myristate (**2.3.2b**) (DMSO-d_6 , 400 MHz). Inset: Photographic image of **2.3.2b**.

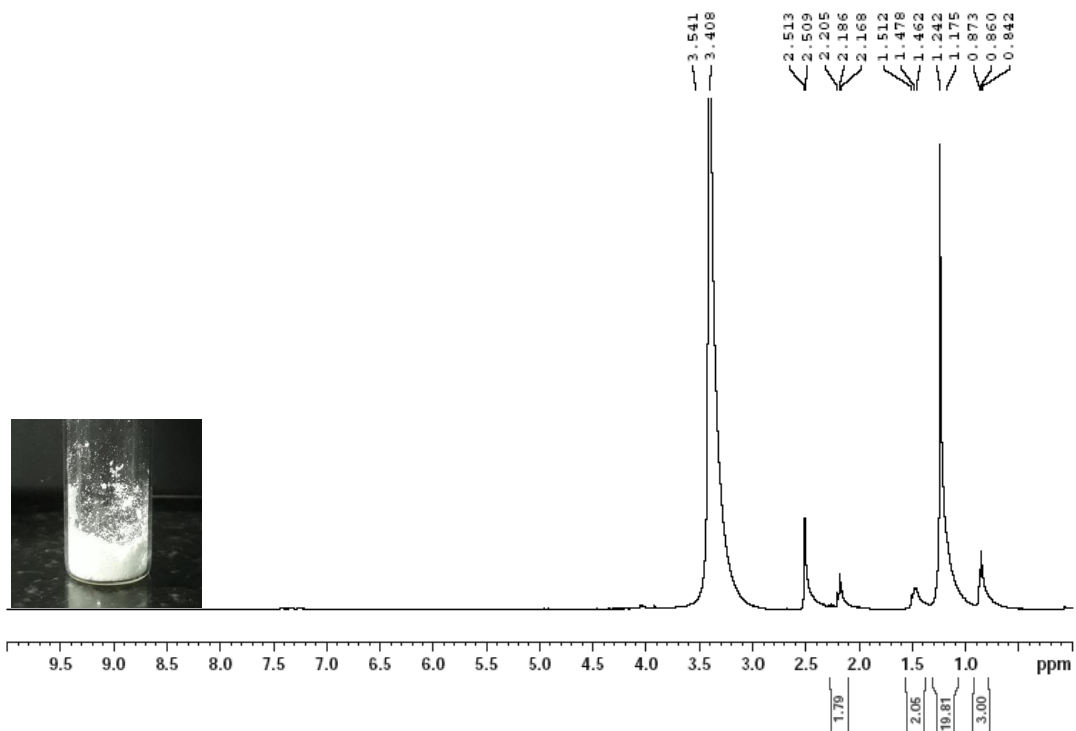


Figure A2.8: ^1H NMR spectrum of mono-substituted indium myristate (**2.3.2c**) (DMSO-d_6 , 400 MHz). Inset: Photographic image of **2.3.2c**.

A2.1.3. Copies of mass spectra

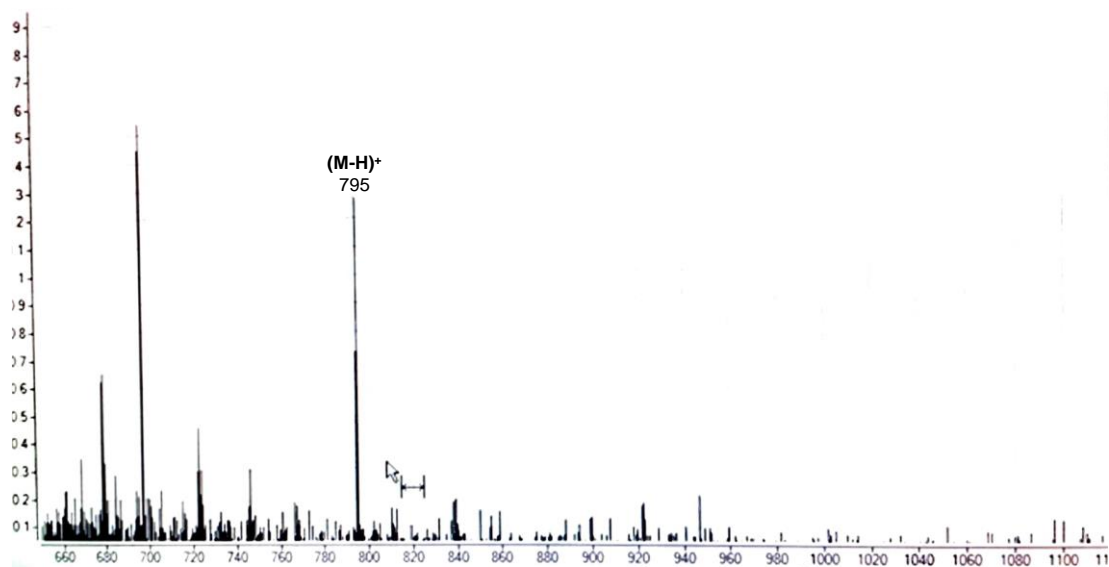


Figure A2.9: Mass spectrum of indium myristate (**2.3.2a**)

A2.2. DBU-catalysed synthesis of MFAs:

A2.2.1. Copies of FTIR spectra and TGA thermogram.

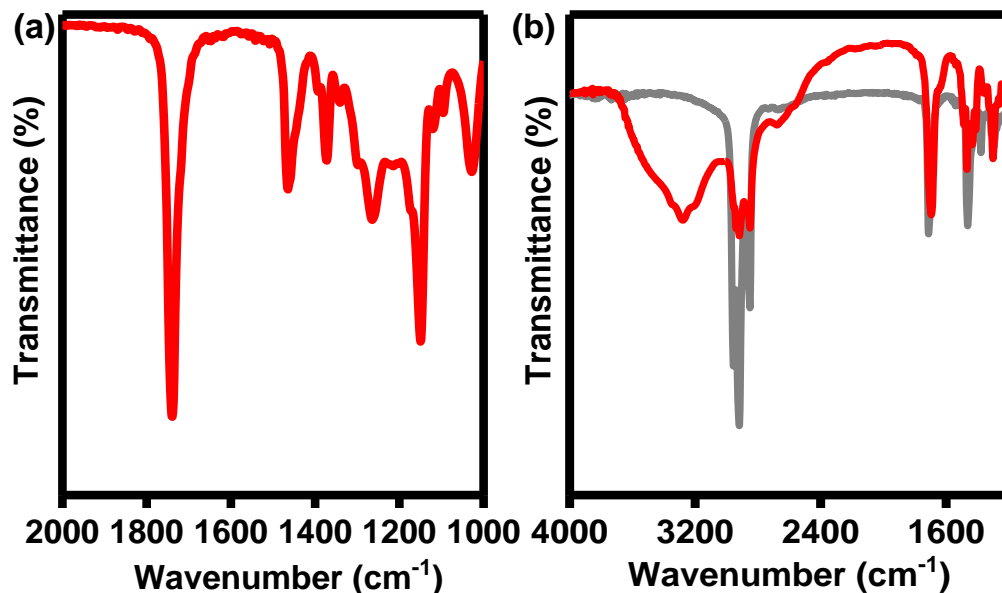


Figure A2.10. FTIR of (a) α -bromomyristic acid (2.4.1e) and (b) 9,10- hydroxystearic acid (2.4.1f, red) compared with stearic acid (grey). A broad peak at 3200-3400 cm^{-1} indicated the addition of -OH groups which are absent in stearic acid.

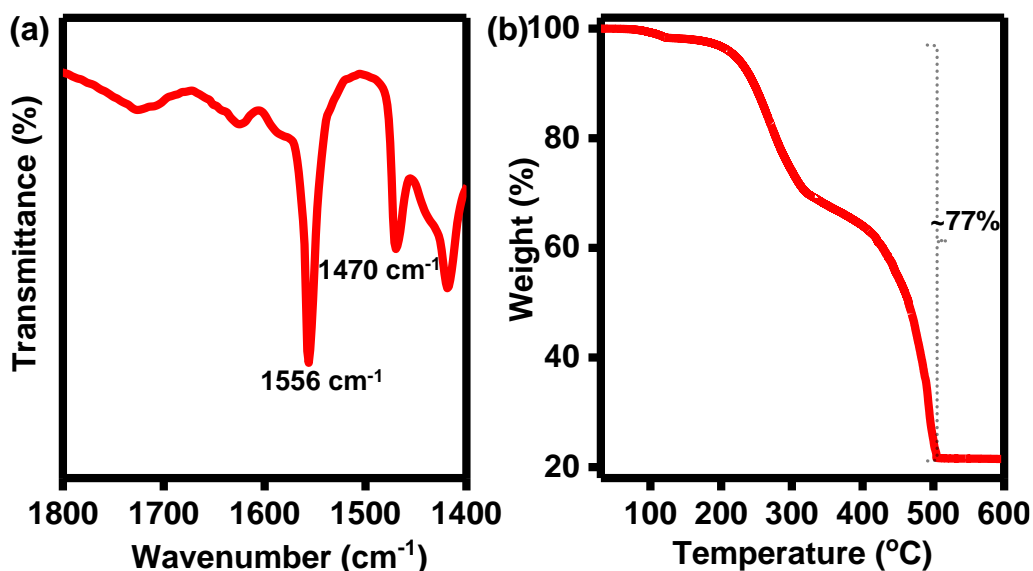


Figure A2.11. (a) FTIR spectrum of potassium stearate (2.4.2b) showing characteristic $-\text{COO}^-$ asymmetric stretching at 1556 cm^{-1} and symmetric stretching at 1470 cm^{-1} . (b) TGA thermogram of potassium stearate (2.4.2b) depicting ~77 % loss of weight in the temperature range 220-510 $^{\circ}\text{C}$ corresponding to one stearate.

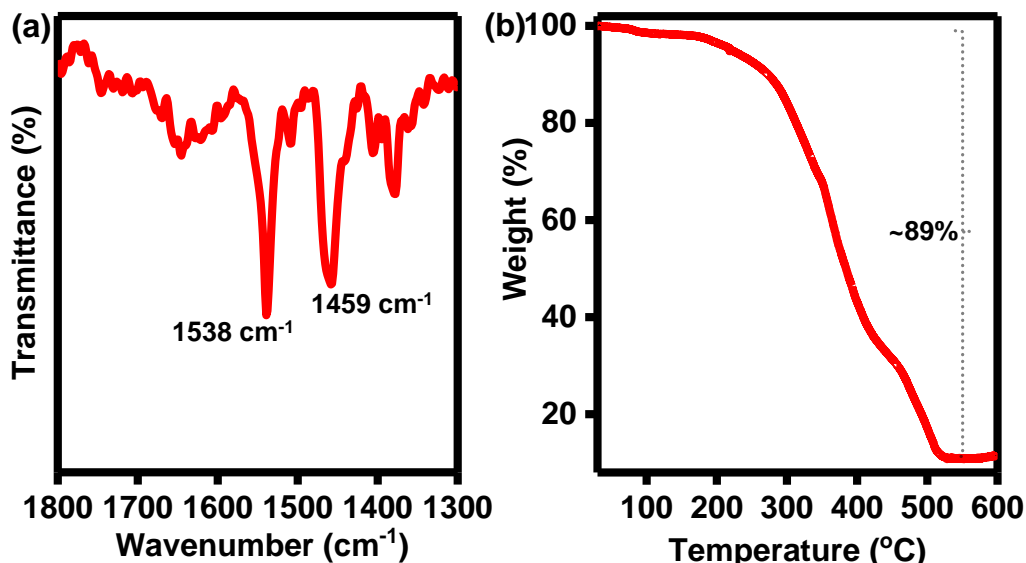


Figure A2.12. (a) FTIR spectrum of magnesium stearate (2.4.2c) depicting characteristic -COO⁻ asymmetric stretching at 1538 cm⁻¹ and symmetric stretching at 1459 cm⁻¹. (b) TGA thermogram of magnesium stearate (2.4.2c) showing ~89 % loss of weight in temperature range 177-520 °C corresponding to two stearates.

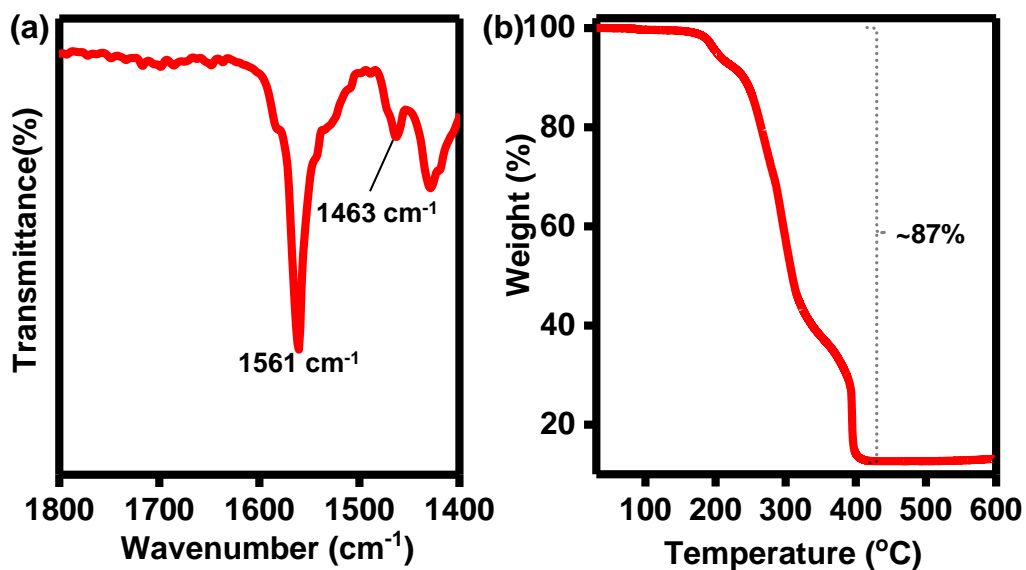


Figure A2.13. (a) FTIR spectrum of manganese stearate (2.4.2d) showing characteristic m-COO⁻ asymmetric stretching at 1561 cm⁻¹ and symmetric stretching at 1463 cm⁻¹. (b) TGA thermogram of manganese stearate (2.4.2d) showing ~87 % loss of weight in temperature range 130-450 °C corresponding to two stearates.

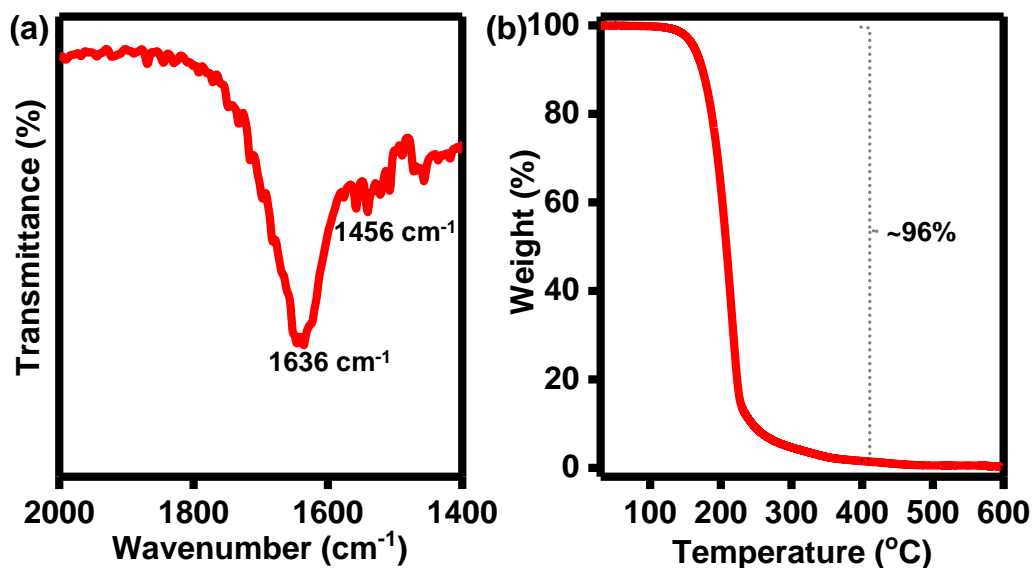


Figure A2.14. (a) FTIR spectrum of ferric stearate (2.4.2e) indicating characteristic -COO⁻ asymmetric stretching at 1636 cm⁻¹ and symmetric stretching at 1456 cm⁻¹. (b) TGA thermogram of ferric stearate (2.4.2e) depicting ~96 % loss of weight in temperature range 140-360 °C consistent with three stearates.

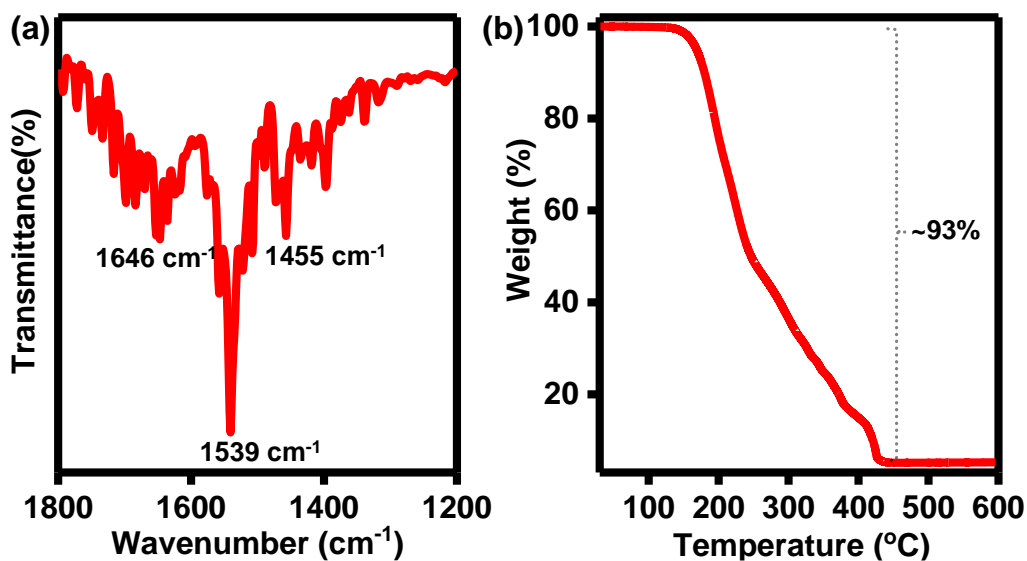


Figure A2.15. (a) FTIR spectrum of cobalt stearate (2.4.2f) showing characteristic -COO⁻ asymmetric stretching at 1646 cm⁻¹ and 1539 cm⁻¹ and symmetric stretching at 1455 cm⁻¹. (b) TGA thermogram of cobalt stearate (2.4.2f) indicating ~93 % loss of weight in temperature range 145-430 °C consistent with two stearates.

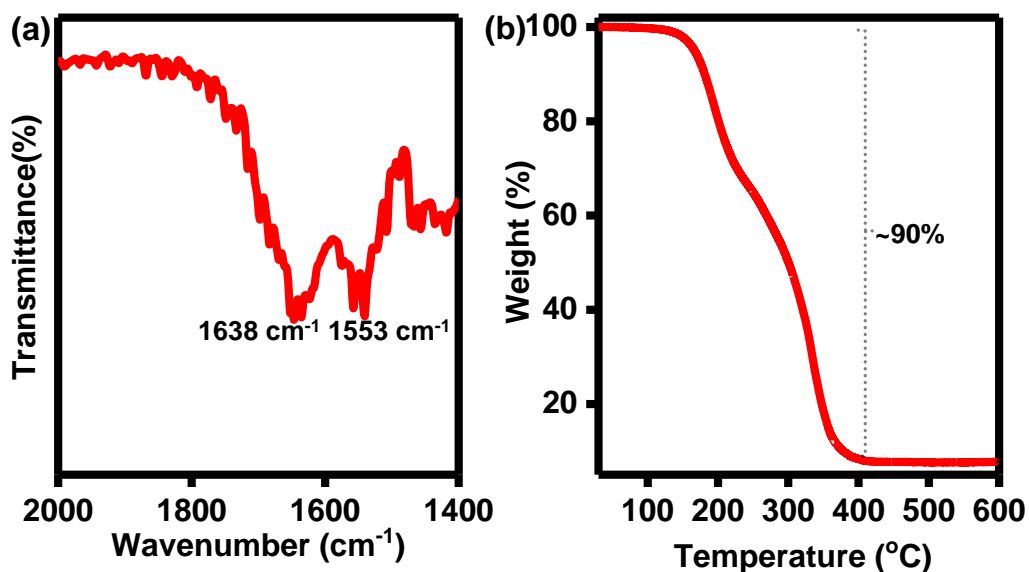


Figure A2.16. (a) FTIR spectrum of nickel stearate (2.4.2g) displaying characteristic -COO⁻ asymmetric stretching at 1638 cm⁻¹ and 1553 cm⁻¹. (b) TGA thermogram of nickel stearate (2.4.2g) depicting ~90 % loss of weight in temperature range 150-410 °C corresponding to two stearates.

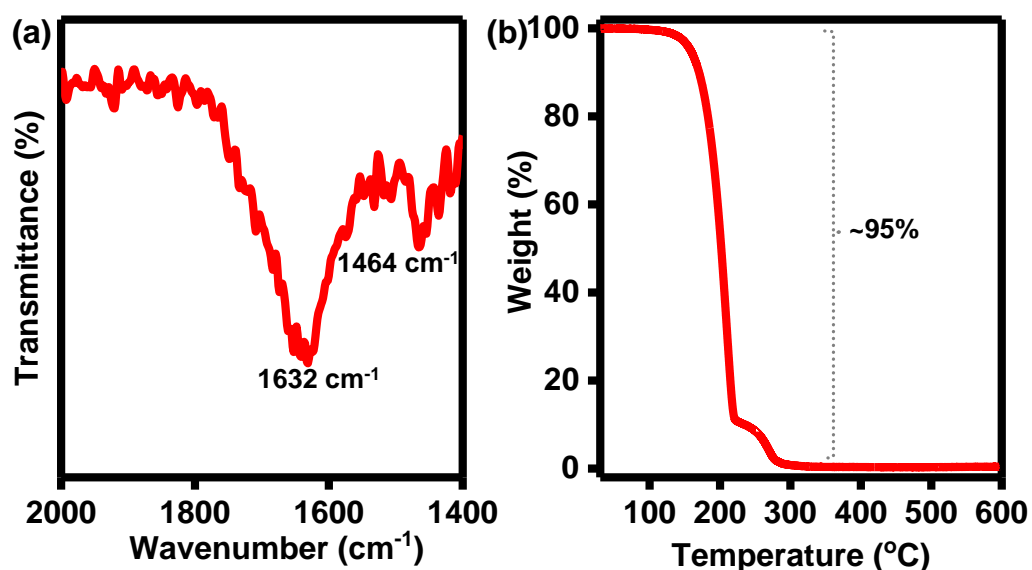


Figure A2.17. (a) FTIR spectrum of copper stearate (2.4.2h) showing characteristic -COO⁻ asymmetric stretching at 1632 cm⁻¹ and symmetric stretching at 1464 cm⁻¹. (b) TGA thermogram of copper stearate (2.4.2h) indicating ~95 % loss of weight in temperature range 140-290 °C corresponding to two stearates.

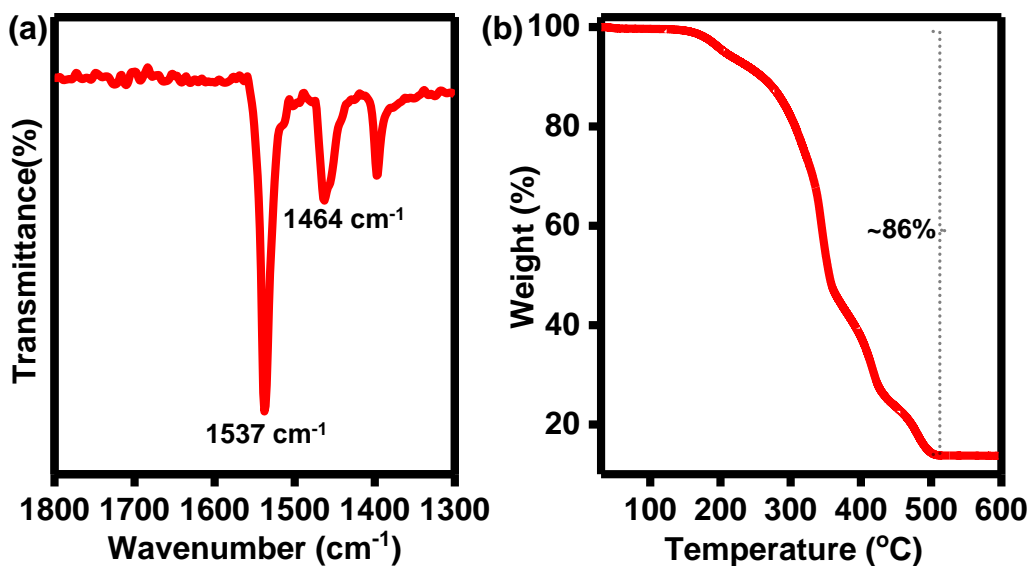


Figure A2.18. (a) FTIR spectrum of zinc stearate (2.4.2i) depicting characteristic -COO⁻ asymmetric stretching at 1537 cm⁻¹ and symmetric stretching at 1464 cm⁻¹. (b) TGA thermogram of zinc stearate (2.4.2i) showing ~86 % loss of weight in the temperature range 170-500 °C corresponding to two stearates.

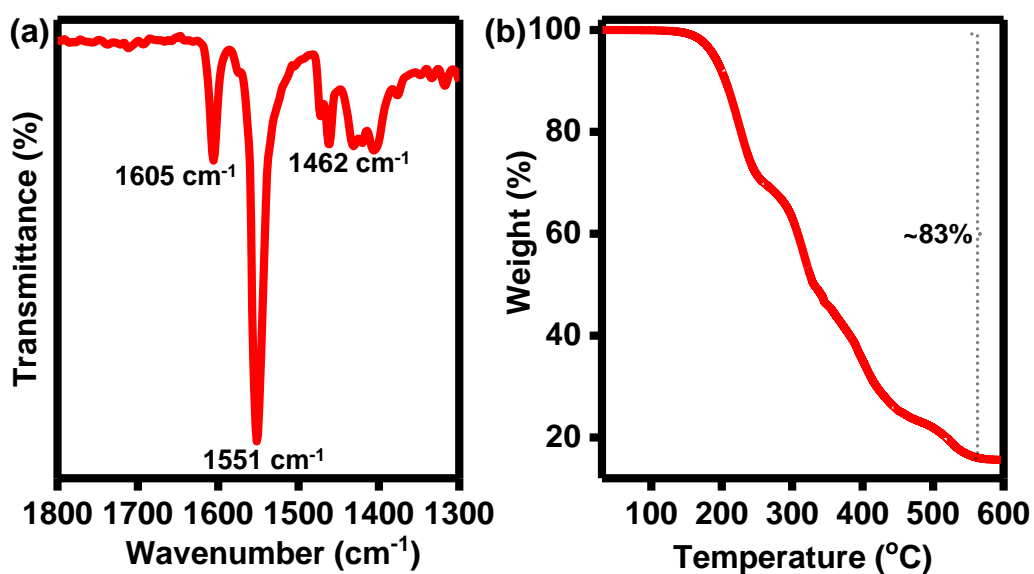


Figure A2.19. (a) FTIR spectrum of cadmium stearate (2.4.2j) indicating characteristic -COO⁻ asymmetric stretching at 1605 cm⁻¹ and 1551 cm⁻¹ and symmetric stretching at 1462 cm⁻¹. (b) TGA thermogram of cadmium stearate (2.4.2j) showing ~83 % loss of weight in the temperature range 160-570 °C corresponding to two stearates.

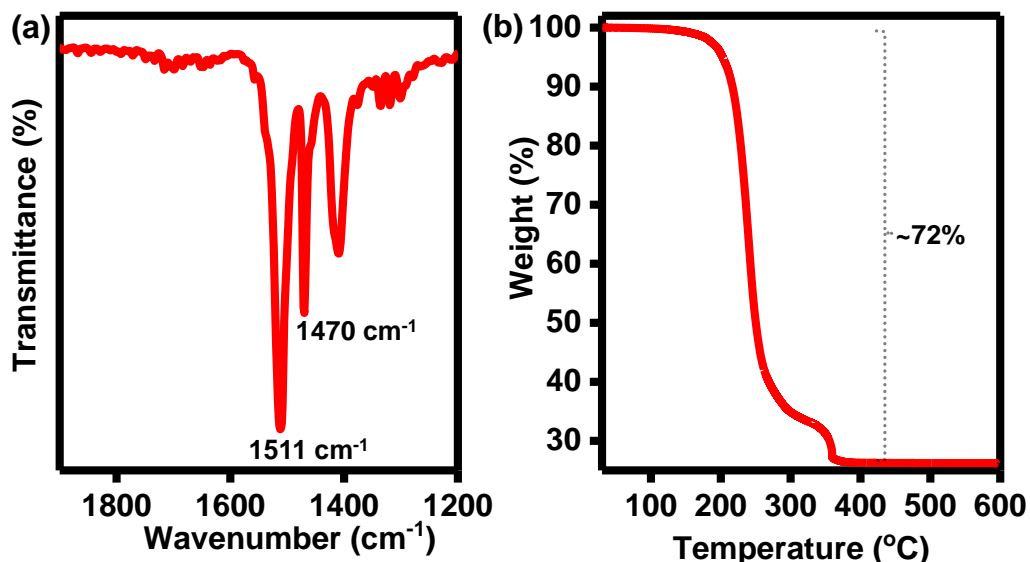


Figure A2.20. (a) FTIR spectrum of silver stearate (2.4.2k) showing characteristic -COO⁻ asymmetric stretching at 1511 cm⁻¹ and symmetric stretching at 1470 cm⁻¹. (b) TGA thermogram of silver stearate (2.4.2k) depicting ~72 % loss of weight in temperature range 180-360 °C consistent with one stearate.

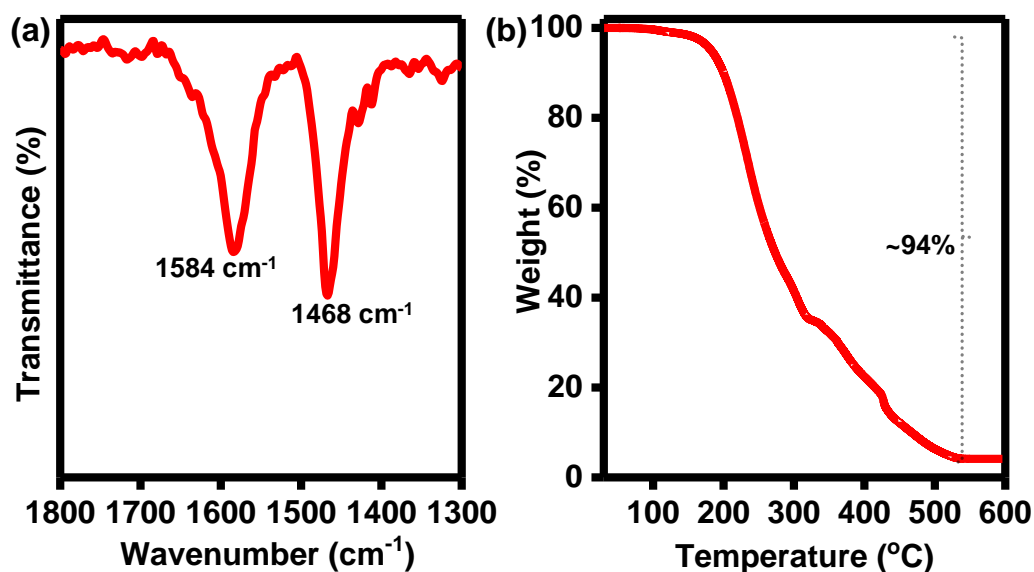


Figure A2.21. (a) FTIR spectrum of aluminium stearate (2.4.2l) showing characteristic -COO⁻ asymmetric stretching at 1584 cm⁻¹ and symmetric stretching at 1468 cm⁻¹. (b) TGA thermogram of aluminium stearate (2.4.2l) indicating ~94 % loss of weight in temperature range 170-530 °C corresponding to three stearates.

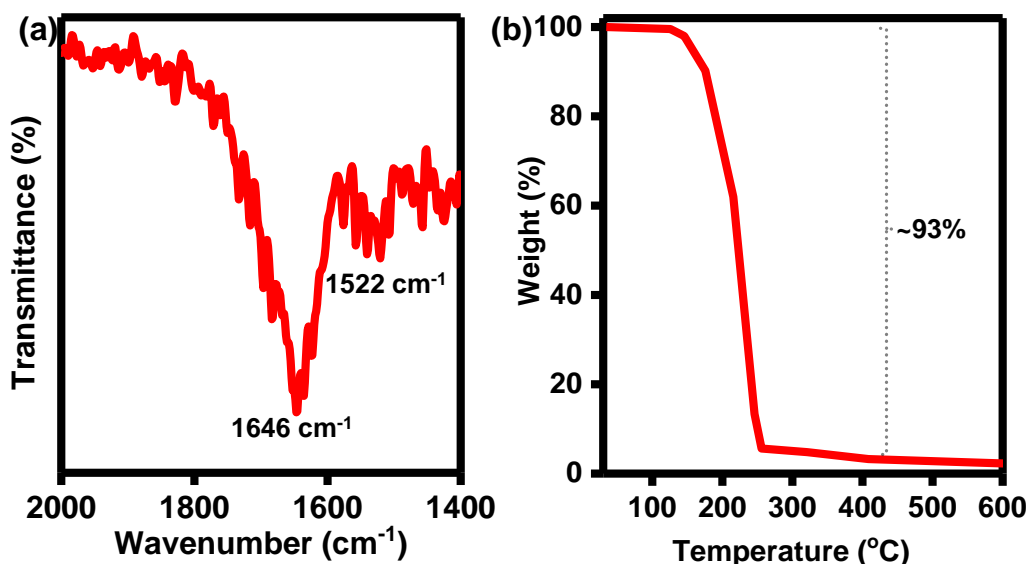


Figure A2.22. (a) FTIR spectrum of gallium stearate (**2.4.2m**) depicting characteristic -COO⁻ asymmetric stretching at 1646 cm⁻¹ and 1522 cm⁻¹. (b) TGA thermogram of gallium stearate (**2.4.2m**) showing ~93 % loss of weight in the temperature range 130-260 °C corresponding to three stearates

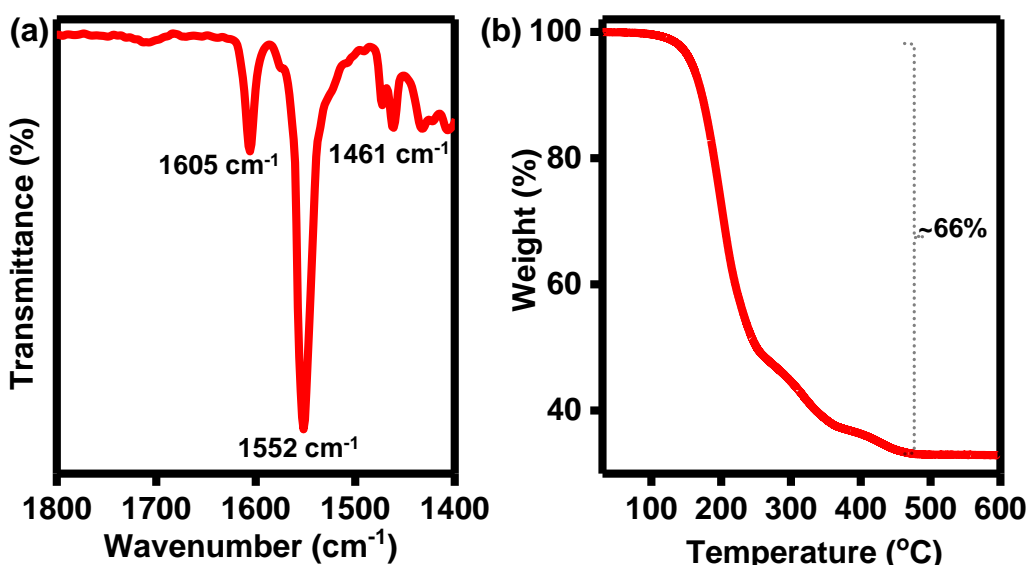


Figure A2.23. (a) FTIR spectrum of tin stearate (**2.4.2n**) indicating characteristic -COO⁻ asymmetric stretching at 1605 cm⁻¹ and 1552 cm⁻¹ and symmetric stretching at 1461 cm⁻¹. (b) TGA thermogram of tin stearate (**2.4.2n**) displaying ~66 % loss of weight in the temperature range 130-470 °C corresponding to two stearates.

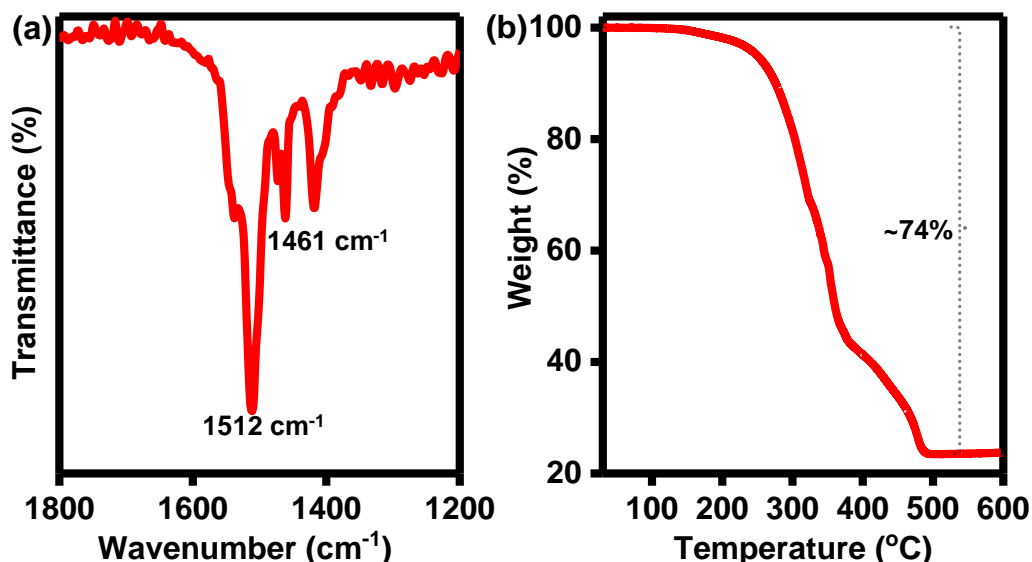


Figure A2.24. (a) FTIR spectrum of lead stearate (**2.4.2o**) showing asymmetric -COO^- asymmetric stretching at 1512 cm^{-1} and symmetric stretching at 1461 cm^{-1} . (b) TGA thermogram of lead stearate (**2.4.2o**) displaying $\sim 74\%$ loss of weight in temperature range $210\text{-}490\text{ }^\circ\text{C}$ corresponding to two stearates.

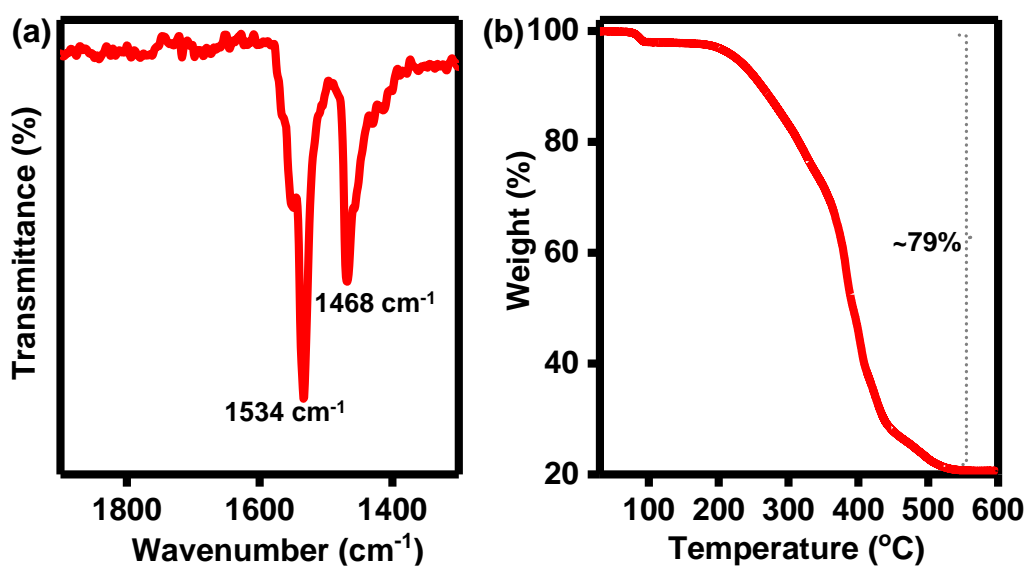


Figure A2.25. (a) FTIR spectrum of gadolinium stearate (**2.4.2p**) showing characteristic -COO^- asymmetric stretching at 1534 cm^{-1} and symmetric stretching at 1468 cm^{-1} . (b) TGA thermogram of gadolinium stearate (**2.4.2p**) displaying $\sim 79\%$ loss of weight in the temperature range $200\text{-}540\text{ }^\circ\text{C}$ corresponding to three stearates.

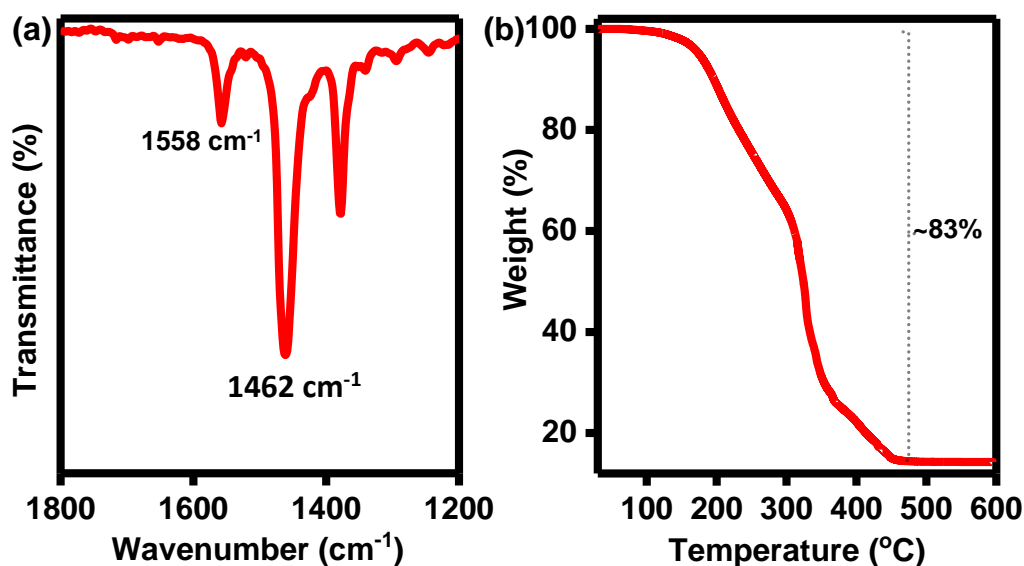


Figure A2.26. (a) FTIR spectrum of indium myristate (2.4.2q) indicating characteristic -COO⁻ asymmetric stretching at 1558 cm⁻¹ and symmetric stretching at 1462 cm⁻¹. (b) TGA thermogram of indium myristate (2.4.2q) depicting ~83 % loss of weight in the temperature range 160-450 °C corresponding to three myristates.

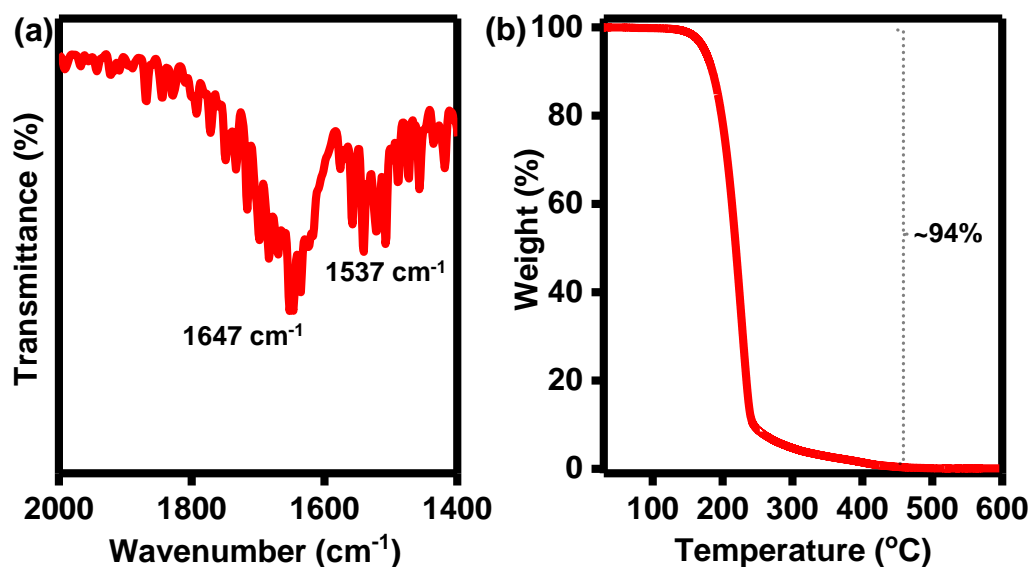


Figure A2.27. (a) FTIR spectrum of indium palmitate (2.4.2r) showing characteristic -COO⁻ asymmetric stretching at 1647 cm⁻¹ and 1537 cm⁻¹. (b) TGA thermogram of indium palmitate (2.4.2r) displaying ~94 % loss of weight in the temperature range 152-450 °C corresponding to three palmitates.

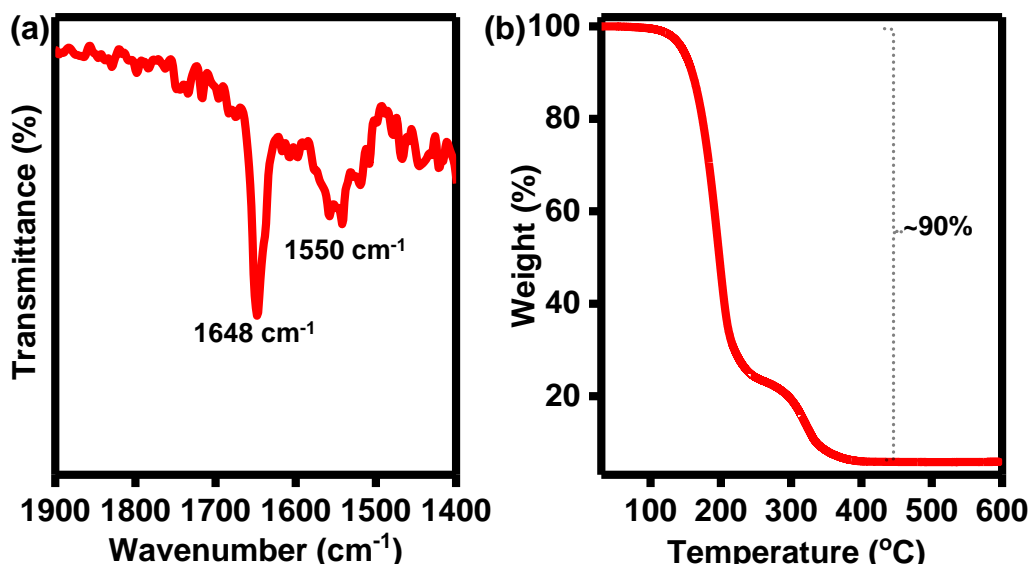


Figure A2.28. (a) FTIR spectrum of indium laurate (**2.4.2s**) showing characteristic -COO⁻ asymmetric stretching at 1648 cm⁻¹ and 1550 cm⁻¹. (b) TGA thermogram of indium laurate (**2.4.2s**) depicting ~90 % loss of weight in the temperature range 130-400 °C corresponding to three laurates.

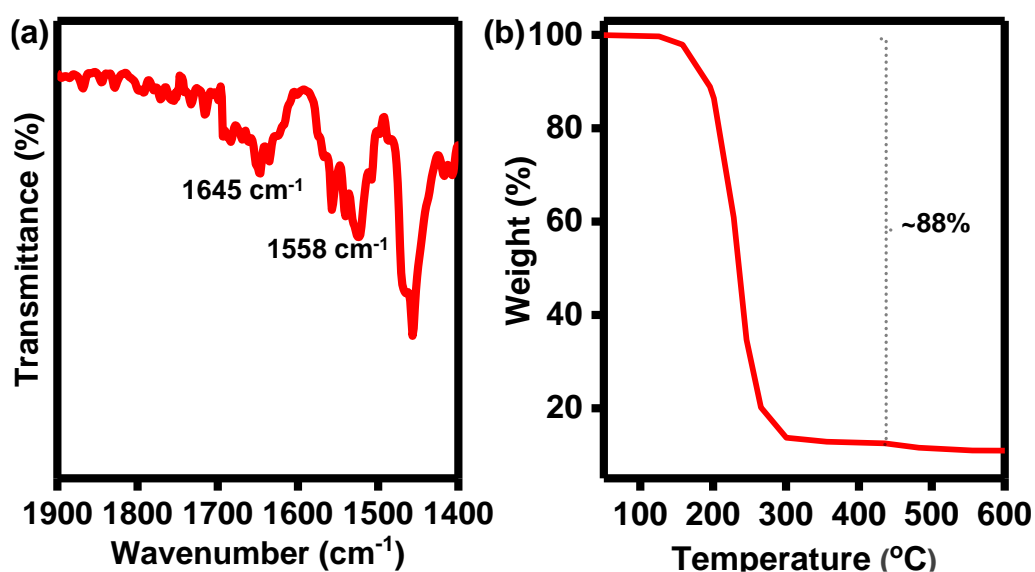


Figure A2.29. (a) FTIR spectrum of Indium (α -bromomyristate)₃ (**2.4.2t**) showing characteristic -COO⁻ asymmetric stretching at 1645 cm⁻¹ and 1558 cm⁻¹. (b) TGA thermogram of Indium (α -bromomyristate)₃ (**2.4.2t**) displaying ~88 % loss of weight in the temperature range 155-308 °C corresponding to three α -bromomyristate.

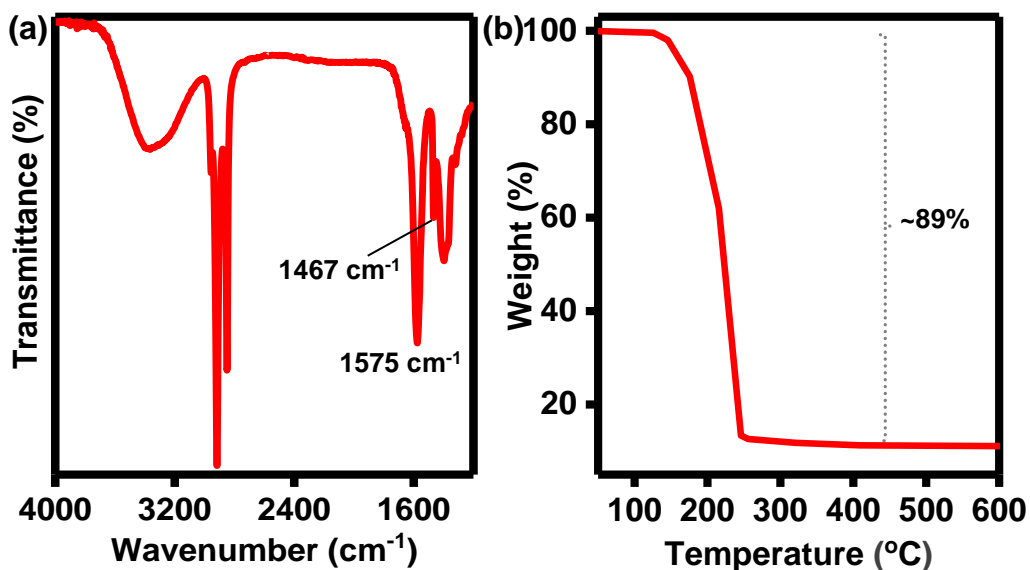


Figure A2.30. (a) FTIR spectrum of Indium (9, 10- hydroxystearate)₃ (2.4.2u) showing characteristic -COO⁻ asymmetric stretching at 1575 cm⁻¹ and 1467 cm⁻¹. (b) TGA thermogram of Indium (9, 10- hydroxystearate)₃ (2.4.2u) displaying ~90 % loss of weight in the temperature range 130-250 °C corresponding to three 9, 10- hydroxystearate.

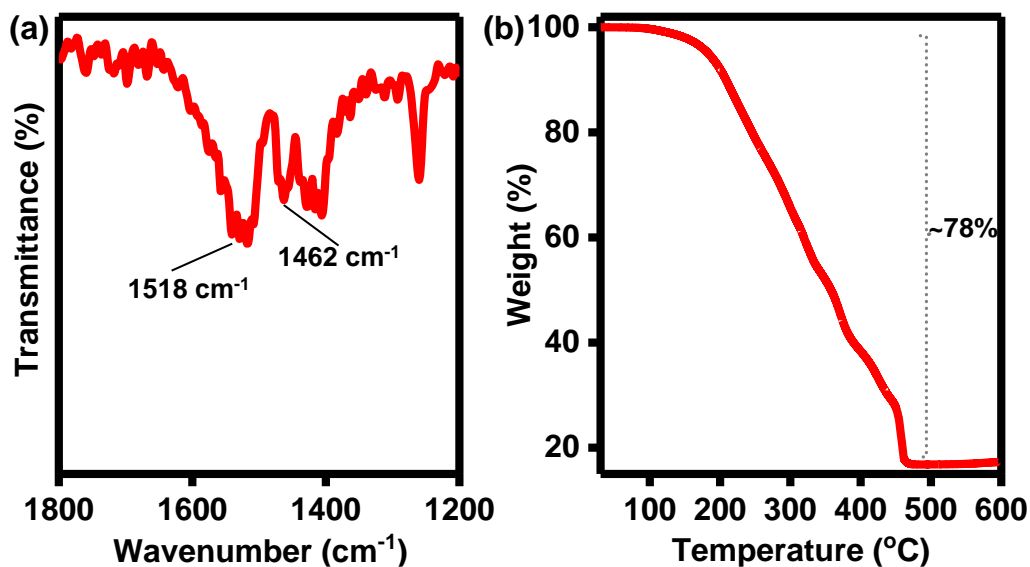
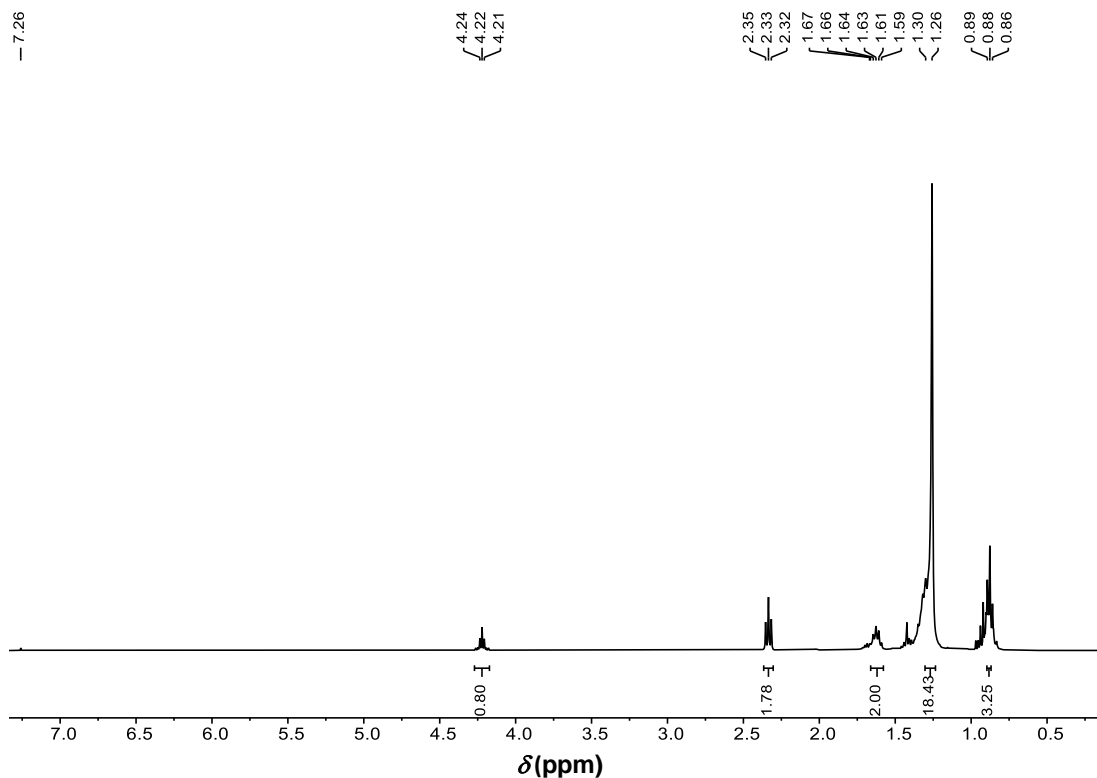
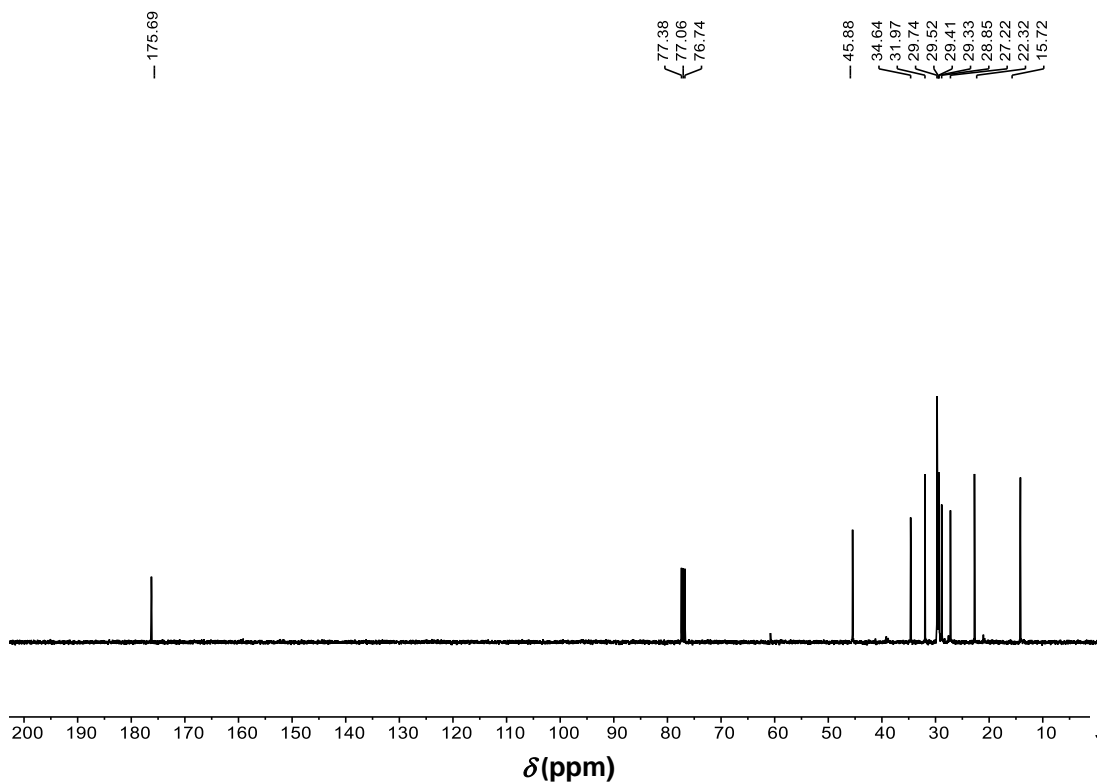


Figure A2.31. (a) FTIR spectrum of lead oleate (2.4.2v) showing characteristic -COO⁻ asymmetric stretching at 1518 cm⁻¹ and symmetric stretching at 1462 cm⁻¹. (b) TGA thermogram of lead oleate (2.4.2v) indicating ~78 % loss of weight in the temperature range 170-470 °C corresponding to two oleates.

A2.2.2. Copies of NMR spectra.**A2.2.2.1. For acid precursors.****Figure A2.32.** ^1H NMR of α -bromomyristic acid (**2.4.1e**) (CDCl_3 , 400 MHz)**Figure A2.33.** ^{13}C $\{^1\text{H}\}$ NMR of α -bromomyristic acid (**2.4.1e**) (CDCl_3 , 100 MHz)

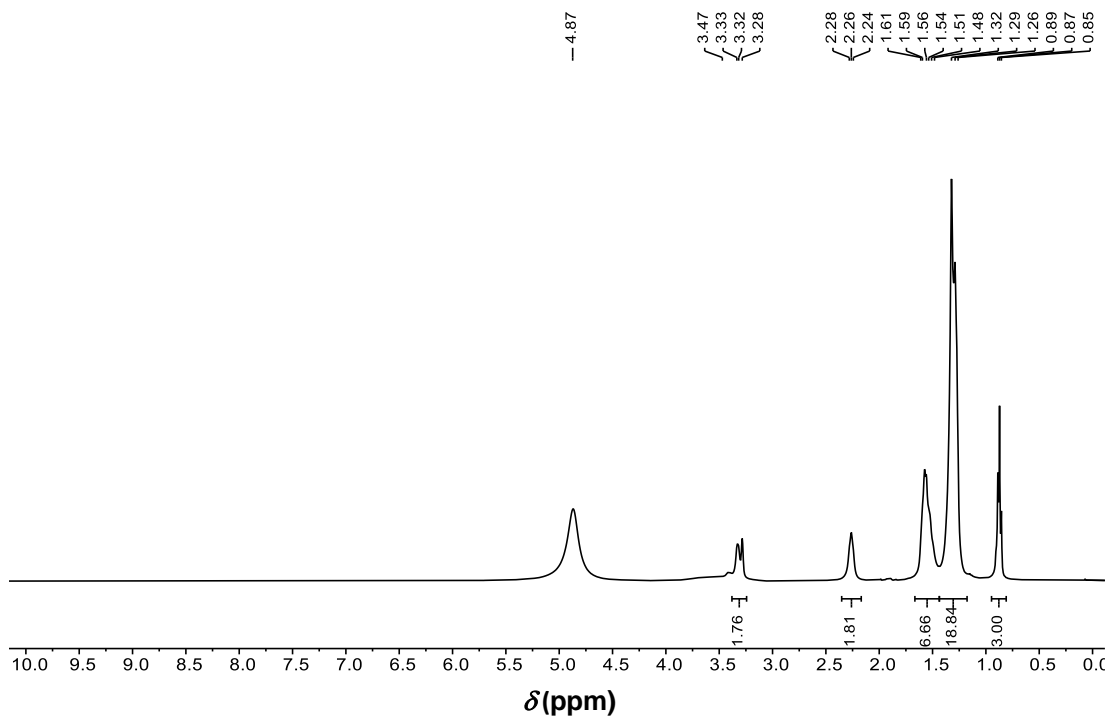


Figure A2.34. ^1H NMR of 9,10- hydroxystearic acid (**2.4.1f**) (CD_3OD , 400 MHz)

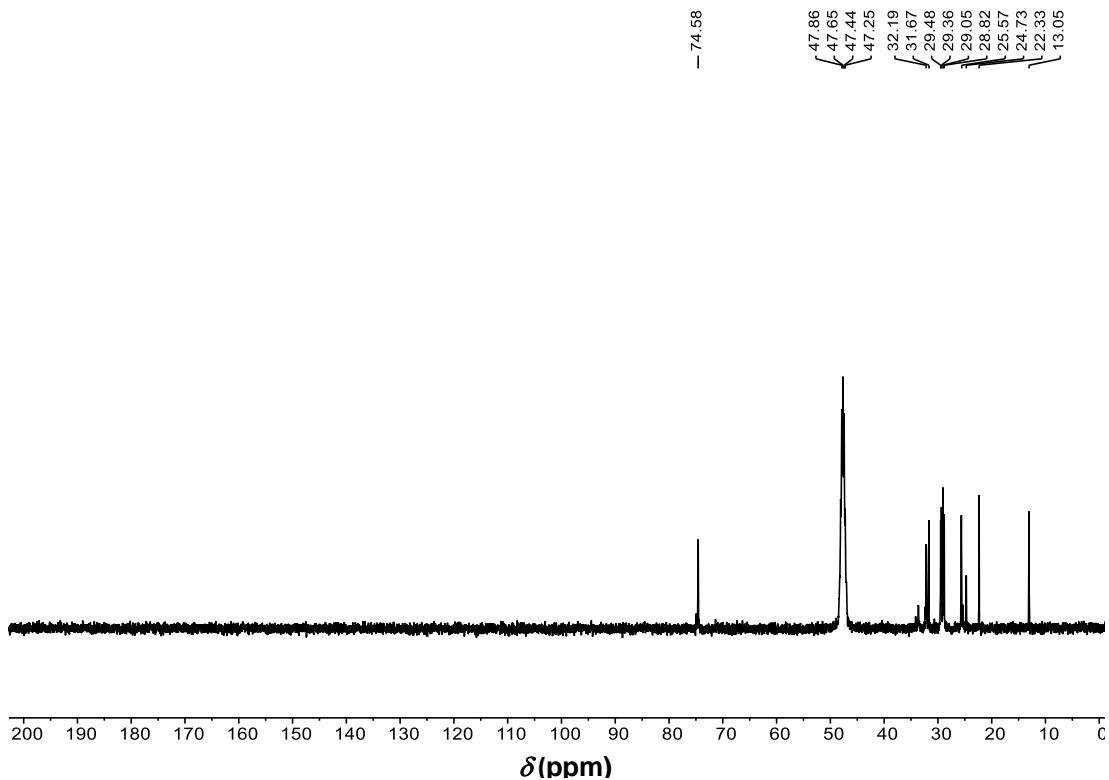


Figure A2.35. ^{13}C $\{^1\text{H}\}$ NMR of 9,10- hydroxystearic acid (**2.4.1f**) (CD_3OD , 100 MHz)

A2.2.2.1. For MFAs. *NMR were determined for MFAs with diamagnetic metals.

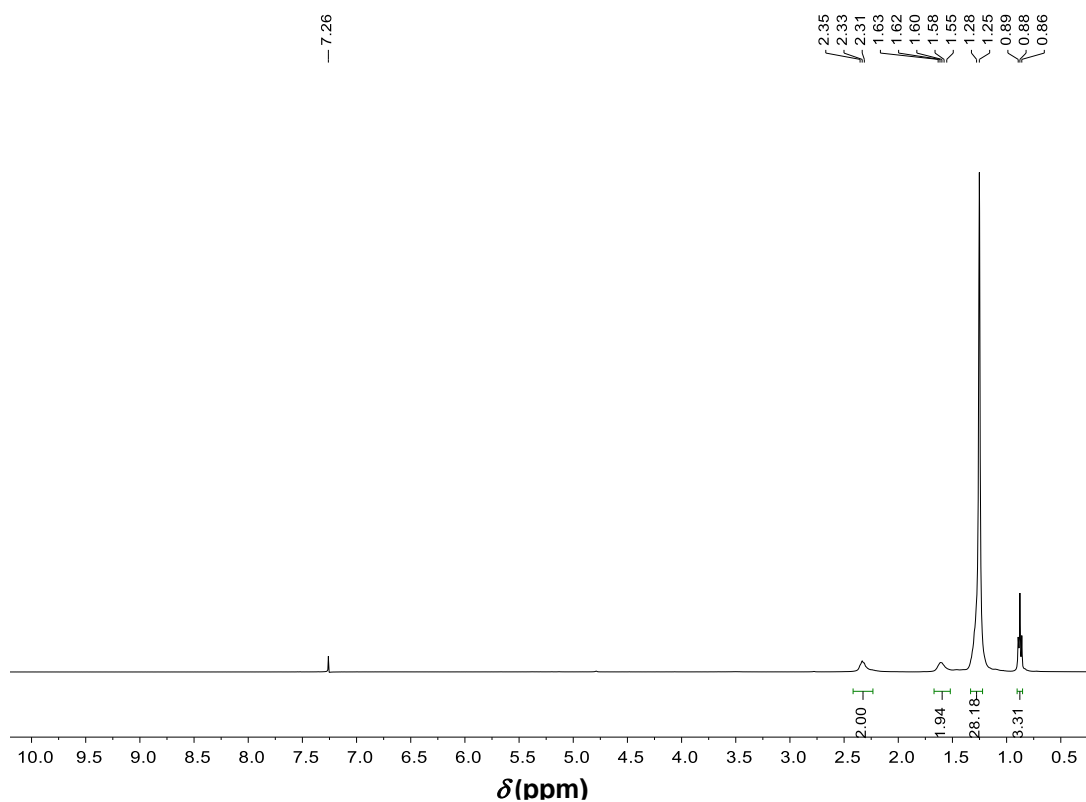


Figure A2.36. ^1H NMR spectrum of indium stearate (2.4.2a) (400 MHz, CDCl_3)

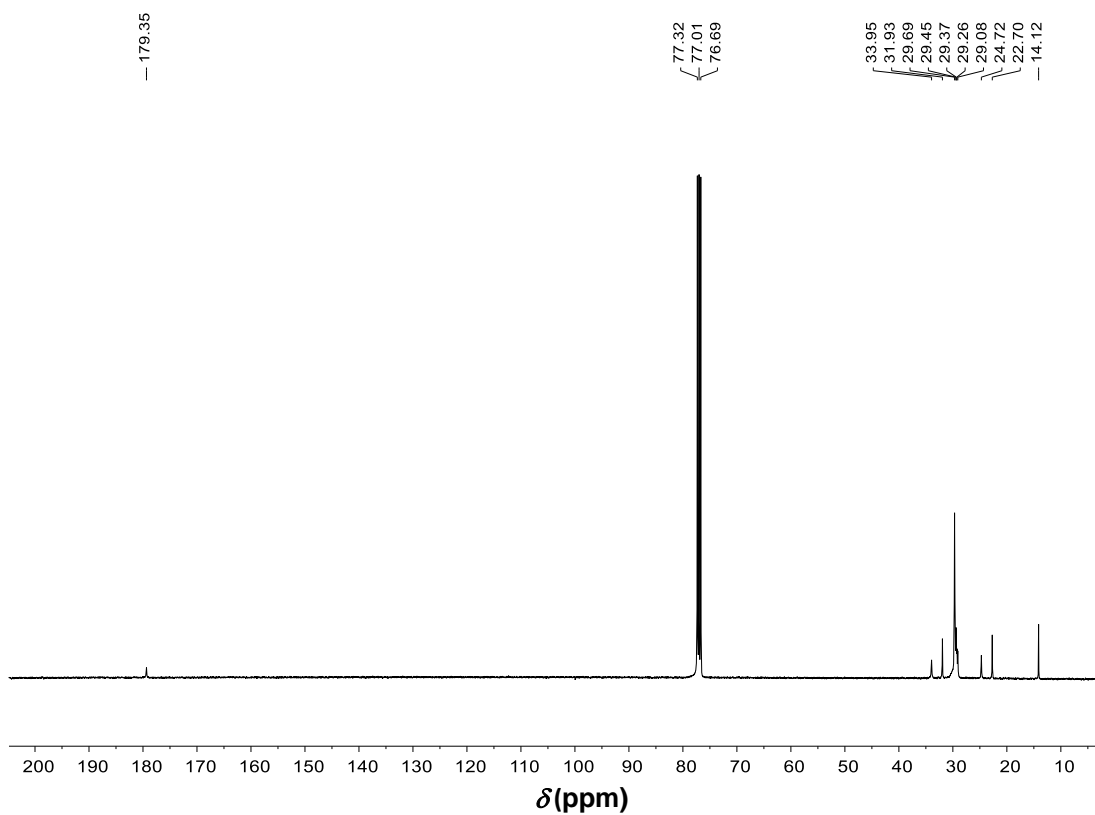


Figure A2.37. ^{13}C $\{^1\text{H}\}$ NMR spectrum of indium stearate (2.4.2a) (100 MHz, CDCl_3)

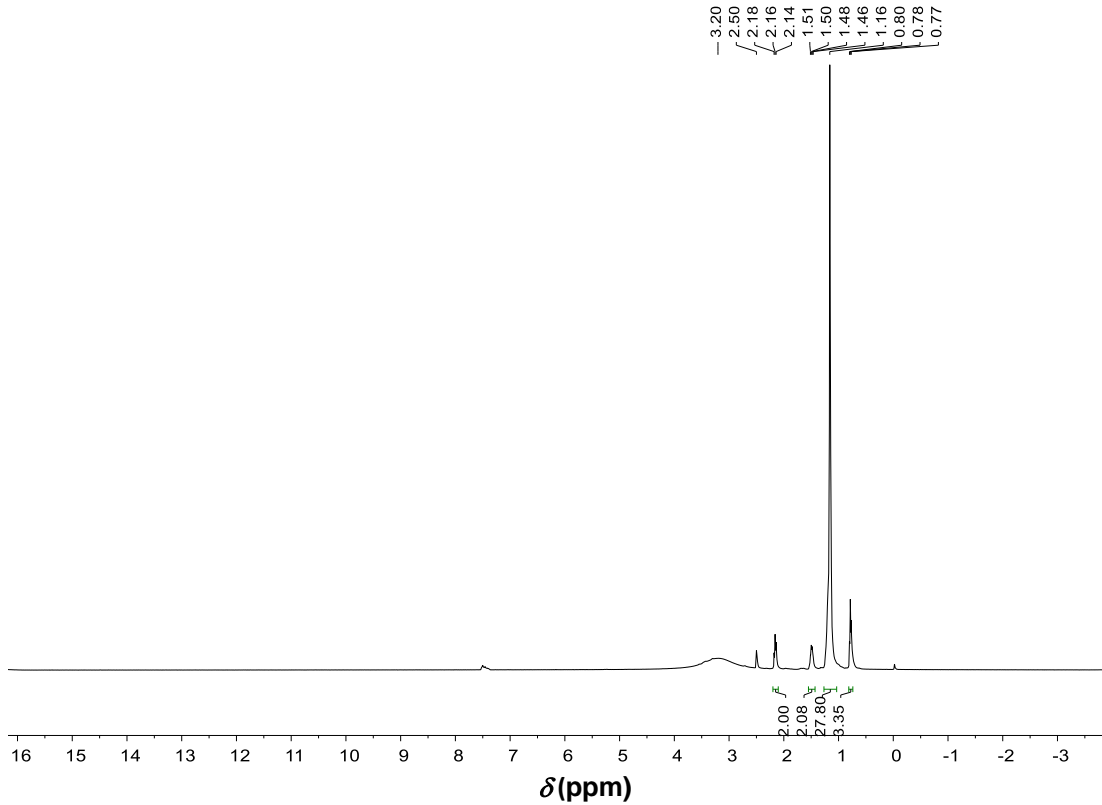


Figure A2.38. ^1H NMR of potassium stearate (2.4.2b) (CDCl_3 , DMSO-d_6 , 400 MHz)

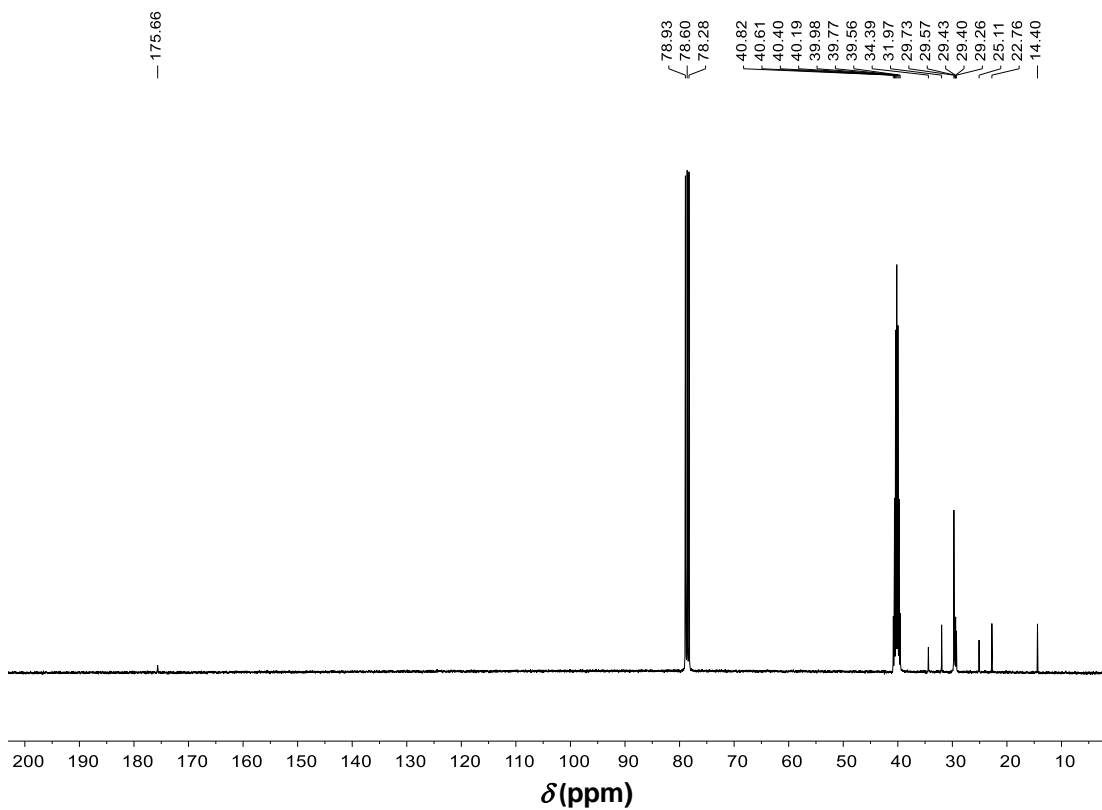


Figure A2.39. ^{13}C $\{^1\text{H}\}$ NMR of potassium stearate (2.4.2b) (CDCl_3 , DMSO-d_6 , 100 MHz)

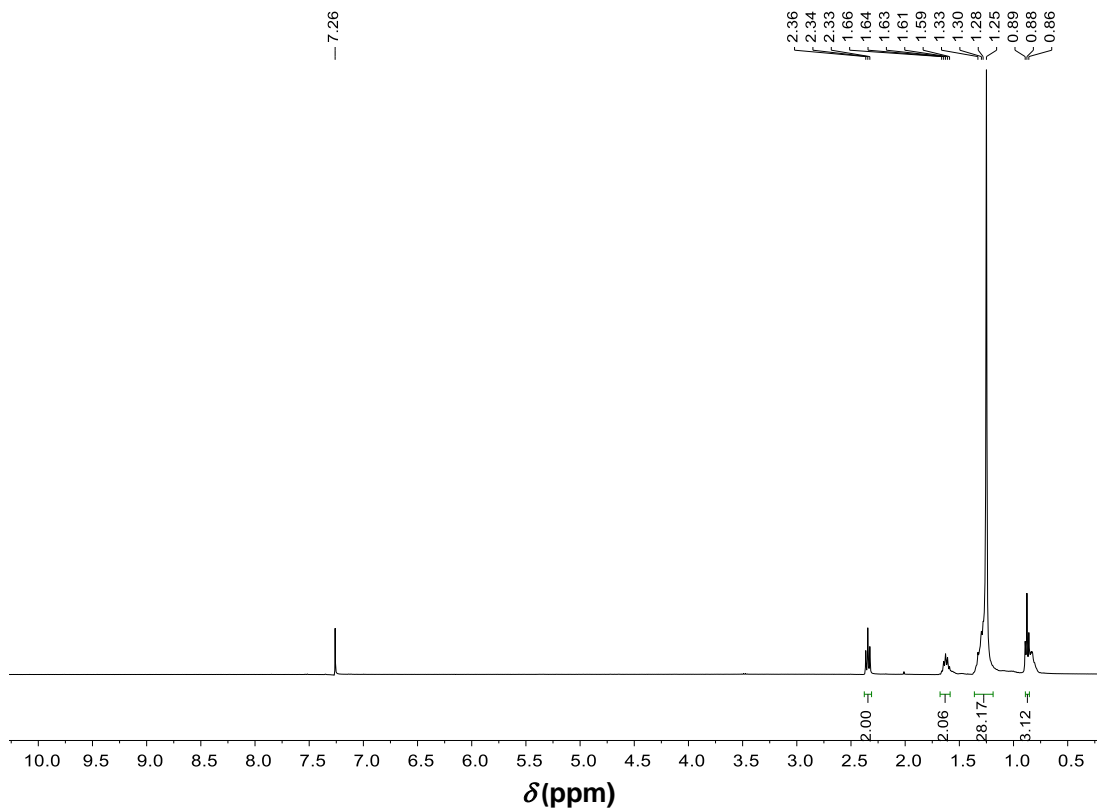


Figure A2.40. ^1H NMR of magnesium stearate (**2.4.2c**) (CDCl_3 , 400 MHz)

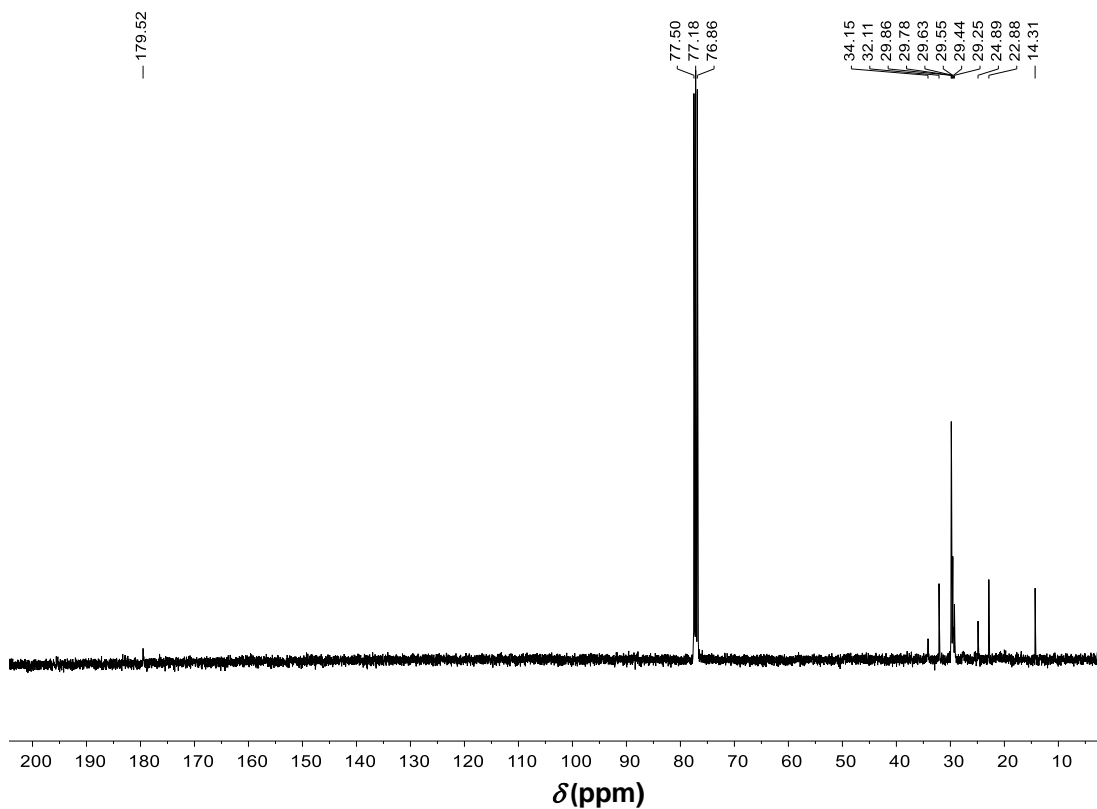


Figure A2.41. ^{13}C $\{^1\text{H}\}$ NMR of magnesium stearate (**2.4.2c**) (CDCl_3 , 100 MHz)

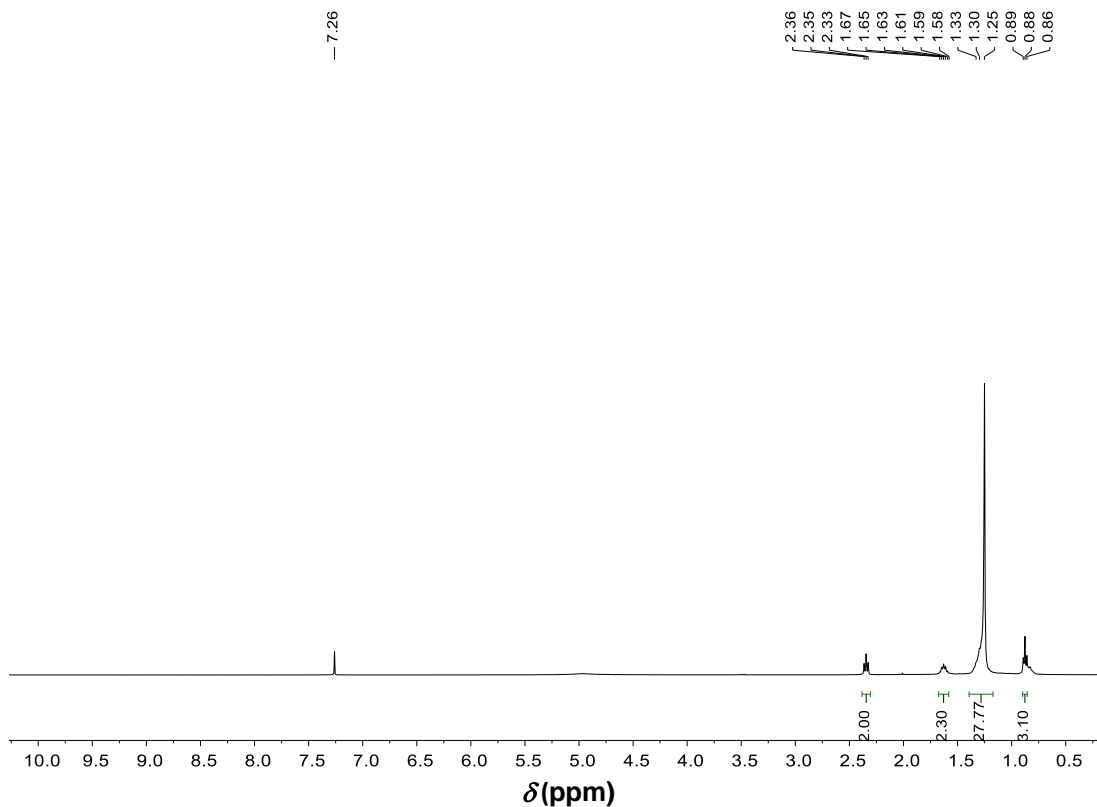


Figure A2.42. ^1H NMR of zinc stearate (2.4.2i) (CDCl_3 , 400 MHz)

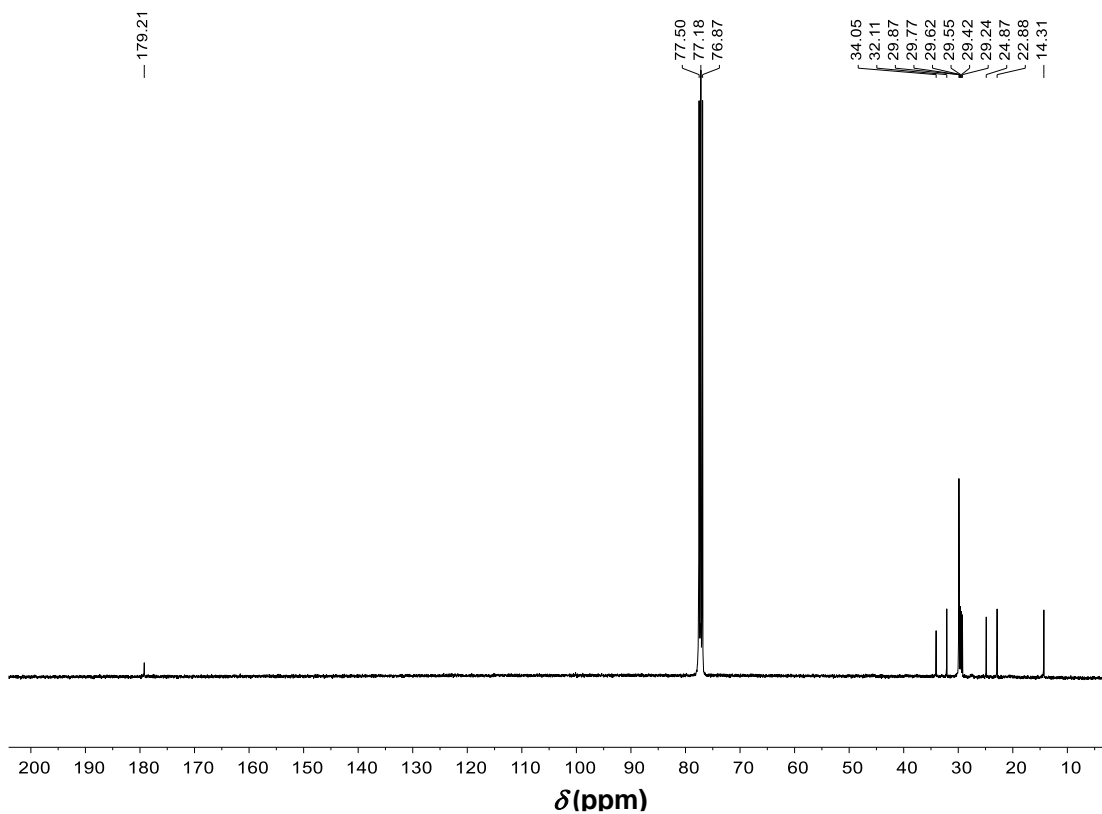


Figure A2.43. ^{13}C $\{^1\text{H}\}$ NMR of zinc stearate (2.4.2i) (CDCl_3 , 100 MHz)

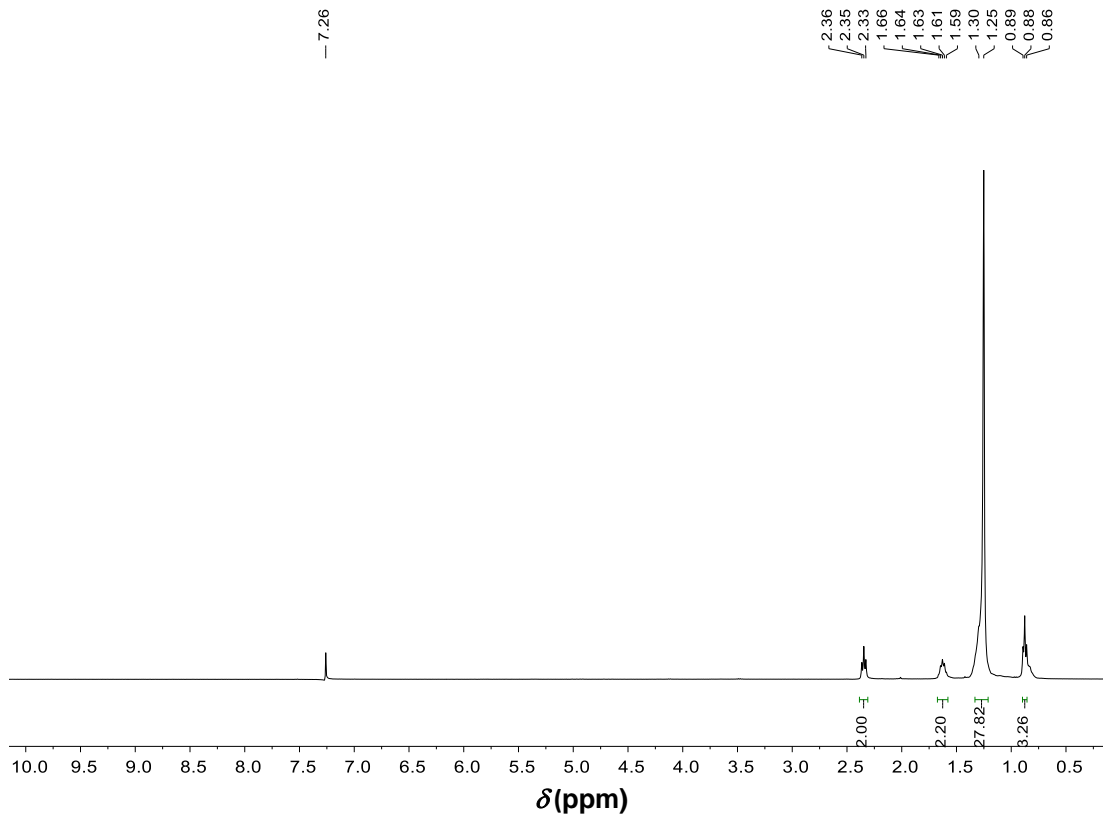


Figure A2.44. ^1H NMR of cadmium stearate (2.4.2j) (CDCl_3 , 400 MHz)

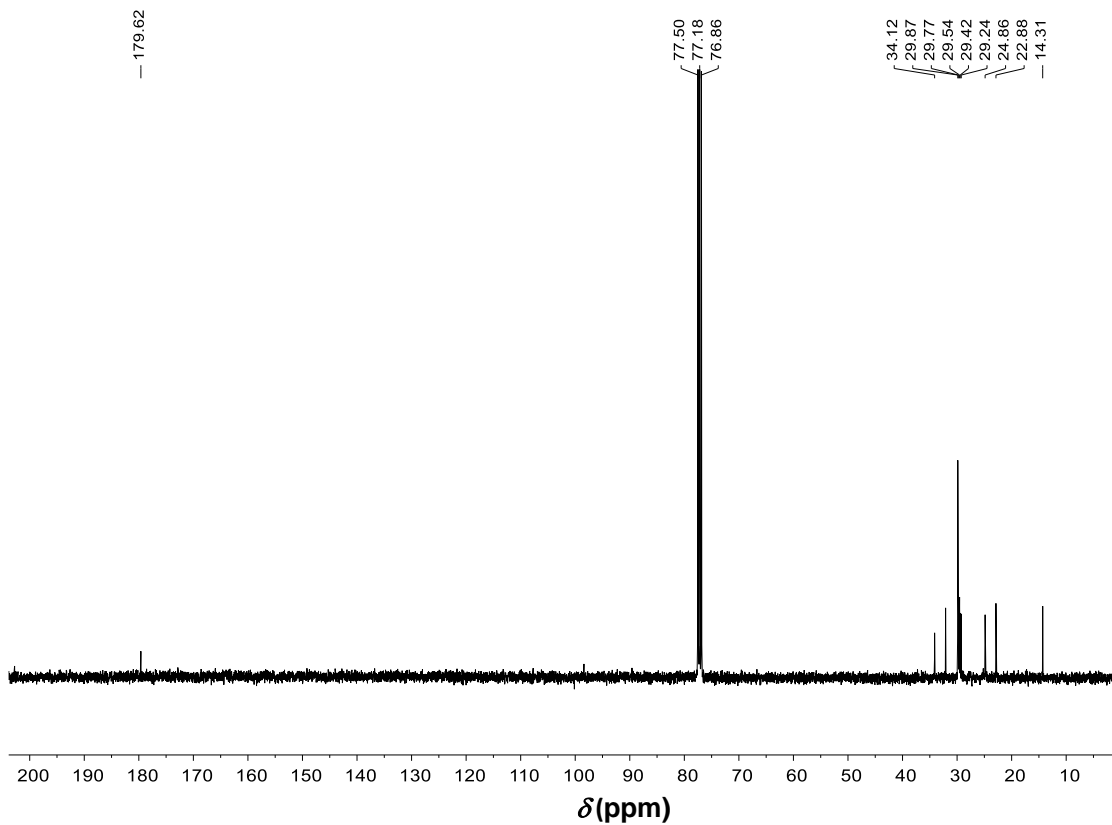


Figure A2.45. ^{13}C $\{^1\text{H}\}$ NMR of cadmium stearate (2.4.2j) (CDCl_3 , 100 MHz)

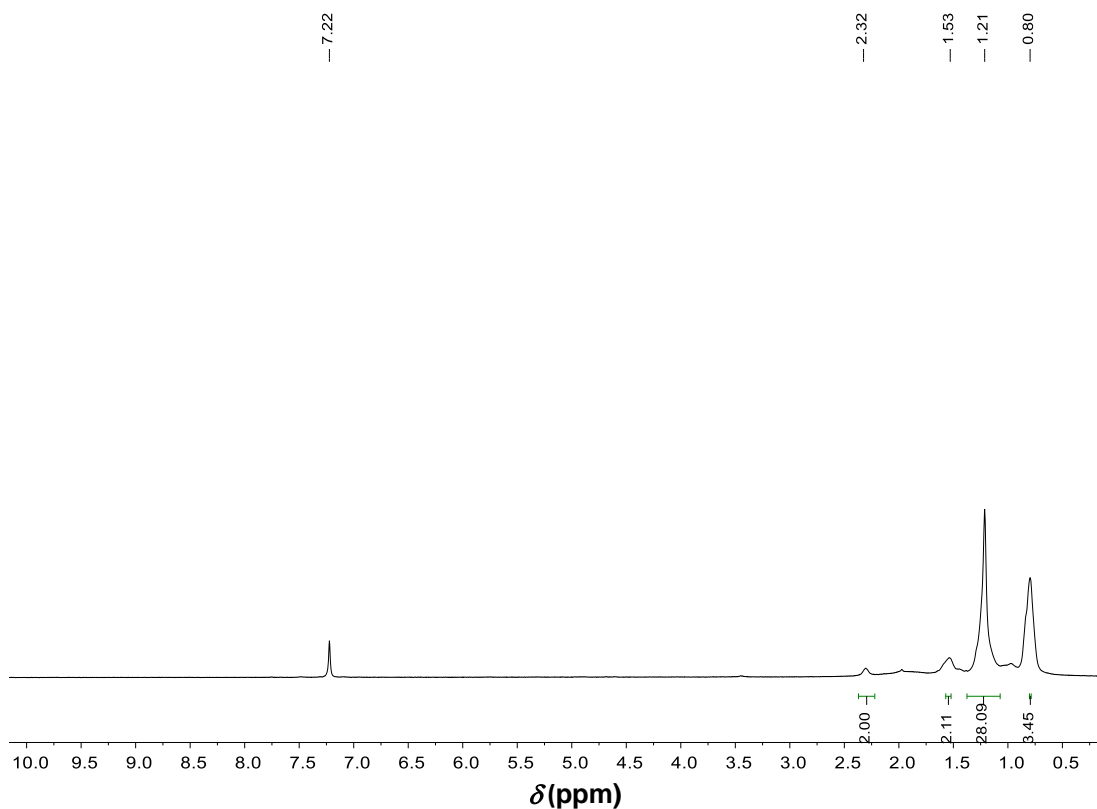


Figure A2.46. ^1H NMR of silver stearate (**2.4.2k**) (CDCl_3 , 400 MHz)

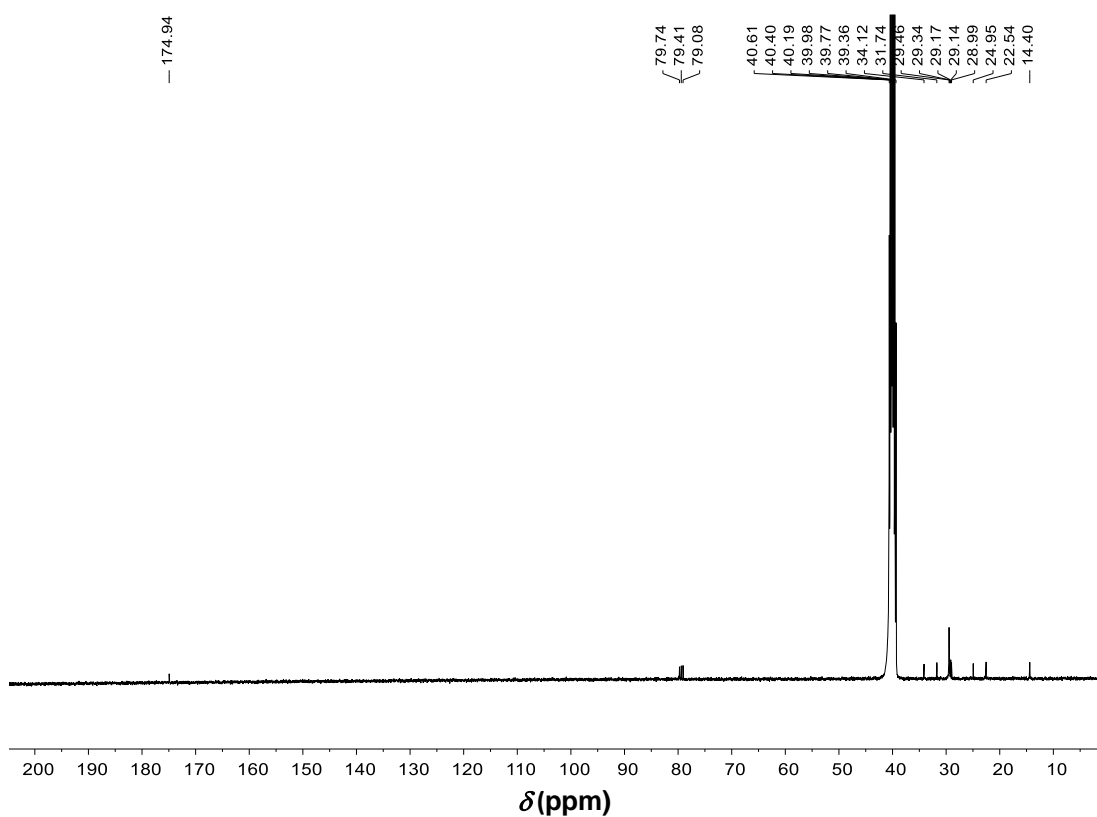


Figure A2.47. ^{13}C $\{^1\text{H}\}$ NMR of silver stearate (**2.4.2k**) (CDCl_3 , DMSO-d_6 , 100 MHz)

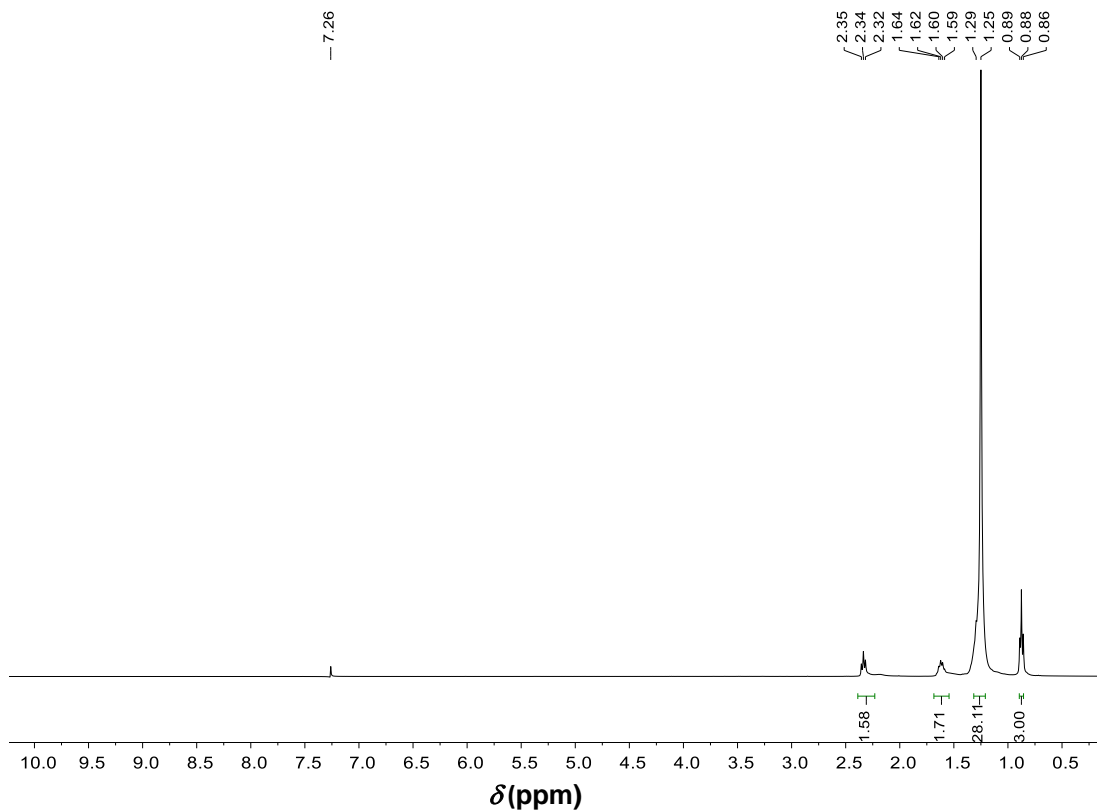


Figure A2.48. ^1H NMR of aluminium stearate (2.4.21) (CDCl_3 , 400 MHz)

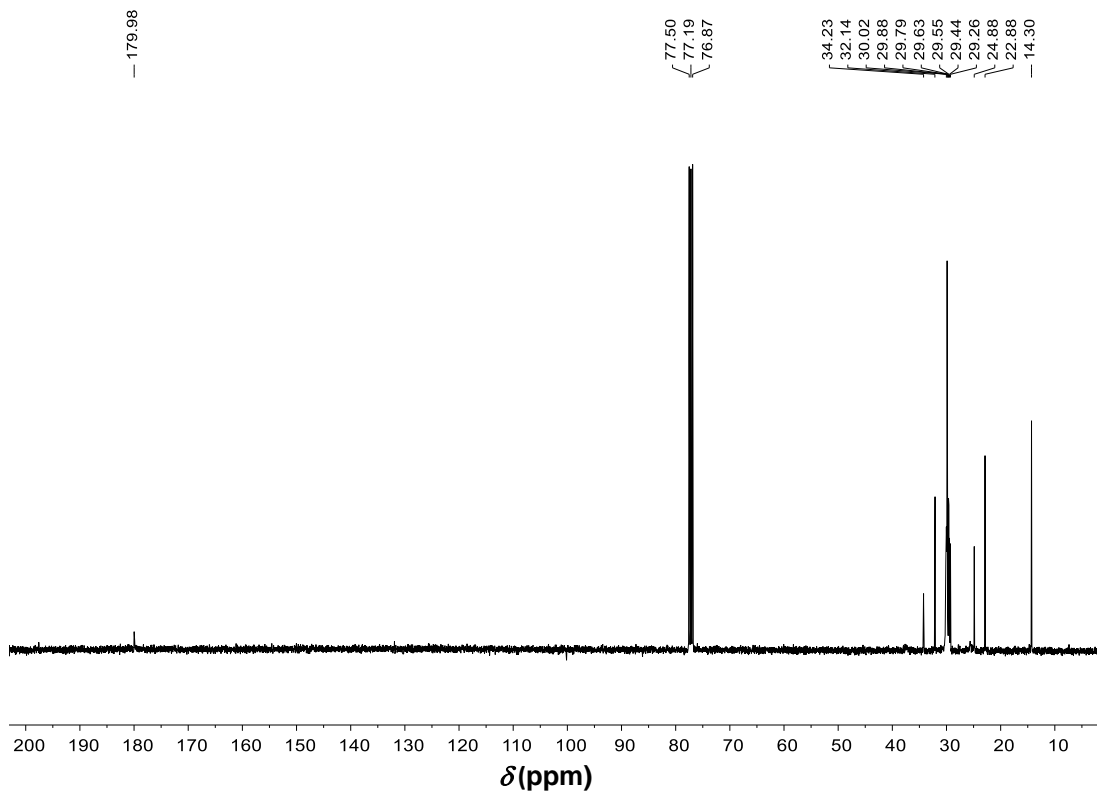


Figure A2.49. ^{13}C $\{^1\text{H}\}$ NMR of aluminium stearate (2.4.21) (CDCl_3 , 100 MHz)

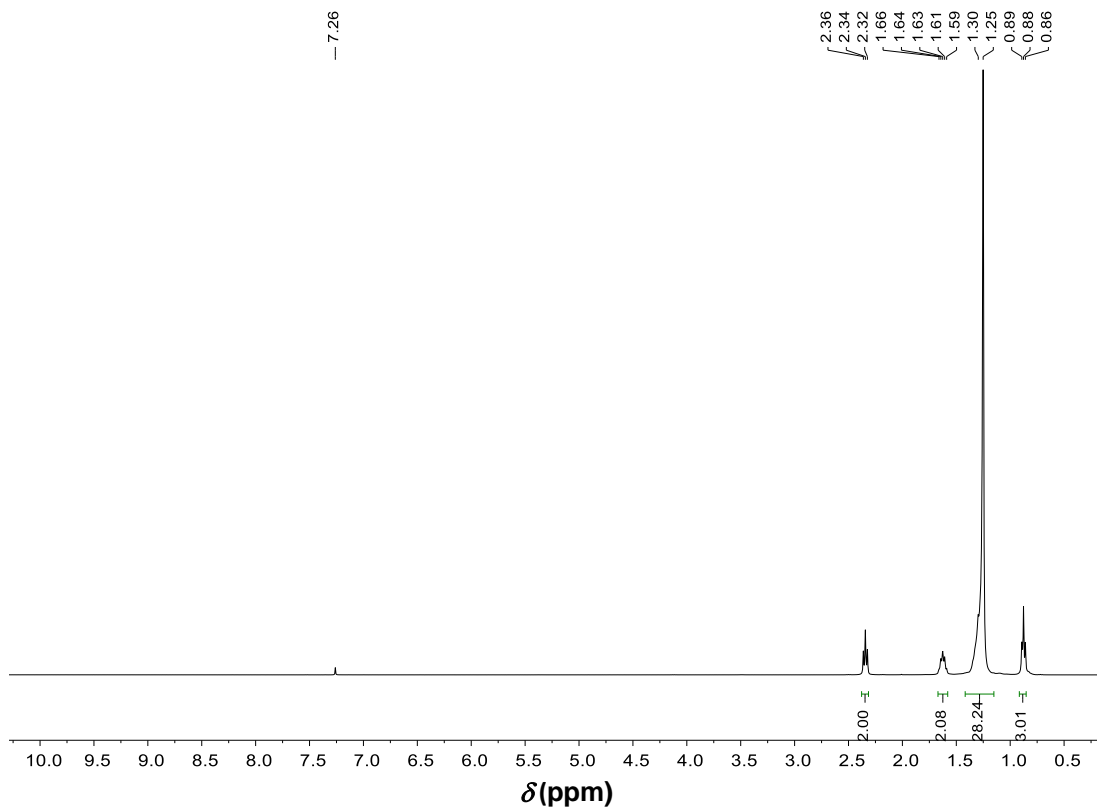


Figure A2.50. ^1H NMR of gallium stearate (2.4.2m) (CDCl_3 , 400 MHz)

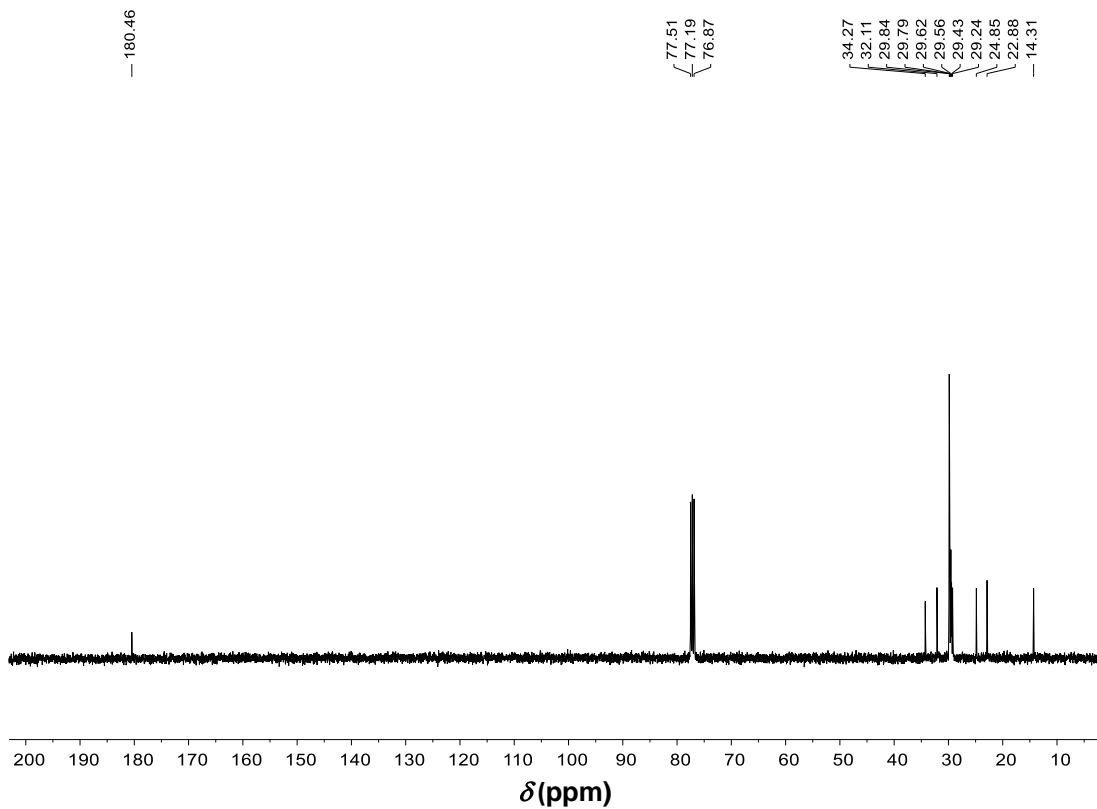


Figure A2.51. ^{13}C $\{^1\text{H}\}$ NMR of gallium stearate (2.4.2m) (CDCl_3 , 100 MHz)

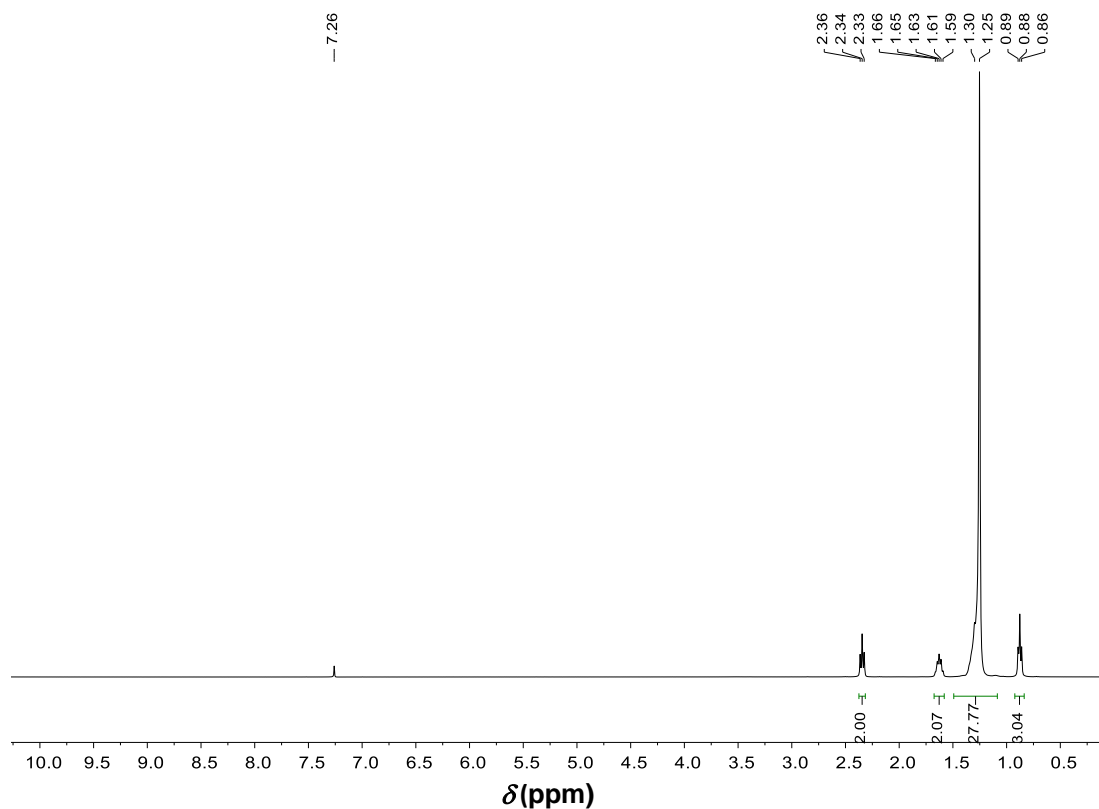


Figure A2.52. ^1H NMR of tin (II) stearate (**2.4.2n**) (CDCl_3 , 400 MHz)

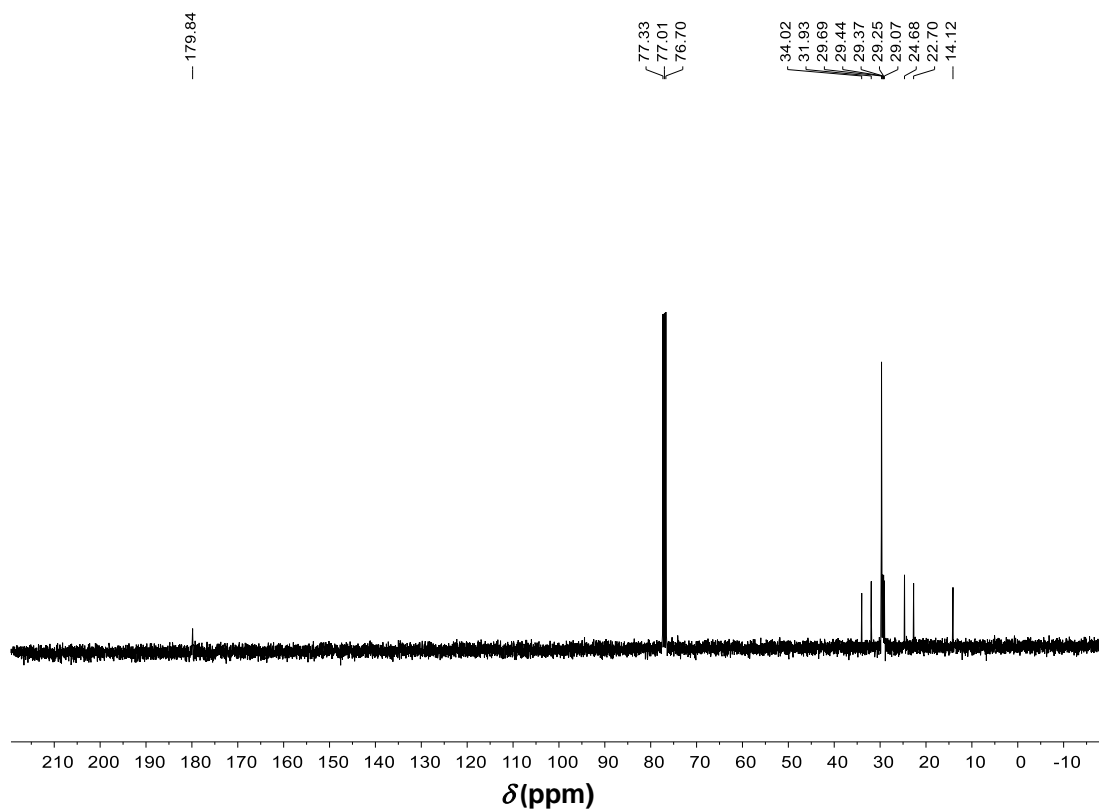


Figure A2.53. ^{13}C $\{^1\text{H}\}$ NMR of tin (II) stearate (**2.4.2n**) (CDCl_3 , 100 MHz)

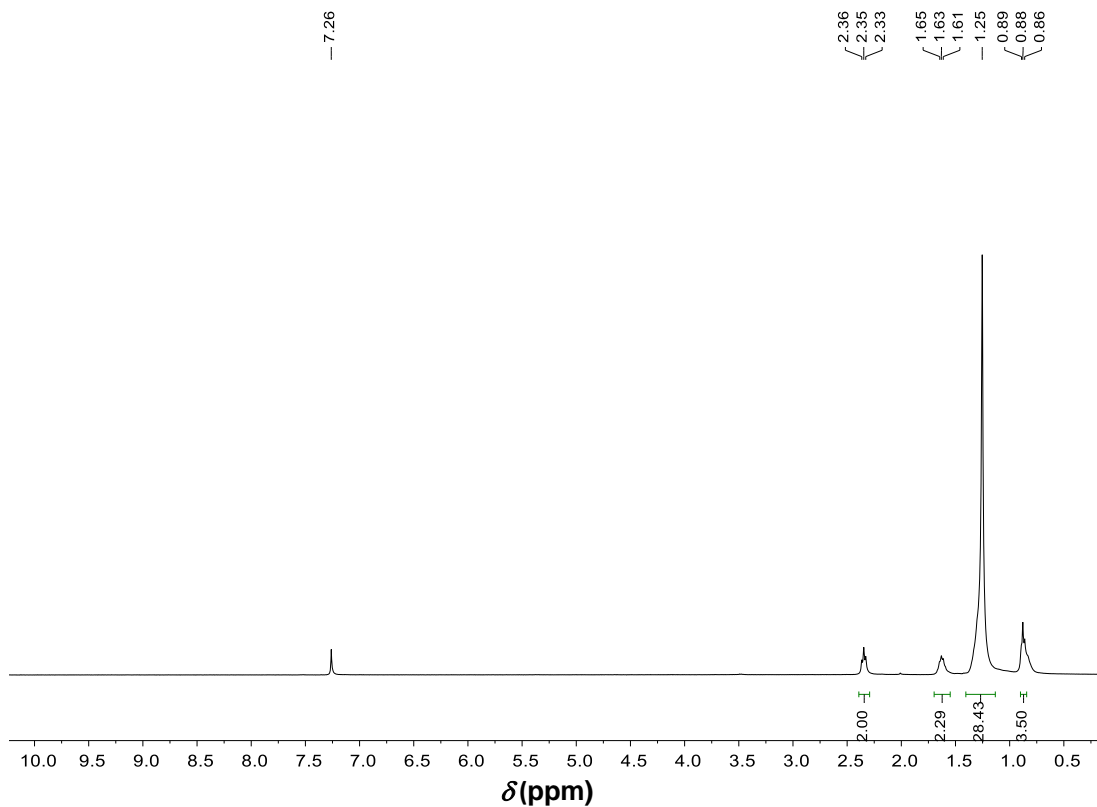


Figure A2.54. ^1H NMR of lead stearate (**2.4.2o**) (CDCl_3 , 400 MHz)

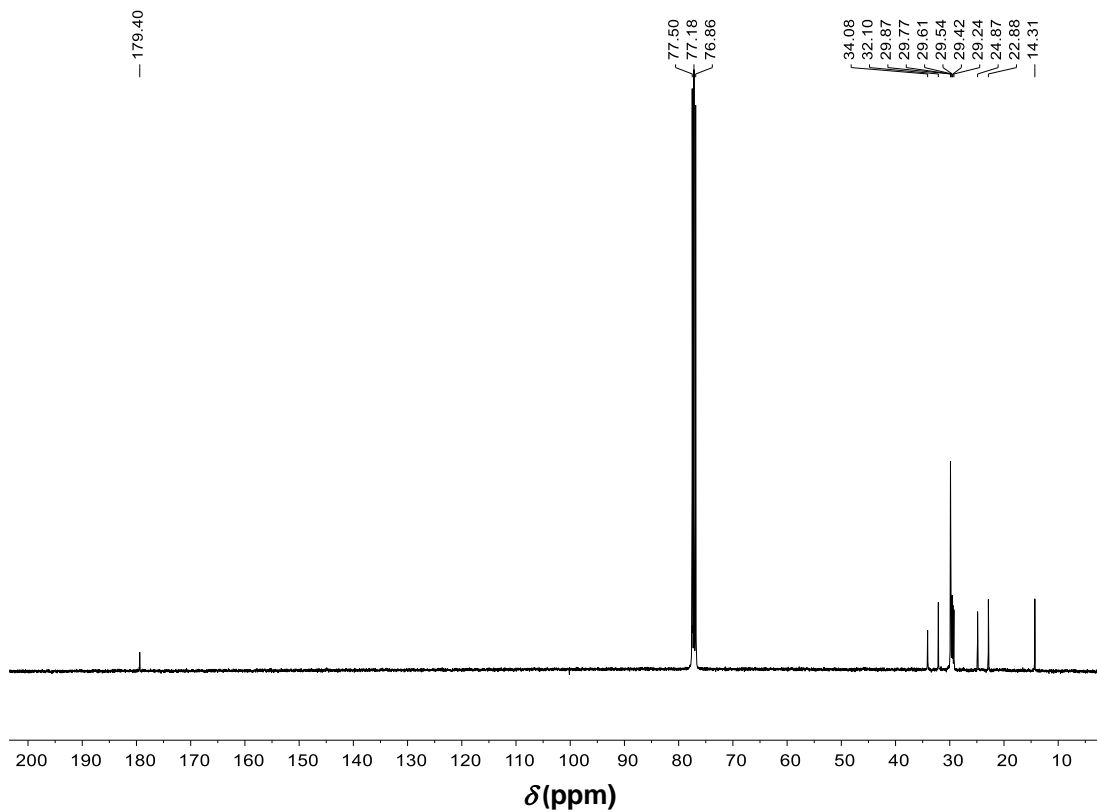


Figure A2.55. ^{13}C $\{^1\text{H}\}$ NMR of lead stearate (**2.4.2o**) (CDCl_3 , 100 MHz)

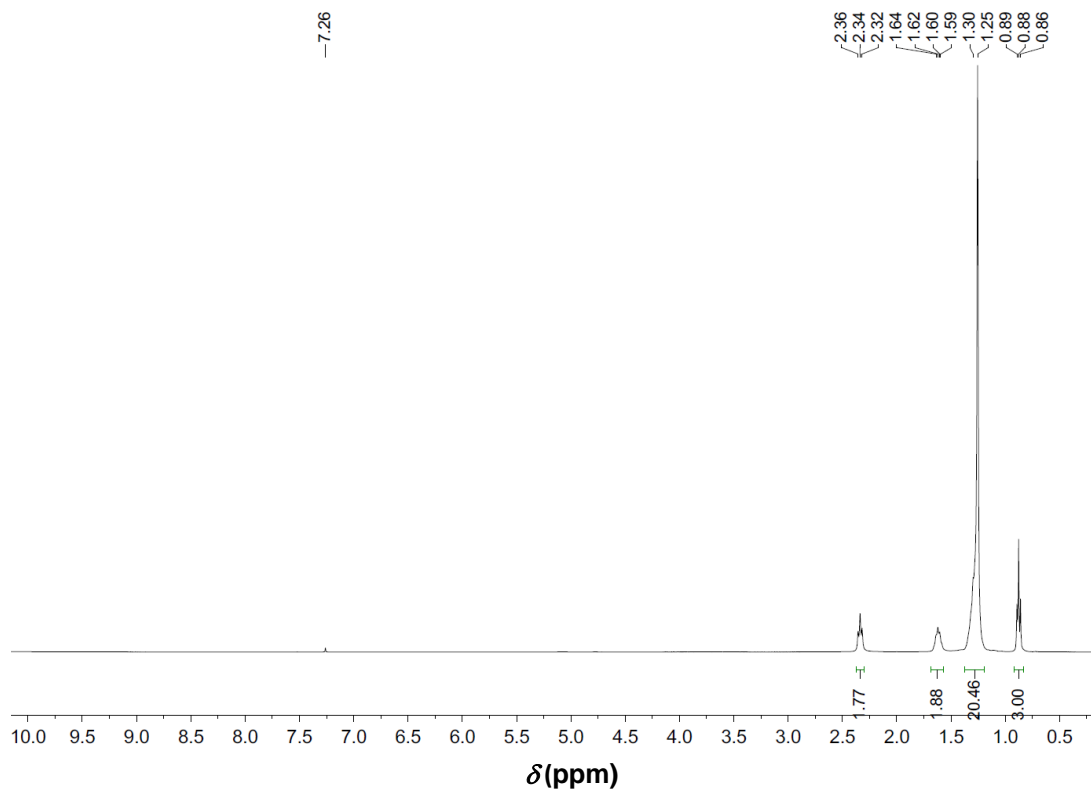


Figure A2.56. ^1H NMR of indium myristate (**2.4.2q**) (CDCl_3 , 400 MHz)

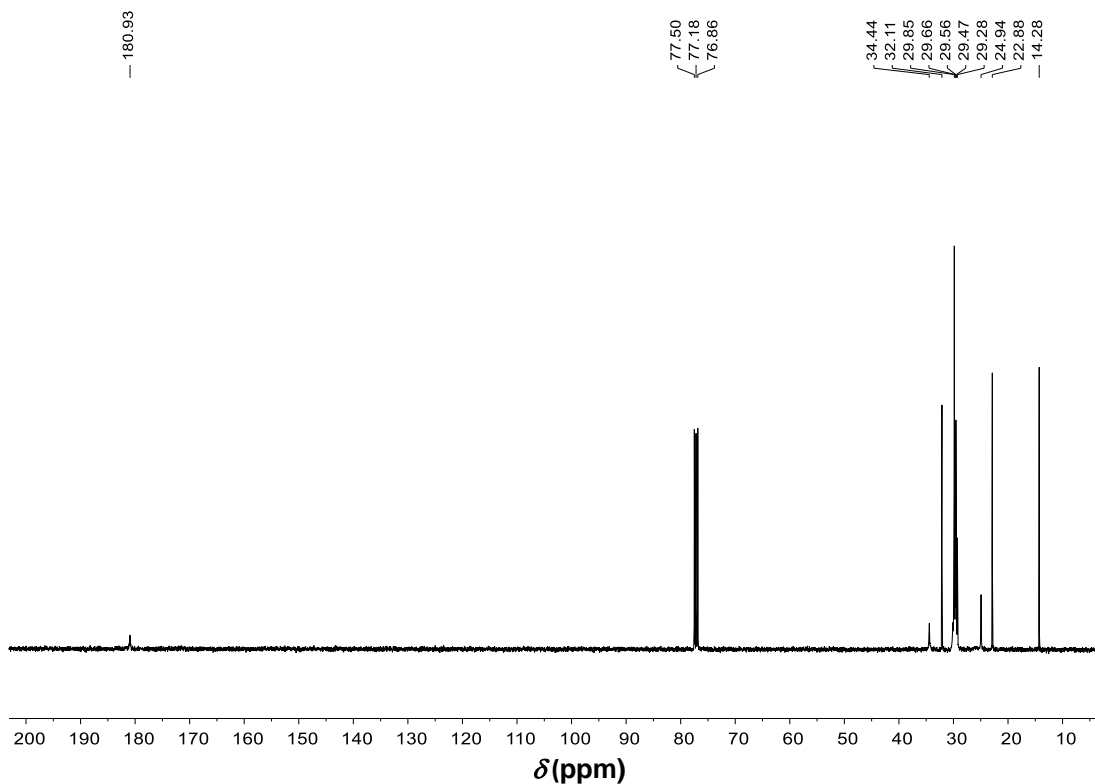


Figure A2.57. ^{13}C $\{^1\text{H}\}$ NMR of indium myristate (**2.4.2q**) (CDCl_3 , 100 MHz)

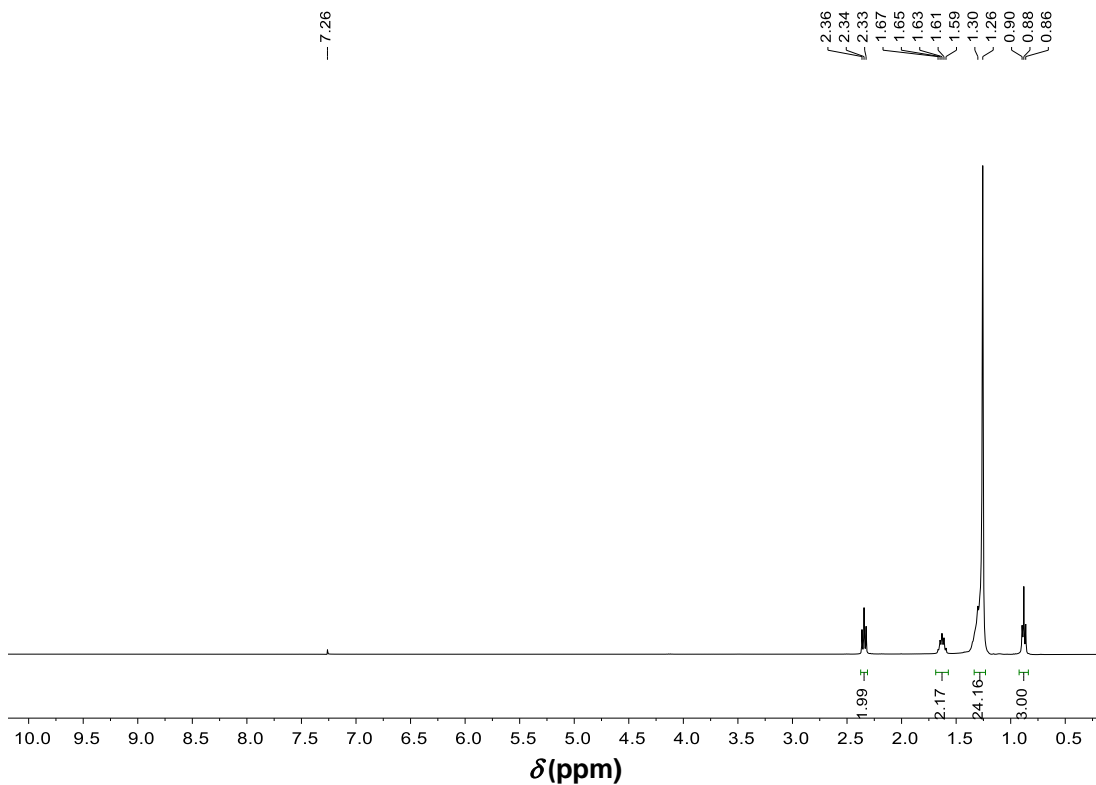


Figure A2.58. ^1H NMR of indium palmitate (**2.4.2r**) (CDCl_3 , 400 MHz)

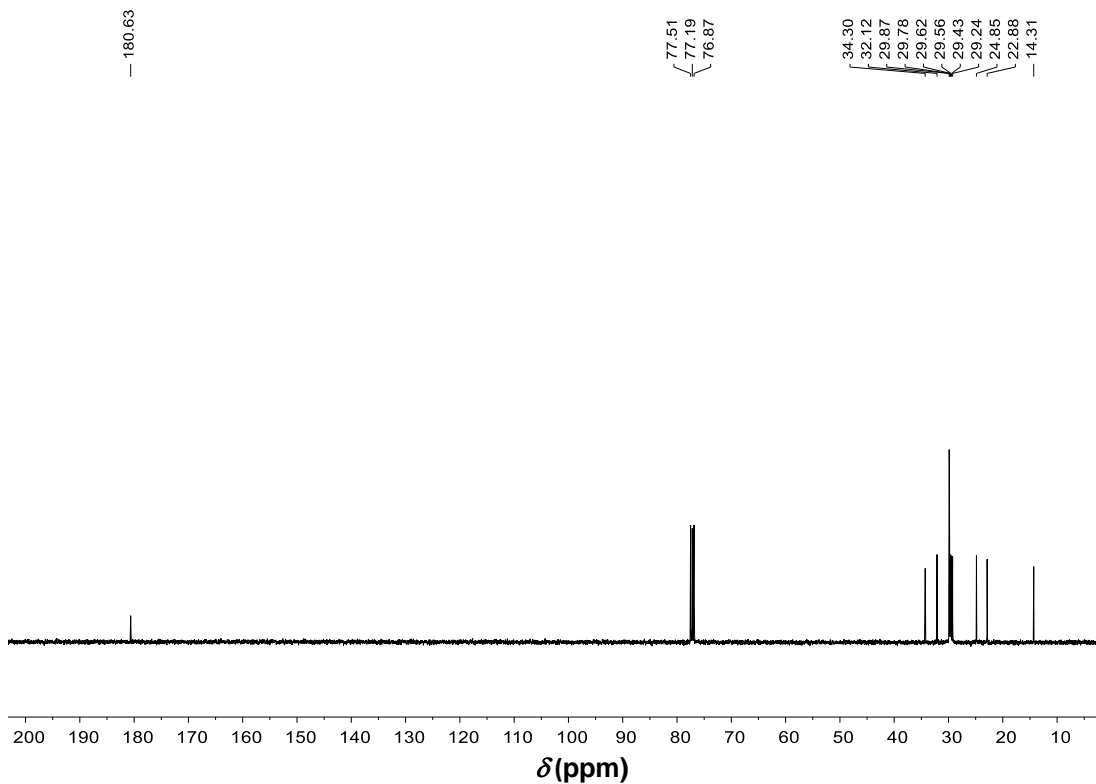


Figure A2.59. ^{13}C $\{^1\text{H}\}$ NMR of indium palmitate (**2.4.2r**) (CDCl_3 , 100 MHz)

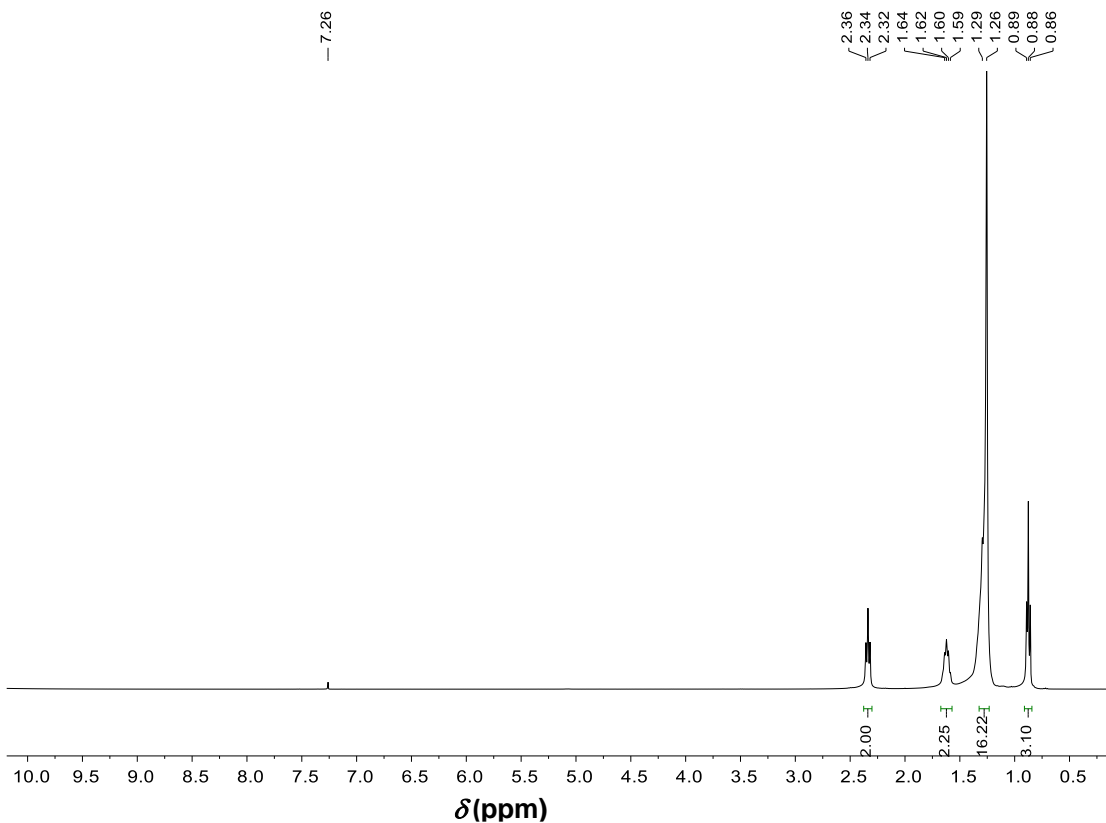


Figure A2.60. ^1H NMR of indium laurate (2.4.2s) (CDCl_3 , 400 MHz)

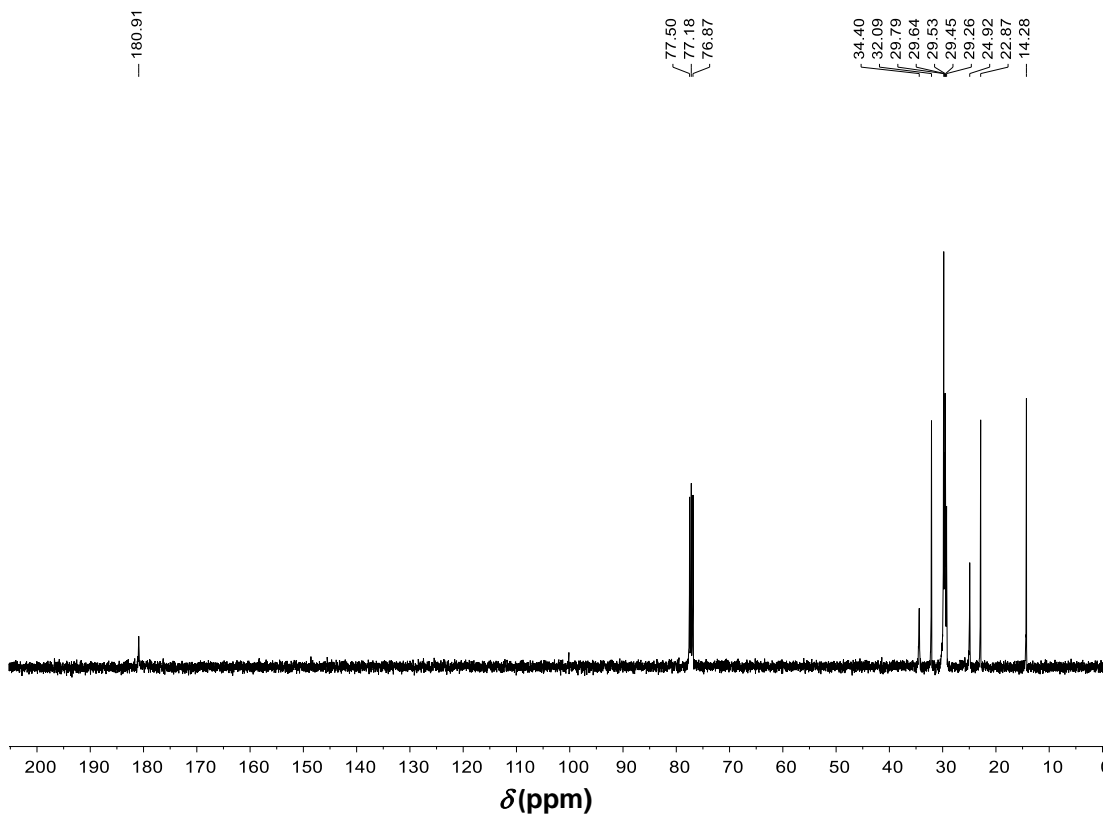


Figure A2.61. ^{13}C $\{^1\text{H}\}$ NMR of indium laurate (2.4.2s) (CDCl_3 , 100 MHz)

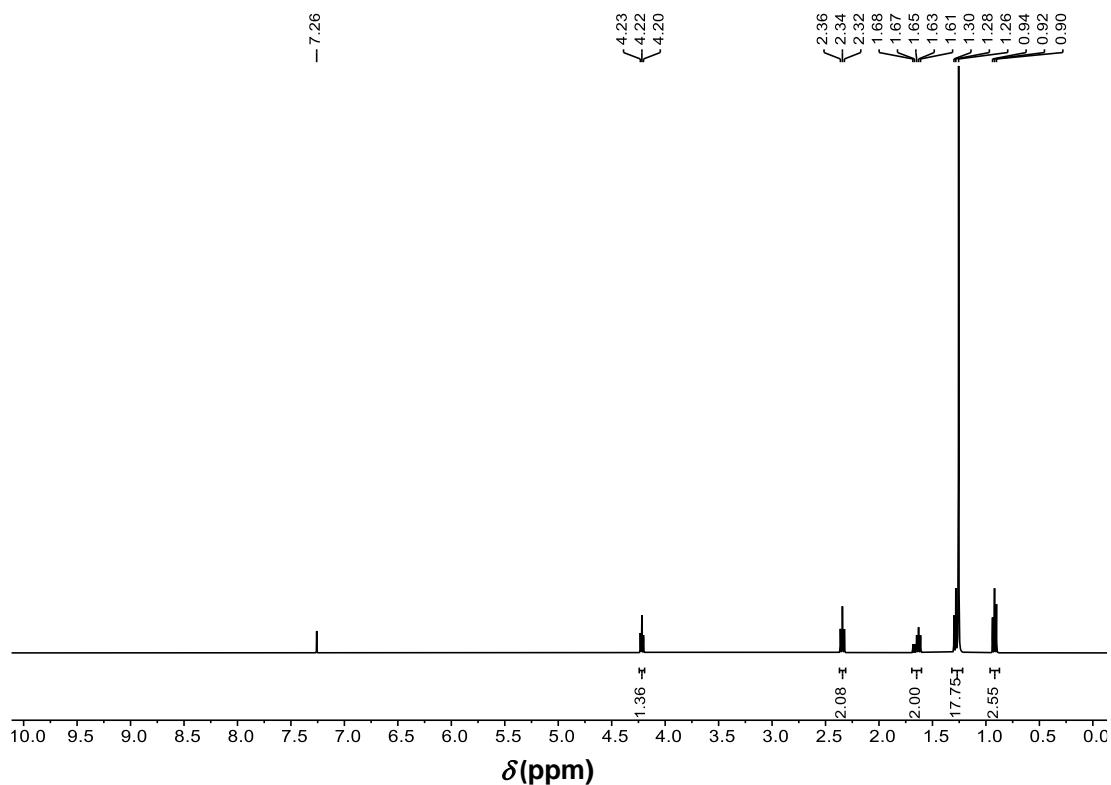


Figure A2.62. ^1H NMR of Indium (α -bromomyristate) $_3$ (**2.4.2t**) (CDCl_3 , 400 MHz)

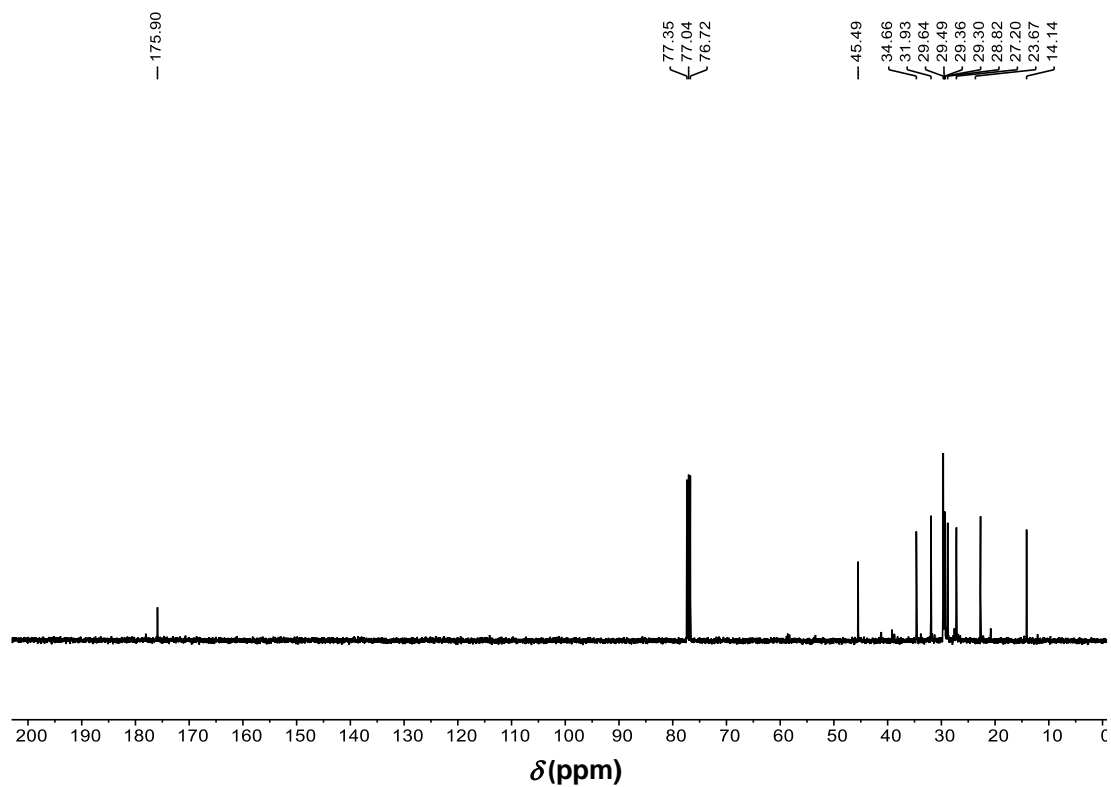


Figure A2.63. ^{13}C $\{^1\text{H}\}$ NMR of Indium (α -bromomyristate) $_3$ (**2.4.2t**) (CDCl_3 , 100 MHz)

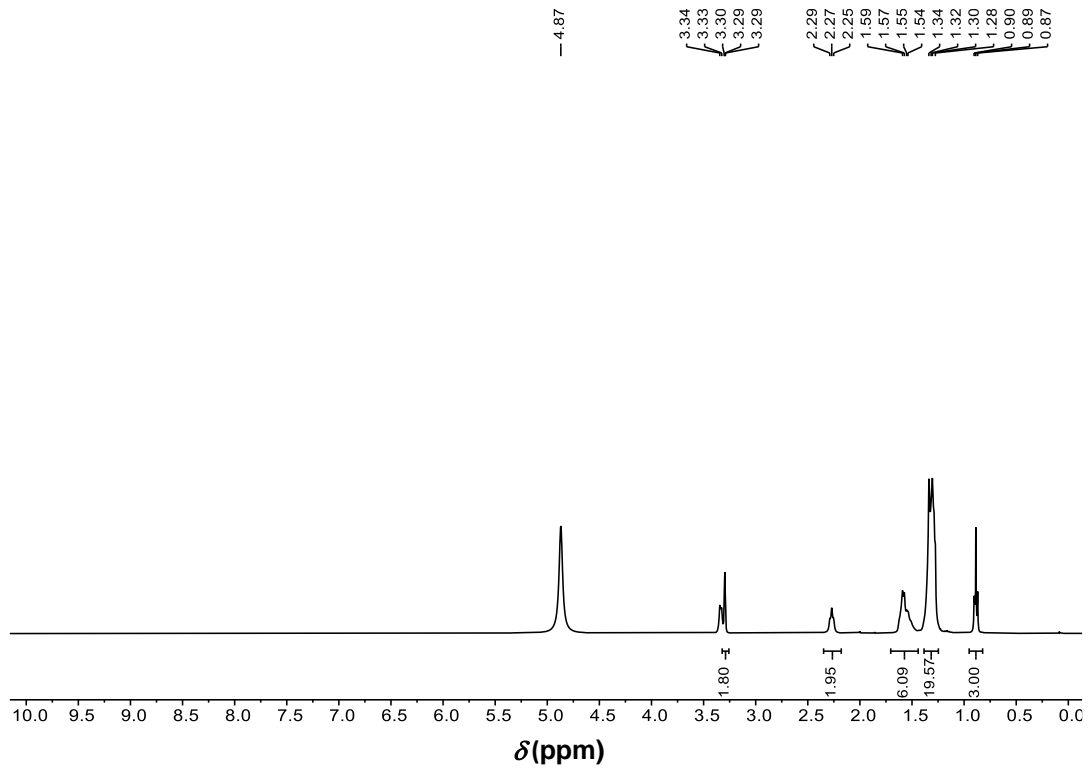


Figure A2.64. ^1H NMR of Indium (9, 10- hydroxystearate) $_3$ (**2.4.2u**) (CD_3OD , 400 MHz)

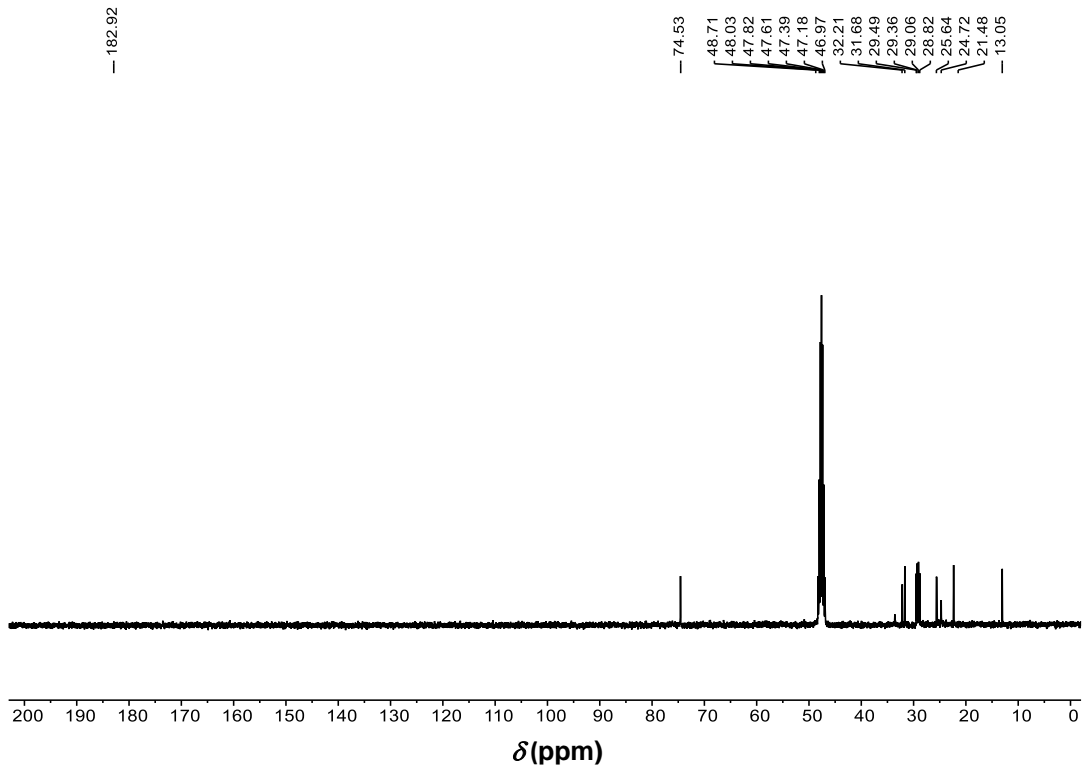


Figure A2.65. ^{13}C $\{^1\text{H}\}$ NMR of Indium (9, 10- hydroxystearate) $_3$ (**2.4.2u**) (CD_3OD ,

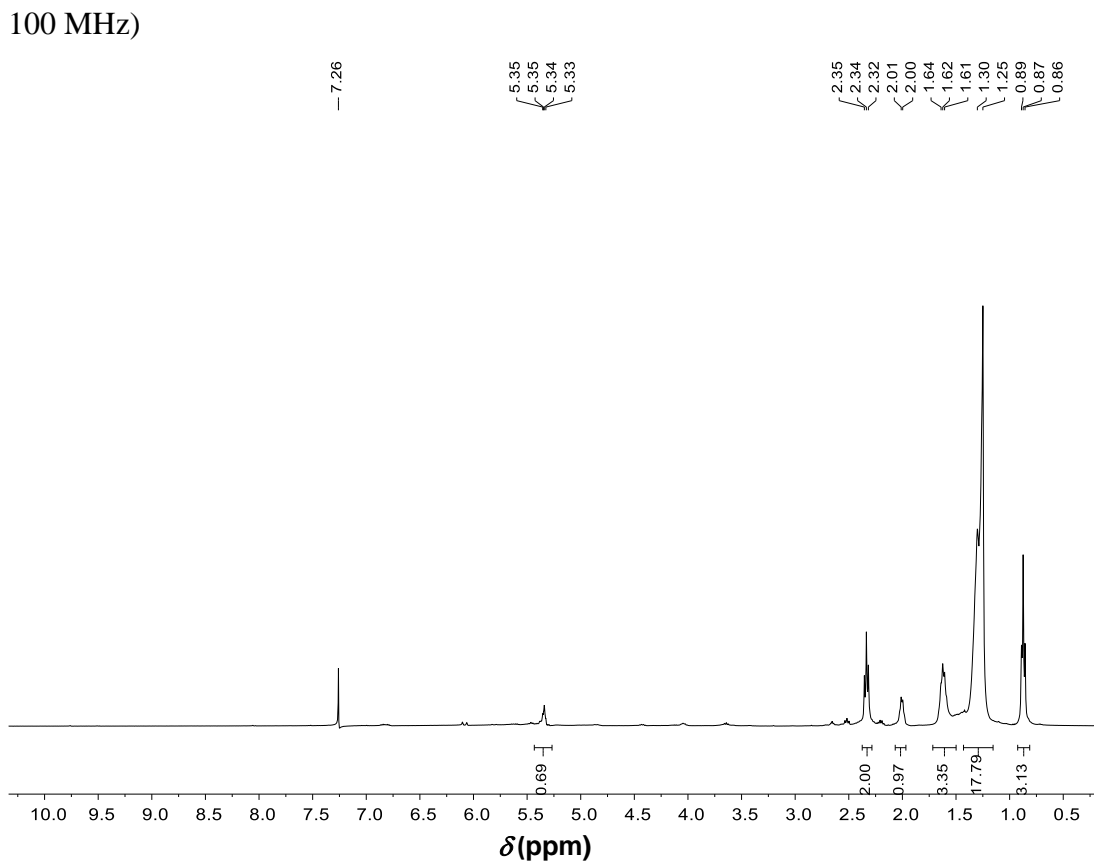


Figure A2.66. ^1H NMR of lead oleate (**2.4.2v**) (CDCl_3 , 400 MHz)

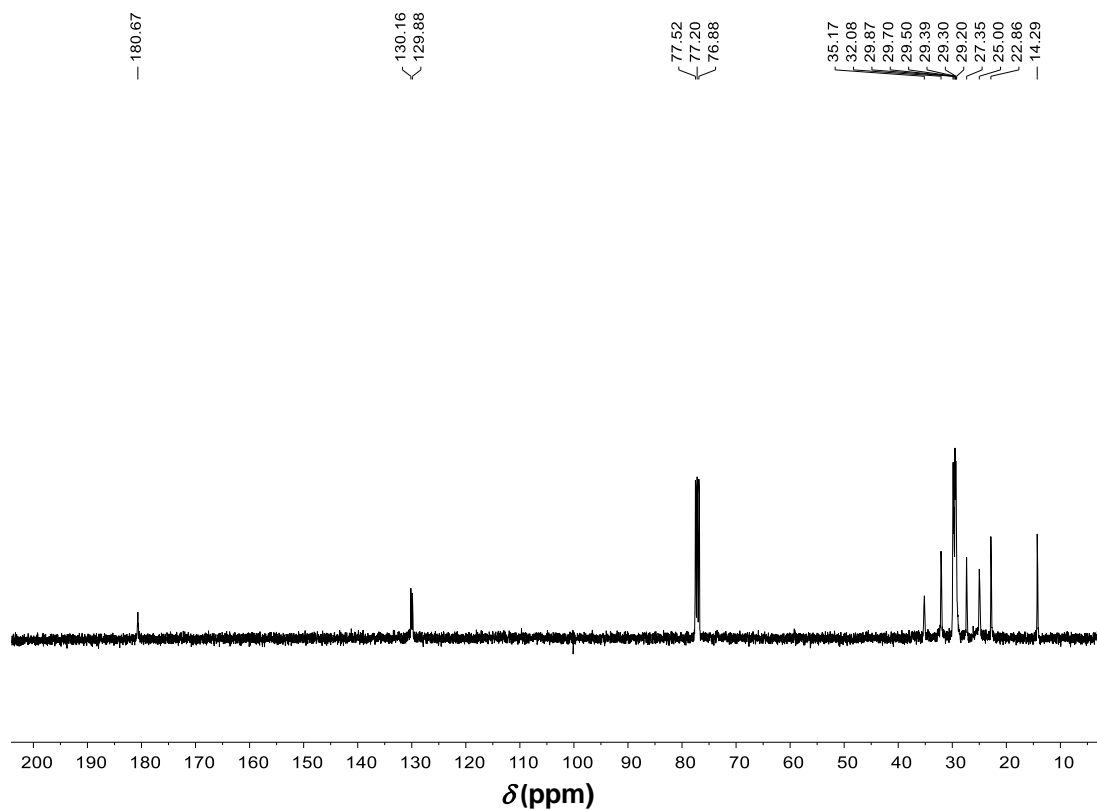
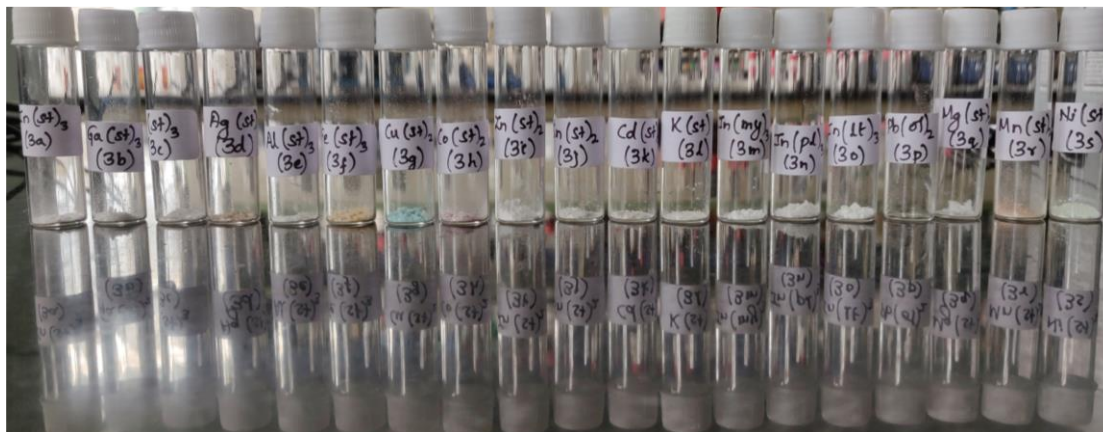
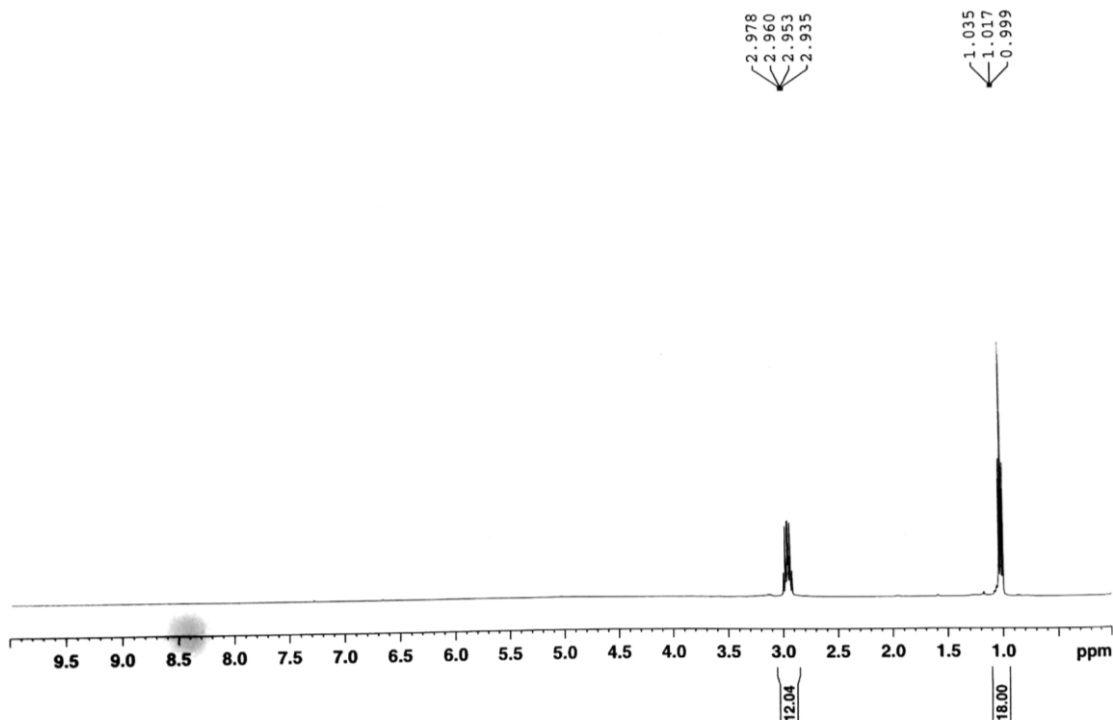


Figure A2.67. ^{13}C $\{^1\text{H}\}$ NMR of lead oleate (**2.4.2v**) (CDCl_3 , 100 MHz)

A2.2.3. Photographic image of different MFAs obtained from DBU method:**A2.3. Preparation of tris(diethylamino)phosphine (P(NEt₂)₃).****A2.3.1. Copies of NMR spectra.****Figure A2.68.** ¹H NMR of P(NEt₂)₃ (CDCl₃, 400 MHz)

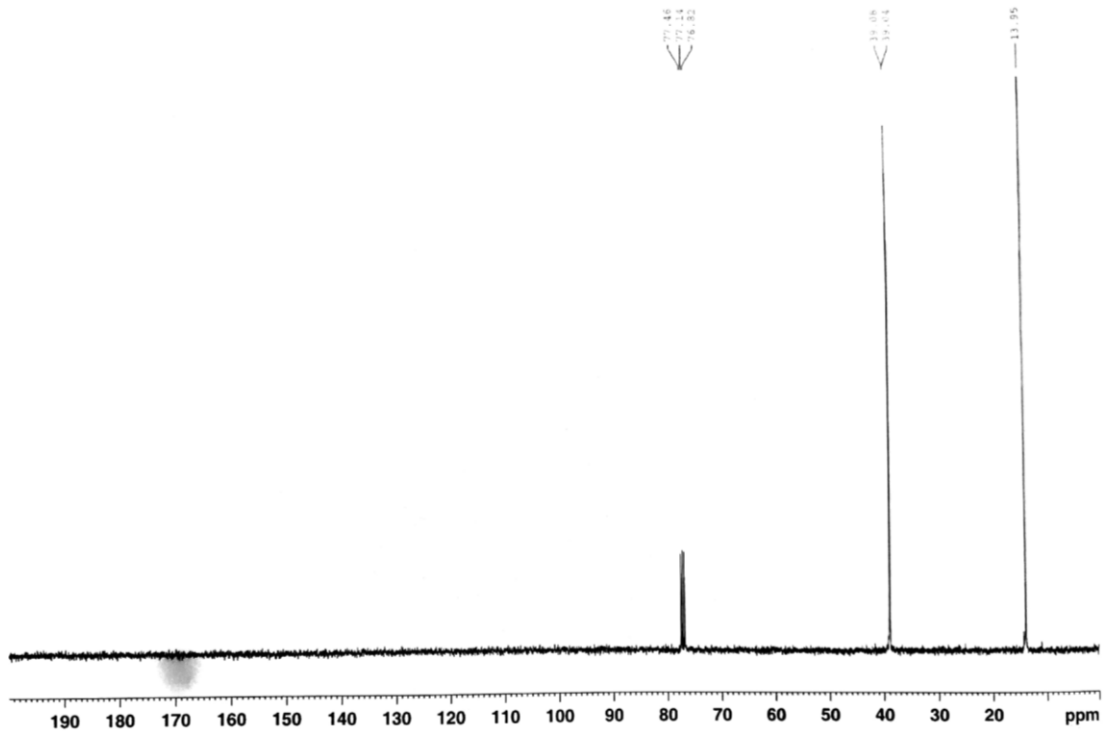


Figure A2.69. ^{13}C $\{^1\text{H}\}$ NMR of $\text{P}(\text{NEt}_2)_3$ (CDCl_3 , 100 MHz)

A2.4. Preparation of thiourea precursor.

A2.4.1. Copies of NMR spectra.

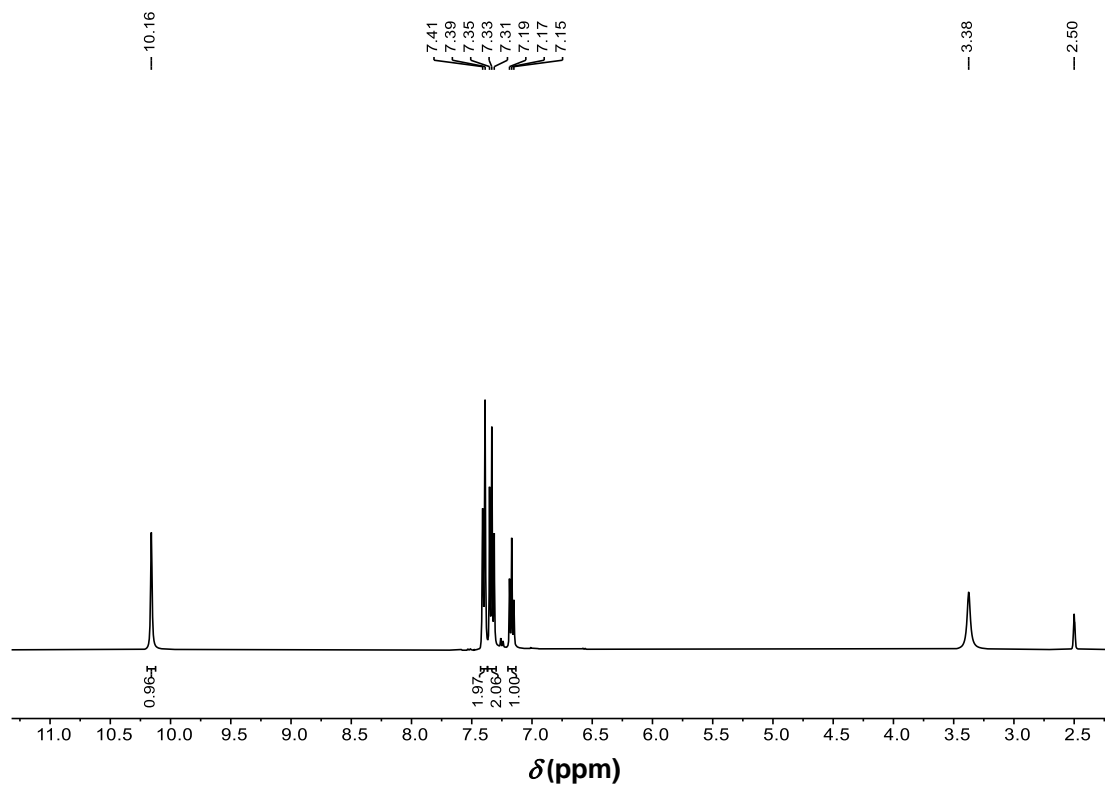


Figure A2.70. ^1H NMR of $(\text{PhNH})_2\text{C}=\text{S}$ (CDCl_3 , 400 MHz)

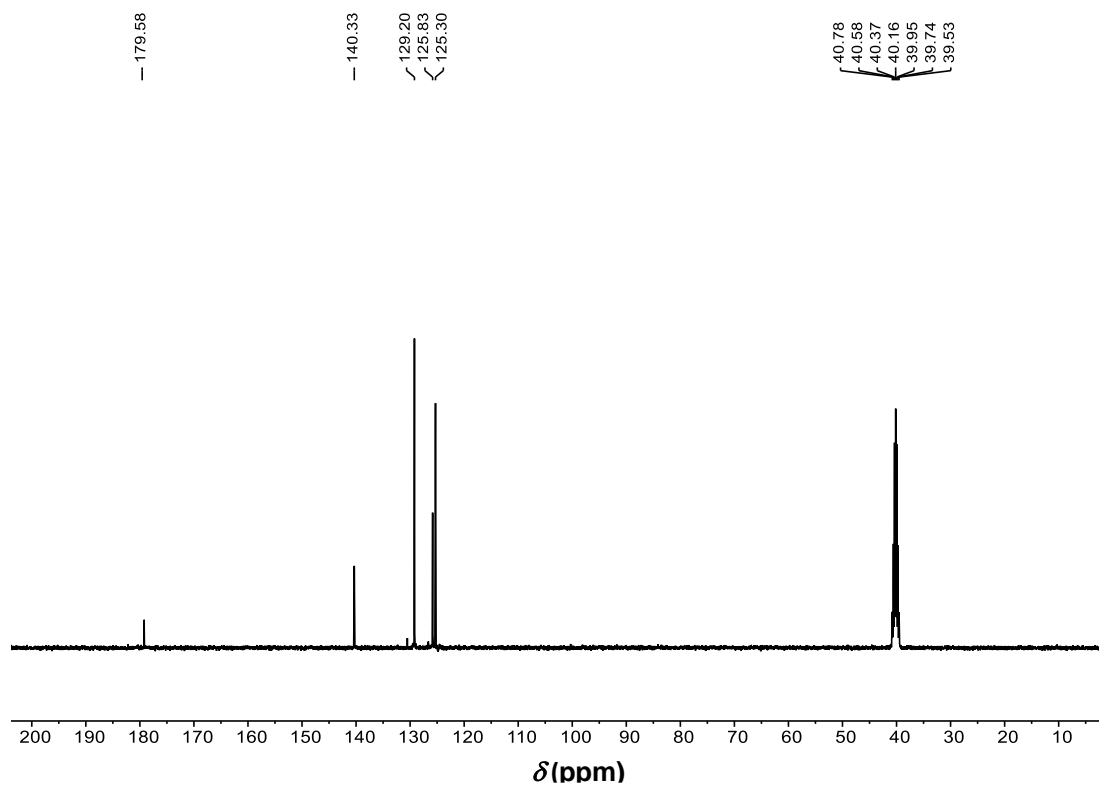


Figure A2.71. ^{13}C $\{^1\text{H}\}$ NMR of $(\text{PhNH})_2\text{C}=\text{S}$ (CDCl_3 , 100 MHz)

Annexure A3

*Additional information for Chapter
III*

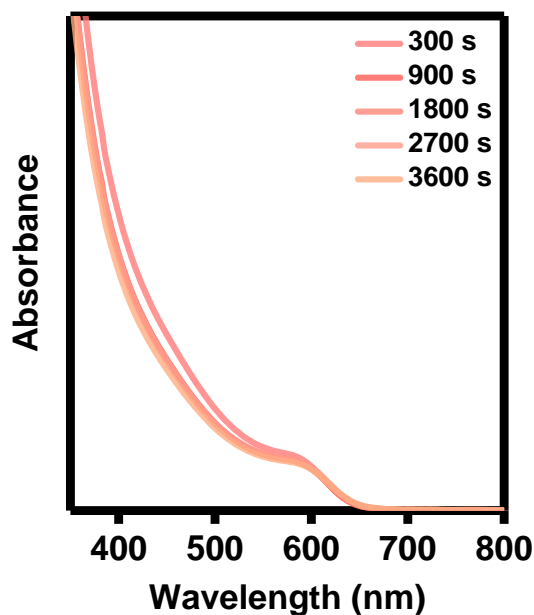
A3.1. Copies of UV-Visible spectra of InP prepared from various precursors.

Figure A3.1. Temporal evolution of UV-Visible absorption spectra of InP NCs prepared from complex 3.1.

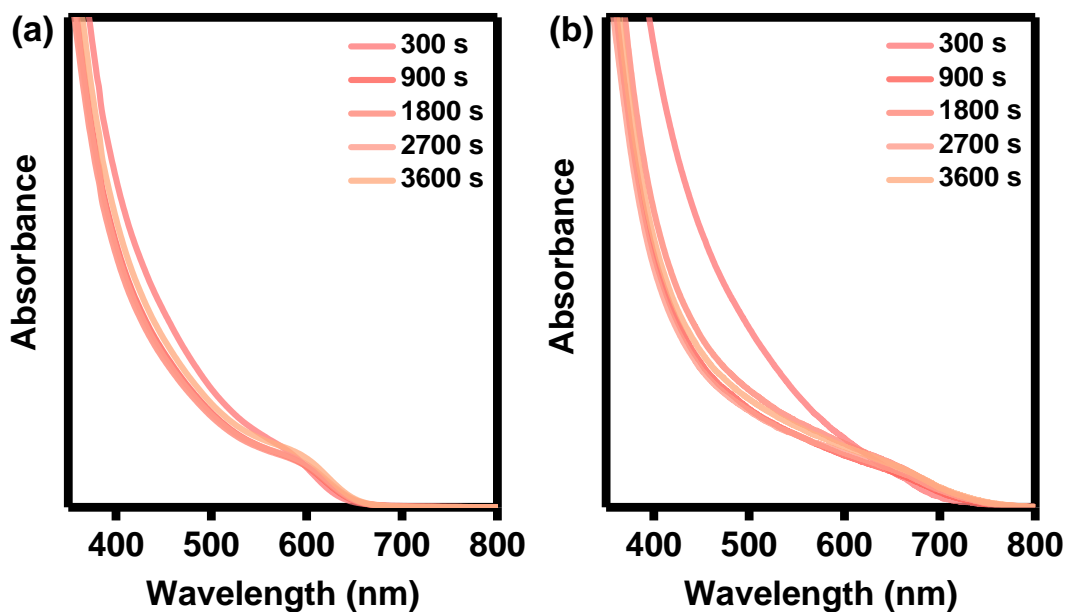


Figure A3.2. Temporal evolution of UV-Visible absorption spectra of InP NCs prepared from (a) experiment 2 and (b) experiment 3.

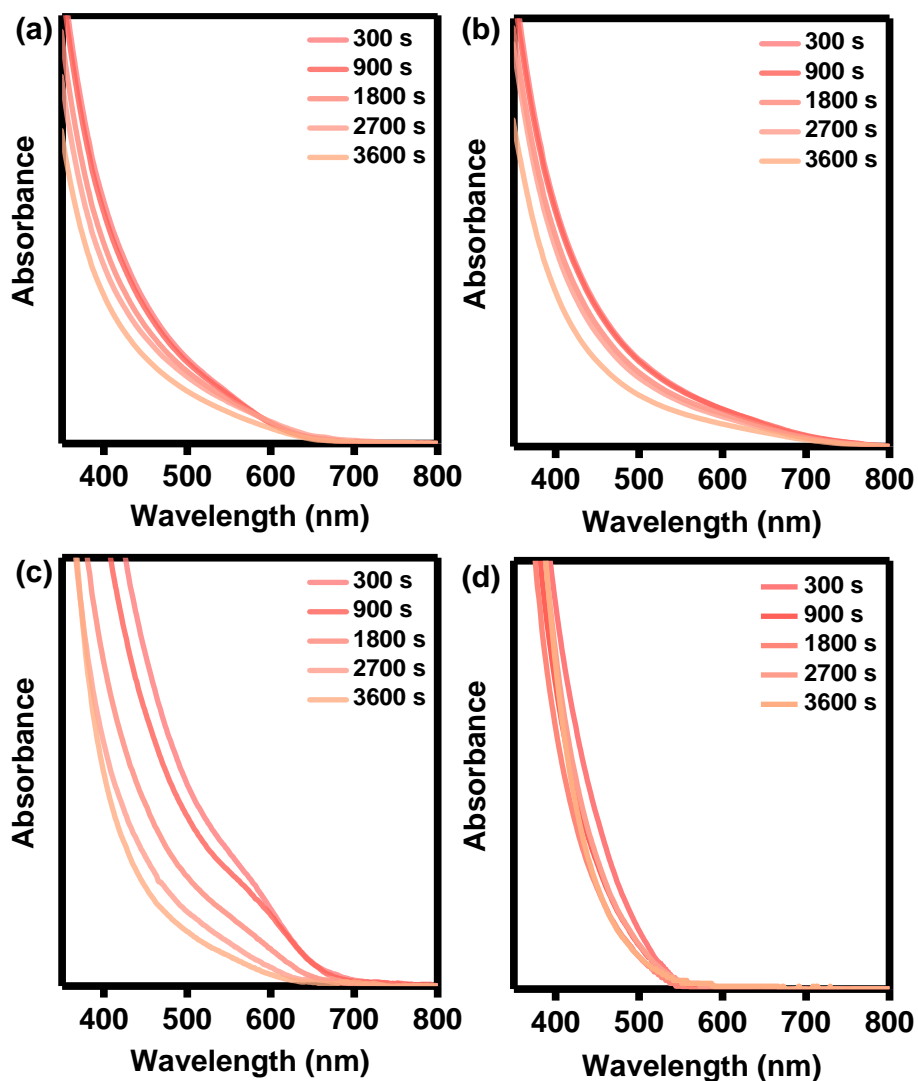


Figure A3.3. Temporal evolution of UV-Visible absorption spectra of second batch of InP NCs prepared from (a) complex 3.3 and (b) complex 3.4. (c) complex 3.4 + 1.0 myristic acid and (d) first batch of InP NCs prepared from complex 3.4 + 2.0 myristic acid.

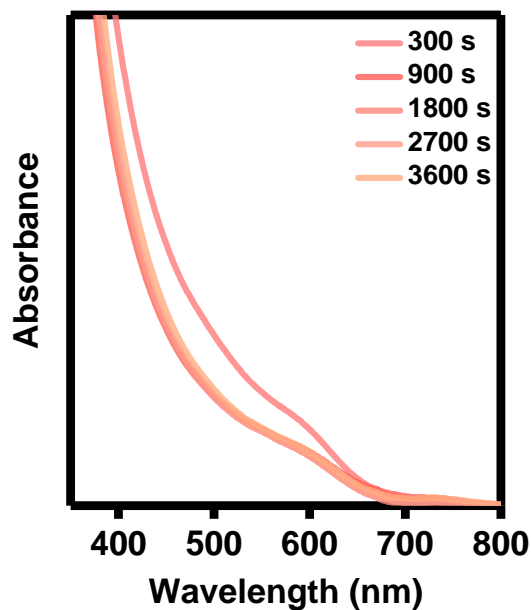


Figure A3.4. Temporal evolution of UV-Visible absorption spectra of InP NCs prepared from complex 3.5.

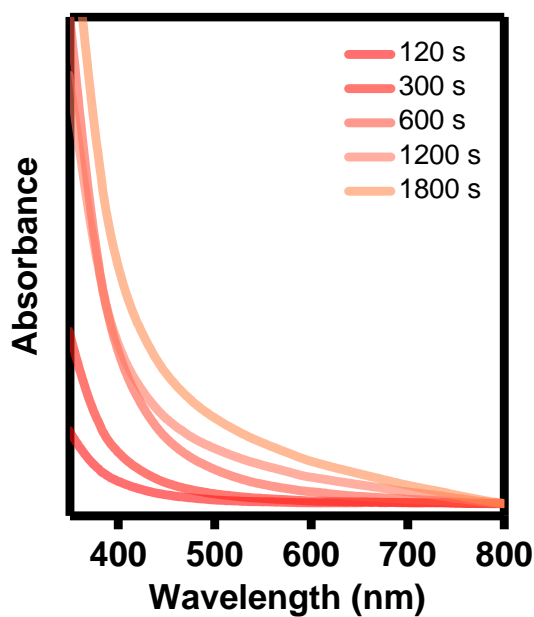


Figure A3.5. Temporal evolution of UV-Visible absorption spectra of InP NCs prepared from complex 3.2 and tris(diethylamino)phosphine.

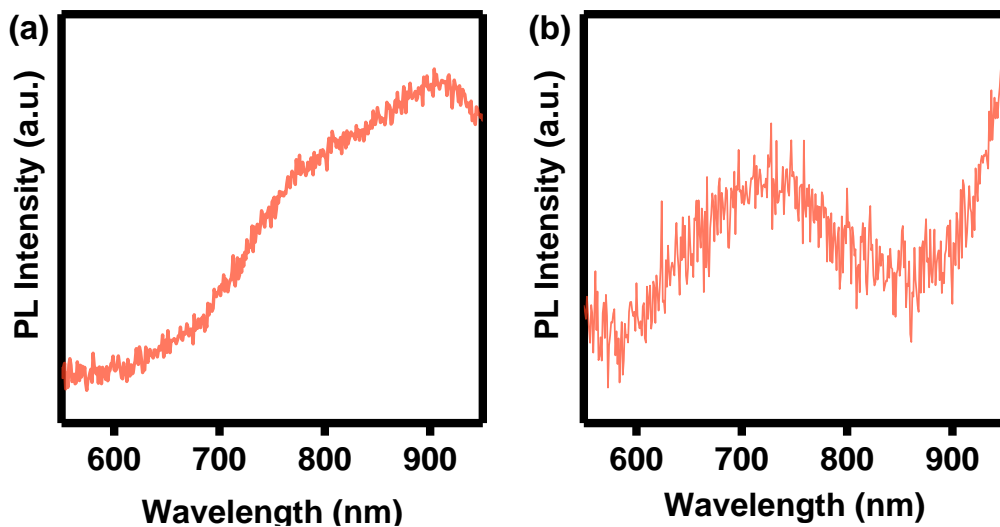
A3.2. Copies of PL spectra of InP prepared from various precursors.

Figure A3.6. PL spectra of InP QDs prepared from (a) complex 3.1 and (b) complex 3.2 (excitation wavelength 500 nm).

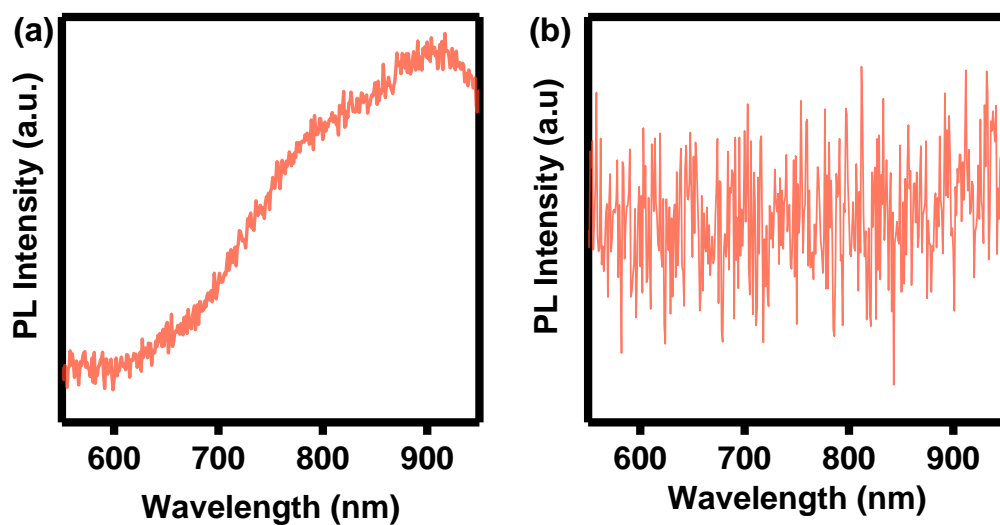


Figure A3.7. PL spectra of InP QDs prepared from (a) experiment 2 and (b) experiment 3 (excitation wavelength 500 nm).

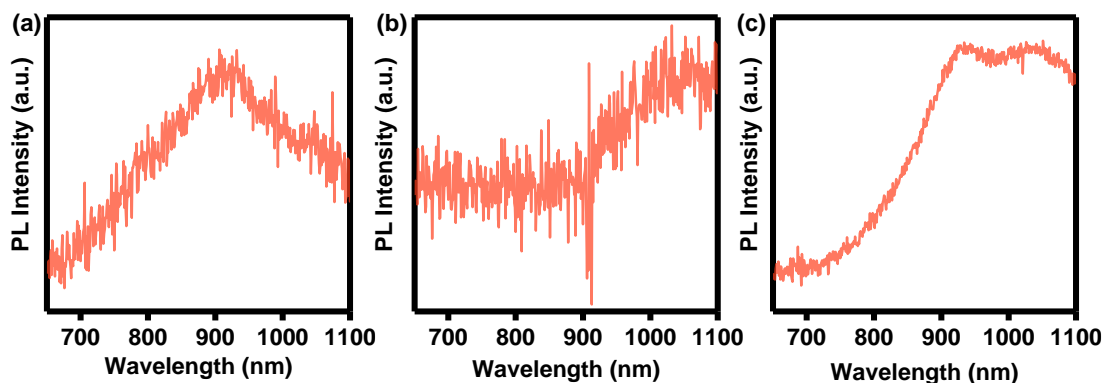


Figure A3.8. PL spectra of InP QDs prepared from (a) complex **3.3** (b) complex **3.4** and (c) complex **3.4** + 1.0 myristic acid (excitation wavelength 600 nm).

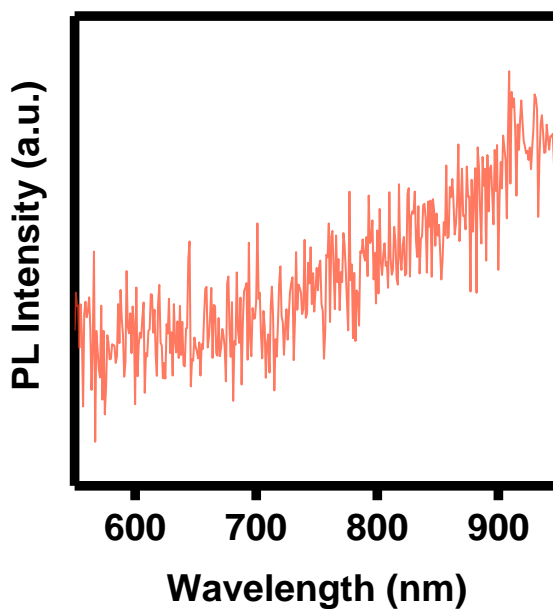


Figure A3.9. PL spectra of InP QDs prepared from complex **3.5**. (excitation wavelength 500 nm).

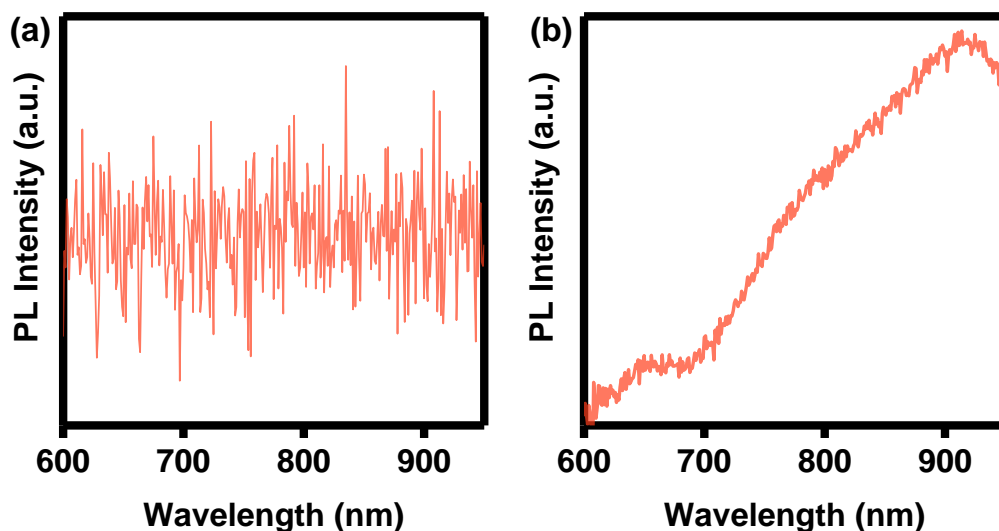


Figure A3.10. PL spectra of InP QDs prepared from (a) complex **3.6** and (b) complex **3.7** (excitation wavelength 550 nm).

A3.3. Copies of NMR spectra.

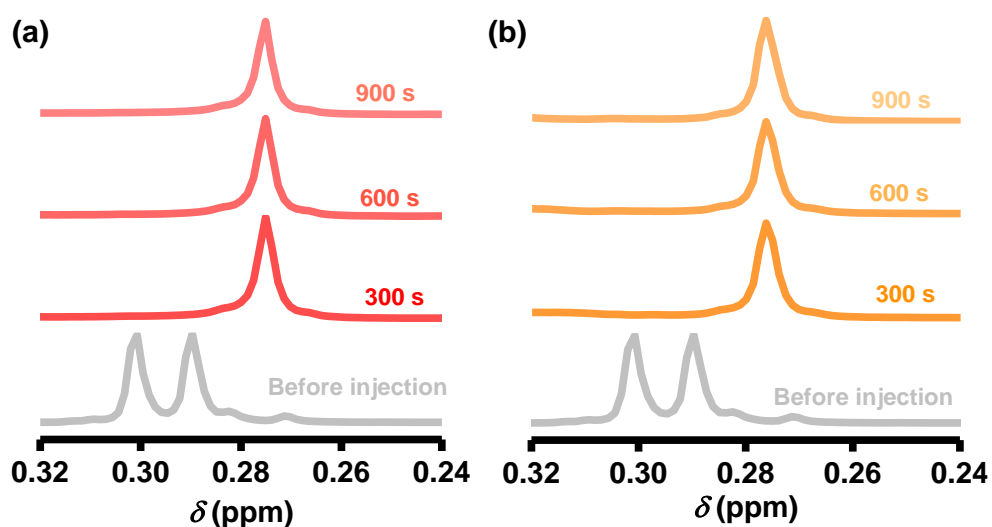
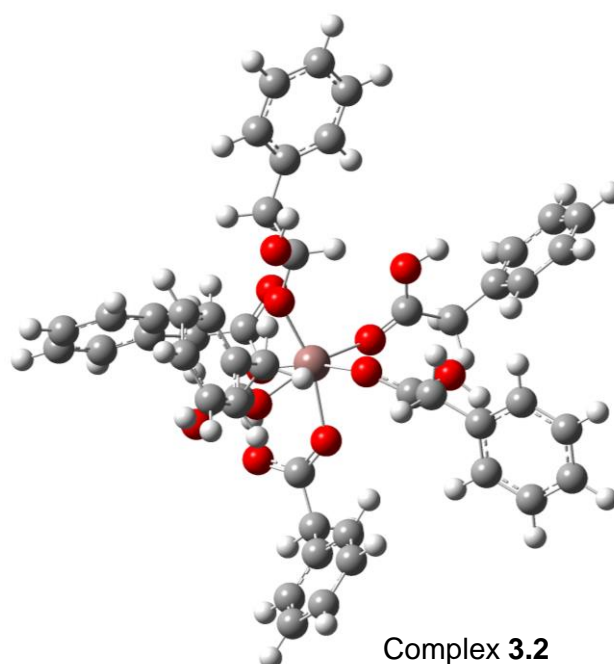


Figure A3.11. Temporal evolution of ^1H NMR of InP NCs reaction before injection (grey) and after injection (red and orange) at time interval of 300 s, 600 s and 900 s for (a) complex **3.2** and (b) complex **3.5** data of which are used in figure 3.9c of chapter 3.

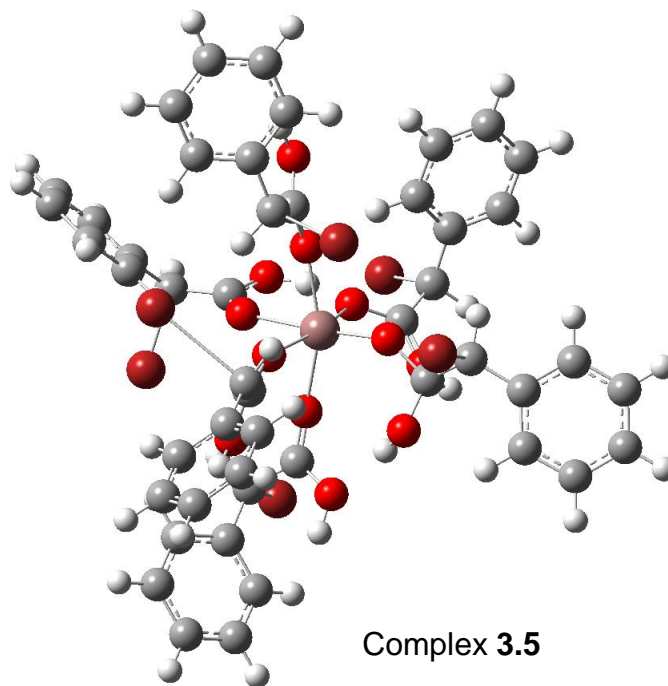
A3.4. Computational studies.**Table A1.1.** Coordinates of complex 3.2.

Atom label	Coordinates (Å)		
	X	Y	Z
O	-1.2868	1.2505	0.2276
In	-0.255	-0.0581	-0.8194
O	1.1127	-0.61	0.5426
O	-1.4866	0.2342	-2.5111
O	-1.3174	2.503	-2.7579
O	0.3089	-1.7983	-2.0128
O	-1.7111	-1.5338	-0.1084
O	1.3154	1.038	-1.831
C	2.3399	-1.1354	0.639
C	2.2238	1.8355	-1.5336
C	-1.9292	1.4379	-2.9729
C	-0.2911	-2.4447	-2.9344
C	-2.2497	-1.7669	0.9964
C	2.7706	-1.5787	2.0408
C	3.4996	1.9287	-2.3619

C	-3.2283	1.3754	-3.7701
C	0.2208	-3.7911	-3.4059
C	-1.7342	-1.1968	2.3083
H	1.9781	-2.2414	2.4154
H	2.7889	-0.7011	2.7111
H	3.1964	2.2437	-3.3684
H	3.8496	0.8935	-2.4442
H	-3.1199	0.6222	-4.5636
H	-3.3547	2.3516	-4.2536
H	1.2355	-3.6201	-3.7941
H	-0.409	-4.1207	-4.2355
H	-0.6849	-1.5132	2.3853
H	-1.6893	-0.1039	2.1809
C	-1.0377	2.33	1.0565
H	0.0407	2.5196	1.1961
C	-1.7371	3.6142	0.5338
H	-1.413	3.7461	-0.5049
H	-2.814	3.4072	0.5242
C	-1.4216	4.8411	1.3686
C	-2.2567	5.2379	2.4395
C	-0.2508	5.5964	1.121
C	-1.9326	6.3515	3.2389
H	-3.1735	4.6832	2.6305
C	0.0784	6.7085	1.9176
H	0.3928	5.3132	0.29
C	-0.7612	7.09	2.9831
H	-2.5931	6.6452	4.0524
H	0.9799	7.2802	1.7064
H	-0.5112	7.9524	3.5972
C	-4.4706	1.0498	-2.9354
C	-4.4682	1.0802	-1.5243
C	-5.6752	0.7483	-3.6095
C	-5.654	0.8231	-0.809

H	-3.5517	1.2869	-0.9761
C	-6.8582	0.4908	-2.8945
H	-5.6877	0.7154	-4.6984
C	-6.852	0.5303	-1.4864
H	-5.6369	0.8491	0.2785
H	-7.7761	0.2598	-3.431
H	-7.7646	0.3311	-0.9288
C	4.576	2.8415	-1.7976
C	5.188	2.5378	-0.5559
C	4.9923	3.9908	-2.5035
C	6.1952	3.3731	-0.0373
H	4.8784	1.6463	-0.0128
C	6.0016	4.8239	-1.9844
H	4.5301	4.233	-3.4584
C	6.6052	4.5172	-0.7498
H	6.6603	3.1287	0.9146
H	6.3145	5.7045	-2.5397
H	7.3858	5.1593	-0.3496
C	-2.5482	-1.5626	3.5357
C	-3.3512	-0.5797	4.1587
C	-2.5201	-2.8689	4.0806
C	-4.1158	-0.8993	5.2964
H	-3.3551	0.4276	3.7491
C	-3.2846	-3.1884	5.2196
H	-1.8829	-3.629	3.6302
C	-4.0866	-2.2038	5.8286
H	-4.7278	-0.1342	5.7685
H	-3.2499	-4.1944	5.6309
H	-4.6762	-2.4483	6.7089
C	4.1163	-2.2905	2.0857
C	5.1073	-1.9134	3.0185
C	4.3992	-3.3585	1.2005
C	6.3443	-2.5855	3.0737

H	4.9071	-1.0929	3.7051
C	5.634	-4.0314	1.2509
H	3.6465	-3.6575	0.474
C	6.6126	-3.6479	2.1895
H	7.0933	-2.2819	3.802
H	5.8305	-4.8524	0.5648
H	7.5663	-4.1688	2.2317
C	0.2662	-4.8544	-2.3075
C	0.9816	-4.6441	-1.1068
C	-0.3933	-6.0854	-2.5055
C	1.0387	-5.6553	-0.1305
H	1.4692	-3.6882	-0.9334
C	-0.3363	-7.0969	-1.527
H	-0.9559	-6.2541	-3.4218
C	0.3832	-6.8857	-0.3365
H	1.5937	-5.4838	0.7895
H	-0.8515	-8.0401	-1.6943
H	0.4315	-7.6659	0.4197
O	-1.3688	-1.9744	-3.5455
O	3.3703	-0.3348	-0.0499
H	4.1828	-0.8827	-0.1066
O	-1.5932	1.9761	2.4059
H	-1.3607	2.6806	3.0495
O	-3.3464	-2.5724	1.0043
H	-3.7046	-2.7046	1.9135
O	2.0595	2.6605	-0.4672
H	2.865	3.1904	-0.2623
H	-1.6142	-0.9862	-3.176

**Table A1.2.** Coordinates of complex 3.5.

Atom Label	Coordinates (Å)		
	X	Y	Z
O	1.8739	0.2713	-1.0617
In	0.4744	0.3961	0.2581
O	-0.8868	-0.7756	-0.6884
O	1.4336	1.7134	1.6178
O	2.3182	3.1305	0.0541
O	-1.0388	0.4215	1.8404
O	1.1187	-1.2606	1.4413
O	-0.7436	2.0829	-0.443
C	-1.6972	-1.0627	-1.631
C	-1.4758	2.6916	-1.2341
C	2.3228	2.653	1.2061
C	-1.1189	0.9434	2.9948
C	1.2581	-2.4468	1.7958
C	-1.6547	-2.2735	-2.3767
C	-2.8142	3.2926	-0.8031
C	3.39	3.11	2.2047
C	-2.3406	0.8234	3.8862

C	0.8112	-3.6517	0.9661
H	-0.7411	-2.8415	-2.2446
H	-3.1577	2.7177	0.0578
H	3.8856	3.9746	1.7656
H	-2.134	1.3609	4.8097
H	-0.2164	-3.4706	0.6225
C	2.2868	0.9201	-2.2328
H	2.6599	1.9296	-1.9816
C	3.4672	0.1669	-2.8789
H	4.0961	-0.1979	-2.0657
C	4.2752	0.9279	-3.9006
C	3.6648	1.643	-4.9578
C	5.6847	0.9292	-3.799
C	4.4528	2.3464	-5.8845
H	2.5829	1.6256	-5.0382
C	6.4731	1.6349	-4.7265
H	6.1642	0.375	-2.9939
C	5.8583	2.3469	-5.7736
H	3.9745	2.8907	-6.6962
H	7.5569	1.6272	-4.6341
H	6.4646	2.8908	-6.4947
C	4.3894	2.0819	2.6641
C	4.0428	0.7394	2.9431
C	5.7353	2.4901	2.8212
C	5.0252	-0.1684	3.3736
H	3.0191	0.4046	2.8228
C	6.7159	1.5801	3.25
H	6.0116	3.5214	2.6104
C	6.3622	0.2456	3.5302
H	4.7426	-1.1964	3.5859
H	7.7461	1.9082	3.3645
H	7.1188	-0.4606	3.8644
C	-3.8547	3.3778	-1.8956

C	-4.8949	2.4222	-1.904
C	-3.7923	4.3446	-2.9279
C	-5.8504	2.4252	-2.9367
H	-4.9499	1.6781	-1.1135
C	-4.7472	4.3407	-3.9608
H	-3.0501	5.1398	-2.8872
C	-5.776	3.3788	-3.9701
H	-6.6509	1.6902	-2.9308
H	-4.6981	5.0935	-4.7431
H	-6.5172	3.3809	-4.7648
C	0.9395	-4.992	1.6518
C	2.1986	-5.5115	2.0485
C	-0.2296	-5.7424	1.9067
C	2.278	-6.7463	2.716
H	3.1148	-4.9888	1.7787
C	-0.1429	-6.9798	2.5723
H	-1.1905	-5.3634	1.5667
C	1.1056	-7.4808	2.9855
H	3.2479	-7.1412	3.008
H	-1.048	-7.5522	2.7577
H	1.1683	-8.4384	3.4962
C	-2.5132	-2.5843	-3.5217
C	-1.931	-3.1832	-4.6711
C	-3.913	-2.3235	-3.5337
C	-2.7066	-3.4655	-5.806
H	-0.8657	-3.4003	-4.6707
C	-4.6847	-2.6101	-4.6724
H	-4.4091	-2.0148	-2.6154
C	-4.0856	-3.1707	-5.818
H	-2.2394	-3.9146	-6.6791
H	-5.7568	-2.4269	-4.6558
H	-4.6857	-3.3956	-6.6962
C	-2.8871	-0.5488	4.1371

C	-3.0315	-1.5173	3.1156
C	-3.2846	-0.8665	5.4584
C	-3.5638	-2.7818	3.4187
H	-2.7428	-1.2906	2.0948
C	-3.812	-2.1335	5.7581
H	-3.1817	-0.1236	6.2472
C	-3.9543	-3.0934	4.7365
H	-3.6733	-3.5062	2.6164
H	-4.1123	-2.3682	6.7763
H	-4.3693	-4.0726	4.9641
O	-0.1358	1.6435	3.5426
O	-2.6253	-0.0647	-1.9415
H	-3.1619	-0.3057	-2.7315
O	1.2173	1.0622	-3.2194
H	0.5864	1.7624	-2.9427
O	1.819	-2.6698	3.0126
H	1.8681	-3.6303	3.2435
O	-1.0796	2.8303	-2.5284
H	-1.762	3.221	-3.124
H	0.6775	1.7727	2.8792
Br	-2.8043	-3.794	-0.2145
Br	-2.3544	5.1338	-0.001
Br	-3.7822	2.0768	2.9982
Br	1.9065	-3.5532	-0.774
Br	2.8315	-1.632	-3.731
Br	2.4124	3.9834	3.8415

Annexure A4

*Additional information for Chapter
IV*

A4.1. Copies of UV-Visible spectra of InP MSCs prepared from different precursors.

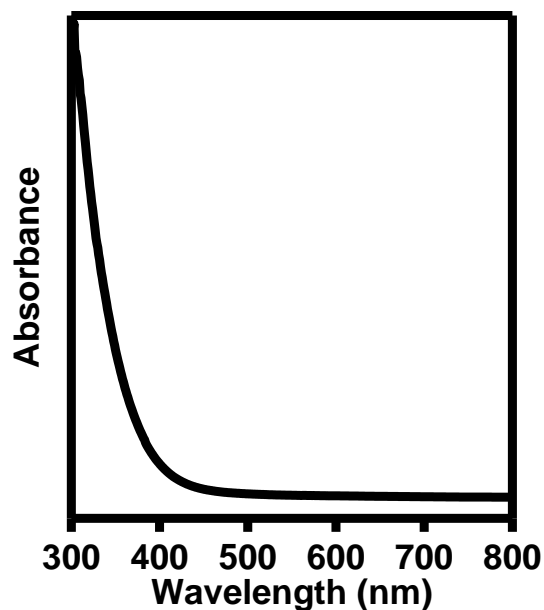


Figure A4.1. The UV-Visible absorption spectrum of InP MSCs, prepared from In-My1, shows no distinct excitonic peak, indicating that it was not formed

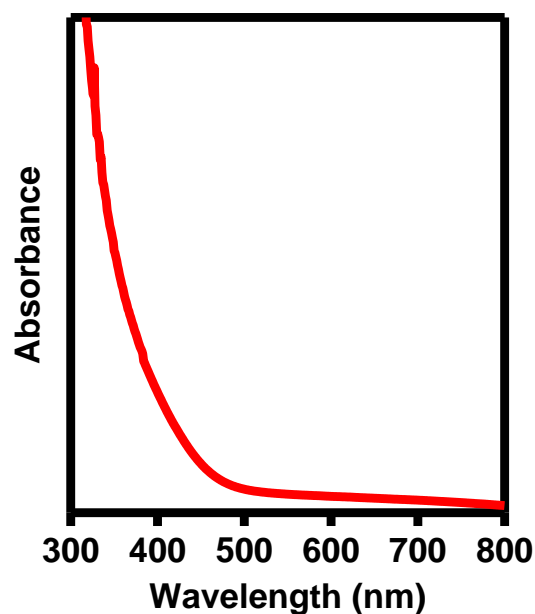


Figure A4.2. The UV-Visible absorption spectrum of InP MSCs, prepared from pure indium myristate complex at 110 °C, shows no distinct excitonic peak, indicating that it was not formed.

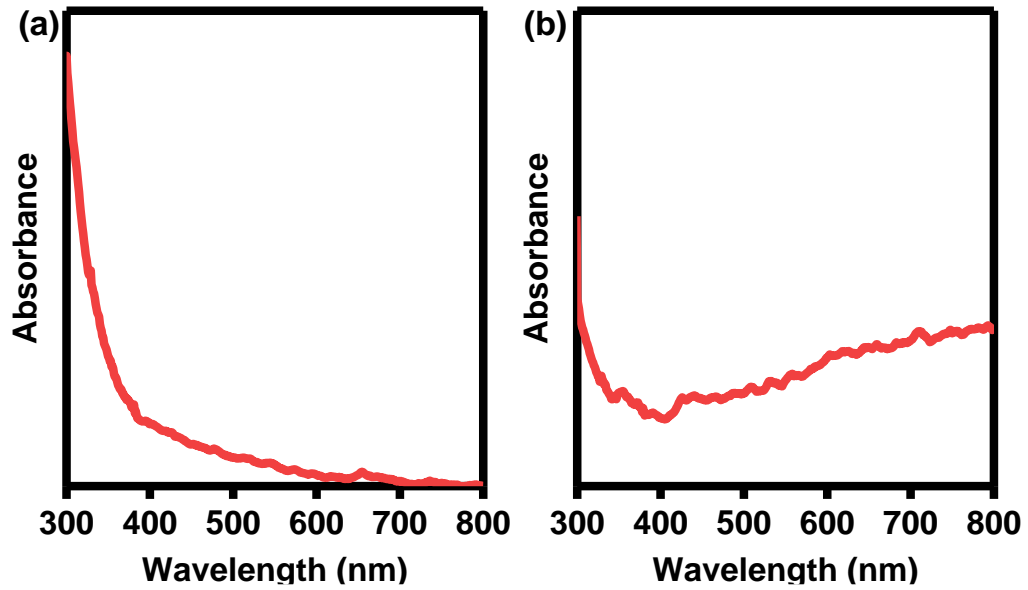


Figure A4.3. The UV-Visible absorption spectrum of InP MSCs, prepared with (a) α -bromomyristic acid and (b) 9,10- hydroxystearic acid as ligand, shows no distinct excitonic peak, indicating that it was not formed.

A4.3. Copies of PXRD spectra.

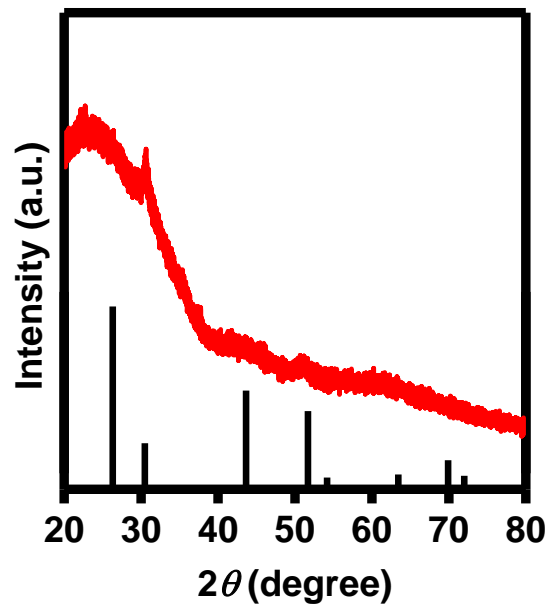
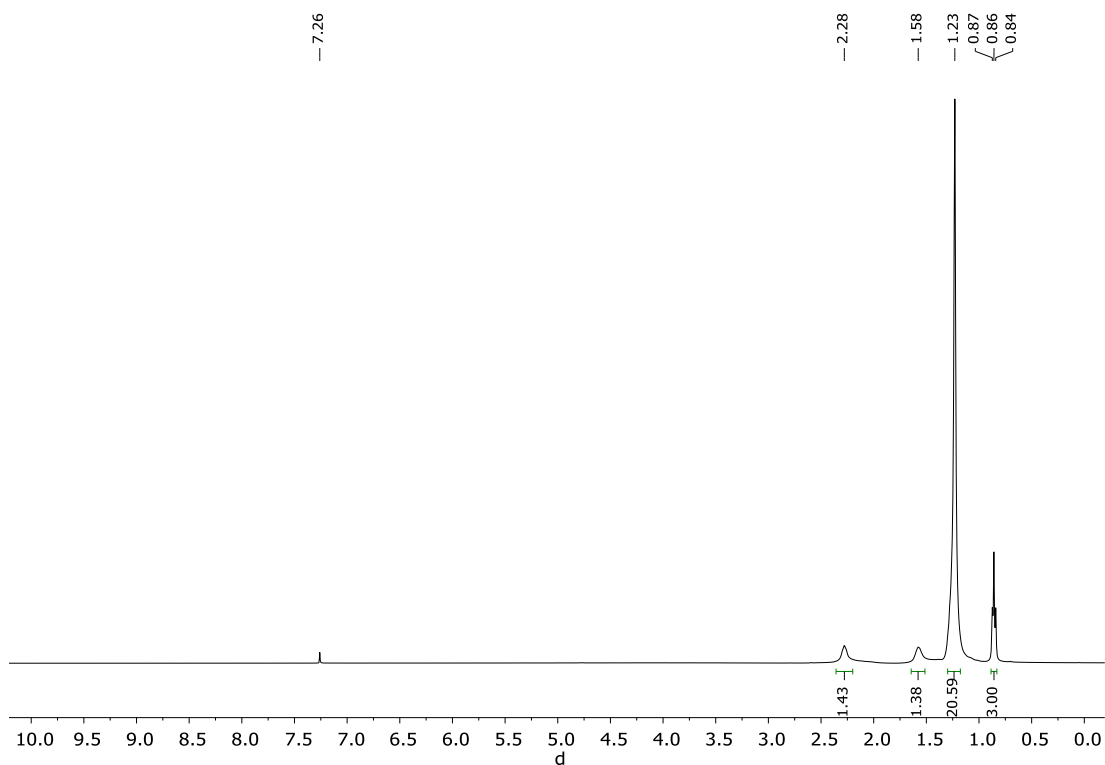
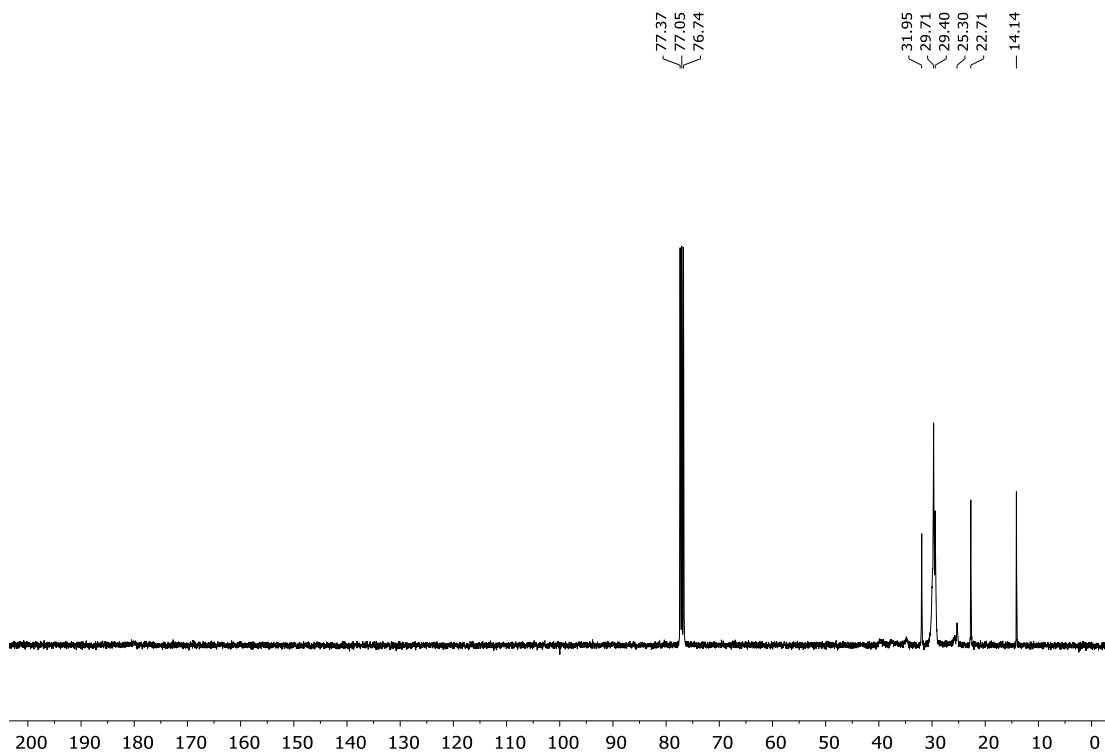


Figure A4.4. Powder X-ray diffractogram of InP QDs (red) prepared from $\text{In}(\text{My})_3$ indexed with standard zinc blende crystal phase of bulk InP (PDF number: 96-101-0147, black)

A4.3. Copies of NMR spectra.**Figure A4.5.** ^1H NMR spectrum of In-My2 (CDCl_3 , 400 MHz)**Figure A4.6.** ^{13}C $\{^1\text{H}\}$ NMR spectrum of In-My2 (CDCl_3 , 100 MHz)

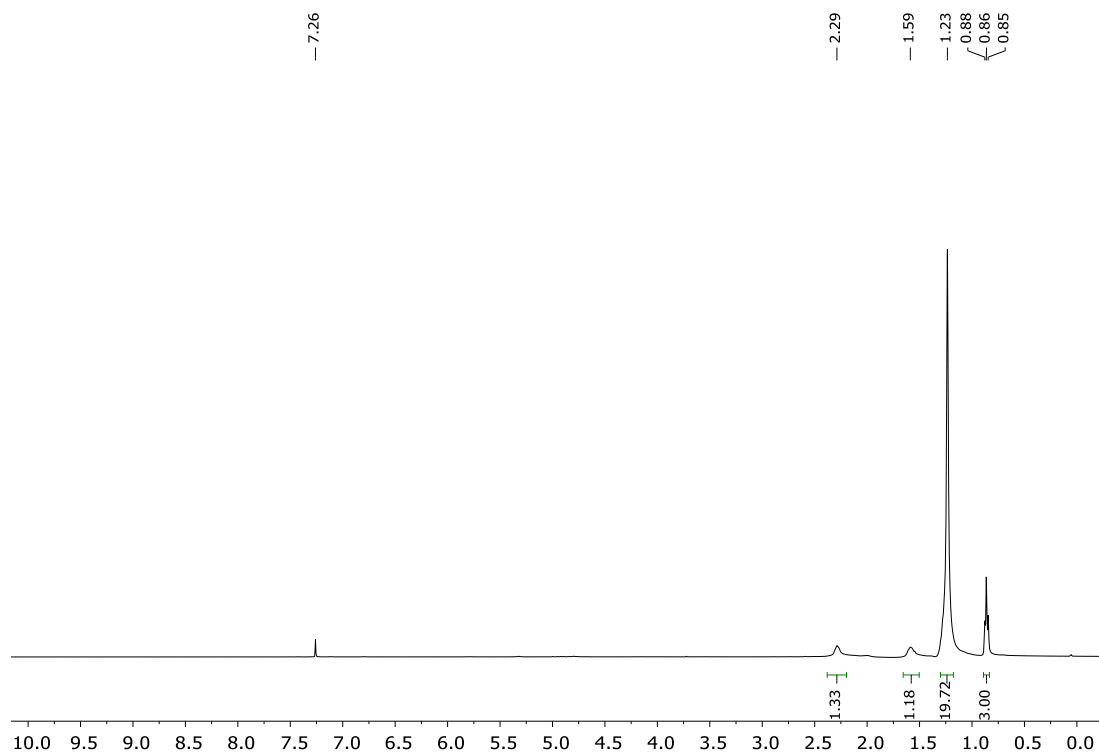


Figure A4.7. ^1H NMR spectrum of In-My3 (CDCl_3 , 400 MHz)

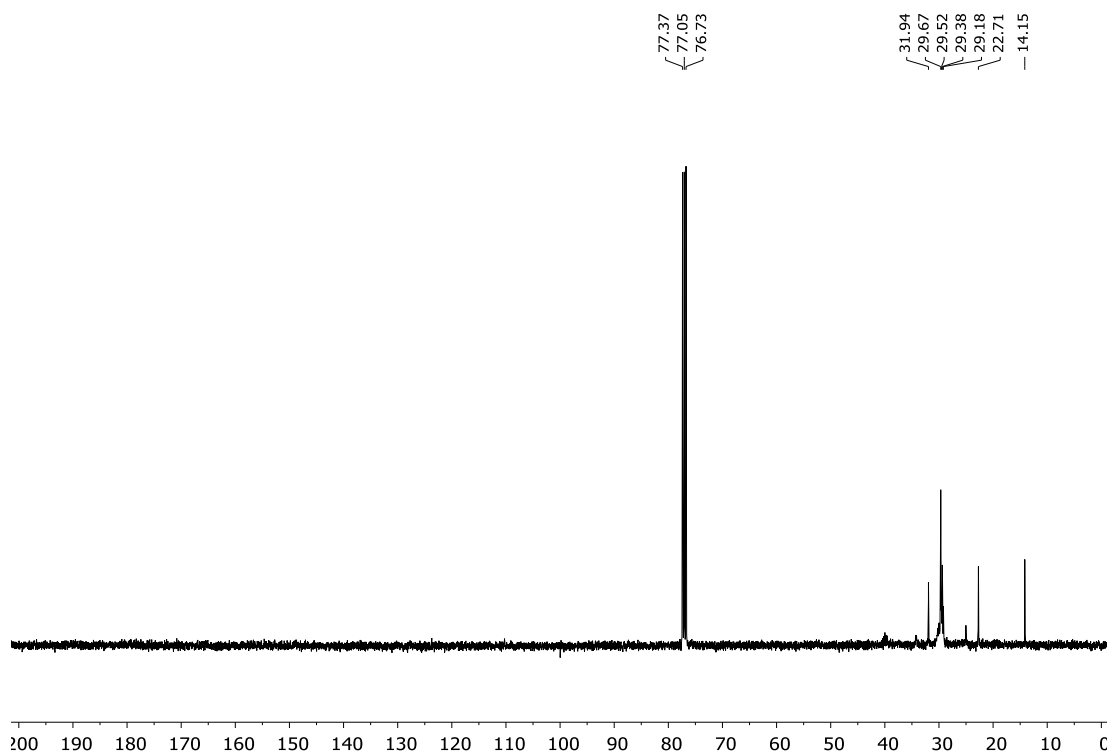


Figure A4.8. ^{13}C $\{^1\text{H}\}$ NMR spectrum of In-My3 (CDCl_3 , 100 MHz)

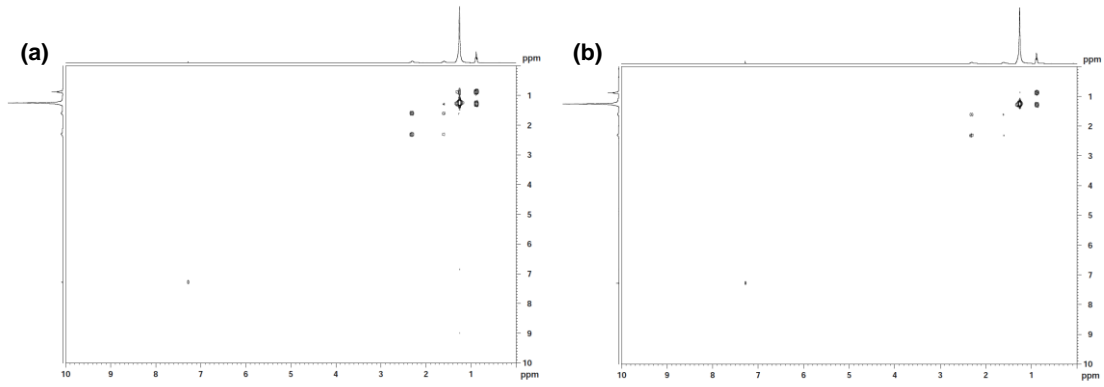


Figure A4.9. ^1H - ^1H COSY spectra of (a) In-My2 and (b) In-My3.

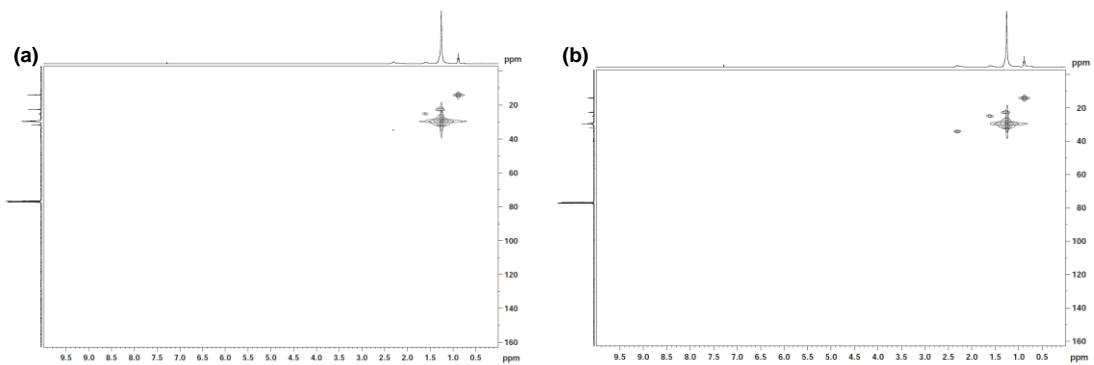


Figure A4.10. ^1H - ^{13}C HMQC spectra of (a) In-My2 and (b) In-My3.

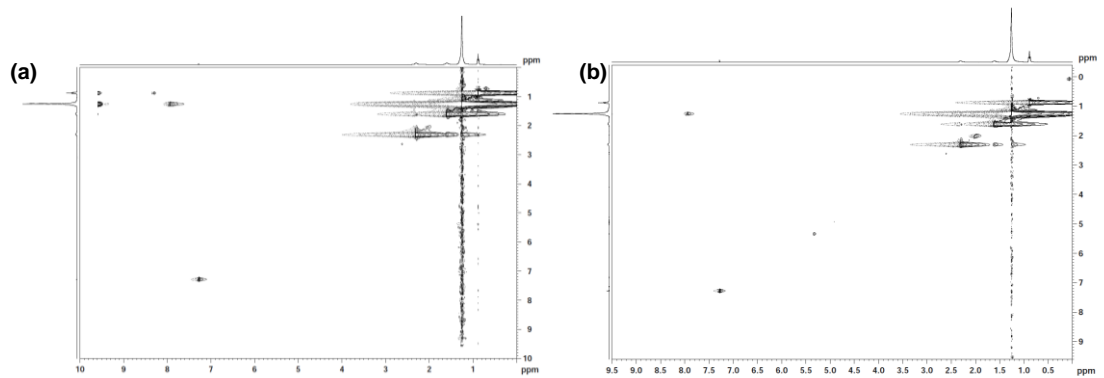


Figure A4.11. ^1H - ^1H NOESY spectra of (a) In-My2 and (b) In-My3.

Annexure B

*List of publications, patents,
conferences and seminars*

B.1. List of publications.

In SCI Journals, in year wise ascending order.

1. "Long-Term Ambient Air-Stable Cubic CsPbBr₃ Perovskite Quantum Dots using Molecular Bromine", Surakcha Thapa, Karishma Bhardwaj, **Siddhant Basel**, Sajan Pradhan, Charlotte Eling, Ali Adawi, Jean-Sebastien Bouillard, Graeme J. Stasiuk, Peter Reiss, Anand Pariyar, and Sudarsan Tamang, *Nanoscale Adv.*, 2019, *1*, 3388-3391. DOI: 10.1039/C9NA00486F
2. "DBU-Catalyzed One-Pot Synthesis of Nearly Any Metal Salt of Fatty Acid (M-FA): A Library of Metal Precursors to Semiconductor Nanocrystal Synthesis", **Siddhant Basel**, Karishma Bhardwaj, Sajan Pradhan, Anand Pariyar, and Sudarsan Tamang, *ACS Omega*, **2020**, *5*, 6666-6675. DOI: 10.1021/acsomega.9b04448
3. "Tunable NIR-II emitting silver chalcogenide quantum dots using thio/selenourea precursors: Preparation of an MRI/NIR-II multimodal imaging agent", Karishma Bhardwaj, Sajan Pradhan, **Siddhant Basel**, Mitchell Clarke, Beatriz Brito, Surakcha Thapa, Pankaj Roy, Sukanya Borthakur, Lakshi Saikia, Amit Shankar, Graeme J Stasiuk, Anand Pariyar, Sudarsan Tamang, *Dalton Trans.*, **2020**, *49*, 15425-15432. DOI: 10.1039/D0DT02974B
4. "Stable lead-halide perovskite quantum dots as efficient visible light photocatalysts for organic transformations", Sajan Pradhan, Deshaj Bhujel, Bikram Gurung, Debesh Sharma, **Siddhant Basel**, Sagarmani Rasaily, Surakcha Thapa, Sukanya Borthakur, Wai Li Ling, Lakshi Saikia, Peter Reiss, Anand Pariyar, Sudarsan Tamang, *Nanoscale Adv.*, **2021**, *3*, 1464-1472. DOI: 10.1039/2516-0230/2018

5. “*CsPbBr₃ Perovskite Quantum Dots as Visible Light Photocatalyst for cyclisation of diamines and amino alcohols: An efficient approach to synthesize Imidazolidines, fused-imidazolines and Oxazolidines.*” Bikram Gurung, Sajan Pradhan, Debesh Sharma, Deshaj Bhujel, **Siddhant Basel**, Shivanand Chettri, Sagarmani Rasaily, Anand Pariyar, Sudarsan Tamang *Catalysis Science and Technology*, **2022**, 12, 5891-5898. DOI: 10.1039/D2CY00799A

B.2. List of patents.

1. *A Simple Process for Production of High Purity Metal Long-Chain Carboxylates (Application No- 202031006346)*

B.3. List of conferences and seminars.

1. International Conference on Emerging Trends in Nanoscience and Nanotechnology, Sikkim Manipal Institute of Technology, 2016 (**Oral presentation**)
2. One week training on computer applications and data analysis at Sikkim University, 2016
3. One-day National Symposium on Recent Trends in Organic Synthesis, organized by Department of Chemistry, Sikkim Government College in association with Royal Society of Chemistry, Eastern India Section (2017)
4. National conference on Recent Trends in Chemistry- Sikkim Manipal Institute of Technology, 2017
5. DST Inspire Review meet, Institute of Advanced Study in Science and Technology (IASST), Guwahati, 2017 (**Poster presented**)
6. DST INSPIRE Science Camp-2018 (Demonstrated the working and technical

- aspects of some sophisticated instruments in research and development).
7. 1st International e-Conference on Recent Advances in Physics & Materials Science-2020 (IC-RAPMS- 2020) organized by Kurseong College and Saint Joseph's College, Darjeeling, West Bengal, India.
 8. Web of science certification programme-2022, organized by Sikkim University, India.
 9. Workshop on Understanding Plagiarism and its Detection organized by Teesta-Indus Central library, Sikkim University, 2022.
 10. Web seminar on Improve your XRD analysis: Guidelines for getting good quality PXRD pattern for pharmaceutical samples, Malvern Panalytical, 2022
 11. Webinar on Planning your Research and Publishing in High Impact Journals organized by Teesta-Indus Central library, Sikkim University, 2022.
 12. 10th Workshop on Computational Chemistry of Materials: Molecule, Solids, Nanoparticles and Biological Activity organized by Centre of Advanced Computational Chemistry Studies, Delhi (2022)

This is an open access article published under an ACS AuthorChoice License, which permits copying and redistribution of the article or any adaptations for non-commercial purposes.



http://pubs.acs.org/journal/acsofd

Article

DBU-Catalyzed One-Pot Synthesis of Nearly Any Metal Salt of Fatty Acid (M-FA): A Library of Metal Precursors to Semiconductor Nanocrystal Synthesis

Siddhant Basel, Karishma Bhardwaj, Sajan Pradhan, Anand Pariyar, and Sudarsan Tamang*

Cite This: *ACS Omega* 2020, 5, 6666–6675

Read Online

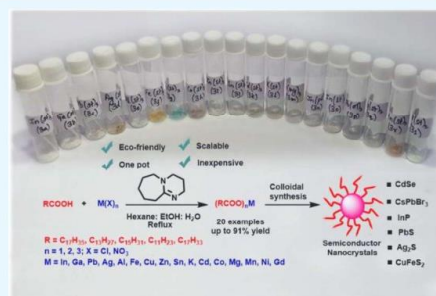
ACCESS |

Metrics & More

Article Recommendations

Supporting Information

ABSTRACT: The metal salts of fatty acid (M-FA) are the most widely used metal precursors to colloidal semiconductor nanocrystals (NCs). They play a key role in controlling the composition, shape, and size of semiconductor NCs, and their purity is essential for attaining impeccable batch-to-batch reproducibility in the optical and electrical properties of the NCs. Herein, we report a novel, one-pot synthesis of a library of highly pure M-FAs at near-quantitative yields (up to 91%) using 1,8-diazabicyclo[5.4.0]undec-7-ene or the related nonionic/noncoordinating base as an inexpensive and ecofriendly catalyst in a green solvent medium. The method is highly general and scalable with vast academic and industrial potential. As a practical application, we also demonstrate the use of these high-quality M-FAs in the synthesis of the spectrum of colloidal semiconductor NCs (III–V, II–VI, IV–VI, I–VI, I–III–VI, and perovskite) having absorption/emission in visible to the near-infrared region.



1. INTRODUCTION

Because a seminal paper by Brus et al. was published in 1983,¹ colloidal synthesis has emerged as a powerful and effective method to prepare high-quality inorganic nanocrystals (NCs).^{2,3} The metal salts of fatty acids (M-FAs) are the most common form of metal precursors in nearly all semiconductor NC syntheses based on the hot injection method in the noncoordinating solvent.^{4–11} In the colloidal synthesis of NCs, M-FA plays a crucial role in solubilizing the metal ions, controlling the precursor reaction, nucleation and growth processes, and passivating the surface and stabilizing the colloidal dispersion.^{12–16} Therefore, the role of M-FAs is decisive for the evolution of crystal phase,¹¹ size,⁵ and shape¹⁷ and even the higher dimensional assembly of the NCs^{17,18} with unique physical and chemical properties. In addition to this, it is well-known that M-FAs are the key ingredients in a plethora of industrial and domestic products including cosmetics,¹⁹ lubricants,^{20–22} paints,²³ biofuels,^{24,25} and rubber.²⁶ Some of the common methods employed for the synthesis of M-FA precursors are the (1) vacuum method; (2) saponification method; (3) precipitation (double decomposition) method; and (4) direct reaction of fatty acids with metals. Conventionally, in the colloidal synthesis of semiconductor NCs, M-FAs are synthesized by the “vacuum method” where metal acetate and the desired fatty acid are vacuumed together at high temperature in high boiling solvents.^{4,5,8,11,13} For example, for the synthesis of InP NCs, the indium salt of fatty acid is prepared in situ by the vacuum method prior to the reaction.

Typically, a mixture of In-acetate and fatty acid (myristic acid, palmitic acid, stearic acid, oleic acid or lauric acid) is mixed in a noncoordinating solvent [1-octadecene (1-ODE)]⁵ and are vacuumed at 110–130 °C for 1–2 h to obtain a “clear solution” of indium carboxylate.^{5,13} Unfortunately, there is no consensus about time, pressure, and temperature of this method with respect to purity and composition of the M-FA formed in situ, and this shortcoming may lead to batch-to-batch inconsistencies in the properties of the NCs. Except for a few special cases,^{6,27,28} where M-FAs have been fully characterized, the purity of the M-FA precursor in most cases were not confirmed prior to the colloidal synthesis and characterization. Therefore, given the sensitivity of these colloidal reactions and in view of the uncertainty involved with the purity of M-FAs prepared by the “vacuum method”, many of the kinetic studies and the conclusions reported therein may not be fully accurate, especially in quantitative studies. Recent reports have preferred pure M-FAs prepared ex situ for the synthesis and kinetic studies of NCs, emphasizing on the growing importance of the compositional purity of the precursor.^{6,29} For example, Owen and coworkers⁶ synthesized

Received: December 26, 2019

Accepted: March 6, 2020

Published: March 18, 2020

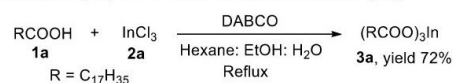
highly pure lead oleate directly from lead oxide and oleic acid in the presence of trifluoroacetic anhydride and triethylamine. They employed the pure lead oleate to study the kinetics of lead chalcogenide formation from a library of thiourea precursors. In another report, an iron oleate precursor was synthesized from ferric chloride and sodium oleate.²⁹ This method is based on the first saponification of fatty acid with an inorganic base such as NaOH or KOH followed by the reaction of the alkali metal oleate with chloride salts of the desired metal ions.^{30,31} Other strategies for the synthesis of M-FA (M = Zn, Ca) include precipitation of M-FA via the double decomposition reaction^{32,33} and the direct reaction of fatty acids with some metals.³⁴ However, most of these methods suffer from some pitfalls such as the presence of the free fatty acid impurity (e.g. the vacuum method), limited substrate scope (e.g. the precipitation method), poor atom economy, and lengthy reactions involving multiple steps (e.g. the saponification and double decomposition method). For example, the saponification and double precipitation methods first require fatty acids to be converted into alkali metal salts using the inorganic base, which will be subsequently purified, isolated, and then used for the preparation of other M-FAs. Clearly, there is a need for the development of a more general and simpler method to address the aforementioned drawbacks. Herein, we report a new approach to access a library of pure M-FA precursors in high yield by direct reaction of commercially available fatty acids with metal salts in the presence of a noncoordinating, sterically hindered organic base as an inexpensive and benign catalyst. The method is one-step and does not require an additional purification step.

2. RESULTS AND DISCUSSION

We noted that the direct reaction of fatty acids with the corresponding metal chlorides essentially required an inorganic base to promote the reaction. However, the use of inorganic bases such as NaOH or KOH is not desirable in many cases because alkali metal ions compete with other intended metal ions in the reaction. This issue could be addressed by the use of nonionic, noncoordinating organic bases having a lower affinity toward metal ions. An ideal candidate would be a strong nitrogenous organic base, that is, accessible, nontoxic, and stable. In this context, initially, we screened 1,4-diazabicyclo[2.2.2]octane (DABCO) for the direct synthesis of M-FA from fatty acid and metal salt in one step. DABCO is an inexpensive, commercially available, and environmentally benign organic base.³⁵ It is sufficiently basic (pK_a conjugate acid ~ 8.7) to abstract proton from fatty acids³⁶ and is an effective catalyst in many organic transformations such as the Baylis–Hillman reaction,³⁷ chlorination of alkenes via activation of *N*-chlorosuccinimide,³⁸ and so forth. To access the feasibility of obtaining M-FA in a single step, we carried out a one-pot substitution reaction between 3.0 equiv of stearic acid (**1a**) and 1.0 equiv of indium trichloride (**2a**) in the presence of 4.0 equiv of DABCO, under reflux conditions in 7:4:3 ratio of hexane/ethanol/water as a green biphasic solvent mixture. We used DABCO as a base in slightly above stoichiometric amounts (4.0 equiv base compared to the fatty acid) in our initial experiments with the sole objective to promote complete deprotonation of fatty acids. The reaction yielded indium stearate (**3a**) in 72% yield in the pure form (Scheme 1).

The biphasic nature of the solvent mixture, that is, the hexane/ethanol/water (7:4:3) system³⁹ simplifies the isolation

Scheme 1. Reaction of Stearic Acid (**1a**) with Indium Trichloride (**2a**) to Obtain Indium Stearate (**3a**)



of the product which is extracted from the nonpolar hexane part, whereas the ionic impurities including the base and other byproducts remain in the aqueous/ethanol part, thus ensuring the high purity of the product. Figure 1 shows the

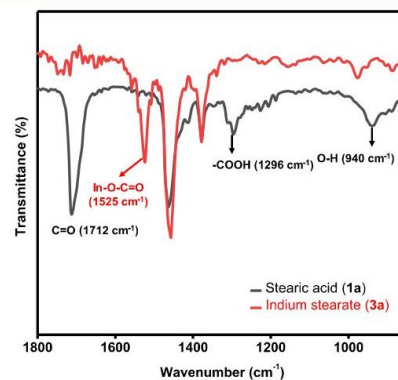


Figure 1. Fourier transform infrared (FTIR) spectrum of stearic acid (**1a**, black) and the indium stearate (**3a**, red) prepared from **1a**. The characteristic stretching and bending signatures related to carboxylic and carboxylate groups are marked for clarity.

characteristic asymmetric COO^- stretching band centered around 1525 cm^{-1} for the intended product, indium stearate (**3a**),⁴⁰ which is clearly distinguishable from the sharp $\text{C}=\text{O}$ stretching peak at $\sim 1712 \text{ cm}^{-1}$ for the free fatty acid (**1a**). Furthermore, the $-\text{OH}$ (bending) and $-\text{COOH}$ (bending) characteristic of **1a** at 940 and 1296 cm^{-1} was also not detected in the product **3a**. The thermogravimetric analysis (TGA) results show the $\sim 85\%$ decrease in weight in the temperature range $150\text{--}500 \text{ }^\circ\text{C}$ consistent with the loss of three stearate groups (Figure S1). Above $500 \text{ }^\circ\text{C}$, constancy in the weight loss exemplified the complete decomposition of indium stearate to afford In_2O_3 . ^1H and ^{13}C NMR further confirmed the formation of **3a** (Figures S2 and S3). The presence of three stearate groups in the product was further confirmed by ^1H NMR analysis using 1,3,5-trimethoxybenzene as the internal standard (Figure S4). The measured melting point of the pure **3a** is $145\text{--}148 \text{ }^\circ\text{C}$.

In principle, other nonionic/uncharged nitrogenous bases with similar attributes (basicity, noncoordinating, and a good leaving group) as DABCO should also be effective for our reaction. In fact, we observed the formation of the desired product using other organic bases such as pyridine (aromatic amine), triethylamine (tertiary alkyl amine), and 1,8-diazabicyclo[5.4.0]undec-7-ene (DBU) which is a sterically hindered base (entries 1–4, Table 1). Based on our screening studies, the best result was obtained with DBU which is a bicyclic amidine compound. The result obtained with DBU was better than with DABCO or other bases tested above which is possibly due to the higher basicity of DBU (pK_a conjugate ~ 13.5).⁴¹ It is well-known that the amidines are a

Table 1. Optimization Studies for the One-Step Synthesis of Indium Stearate (3a)^a

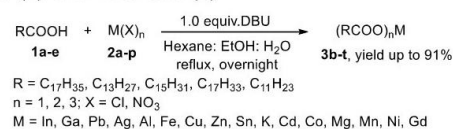
entry	base	equiv	temp (°C)	time (h)	yield (%)
1	DABCO	4.0	reflux	overnight	72
2	pyridine	4.0	reflux	overnight	66
3	triethylamine	4.0	reflux	overnight	32
4 ^a	DBU	4.0	reflux	overnight	78
5 ^b	DBU	3.0	reflux	overnight	80
6 ^c	DBU	1.0	reflux	overnight	85
7 ^d	DBU	0.5	reflux	overnight	66
8 ^e	DBU	1.0	25	overnight	nr
9 ^f	DBU	1.0	40	overnight	22
10 ^g	DBU	1.0	60	overnight	60
11	DBU	1.0	reflux	6 h	60
12	DBU	1.0	reflux	8 h	58
13	DBN	1.0	reflux	overnight	82

^aUnless otherwise noted, all reactions were carried out with 4.0 equiv (with respect to a fatty acid) of the base under reflux conditions. ^bThe reaction was performed with 3.0 equiv of the base. ^cThe reaction was performed with 1.0 equiv of the base. ^dThe reaction was performed with 0.5 equiv of the base. ^enr denotes no reaction. ^fThe reaction was performed at 40 °C. ^gThe reaction was performed at 60 °C.

stronger base than the tertiary amine or amides and are among the strongest nonionic/uncharged bases.⁴² DBU is a stable, inexpensive, nontoxic,⁴³ and accessible base commonly used in organic transformation, therefore qualifying as an ideal candidate for further studies and optimization. Using the reaction between indium chloride and stearic acid in the presence of DBU as the model reaction, we studied the effect of the concentration of the base, temperature, and time on the reaction yield. In our studies so far, 4.0 equiv of the base (compared to a fatty acid) were used (entries 1–4, Table 1) to facilitate complete deprotonation of the carboxylic acid. To further understand the effect of the base on the reaction, we decreased the amount of DBU from 4.0 to 0.5 equiv in succession. The entries 4–6 shows that the yield of the desired product improved from an initial 78% (with 4.0 equiv DBU) to 85% (with 1.0 equiv DBU), when other conditions were constant. However, further lowering the amount of DBU to 0.5 equiv resulted in a decrease in the reaction yield to 66% (entry 7, Table 1). These results show that the role of DBU is catalytic in nature. To study the effect of temperature, we performed reactions at four different temperatures (25, 40, 60 °C, and reflux temperature) using 1.0 equiv of DBU (entries 6, 8–10, Table 1). While at room temperature, the reaction did not take place, the maximum yield was obtained under reflux conditions. Likewise, we investigated the effect of time for this transformation. When the reaction mixture was refluxed for a short period of time (entries 11 and 12, Table 1), the efficiency of the transformation was poor. Therefore, the reaction condition detailed in entry 6 was marked as the best-optimized reaction condition for our reaction. Furthermore, 1,5-diazabicyclo[4.3.0]non-5-ene (DBN), a related amidine compound was also tested as a catalyst and as expected a comparable product yield was achieved (entry 13, Table 1), thus underscoring the effectiveness of analogous amidine compounds in general as a catalyst for this reaction. The

summary of the optimization studies is tabulated below (Table 1).

Next, under optimized conditions, we synthesized a large variety of M-FAs (3b–t) on reacting a series of metal salts (2a–p) with fatty acids (1a–e) in a single step using a catalytic amount of DBU (Scheme 2). All the substrates were well-

Scheme 2. Synthesis of Metal Carboxylates (3) from Fatty Acid (1) and Metal Salt (2)

tolerated under optimized reaction conditions, and the corresponding M-FAs (3b–t) were obtained in high yields (up to 91%, entries 1–19, Table 2). Table 2 presents an overview of the substrate scope of our reaction. In each case, the successful formation M-FAs was confirmed by the presence of characteristic –COO[−] asymmetric (~1510–1650 cm^{−1})⁴⁴ in FTIR (Figures S5–S23). For some M-FAs, we observe two asymmetric vibrations which are attributed to differences in the

Table 2. Synthesis of Metal Carboxylates (3) from Fatty Acid (1) and Metal Salt (2)

entry	fatty acid (1)	metal salt (2)	product (3)	yield (%)
1	stearic acid (1a)	GaCl ₃ (2b)	(C ₁₇ H ₃₃ CO ₂) ₃ Ga (3b)	90
2	stearic acid (1a)	Pb(NO ₃) ₂ (2c)	(C ₁₇ H ₃₃ CO ₂) ₂ Pb (3c)	73
3	stearic acid (1a)	AgNO ₃ (2d)	(C ₁₇ H ₃₃ CO ₂)Ag (3d)	91
4	stearic acid (1a)	AlCl ₃ (2e)	(C ₁₇ H ₃₃ CO ₂) ₃ Al (3e)	35
5	stearic acid (1a)	FeCl ₃ (2f)	(C ₁₇ H ₃₃ CO ₂) ₂ Fe (3f)	90
6	stearic acid (1a)	CuCl ₂ (2g)	(C ₁₇ H ₃₃ CO ₂) ₂ Cu (3g)	91
7	stearic acid (1a)	CoCl ₂ (2h)	(C ₁₇ H ₃₃ CO ₂) ₂ Co (3h)	75
8	stearic acid (1a)	ZnCl ₂ (2i)	(C ₁₇ H ₃₃ CO ₂) ₂ Zn (3i)	87
9	stearic acid (1a)	SnCl ₂ (2j)	(C ₁₇ H ₃₃ CO ₂) ₂ Sn (3j)	90
10	stearic acid (1a)	CdCl ₂ (2k)	(C ₁₇ H ₃₃ CO ₂) ₂ Cd (3k)	81
11	stearic acid (1a)	KNO ₃ (2l)	(C ₁₇ H ₃₃ CO ₂) ₃ K (3l)	85
12	myristic acid (1b)	InCl ₃ (2a)	(C ₁₃ H ₂₇ CO ₂) ₃ In (3m)	90
13	palmitic acid (1c)	InCl ₃ (2a)	(C ₁₅ H ₃₁ CO ₂) ₃ In (3n)	60
14	lauric acid (1d)	InCl ₃ (2a)	(C ₁₁ H ₂₃ CO ₂) ₃ In (3o)	75
15	oleic acid (1e)	Pb(NO ₃) ₂ (2c)	(C ₁₇ H ₃₃ CO ₂) ₂ Pb (3p)	90
16	stearic acid (1a)	Mg(NO ₃) ₂ (2m)	(C ₁₇ H ₃₃ CO ₂) ₂ Mg (3q)	88
17	stearic acid (1a)	MnCl ₂ ·4H ₂ O (2n)	(C ₁₇ H ₃₃ CO ₂) ₂ Mn (3r)	70
18	stearic acid (1a)	NiCl ₂ ·6H ₂ O (2o)	(C ₁₇ H ₃₃ CO ₂) ₂ Ni (3s)	87
19	stearic acid (1a)	GdCl ₃ ·6H ₂ O (2p)	(C ₁₇ H ₃₃ CO ₂) ₃ Gd (3t)	45

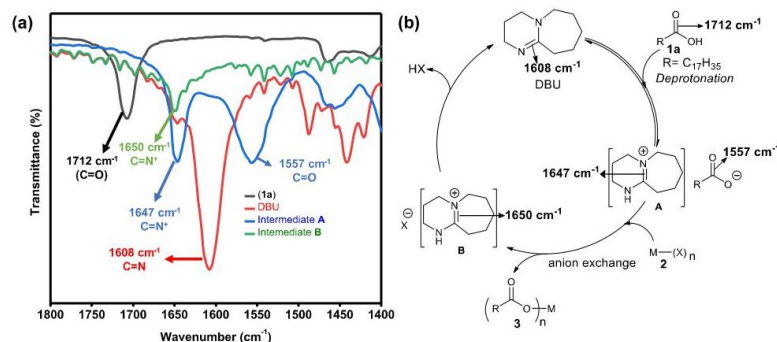


Figure 2. (a) FTIR spectra of the starting compound stearic acid (**1a**, black), the pristine DBU catalyst (red), a mixture of stearic acid and DBU heated to the reaction temperature for 5 min (intermediate A, blue) and the aqueous part of the reaction mixture after 13 h of reaction (intermediate B, green) and (b) proposed mechanistic pathway for the DBU-catalyzed synthesis of M-FAs.

nature of the M–O bonds in the compound.^{45–47} These results show that the effect of coordination of the carboxylic ion with metal and the nature of the M–O bonding is reflected in COO[−] asymmetric frequencies. The characteristic C=O stretching vibration at slightly above 1700 cm^{−1} because of free fatty acids³⁴ (Figure S24) is absent in our samples (Figures S5–S23), confirming their high purity. Furthermore, the TGA thermogram confirmed the weight % loss corresponding to the number of carboxylate groups per metal ion in each case (Figures S5–S23). For M-FAs containing diamagnetic metal ions, additional characterization was performed using ¹H and ¹³C NMR (Figures S25–S50) to confirm the formation of the desired products. This method, thus, allows for the synthesis of highly pure M-FAs of diverse metal ions positioned in various groups of the periodic table. Specifically, we demonstrate the facile synthesis of M-FAs, where M = K (alkaline metal), Mg (alkaline earth metal), Mn, Fe, Co, Ni, Cu, Zn (first row transition metals), Ag, Cd (second row transition metals), Al, Ga, In (triels; group IIIA), Sn, Pb (tetrels, group IVA), and Gd (lanthanide). Especially, the carboxylates of group IIIA metals such as aluminum, gallium, indium, and so forth are in general considered difficult to synthesize under benign conditions because of the tendency of group IIIA metals to form a bond with a more covalent character.¹⁴ On the contrary, our method demonstrates excellent efficiency with nearly all metal ions.

3. MECHANISM

From optimization studies (entry 6, Table 1), it is clear that the DBU is highly efficient when used in a catalytic amounts. Unprotonated DBU has a characteristic C=N stretching at 1608 cm^{−1} (Figure 2a), and free stearic acid has C=O stretching at 1712 cm^{−1}. When DBU and fatty acids (stearic acid) are mixed and heated close to the reaction temperature for 5 min, we observed a strong shift in C=N stretching to 1647 cm^{−1} which is attributed to the protonation of DBU. This observation, taken together with the detection of a shift of C=O stretching of fatty acid from 1712 to 1557 cm^{−1} unambiguously confirms the formation of the intermediate A (Figure 2) during the initial stage of the reaction. A similar observation has been reported for protonation of DBU by Pripol 1009, a commercially available bio-based fatty acid dimer.⁴⁸ After the reaction is complete, we carefully analyzed the aqueous fraction of the biphasic solution system using FTIR. The extracted byproduct (aqueous fraction) exhibited

C=N stretching at 1650 cm^{−1}, a slight deviation from the intermediate A. In addition, we did not detect any carboxylate signature in this fraction, confirming the presence of the intermediate B which contains halide or nitrate as counterions. In other words, we detected the halide or nitrate salt of DBU in the solution after the reaction is completed (Figure 2a). Based on these observations, we propose a simple anion exchange mechanism involving DBU as a catalyst as depicted in Figure 2b.

Thus, the reaction proceeds via deprotonation of the carboxylic functionality of fatty acid (**1a**) in the presence of DBU under reflux conditions to generate the corresponding intermediate A (Figure 2), which further takes part in the anion exchange reaction with metal salt (**2**) to form intermediate B followed by the expulsion of halogen acid (HX) from B to generate DBU (the base catalyst) which further enters into another catalytic cycle. The driving force for the transformation of intermediate A to B in the presence of metal salt is the strong oxyphilic nature of the metal ions.^{49,50}

4. MULTIGRAM SCALE SYNTHESIS

Because most of these M-FAs have potential commercial use, the scale-up of the reaction is desirable. We demonstrate the successful extension of our protocol to the multigram synthesis of M-FA. As a representative example, 5.0 g of ZnCl₂ (**2i**) was reacted with 20.0 g of stearic acid (**1a**) in the presence of 5.5 mL DBU under optimized reaction conditions to obtain the corresponding zinc stearate (**3i**) in 19.7 g (86% yield, Figure 3a). The products were isolated in a pure form directly from the hexane fraction and characterized using FTIR (Figure 3b), NMR (Figures S33 and S34), and TGA (Figure S12). The measured melting point of the product obtained using the digital melting point apparatus was 128–130 °C, which is consistent with the literature value (130 °C).⁵¹ This further confirms the high purity of the product formed.

5. APPLICATION

5.1. Synthesis of Colloidal Semiconductor NCs from the As-Prepared M-FA Precursors. The easy access to the library of highly pure M-FAs has tremendous importance in the growing field of colloidal semiconductor NCs or quantum dots exhibiting a unique optical and electrical property in the quantum confinement regime.^{52,53} In particular, we expect that our method will allow for the more precise study of reaction

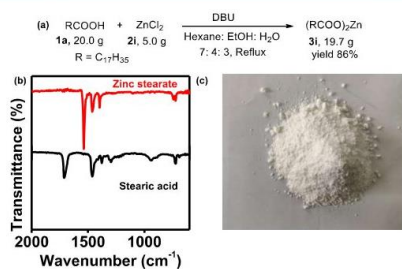


Figure 3. (a) Scheme for reaction between ZnCl_2 (2i) and stearic acid (1a) to yield zinc stearate (3i); (b) FTIR spectrum zinc stearate (3i, red) showing lower carbonyl stretching compared to the stearic acid (1a); and (c) photographic image of 19.7 g zinc stearate (3i).

kinetics and efficient control of the properties of the NCs for meaningful application in many technologically important areas including optoelectronics,⁵⁴ photovoltaics,⁵⁵ bio-molecular imaging,^{56,57} and photocatalysis.^{58,59} We demonstrate the colloidal synthesis of different types of a semiconductor NCs such as CsPbBr_3 perovskite, PbS (IV–VI),⁶ CdSe (II–VI),³ CuFeS_2 (I–III–VI),⁶⁰ Ag_2S (I–VI),⁶¹ and InP (III–V)⁵ NCs using pure M-FAs obtained from this work (Table 3). All these

Table 3. Various Semiconductor NCs Synthesized from the As-Prepared M-FA Precursors

entry	M-FA precursors	semiconductor type	semiconductor NCs
1	$\text{Pb}(\text{oleate})_2$	perovskite	CsPbBr_3
2	$\text{Pb}(\text{oleate})_2$	IV–VI	PbS
3	$\text{Cd}(\text{stearate})_2$	II–VI	CdSe
4	$\text{Cu}(\text{stearate})_2$ and $\text{Fe}(\text{stearate})_2$	I–III–VI	CuFeS_2
5	$\text{Ag}(\text{stearate})$	I–VI	Ag_2S
6	$\text{In}(\text{stearate})_3$	III–V	InP

materials are widely studied and applied for a range of applications such as photovoltaics (PbS and CuFeS_2),^{62,63} light-emitting diodes (CdSe , InP , and CsPbBr_3),^{64–66} bio-imaging in visible and near-infrared (InP and Ag_2S),^{67,68} regions, and photocatalysis of organic transformation (CsPbBr_3 , CdSe , and InP).^{69–71} The respective M-FAs employed for the synthesis of these NCs are listed in Table 3, and their synthetic details are furnished in the Experimental Section. The NCs synthesized were highly stable as colloidal dispersion (Figure S51) and exhibited their characteristic optical properties (Figures 4 and S52). The powdered X-ray diffraction (PXRD) studies confirmed their crystal structure and high phase purity (Figure 5). The absorption and emission band widths expressed as half-width at half maximum (HWHM) or full-width at half maximum (fwhm) of the NCs were comparable to those reported for conventionally prepared NCs.^{72–75}

6. CONCLUSIONS

In summary, we demonstrated an easy, scalable, and generalized methodology for the synthesis of highly pure M-FAs with metal ions from all blocks (s, p, d, and f blocks) of the periodic table. The sterically hindered, noncoordinating DBU and the analogous base were found to catalyze the formation of M-FAs via the abstraction of a proton from fatty

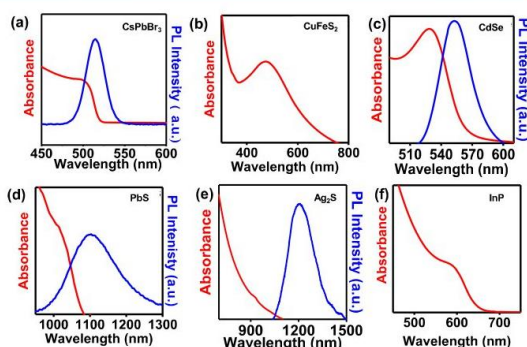


Figure 4. (a) UV–vis (red) and PL spectra (blue) of CsPbBr_3 perovskite NCs (excitation: 400 nm, emission: 515 nm, fwhm = 28 nm); (b) UV–vis spectrum of CuFeS_2 NCs exhibiting a typical surface plasmon resonance band⁷⁶ (HWHM: 156 nm); (c) UV–vis (red) and PL (blue) spectra of CdSe NCs (excitation: 480 nm, emission: 552 nm, fwhm: 33 nm); (d) UV–vis–NIR (red) and PL Spectra (blue) PbS NCs (excitation: 950 nm, emission: 1102 nm, fwhm: 149 nm); (e) UV–vis–NIR (red) and PL spectra (blue) of Ag_2S NCs (excitation: 800 nm, emission: 1206 nm, fwhm: 186 nm); and (f) UV–vis spectra of InP NCs (HWHM: 37 nm).

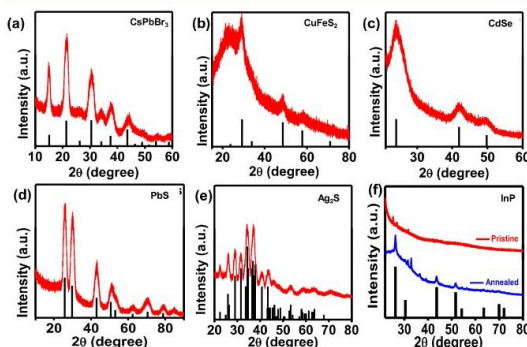


Figure 5. PXRD of (a) CsPbBr_3 perovskite (cubic phase, JCPDS 00-054-0752); (b) CuFeS_2 NCs (tetragonal, JCPDS 00-037-0471); (c) CdSe NCs (zinc blende, JCPDS 65-2891); (d) PbS NCs (rock salt, JCPDS 05-0592); (e) Ag_2S NCs (monoclinic, JCPDS 00-014-0072); and (f) as-synthesized InP (pristine, red color) and corresponding spectrum (blue color) of the annealed (270 °C, 4 h) InP film (zinc blende, JCPDS 96-101-0147). Spectra in (a–e) have been obtained from the as-prepared samples without any annealing step to improve crystallinity.

acid to form fatty acid salt followed by anion exchange with a metal salt. The method was highly scalable, and the products were obtained on a multigram scale. The practical use of this methodology is also presented by using the as-synthesized M-FAs as the metal precursors for the formation of various semiconductor NCs such as CsPbBr_3 , InP , PbS , CdSe , CuFeS_2 , and Ag_2S . We believe that our findings would be valuable for both academic and industrial settings with wide applications in the field of colloidal NCs, surfactants, emulsions, and so forth.

7. EXPERIMENTAL SECTION

7.1. General Information: Materials and General Considerations. InCl_3 (99.99%), GaCl_3 (99.99%), lauric

acid (98%), palmitic acid (99%), $\text{Cs}_2(\text{CO}_3)$ (99.9%), $\text{GdCl}_3 \cdot 6\text{H}_2\text{O}$ (99.9%), Br_2 ($\geq 99\%$), oleylamine (technical grade), 1-ODE (technical grade), Se ($\geq 99.5\%$), trioctylphosphine (97%) 1, and 2-dimethoxyethane (99.5%) were all purchased from Sigma-Aldrich, India. $\text{Pb}(\text{NO}_3)_2$ (99%), FeCl_3 (96%), $\text{CoCl}_2 \cdot 6\text{H}_2\text{O}$ (98%), NiCl_2 (97%), MnCl_2 (99%), $\text{Mg}(\text{NO}_3)_2$ (99%), and oleic acid (65–88%) were purchased from Merck, India. 1-Dodecanthiol (98%) was purchased from Loba Chemie. $\text{CuCl}_2 \cdot 2\text{H}_2\text{O}$ (99%), ZnCl_2 (97%), $\text{CdCl}_2 \cdot \text{H}_2\text{O}$ (98%), KNO_3 (99%), $\text{SnCl}_2 \cdot 2\text{H}_2\text{O}$, and stearic acid (90%) were purchased from Thomas Baker, India. Myristic acid (95%), AgNO_3 (99.8%), and AlCl_3 (96%) were purchased from SRL, Rankem, and Finar, respectively. All the FTIR spectra were acquired using Bruker ALPHA E, 200396; the TGA data were recorded on the TA Instrument Q-50 TGA. ^1H NMR was obtained in CDCl_3 and $\text{DMSO}-d_6$ using Bruker ASCEND 400. The UV–visible spectra were collected using PerkinElmer (model: LS 55). The PL spectra were acquired using the HORIBA scientific spectrophotometer (model: PTI-QM 510), and PXRD was recorded on a PANalytical X-ray diffractometer using $\text{Cu K}\alpha$ ($\lambda = 1.54 \text{ \AA}$) as the incident radiation (40 kV and 30 mA).

7.2. Preparation of M-FA Salts (Method A). In a typical synthesis, 0.1 g of metal salt (1.0 equiv) was taken in a round bottom flask, and 3.0 equiv of fatty acid and 1.0 equiv of DBU were added to it. A mixture of hexane, ethanol, and water (ratio 7:4:3) was added to the above-mentioned mixture. It was then stirred for 2–3 min at room temperature. The reaction mixture was then refluxed overnight (13 h). In the following day, the product was extracted from the nonpolar hexane part and was dried under vacuum.

7.3. Preparation of CsPbBr_3 NCs Using the As-Synthesized Lead Oleate (3p). Colloidal CsPbBr_3 NCs were synthesized following the reported method.¹¹ Briefly, 0.077 g (0.1 mmol) of lead oleate, 30 μL (0.6 mmol), and 0.5 mL of oleylamine were mixed with 4 mL of 1-ODE and degassed for 30 min at room temperature followed by 30 min at 120 °C. The reaction vessel was back-filled with nitrogen and heated to 200 °C. At this temperature, cesium oleate solution (0.4 mL) was injected. After 10 s the reaction vessel was quenched by immersing in an ice bath. The purification was carried out through a centrifugation method, where 4 mL of crude solution was mixed with 4 mL of anhydrous toluene and centrifuged at 5000 rpm for 10 min. The supernatant was discarded, and the solid residue was washed again with anhydrous toluene at 5000 rpm for 5 min. Finally, the purified CsPbBr_3 NCs were dispersed in anhydrous hexane.

7.4. Preparation of CdSe NCs Using the As-Synthesized Cadmium Stearate (3k). Colloidal CdSe NCs were synthesized following the method reported earlier with slight modification.^{3,4} Briefly, 0.068 g (0.1 mmol) of cadmium stearate, 0.147 mL (0.5 mmol) of oleylamine, and 6 mL of 1-ODE were heated at 120 °C under vacuum for 1 h. After 1 h the flask was back-filled with nitrogen, and the reaction mixture was slowly heated to 150 °C. Separately, 0.15 g (1.9 mmol) of selenium powder was dissolved in 2 mL of trioctylphosphine. This solution was injected into the formerly prepared cadmium stearate solution to obtain CdSe NCs. The purification was done by taking 5 mL of crude solution and mixing with anhydrous toluene and anhydrous ethanol (1:4). The mixture was centrifuged at 5000 rpm for 10 min. The supernatant was discarded, and the solid residue was centrifuged again following the same procedure. After washing

the CdSe NCs for three times, it was dispersed in anhydrous hexane.

7.5. Preparation of InP NCs Using the As-Synthesized Using Indium Stearate (3a). Colloidal InP NCs were synthesized following the reported method with slight modification.^{5,77} Briefly, 0.097 g (0.1 mmol) of indium stearate was dissolved in 4 mL of 1-ODE by degassing it at 120 °C for 1 h. A clear solution was obtained which was heated under nitrogen in a Schlenk line until the temperature reached 270 °C. 12.5 mg (0.05 mmol, 14.5 μL) of tris(trimethylsilyl) phosphine in 0.5 mL 1-ODE was injected, and the reaction was carried out for 1 h. The purification was carried out through a centrifugation method, where 2 mL of crude solution was mixed with 2 mL of anhydrous hexane and 8 mL of anhydrous ethanol. The mixture was centrifuged at 5000 rpm for 10 min. The supernatant was discarded and the solid residue was washed again with (1:4) mixture of anhydrous hexane and anhydrous ethanol at 5000 rpm for 10 min. The purified NCs were dispersed in hexane.

7.6. Preparation of PbS Using As-Synthesized Lead Oleate (3p). Colloidal PbS NCs were synthesized following the method reported earlier with slight modification.⁶ Briefly, 0.030 g (0.0389 mmol) of lead oleate was dissolved in 5 mL of 1-ODE at 120 °C for 30 min under vacuum. The flask was back-filled with nitrogen, and the temperature was brought down to 80 °C. Separately the 1,3-diphenyl thiourea prepared in the lab was dissolved in 1,2-dimethoxyethane and then injected in the reaction mixture. After the injection, the reaction was carried out for 15 min to obtain a black coloration of PbS NCs. For purification, the crude 4 mL of anhydrous toluene and 16 mL of anhydrous ethanol was added to 4 mL of crude PbS NCs, and the mixture was centrifuged at 5000 rpm for 10 min. The residue obtained was washed three times using the same method. The purified NCs were dispersed in hexane.

7.7. Preparation of Ag_2S NCs Using the As-Synthesized Silver Stearate (3d). Colloidal Ag_2S NCs were synthesized following the reported method with slight modification.^{61,78} Briefly, 0.039 g (0.1 mmol) of silver stearate was mixed with 3 mL of 1-ODE and was vacuumed for 1 h at room temperature. After 1 h, the reaction temperature was increased to 100 °C and the degassing was continued for 30 min. This silver stearate solution was back-filled with nitrogen and the temperature was increased to 140 °C. Separately, 0.023 g (0.1 mmol) of 1,3-diphenyl thiourea and 0.3 mL of 1-DDT was vacuumed for 1 h at room temperature. This solution was swiftly injected into the silver stearate solution and was kept at 140 °C for 5 min. After 5 min, the reaction was allowed to come down to room temperature. The purification was carried out through a centrifugation method, where 3 mL of crude solution was mixed with 3 mL of anhydrous ethanol and centrifuged at 5000 rpm for 5 min. The supernatant was discarded, and the residue was washed again with anhydrous ethanol. This process was repeated two times. The final two washings were done with a mixture of anhydrous ethanol and anhydrous hexane (3:1) and centrifuged at 5000 rpm for 5 min. Finally, the purified Ag_2S NCs were dispersed in anhydrous hexane.

7.8. Preparation of CuFeS_2 NCs Using the As-Synthesized Iron Stearate (3f) and Copper Stearate (3g). Colloidal CuFeS_2 NCs were synthesized following the method reported earlier with slight modification.⁶⁰ Briefly, 0.006 g (0.2 mmol) of sulfur was mixed with 2.5 mL of oleylamine and 1 mL of 1-ODE, and it was heated at 120 °C

under vacuum for 30 min. Under nitrogen, the temperature was increased to 160 °C, and it was kept at this temperature. 0.090 g (0.1 mmol) of iron stearate and 0.063 g (0.1 mmol) of copper stearate was mixed with 3 mL of 1-ODE. The mixture was degassed for 1 h at 120 °C. The reaction flask was filled with nitrogen, and 1.5 mL of dodecanethiol was added. The temperature of the reaction was slowly increased to 180 °C. Sulfur solution was injected dropwise. After the addition of sulfur, the reaction was continued for another 10 min and then quenched in cold water. The purification was carried out through a centrifugation method, where 4 mL of crude solution was mixed with 4 mL of anhydrous toluene and 16 mL of anhydrous ethanol and centrifuged at 5000 rpm for 10 min. The supernatant was discarded, and the solid residue was washed again with a (1:4) hexane/ethanol mixture at 5000 rpm for 5 min. The NCs were finally centrifuged with the same solvent mixture at 5000 rpm for 3 min to obtain purified CuFeS₂ NCs. The purified NCs were dispersed in hexane.

7.9. Spectral (NMR) Analyses, Melting Point, and Specification of Experimental Conditions.

7.9.1. Indium(III) Stearate (3a). It was prepared according to the general procedure discussed in method A. Indium chloride was used as a metal precursor and stearic acid as a carboxylate precursor. The product was obtained as a white powder in 85% yield. mp 145–148 °C; ¹H NMR (CDCl₃, 400 MHz): δ ppm 0.88 (t, 3H, J = 8 Hz), 1.27 (m, 28H), 1.60 (m, 2H), 2.33 (t, 2H, J = 8 Hz). ¹³C NMR (CDCl₃, 100 MHz): δ ppm 14.12, 22.70, 24.72, 29.08, 29.26, 29.37, 29.45, 29.69, 31.93, 33.95, 179.35.

7.9.2. Gallium(III) Stearate (3b). It was prepared according to the general procedure discussed in method A. Gallium chloride was used as a metal precursor and stearic acid as a carboxylate precursor. The product was obtained in 90% yield. ¹H NMR (CDCl₃, 400 MHz): δ ppm 0.88 (t, 3H, J = 8 Hz), 1.27 (m, 28H), 1.63 (m, 2H), 2.34 (t, 2H, J = 8 Hz). ¹³C NMR (CDCl₃, 100 MHz): δ ppm 14.31, 22.88, 24.85, 29.24, 29.43, 29.56, 29.62, 29.79, 29.84, 32.11, 34.27, 180.46.

7.9.3. Lead(II) Stearate (3c). It was prepared according to the general procedure discussed in method A. Lead nitrate was used as a metal precursor and stearic acid as a carboxylate precursor. The product was obtained in 73% yield. ¹H NMR (CDCl₃, 400 MHz): δ ppm 0.88 (t, 3H, J = 8 Hz), 1.25 (m, 28H), 1.63 (m, 2H), 2.35 (t, 2H, J = 8 Hz). ¹³C NMR (CDCl₃, 100 MHz): δ ppm 14.31, 22.88, 24.87, 29.24, 29.42, 29.54, 29.61, 29.77, 29.87, 32.10, 34.08, 179.40.

7.9.4. Silver(I) Stearate (3d). It was prepared according to the general procedure discussed in method A. Silver nitrate was used as a metal precursor and stearic acid as a carboxylate precursor. The product was obtained in 91% yield. mp 204–207 °C; ¹H NMR (CDCl₃, 400 MHz): δ ppm 0.80 (m, 3H), 1.21 (m, 28H), 1.53 (m, 2H), 2.32 (m, 2H). ¹³C NMR (CDCl₃, DMSO-*d*₆, 3:1, 100 MHz): δ ppm 14.31, 22.54, 24.95, 28.99, 29.14, 29.17, 29.34, 29.46, 31.74, 34.12, 174.94.

7.9.5. Aluminum(III) Stearate (3e). It was prepared according to the general procedure discussed in method A. Aluminum chloride was used as a metal precursor and stearic acid as a carboxylate precursor. The product was obtained in 35% yield. ¹H NMR (CDCl₃, 400MHz): δ ppm 0.88 (t, 3H, J = 8 Hz), 1.27 (m, 28H), 1.61 (m, 2H), 2.34 (t, 2H, J = 8 Hz). ¹³C NMR (CDCl₃, 100 MHz): δ ppm 14.30, 22.88, 24.88, 29.26, 29.44, 29.55, 29.63, 29.79, 29.88, 30.02, 32.14, 34.23, 179.98.

7.9.6. Ferric(III) Stearate (3f). It was prepared according to the general procedure discussed in method A. Ferric chloride

was used as a metal precursor and stearic acid as a carboxylate precursor. The product was obtained in 90% yield.

7.9.7. Copper(II) Stearate (3g). It was prepared according to the general procedure discussed in method A. Copper chloride was used as a metal precursor and stearic acid as a carboxylate precursor. The product was obtained in 91% yield. mp 248–251 °C.

7.9.8. Cobalt(II) Stearate (3h). It was prepared according to the general procedure discussed in method A. Cobalt chloride was used as a metal precursor and stearic acid as a carboxylate precursor. The product was obtained in 75% yield. mp 110–113 °C.

7.9.9. Zinc(II) Stearate (3i). It was prepared according to the general procedure discussed in method A. Zinc chloride was used as a metal precursor and stearic acid as a carboxylate precursor. The product was obtained in 87% yield. mp 128–130 °C; ¹H NMR (CDCl₃, 400 MHz): δ ppm 0.88 (t, 3H, J = 8 Hz), 1.30 (m, 28H), 1.62 (m, 2H), 2.35 (t, 2H, J = 8 Hz). ¹³C NMR (CDCl₃, 100MHz): δ ppm 14.31, 22.88, 24.87, 29.24, 29.42, 29.55, 29.62, 29.77, 29.87, 32.11, 34.05, 179.21.

7.9.10. Tin Stearate (3j). It was prepared according to the general procedure discussed in method A. Tin(II) chloride was used as a metal precursor and stearic acid as a carboxylate precursor. The product was obtained in 90% yield. ¹H NMR (CDCl₃, 400 MHz): δ ppm 0.88 (t, 3H, J = 8 Hz), 1.28 (m, 28H), 1.63 (m, 2H), 2.34 (t, 2H, J = 8 Hz). ¹³C NMR (CDCl₃, 100 MHz): δ ppm 14.12, 22.70, 24.68, 29.07, 29.25, 29.37, 29.44, 29.69, 31.93, 34.02, 179.84.

7.9.11. Cadmium(II) Stearate (3k). It was prepared according to the general procedure discussed in method A. Cadmium chloride was used as a metal precursor and stearic acid as a carboxylate precursor. The product was obtained in 81% yield. mp 132–135 °C; ¹H NMR (CDCl₃, 400 MHz): δ ppm 0.88 (t, 3H, J = 8 Hz), 1.27 (m, 28H), 1.61 (m, 2H), 2.35 (t, 2H, J = 8 Hz). ¹³C NMR (CDCl₃, 100 MHz): δ ppm 14.31, 22.88, 24.86, 29.24, 29.42, 29.54, 29.77, 29.87, 34.12, 179.62.

7.9.12. Potassium Stearate (3l). It was prepared according to the general procedure discussed in method A. Potassium nitrate was used as a metal precursor and stearic acid as a carboxylate precursor. The product was obtained in 85% yield. ¹H NMR (CDCl₃, DMSO-*d*₆, 3:1, 400 MHz): δ ppm 0.78 (t, 3H, J = 8 Hz), 1.16 (m, 28H), 1.49 (m, 2H), 2.16 (t, 2H, J = 8 Hz). ¹³C NMR (CDCl₃, DMSO-*d*₆, 3:1 100 MHz): δ ppm 14.40, 22.76, 25.11, 29.26, 29.40, 29.43, 29.57, 29.73, 31.97, 34.39, 175.66.

7.9.13. Indium(III) Myristate (3m). It was prepared according to the general procedure discussed in method A. Indium chloride was used as a metal precursor and myristic acid as a carboxylate precursor. The product was obtained in 90% yield. mp 142–145 °C; ¹H NMR (CDCl₃, 400 MHz): δ ppm 0.88 (t, 3H, J = 8 Hz), 1.27 (m, 20H), 1.61 (m, 2H), 2.34 (t, 2H, J = 8 Hz). ¹³C NMR (CDCl₃, 100 MHz): δ ppm 14.28, 22.88, 24.94, 29.28, 29.47, 29.56, 29.66, 29.85, 32.11, 34.44, 180.93.

7.9.14. Indium(III) Palmitate (3n). It was prepared according to the general procedure discussed in method A. Indium chloride was used as a metal precursor and palmitic acid as a carboxylate precursor. The product was obtained in 60% yield. ¹H NMR (CDCl₃, 400 MHz): δ ppm 0.88 (t, 3H, J = 8 Hz), 1.28 (m, 24H), 1.62 (m, 2H), 2.34 (t, 2H, J = 8 Hz). ¹³C NMR (CDCl₃, 100 MHz): δ ppm 14.31, 22.88, 24.85, 29.24, 29.43, 29.56, 29.62, 29.78, 29.87, 32.12, 34.30, 180.63.

7.9.15. Indium(III) Laurate (3o). It was prepared according to the general procedure discussed in method A. Indium chloride was used as a metal precursor and lauric acid as carboxylate precursor. The product was obtained in 75% yield. ^1H NMR (CDCl_3 , 400 MHz): δ ppm 0.88 (t, 3H, $J = 8$ Hz), 1.27 (m, 16H), 1.61 (m, 2H), 2.34 (t, 2H, $J = 8$ Hz). ^{13}C NMR (CDCl_3 , 100 MHz): δ ppm 14.28, 22.87, 24.92, 29.26, 29.45, 29.53, 29.64, 29.79, 32.09, 34.40, 180.91.

7.9.16. Lead(II) Oleate (3p). It was prepared according to the general procedure discussed in method A. Lead nitrate was used as a metal precursor and oleic acid as a carboxylate precursor. The product was obtained in 90% yield. mp 91–94 °C; ^1H NMR (CDCl_3 , 400 MHz): δ ppm 0.87 (t, 3H, $J = 8$ Hz), 1.27 (m, 18H), 1.62 (m, 2H), 2.01 (m, 1H), 2.34 (t, 2H, $J = 8$ Hz), 5.34 (dd, 1H, $J = 4$ Hz). ^{13}C NMR (CDCl_3 , 100 MHz): δ ppm 14.29, 22.86, 25.00, 27.35, 29.20, 29.30, 29.39, 29.50, 29.70, 29.87, 32.08, 35.17, 129.88, 130.16, 180.67.

7.9.17. Magnesium(II) Stearate (3q). It was prepared according to the general procedure discussed in method A. Magnesium nitrate was used as a metal precursor and stearic acid as a carboxylate precursor. The product was obtained in 88% yield. mp 118–122 °C ^1H NMR (CDCl_3 , 400 MHz): δ ppm 0.88 (t, 3H, $J = 8$ Hz), 1.29 (m, 28H), 1.62 (m, 2H), 2.34 (t, 2H, $J = 8$ Hz). ^{13}C NMR (CDCl_3 , 100 MHz): δ ppm 14.31, 22.88, 22.89, 24.89, 29.25, 29.44, 29.55, 29.63, 29.78, 29.86, 32.11, 34.15, 179.52.

7.9.18. Manganese(II) Stearate (3r). It was prepared according to the general procedure discussed in method A. Manganese chloride was used as a metal precursor and stearic acid as a carboxylate precursor. The product was obtained in 70% yield. mp 108–111 °C.

7.9.19. Nickel(II) Stearate (3s). It was prepared according to the general procedure discussed previously. Zinc chloride was used as a metal precursor and stearic acid as a carboxylate precursor. The product was obtained in 87% yield. mp 84–87 °C.

7.9.20. Gadolinium(III) Stearate (3t). It was prepared according to the general procedure discussed in method A. Gadolinium chloride was used as a metal precursor and stearic acid as a carboxylate precursor. The product was obtained in 45% yield. mp 107–110 °C.

■ ASSOCIATED CONTENT

Supporting Information

The Supporting Information is available free of charge at <https://pubs.acs.org/doi/10.1021/acsomega.9b04448>.

NMR spectra, FTIR spectra, and TGA spectra of metal carboxylates. Photoluminescence excitation spectrum of CsPbBr_3 NCs and photographs of colloidal solutions of different NCs (PDF)

■ AUTHOR INFORMATION

Corresponding Author

Sudarsan Tamang – Department of Chemistry, School of Physical Sciences, Sikkim University, Gangtok 737102, Sikkim, India; orcid.org/0000-0002-2742-4060; Email: stamang@cus.ac.in

Authors

Siddhant Basel – Department of Chemistry, School of Physical Sciences, Sikkim University, Gangtok 737102, Sikkim, India

Karishma Bhardwaj – Department of Chemistry, School of Physical Sciences, Sikkim University, Gangtok 737102, Sikkim, India

Sajan Pradhan – Department of Chemistry, School of Physical Sciences, Sikkim University, Gangtok 737102, Sikkim, India

Anand Pariyar – Department of Chemistry, School of Physical Sciences, Sikkim University, Gangtok 737102, Sikkim, India; orcid.org/0000-0002-3073-5521

Complete contact information is available at: <https://pubs.acs.org/10.1021/acsomega.9b04448>

Author Contributions

S.B. carried out syntheses, characterization, and mechanistic studies of M-FAs; he also contributed to data analysis and paper writing. S.B. and K.B. contributed in the conceptualization, synthesis, and characterization of NCs. S.P., A.P., and S.T. contributed to experiment design, data analysis, explanation of results, and paper writing. S.T. verified the results and drafted the paper. All authors have given approval to the final version of the manuscript.

Notes

The authors declare no competing financial interest.

■ ACKNOWLEDGMENTS

S.T., S.P., and K.B. acknowledge the SERB-DST, Government of India for research funding (EEQ/2016/000751 and EMR/2016/002505). S.B. would like to thank the Department of Science and Technology, Government of India (DST/INSPIRE/03/2016/001207) [IF160689] for financial support under the DST-INSPIRE Scheme. A.P. acknowledges the SERB-DST (EEQ/2016/000685) and the DST-Inspire (DST/INSPIRE/04/2015/002674), for financial assistance. The authors thank Nimuka Tamang and Subas Chandra Mohanta for help with synthesis of NCs.

■ REFERENCES

- Rossetti, R.; Nakahara, S.; Brus, L. E. Quantum Size Effects in the Redox Potentials, Resonance Raman Spectra, and Electronic Spectra of CdS Crystallites in Aqueous Solution. *J. Chem. Phys.* **1983**, *79*, 1086–1088.
- Brust, M.; Walker, M.; Bethell, D.; Schiffrin, D. J.; Whyman, R. Synthesis of Thiol-Derivatized Gold Nanoparticles in a Two-Phase Liquid-Liquid System. *J. Chem. Soc., Chem. Commun.* **1994**, 801–802.
- Murray, C. B.; Norris, D. J.; Bawendi, M. G. Synthesis and Characterization of Nearly Monodisperse CdE (E = S, Se, Te) Semiconductor Nanocrystallites. *J. Am. Chem. Soc.* **1993**, *115*, 8706–8715.
- Yu, W. W.; Peng, X. Formation of High-Quality CdS and Other II-VI Semiconductor Nanocrystals in Noncoordinating Solvents: Tunable Reactivity of Monomers. *Angew. Chem., Int. Ed.* **2002**, *41*, 2368–2371.
- Battaglia, D.; Peng, X. Formation of High Quality InP and InAs Nanocrystals in a Noncoordinating Solvent. *Nano Lett.* **2002**, *2*, 1027–1030.
- Hendricks, M. P.; Campos, M. P.; Cleveland, G. T.; Jen-La Plante, I.; Owen, J. S. A Tunable Library of Substituted Thiourea Precursors to Metal Sulfide Nanocrystals. *Science* **2015**, *348*, 1226–1230.
- Protesescu, L.; Yakunin, S.; Bodnarchuk, M. I.; Krieg, F.; Caputo, R.; Hendon, C. H.; Yang, R. X.; Walsh, A.; Kovalenko, M. V. Nanocrystals of Cesium Lead Halide Perovskites (CsPbX_3 , X = Cl, Br, and I): Novel Optoelectronic Materials Showing Bright Emission with Wide Color Gamut. *Nano Lett.* **2015**, *15*, 3692–3696.
- Akkerman, Q. A.; Martínez-Sarti, L.; Goldoni, L.; Imran, M.; Baranov, D.; Bolink, H. J.; Palazon, F.; Manna, L. Molecular Iodine

- for a General Synthesis of Binary and Ternary Inorganic and Hybrid Organic–Inorganic Iodide Nanocrystals. *Chem. Mater.* **2018**, *30*, 6915–6921.
- (9) Reiss, P.; Protière, M.; Li, L. Core/Shell Semiconductor Nanocrystals. *Small* **2009**, *5*, 154–168.
- (10) Imran, M.; Caligiuri, V.; Wang, M.; Goldoni, L.; Prato, M.; Krahne, R.; De Trizio, L.; Manna, L. Benzoyl Halides as Alternative Precursors for the Colloidal Synthesis of Lead-Based Halide Perovskite Nanocrystals. *J. Am. Chem. Soc.* **2018**, *140*, 2656–2664.
- (11) Thapa, S.; Bhardwaj, K.; Basel, S.; Pradhan, S.; Eling, C. J.; Adawi, A. M.; Bouillard, J.-S. G.; Stasiuk, G. J.; Reiss, P.; Pariyar, A.; Tamang, S. Long-Term Ambient Air-Stable Cubic CsPbBr₃ Perovskite Quantum Dots Using Molecular Bromine. *Nanoscale Adv.* **2019**, *1*, 3388–3391.
- (12) Gary, D. C.; Cossairt, B. M. Role of Acid in Precursor Conversion During InP Quantum Dot Synthesis. *Chem. Mater.* **2013**, *25*, 2463–2469.
- (13) Li, L.; Reiss, P. One-Pot Synthesis of Highly Luminescent InP/ZnS Nanocrystals without Precursor Injection. *J. Am. Chem. Soc.* **2008**, *130*, 11588–11589.
- (14) Tamang, S.; Lincheneau, C.; Hermans, Y.; Jeong, S.; Reiss, P. Chemistry of InP Nanocrystal Syntheses. *Chem. Mater.* **2016**, *28*, 2491–2506.
- (15) Reiss, P.; Carrière, M.; Lincheneau, C.; Vaure, L.; Tamang, S. Synthesis of Semiconductor Nanocrystals, Focusing on Nontoxic and Earth-Abundant Materials. *Chem. Rev.* **2016**, *116*, 10731–10819.
- (16) Thanh, N. T. K.; Maclean, N.; Mahiddine, S. Mechanisms of Nucleation and Growth of Nanoparticles in Solution. *Chem. Rev.* **2014**, *114*, 7610–7630.
- (17) Almeida, G.; Goldoni, L.; Akkerman, Q.; Dang, Z.; Khan, A. H.; Marras, S.; Moreels, I.; Manna, L. Role of Acid-Base Equilibria in the Size, Shape, and Phase Control of Cesium Lead Bromide Nanocrystals. *ACS Nano* **2018**, *12*, 1704–1711.
- (18) Schliehe, C.; Juarez, B. H.; Pelletier, M.; Jander, S.; Greshnykh, D.; Nagel, M.; Meyer, A.; Foerster, S.; Kornowski, A.; Klinke, C.; et al. Ultrathin PbS Sheets by Two-Dimensional Oriented Attachment. *Science* **2010**, *329*, 550–553.
- (19) Dasgupta, B. R.; Huang, L.; Sanzgiri, V. R.; Sethna, S. D.; Shah, P. C. Novel Cosmetic Cream Composition. WO 2008104591 A2, PCT/EP2008/052433, 2008.
- (20) Sahoo, R. R.; Biswas, S. K. Frictional Response of Fatty Acids on Steel. *J. Colloid Interface Sci.* **2009**, *333*, 707–718.
- (21) Gregory, J. N.; Spink, J. A. Lubricating Properties of Molecular Layers of Stearic Acid and Calcium Stearate on Metal Surfaces. *Nature* **1947**, *159*, 403.
- (22) Li, J.; Wu, Y. Lubricants in Pharmaceutical Solid Dosage Forms. *Lubricants* **2014**, *2*, 21–43.
- (23) Hermans, J. J.; Keune, K.; Van Loon, A.; Iedema, P. D. An Infrared Spectroscopic Study of the Nature of Zinc Carboxylates in Oil Paintings. *J. Anal. At. Spectrom.* **2015**, *30*, 1600–1608.
- (24) Lappi, H.; Alén, R. Pyrolysis of Vegetable Oil Soaps-Palm, Olive, Rapeseed and Castor Oils. *J. Anal. Appl. Pyrolysis* **2011**, *91*, 154–158.
- (25) Pratiwi, M.; Neonufa, G. F.; Prakoso, T.; Soerawidjaja, T. H. The Synthesis of Magnesium Soaps as Feed for Biohydrocarbon Production. *MATEC Web Conf.* **2018**, *156*, 03001.
- (26) Rakhmatullina, A. P.; Akhmed'yanova, R. A.; Liakumovich, A. G.; Portnoi, T. B.; Mokhnatkina, E. G.; Il'yasov, R. S. Active Processing Additives Based on Zinc and Calcium Salts of Stearic and Oleic Acids and Their Mixtures. *Int. Polym. Sci. Technol.* **2004**, *31*, 29–32.
- (27) Wang, F.; Yu, H.; Li, J.; Hang, Q.; Zemlyanov, D.; Gibbons, P. C.; Wang, L.; Janes, D. B.; Buhro, W. E. Spectroscopic Properties of Colloidal Indium Phosphide Quantum Wires. *J. Am. Chem. Soc.* **2007**, *129*, 14327–14335.
- (28) Franke, D.; Harris, D. K.; Xie, L.; Jensen, K. F.; Bawendi, M. G. The Unexpected Influence of Precursor Conversion Rate in the Synthesis of III-V Quantum Dots. *Angew. Chem., Int. Ed.* **2015**, *54*, 14299–14303.
- (29) Park, J.; An, K.; Hwang, Y.; Park, J.-G.; Noh, H.-J.; Kim, J.-Y.; Park, J.-H.; Hwang, N.-M.; Hyeon, T. Ultra-Large-Scale Syntheses of Monodisperse Nanocrystals. *Nat. Mater.* **2004**, *3*, 891–895.
- (30) Wolfgang, S. M.; Heider, T. P. Stearate Composition and Method of Production Thereof. U.S. Patent 7,456,306 B2, 2008.
- (31) Phanstiel, O.; Dueno, E.; Wang, Q. X. Synthesis of Exotic Soaps in the Chemistry Laboratory. *J. Chem. Educ.* **1998**, *75*, 612.
- (32) Gönen, M.; Ozturk, S.; Balköse, D.; Okur, S.; Ulku, S. Preparation and Characterization of Calcium Stearate Powders and Films Prepared by Precipitation and Langmuir-Blodgett Techniques. *Ind. Eng. Chem. Res.* **2010**, *49*, 1732–1736.
- (33) Gönen, M.; Balköse, D.; Inal, F.; Ulku, S. Zinc Stearate Production by Precipitation and Fusion Processes. *Ind. Eng. Chem. Res.* **2005**, *44*, 1627–1633.
- (34) Dou, Q.; Ng, K. M. Synthesis of Various Metal Stearates and the Corresponding Monodisperse Metal Oxide Nanoparticles. *Powder Technol.* **2016**, *301*, 949–958.
- (35) Baghernejad, B. 1,4-Diazabicyclo[2.2.2]Octane (DABCO) as a Useful Catalyst in Organic Synthesis. *Eur. J. Chem.* **2010**, *1*, 54–60.
- (36) Aggarwal, V. K.; Emme, L.; Fulford, S. Y. Correlation between PK_a and Reactivity of Quinuclidine-Based Catalysts in the Baylis-Hillman Reaction: Discovery of Quinuclidine as Optimum Catalyst Leading to Substantial Enhancement of Scope. *J. Org. Chem.* **2003**, *68*, 692–700.
- (37) Faltin, C.; Fleming, E. M.; Connon, S. J. Acrylamide in the Baylis-Hillman Reaction: Expanded Reaction Scope and the Unexpected Superiority of DABCO over More Basic Tertiary Amine Catalysts. *J. Org. Chem.* **2004**, *69*, 6496–6499.
- (38) Pimenta, L. S.; Gusevskaya, E. V.; Alberto, E. E. Intermolecular Halogenation/Esterification of Alkenes with N-Halosuccinimide and Acetic Acid Catalyzed by 1,4-Diazabicyclo[2.2.2]Octane. *Adv. Synth. Catal.* **2017**, *359*, 2297–2303.
- (39) Röhlich, C.; Wirth, A. S.; Köhler, K. Suzuki Coupling Reactions in Neat Water as the Solvent: Where in the Biphasic Reaction Mixture Do the Catalytic Reaction Steps Occur? *Chem.—Eur. J.* **2012**, *18*, 15485–15494.
- (40) Luo, S.; Feng, J.; Ng, K. M. Large Scale Synthesis of Nearly Monodisperse, Variable-Shaped In₂O₃ Nanocrystals via a One-Pot Pyrolysis Reaction. *CrystEngComm* **2014**, *16*, 9236–9244.
- (41) Kaupmees, K.; Trummal, A.; Leito, I. Basicities of Strong Bases in Water: A Computational Study. *Croat. Chem. Acta* **2014**, *87*, 385–395.
- (42) Shekouhy, M.; Khalafi-Nezhad, A. Polyethylene Glycol-Bonded 1,8-Diazabicyclo[5.4.0]Undec-7-Ene (PEG-DBU) as a Surfactant-Combined Base Catalyst for the Application of Nucleosides as Reagents in Multi-Component Syntheses of 8-Substituted Pyrido[2,3-d]Pyrimidine-6-Carbonitriles in Water. *Green Chem.* **2015**, *17*, 4815–4829.
- (43) Shieh, W.-C.; Lozanov, M.; Loo, M.; Repič, O.; Blacklock, T. J. DABCO- and DBU-Accelerated Green Chemistry for N-, O-, and S-Benzoylation with Dibenzyl Carbonate. *Tetrahedron Lett.* **2003**, *44*, 4563–4565.
- (44) Bronstein, L. M.; Huang, X.; Retrum, J.; Schmucker, A.; Pink, M.; Stein, B. D.; Dragnea, B. Influence of Iron Oleate Complex Structure on Iron Oxide Nanoparticle Formation. *Chem. Mater.* **2007**, *19*, 3624–3632.
- (45) Jóna, E.; Ondrušová, D.; Pajtašová, M.; Šimon, P.; Michálek, J. A Study of Curative Interactions in the Presence of Cobalt(II) Stearate. *J. Appl. Polym. Sci.* **2001**, *81*, 2936–2943.
- (46) Roy, P. K.; Surekha, P.; Rajagopal, C.; Choudhary, V. Effect of Cobalt Carboxylates on the Photo-Oxidative Degradation of Low-Density Polyethylene. Part-I. *Polym. Degrad. Stab.* **2006**, *91*, 1980–1988.
- (47) Gönen, M.; Egbuchunam, T. O.; Balköse, D.; Inal, F.; Ülkü, S. Preparation and Characterization of Magnesium Stearate, Cobalt Stearate, and Copper Stearate and Their Effects on Poly(Vinyl Chloride) Dehydrochlorination. *J. Vinyl Addit. Technol.* **2015**, *21*, 235–244.

- (48) Torron, S.; Hult, D.; Pettersson, T.; Johansson, M. Tailoring Soft Polymer Networks Based on Sugars and Fatty Acids toward Pressure Sensitive Adhesive Applications. *ACS Sustainable Chem. Eng.* **2017**, *5*, 2632–2638.
- (49) Bunting, J. W.; Thong, K. M. Stability Constants for Some 1:1 Metal-Carboxylate Complexes. *Can. J. Chem.* **1970**, *48*, 1654.
- (50) Bala, T.; Prasad, B. L. V.; Sastry, M.; Kahaly, M. U.; Waghmare, U. V. Interaction of Different Metal Ions with Carboxylic Acid Group: A Quantitative Study. *J. Phys. Chem. A* **2007**, *111*, 6183–6190.
- (51) Lide, D. R.; Baysinger, G. *CRC Handbook of Chemistry and Physics*; CRC Press, Taylor & Francis Group: Boca Raton, FL, 2007.
- (52) Wise, F. W. Lead Salt Quantum Dots: The Limit of Strong Quantum Confinement. *Acc. Chem. Res.* **2000**, *33*, 773–780.
- (53) Luo, X.; Lai, R.; Li, Y.; Han, Y.; Liang, G.; Liu, X.; Ding, T.; Wang, J.; Wu, K. Triplet Energy Transfer from CsPbBr₃ Nanocrystals Enabled by Quantum Confinement. *J. Am. Chem. Soc.* **2019**, *141*, 4186–4190.
- (54) Talapin, D. V.; Lee, J.-S.; Kovalenko, M. V.; Shevchenko, E. V. Prospects of Colloidal Nanocrystals for Electronic and Optoelectronic Applications. *Chem. Rev.* **2010**, *110*, 389–458.
- (55) Dayal, S.; Kopidakis, N.; Olson, D. C.; Ginley, D. S.; Rumbles, G. Photovoltaic Devices with a Low Band Gap Polymer and CdSe Nanostructures Exceeding 3% Efficiency. *Nano Lett.* **2010**, *10*, 239–242.
- (56) Zhang, Y.; Hong, G.; Zhang, Y.; Chen, G.; Li, F.; Dai, H.; Wang, Q. Ag₂S Quantum Dot: A Bright and Biocompatible Fluorescent Nanoprobe in the Second near-Infrared Window. *ACS Nano* **2012**, *6*, 3695–3702.
- (57) Michalet, X.; Pinaud, F. F.; Bentolila, L.; Tsay, J. M.; Doose, S.; Li, J. J.; Sundaresan, G.; Wu, A. M.; Gambhir, S. S.; Weiss, S. Quantum Dots for Live Cells, in Vivo Imaging, and Diagnostics. *Science* **2005**, *307*, 538–544.
- (58) Li, X.-B.; Tung, C.-H.; Wu, L.-Z. Semiconducting Quantum Dots for Artificial Photosynthesis. *Nat. Rev. Chem.* **2018**, *2*, 160–173.
- (59) Pal, A.; Ghosh, I.; Sapra, S.; König, B. Quantum Dots in Visible-Light Photoredox Catalysis: Reductive Dehalogenations and C-H Arylation Reactions Using Aryl Bromides. *Chem. Mater.* **2017**, *29*, 5225–5231.
- (60) Bhattacharyya, B.; Pandey, A. CuFeS₂ Quantum Dots and Highly Luminescent CuFeS₂ Based Core/Shell Structures: Synthesis, Tunability, and Photophysics. *J. Am. Chem. Soc.* **2016**, *138*, 10207–10213.
- (61) Jiang, P.; Tian, Z.-Q.; Zhu, C.-N.; Zhang, Z.-L.; Pang, D.-W. Emission-Tunable Near-Infrared Ag₂S Quantum Dots. *Chem. Mater.* **2012**, *24*, 3–5.
- (62) Liu, M.; Voznyy, O.; Sabatini, R.; García de Arquer, F. P.; Munir, R.; Balawi, A. H.; Lan, X.; Fan, F.; Walters, G.; Kirmani, A. R.; et al. Hybrid Organic-Inorganic Inks Flatten the Energy Landscape in Colloidal Quantum Dot Solids. *Nat. Mater.* **2017**, *16*, 258–263.
- (63) Wu, Y.; Zhou, B.; Yang, C.; Liao, S.; Zhang, W.-H.; Li, C. CuFeS₂ Colloidal Nanocrystals as an Efficient Electrocatalyst for Dye Sensitized Solar Cells. *Chem. Commun.* **2016**, *52*, 11488–11491.
- (64) Son, D. I.; Kim, H. H.; Hwang, D. K.; Kwon, S.; Choi, W. K. Inverted CdSe-ZnS Quantum Dots Light-Emitting Diode Using Low-Work Function Organic Material Polyethylenimine Ethoxylated. *J. Mater. Chem. C* **2014**, *2*, 510–514.
- (65) Li, D.; Kristal, B.; Wang, Y.; Feng, J.; Lu, Z.; Yu, G.; Chen, Z.; Li, Y.; Li, X.; Xu, X. Enhanced Efficiency of InP-Based Red Quantum Dot Light-Emitting Diodes. *ACS Appl. Mater. Interfaces* **2019**, *11*, 34067–34075.
- (66) Yuan, S.; Wang, Z.-K.; Zhuo, M.-P.; Tian, Q.-S.; Jin, Y.; Liao, L.-S. Self-Assembled High Quality CsPbBr₃ Quantum Dot Films toward Highly Efficient Light-Emitting Diodes. *ACS Nano* **2018**, *12*, 9541–9548.
- (67) Stasiuk, G. J.; Tamang, S.; Imbert, D.; Poillot, C.; Giardiello, M.; Tisseyre, C.; Barbier, E. L.; Fries, P. H.; De Waard, M.; Reiss, P.; et al. Cell-Permeable Ln(III) Chelate-Functionalized InP Quantum Dots as Multimodal Imaging Agents. *ACS Nano* **2011**, *5*, 8193–8201.
- (68) Tang, R.; Xue, J.; Xu, B.; Shen, D.; Sudlow, G. P.; Achilefu, S. Tunable Ultrasmall Visible-to-Extended near-Infrared Emitting Silver Sulfide Quantum Dots for Integrin-Targeted Cancer Imaging. *ACS Nano* **2015**, *9*, 220–230.
- (69) Zhu, X.; Lin, Y.; Sun, Y.; Beard, M. C.; Yan, Y. Lead-Halide Perovskites for Photocatalytic α -Alkylation of Aldehydes. *J. Am. Chem. Soc.* **2019**, *141*, 733–738.
- (70) Harris, C.; Kamat, P. V. Photocatalytic Events of CdSe Quantum Dots in Confined Media. Electrode Behavior of Coupled Platinum Nanoparticles. *ACS Nano* **2010**, *4*, 7321–7330.
- (71) Chakraborty, I. N.; Roy, S.; Devatha, G.; Rao, A.; Pillai, P. P. InP/ZnS Quantum Dots as Efficient Visible-Light Photocatalysts for Redox and Carbon-Carbon Coupling Reactions. *Chem. Mater.* **2019**, *31*, 2258–2262.
- (72) Huang, X.; Parashar, V. K.; Gijis, M. A. M. Nucleation and Growth Behavior of CdSe Nanocrystals Synthesized in the Presence of Oleylamine Coordinating Ligand. *Langmuir* **2018**, *34*, 6070–6076.
- (73) Hou, B.; Cho, Y.; Kim, B. S.; Hong, J.; Park, J. B.; Ahn, S. J.; Sohn, J. I.; Cha, S.; Kim, J. M. Highly Monodispersed PbS Quantum Dots for Outstanding Cascaded-Junction Solar Cells. *ACS Energy Lett.* **2016**, *1*, 834–839.
- (74) Duman, F. D.; Hocaoglu, I.; Ozturk, D. G.; Gozuacik, D.; Kiraz, A.; Yagci Acar, H. Highly Luminescent and Cytocompatible Cationic Ag₂S NIR-Emitting Quantum Dots for Optical Imaging and Gene Transfection. *Nanoscale* **2015**, *7*, 11352–11362.
- (75) Curley, J. J.; Slugocki, T.; Hotz, C. Use of Heteroleptic Indium Hydroxides as Precursors for InP Nanocrystals. U.S. Patent 20,170,137,360 A1, 2017.
- (76) Sugathan, A.; Bhattacharyya, B.; Kishore, V. V. R.; Kumar, A.; Rajasekar, G. P.; Sarma, D. D.; Pandey, A. Why Does CuFeS₂ Resemble Gold? *J. Phys. Chem. Lett.* **2018**, *9*, 696–701.
- (77) Gary, D. C.; Cossairt, B. M. Role of Acid in Precursor Conversion during InP Quantum Dot Synthesis. *Chem. Mater.* **2013**, *25*, 2463–2469.
- (78) Ji, C.; Zhang, Y.; Zhang, X.; Wang, P.; Shen, H.; Gao, W.; Wang, Y.; Yu, W. W. Synthesis and Characterization of Ag₂S_xSe_{1-x} Nanocrystals and Their Photoelectrochemical Property Change. *Nanotechnology* **2017**, *28*, 065602.

Cite this: *Nanoscale Adv.*, 2019, 1, 3388Received 7th August 2019
Accepted 9th August 2019

DOI: 10.1039/c9na00486f

rsc.li/nanoscale-advances

Long-term ambient air-stable cubic CsPbBr₃ perovskite quantum dots using molecular bromine†

 Surakcha Thapa,^{‡a} Karishma Bhardwaj,^{‡a} Siddhant Basel,^{‡a} Sajan Pradhan,^a
 Charlotte J. Eling,^b Ali M. Adawi,^c Jean-Sebastien G. Bouillard,^c
 Graeme J. Stasiuk,^b Peter Reiss,^d Anand Pariyar^a and Sudarsan Tamang^{*,a}

We report unprecedented phase stability of cubic CsPbBr₃ quantum dots in ambient air obtained by using Br₂ as halide precursor. Mechanistic investigation reveals the decisive role of temperature-controlled *in situ* generated, oleylammonium halide species from molecular halogen and amine for the long term stability and emission tunability of CsPbX₃ (X = Br, I) nanocrystals.

High photoluminescence quantum yield (PL QY), narrow emission linewidth, tunable band gap, large diffusion lengths and low exciton binding energies are some of the key attributes of all-inorganic caesium lead halide perovskite nanocrystals (LHP NCs) *i.e.*, CsPbX₃, X = I, Br, Cl.^{1–6} This novel class of NCs has been shown to be highly “defect tolerant”, *i.e.* defect states are either shallow or localized in the valence or the conduction band.^{1,2} Unlike conventional semiconductor NCs, the rigorous passivation of their surface *via* formation of core/shell structures or other methods is not required to achieve high QY. These LHP NCs are promising building blocks for light emitting diode,^{3,4} solar cell,^{5,6} laser,⁷ photocatalysis⁸ and detector.⁹ Despite the recent surge of studies on CsPbX₃ perovskite NCs, a persisting drawback is their poor phase stability in ambient air. For example, cubic (α) “black” phase CsPbI₃ ($E_g = 1.73$ eV) perovskite NCs undergo rapid phase transformation to non-luminescent orthorhombic (δ) “yellow” phase in ambient condition (Fig. S1†) leading to undesired changes of the band gap, optical and electrical properties.^{6,10,11} Similarly, cubic (α) CsPbBr₃ ($E_g = 2.25$ eV) is unstable at ambient condition.¹² For successful integration of these materials into devices, the issue

of long-term phase stability must thus be addressed.^{6,13} Most of the reported strategies involve the use of additives such as halide salt,¹² phosphinic acid,¹⁴ ammonium halide,¹¹ 2,2'-iminodibenzoic acid¹⁵ sulphides and metal ions¹⁶ and polymers⁵ or *via* special post-synthetic purification step.^{6,10} Herein, we report the first synthesis of highly stable, cubic α-CsPbBr₃ perovskite NCs using Br₂ as an independent halide precursor. In a typical synthesis, lead acetate is dissolved in 1-octadecene in the presence of oleyl amine (OAm) and oleic acid (OA). To this solution, Br₂ (warning: handle the liquid Br₂ in fume hood, Br₂ vapors are toxic) and caesium oleate solutions (both dissolved in ODE) are sequentially added. Phase stability and emission colour tunability are achieved by controlling the reaction temperature (75–200 °C) and amount of Br₂ (0.6–1.2 mmol) under air-free synthetic condition (*cf.* ESI; Experimental section†). The “three-precursor” nature^{16–18} of our synthetic scheme allows for independent tuning of the amount of the individual elements *viz.*, Cs⁺, Pb²⁺ and X[−] ions and in turn, allows for the precise control over the surface chemistry.¹⁷ Highly crystalline, monodisperse 7.62 ± 1.0 nm sized cubic α-CsPbBr₃ NCs (Fig. 1a) were synthesised under optimized conditions using Cs : Pb : Br₂ ratio of 1 : 1 : 6 at 200 °C. High-resolution transmission electron microscopy (HRTEM) and powder X-ray diffraction (PXRD) analyses of the purified sample confirmed the pure cubic perovskite phase. HRTEM reveals (100) lattice fringes with a *d*-spacing of 0.58 nm (Fig. S2†). PXRD spectra of α-CsPbBr₃ NCs sample exposed to ambient air (relative humidity of ~50–60%) for a period of 60 days showed no alteration (Fig. 1b). The observed stability is much higher than the previously reported (max. 8 days) achieved *via* passivation of cubic CsPbBr₃ NCs with ZnBr₂.¹² Untreated pristine cubic CsPbBr₃ NCs, synthesised *via* conventional method typically transforms into orthorhombic phase within 1–2 days.¹² We reproduced halide salt passivated CsPbBr₃ NCs reported by Woo *et al.* For comparison, we purified and stored the NCs (control) under conditions similar to our cubic CsPbBr₃ NCs.

Consistent with their report, the halide passivation did improve the stability from 2 days to 6 days, thereafter the phase

^aDepartment of Chemistry, School of Physical Sciences, Sikkim University, India, 737102. E-mail: stamang@cus.ac.in

^bDepartment of Biomedical Sciences, University of Hull, Hull, HU6 7RX, UK

^cDepartment of Physics, University of Hull, Hull, HU6 7RX, UK

^dUniv. Grenoble Alpes, CEA, CNRS, IRIG/SyMMES/STEP, 38000 Grenoble, France

† Electronic supplementary information (ESI) available: Full description of the experimental details and additional experimental data are available. See DOI: 10.1039/c9na00486f

‡ These authors contributed equally to this work.



Cite this: *Dalton Trans.*, 2020, **49**, 15425

Tunable NIR-II emitting silver chalcogenide quantum dots using thio/selenourea precursors: preparation of an MRI/NIR-II multimodal imaging agent†

Karishma Bhardwaj,^{‡a} Sajan Pradhan,^{‡a} Siddhant Basel,^a Mitchell Clarke,^b Beatriz Brito,^{‡b,c} Surakcha Thapa,^a Pankaj Roy,^a Sukanya Borthakur,^d Lakshi Saikia,^{‡d} Amit Shankar,^{‡e} Graeme J. Stasiuk,^{‡b,c} Anand Pariyar^{‡a} and Sudarsan Tamang^{‡a}

Aqueous-stable, Cd- and Pb-free colloidal quantum dots with fluorescence properties in the second near-infrared region (NIR-II, 1000–1400) are highly desirable for non-invasive deep-tissue optical imaging and biosensing. The low band-gap semiconductor, silver chalcogenide, offers a non-toxic and stable alternative to existing Pd, As, Hg and Cd-based NIR-II colloidal quantum dots (QDs). We report facile access to NIR-II emission windows with Ag₂X (X = S, Se) QDs using easy-to-prepare thio/selenourea precursors and their analogues. The aqueous phase transfer of these QDs with a high conservation of fluorescence quantum yield (retention up to ~90%) and colloidal stability is demonstrated. A bimodal NIR-II/MRI contrast agent with a tunable fluorescence and high T₁ relaxivity of 408 mM⁻¹ s⁻¹ per QD (size ~ 2.2 nm) and 990 mM⁻¹ s⁻¹ per QD (size ~ 4.2 nm) has been prepared by grafting 50 and 120 monoqua Gd(III) complexes respectively to two differently sized Ag₂S QDs. The size of the nanocrystals is crucial for tuning the Gd payload and the relaxivity.

Received 25th August 2020,
Accepted 24th September 2020

DOI: 10.1039/d0dt02974b

rsc.li/dalton

Introduction

In biological imaging, the second near-infrared (NIR-II, 1000–1400 nm) emitting fluorophores afford, in principle, a higher signal-to-noise ratio compared to their visible (400–750 nm) and NIR-I (750–900 nm region) counterparts.^{1–8} A combination of factors such as low absorbance of water and other biomolecules and low scattering/autofluorescence by tissue makes the NIR-II window ideal for deep-tissue optical

imaging and sensing with a high spatial and molecular resolution.^{5–9} Compared to organic dyes, colloidal quantum dot (QD) based NIR-II fluorophores show a superior quantum yield, size-tunable fluorescence, broad absorption window and high molar extinction coefficient.^{10–12} In addition, the surface of the QDs can be grafted with a high payload of functional molecules such as drugs, antibodies, peptides, nucleic acids, cell-penetrating peptides, MRI contrast agents *etc.*^{13–17} In particular, functionalizing QDs with another imaging agent such as an MRI contrast agent leads to the formation of a multimodal contrast agent which facilitates better visualization compared to a single imaging technique.^{17–19} For example, MRI/NIR-II fluorescent imaging probes enable both excellent molecular level sensitivity (fluorescence) and anatomic resolution (MRI) due to the combination of fluorescence and MRI techniques. In recent years, multimodal imaging agents have gained immense significance in the domain of biomedical imaging.^{18–22}

The majority of the existing lines of QD-based NIR-II fluorophores contain highly toxic Cd²⁺, As^{3–}, Pb²⁺ and Hg²⁺ ions^{23,24} posing a real concern and practical barrier for their application in bio-imaging. In this respect, silver chalcogenides have tremendous potential in the field of *in vivo* bioimaging and sensing.^{2–4,25–27} Ag₂S is non-toxic and has an extremely low

^aDepartment of Chemistry, School of Physical Sciences, Sikkim University, Sikkim 737102, India. E-mail: stamang@cus.ac.in

^bDepartment of Biomedical Sciences, University of Hull, Hull, HU6 7RX, UK

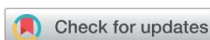
^cDepartment of Imaging Chemistry and Biology, School of Biomedical Engineering and Imaging, King's College London, St Thomas' Hospital, London, SE1 7EH, UK. E-mail: graeme.stasiuk@kcl.ac.uk

^dDepartment of Material Science, North East Institute of Science and Technology (NEIST), Assam 785006, India

^eDepartment of Physics, Kurseong College, West Bengal, 734203, India

†Electronic supplementary information (ESI) available: NMR spectra, FTIR spectra, and TGA spectra of precursors. Additional optical characterization, photographs and XPS spectra of colloidal quantum dots solution. Optical constants of Ag₂S and DFT calculation. NMR, Mass and FTIR characterization of Gd complex and relaxivity studies data. See DOI: 10.1039/D0DT02974B

‡These authors contributed equally to this work.

Cite this: *Nanoscale Adv.*, 2021, 3, 1464

Stable lead-halide perovskite quantum dots as efficient visible light photocatalysts for organic transformations†

Sajan Pradhan,^a Deshaj Bhujel,^a Bikram Gurung,^a Debesh Sharma,^a Siddhant Basel,^a Sagarmani Rasaily,^a Surakcha Thapa,^a Sukanya Borthakur,^b Wai Li Ling,^{b,c} Lakshi Saikia,^b Peter Reiss,^c Anand Pariyar^b and Sudarsan Tamang^{b,*a}

Lead halide perovskite (LHP) based colloidal quantum dots (CQDs) have tremendous potential for photocatalysis due to their exceptional optical properties. However, their applicability in catalysis is restricted due to poor chemical stability and low recyclability. We report halide-passivated, monodisperse CsPbBr₃ CQDs as a stable and efficient visible-light photocatalyst for organic transformations. We demonstrate oxidative aromatization of a wide range of heterocyclic substrates including examples which are poor hydrogen transfer (HAT) reagents. Two to five-fold higher rate kinetics were observed for reactions catalyzed by CsPbBr₃ CQDs in comparison with bulk-type CsPbBr₃ (PNCs) or conventionally synthesized CsPbBr₃ CQDs and other metal organic dyes (rhodamine 6G and [Ru(bpy)₃]²⁺). Furthermore, these CQDs exhibit improved air-tolerance and photostability and in turn show a higher turnover number (TON) of 200, compared to conventionally prepared CQDs (TON = 166) and state-of-the-art bulk-type perovskite-based catalyst (TON = 177). Our study paves the way for the practical applicability of energy-level tunable, size-controlled LHP CQDs as efficient photocatalysts in organic synthesis.

Received 26th November 2020
Accepted 16th January 2021

DOI: 10.1039/d0na00992j

rsc.li/nanoscale-advances

Introduction

Lead halide perovskites (LHPs) have exceptional light absorbing/emitting properties.^{1–5} In particular, the ability of LHPs to facilitate efficient charge separation and transfer upon photon absorption⁶ has been extensively explored in the domain of photovoltaics^{7–11} with power conversion efficiencies approaching the theoretical limit.^{12,13} These unique photo-physical properties of LHPs are also very appealing for activating organic substrates in photoredox catalysis where light absorption, charge separation and transfer are equally important.^{14–19} LHP based colloidal quantum dots (CQDs) with well-defined size and shape, prepared for example by the hot-injection method,²⁰ may have additional advantages compared to larger sized and polydisperse LHP nanocrystals (PNCs) in photocatalysis: first, naturally they have a larger surface area and the energy levels can be tuned as a function of size^{9,21,22} to

control electronic transfer processes with the substrates. Second, these CQDs are highly dispersible in many organic solvents forming a homogeneous colloidal solution, yet with heterogeneous catalytic attributes such as recyclability and separability. And third, due to their monodisperse, well-defined size, shape and surface morphology, surface facet-controlled catalysis^{23–25} with high specificity and affinity for various substrates could be explored. Unfortunately, conventionally prepared size- and shape-controlled LHP CQDs have poor air and moisture stability,^{14,18} limiting their practical application in the photocatalysis. Furthermore, these nanocrystals are typically prepared in small scale compared to their bulk or polydisperse counterparts.^{14,18} In fact, so far efficient photocatalysis of organic transformations were all achieved using highly polydisperse LHP PNCs (ca. 2–100 nm) with an average size too large to be in quantum confinement regime.^{14,18} Conventionally prepared colloidal LHP CQDs, in turn, exhibited poor catalytic efficiency due to their poor tolerance of moisture, oxygen, substrates and solvents compared to these larger sized PNCs. In the literature, various strategies to improve air and moisture stability of LHPs can be found, specially of CsPbI₃ and CsPbBr₃ based perovskites. These strategies encompass the use of additives such as halide salt,²⁶ phosphinic acid,²⁷ ammonium halide,²⁸ 2,2'-iminodibenzoic acid,²⁹ sulphides and metal ions³⁰ and polymers³¹ or imply the application of specific post-synthetic purification steps.^{9,32} While these approaches have

^aDepartment of Chemistry, School of Physical Sciences, Sikkim University, Sikkim 737102, India

^bDepartment of Material Science, North East Institute of Science and Technology (NEIST), Assam 785006, India

^cUniv. Grenoble Alpes, CEA, CNRS, IRIG/SyMMES/STEP, 38000 Grenoble, France

† Electronic supplementary information (ESI) available: Experimental procedures, characterization of photocatalyst, copies of NMR, CV spectra of substrates, kinetic data and turnover number (TON) calculation. See DOI: 10.1039/d0na00992j



Cite this: *Catal. Sci. Technol.*, 2022, 12, 5891

CsPbBr₃ perovskite quantum dots as a visible light photocatalyst for cyclisation of diamines and amino alcohols: an efficient approach to synthesize imidazolidines, fused-imidazolidines and oxazolidines†

Bikram Gurung,[†] Sajjan Pradhan,[†] Debesh Sharma,[†] Deshaj Bhujel, Siddhant Basel,[†] Shivanand Chettri,[†] Sagaramani Rasaily,[†] Anand Pariyar[†] and Sudarsan Tamang^{†*}

We report the synthesis of highly stable CsPbBr₃ QD based photocatalysts using dibromoisocyanuric acid (DBI) as a benign non-toxic bromide precursor. The QDs were applied as a visible light photocatalyst for intramolecular cyclisation of diamines and amino alcohols to obtain a range of enantiopure bioactive heterocycles such as imidazolidines, fused-imidazolidines and 1,3-oxazolidines in high yields (isolated yield up to 82%, ee >99%). The reaction is simple and operates in open air at room temperature and is scalable. The QDs exhibited a high TON (177) and catalytic efficiency (the rate was three times faster compared to conventionally prepared CsPbBr₃ QDs). The apparent quantum efficiency (AQE) of the reaction was close to unity ($\phi = 0.96$ at 460 nm and $\phi = 0.98$ at 436 nm).

Received 28th April 2022,
Accepted 8th August 2022

DOI: 10.1039/d2cy00799a

rsc.li/catalysis

Introduction

Heterocyclic scaffolds such as imidazolidines and 1,3-oxazolidines are the core structures of various natural products and biologically and medicinally active compounds (Fig. 1).

These scaffolds are attractive synthetic targets due to their intriguing bioactivity profiles. Some examples of imidazolidine ring containing frameworks are kifunensine (i),¹ which is a potent inhibitor of class I *R*-mannosidases, and cyanogramide (ii),¹ which has the capacity to reverse the drug resistance of MCF-7, K562, and KB cell lines.² On the other hand, SYK-146 (iii)³ and cyanocycline A (iv)⁴ bearing 1,3-oxazolidine skeletons are potent agonists for the opioid receptor and antitumor/antimicrobial agent, respectively. Besides, they are also broadly exploited as chiral auxiliaries, ligands and organocatalysts in asymmetric synthesis and

catalysis.^{5–8} Several strategies have been reported to assemble these heterocyclic motifs which include: [3 + 2]-annulation reactions,^{9,10} 1,3-dipolar cycloaddition,^{11,12} the condensation reaction of 1,2-amino alcohol/diamine derivatives with carbonyl compounds,^{5,13,14} the *aza*-Wacker reaction,¹⁵ etc. In 2011, Xiao *et al.* reported sp³ C–H bond functionalisation of the *N*-CH₂Ph (benzylic) group and subsequent intramolecular cyclisation of 1,2-diamines using a Ru-based photocatalyst in the presence of a strong base (Fig. 2a).¹⁶ The cyclisation of amines and amino alcohols has emerged as an attractive

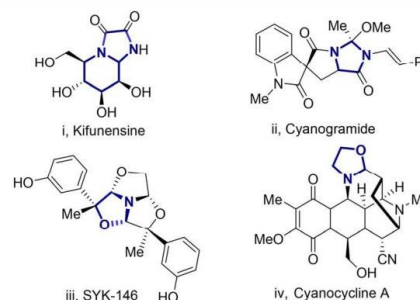


Fig. 1 Selected examples of bioactive imidazolidines and 1,3-oxazolidines.

Department of Chemistry, School of Physical Sciences, Sikkim University, Sikkim 737102, India. E-mail: stamang@cus.ac.in

† Electronic supplementary information (ESI) available: Experimental details, temperature dependent tunability, photoluminescence quantum yield (PLQY) determination, EDX spectra, kinetic studies, recyclability test, TON calculation, CV spectra, quenching experiment, H₂O₂ detection, computational studies, HPLC spectra, ¹H-NMR spectra, and ¹³C-NMR spectra. CIF. CCDC no. 2153616. For ESI and crystallographic data in CIF or other electronic format see DOI: <https://doi.org/10.1039/d2cy00799a>